

THE UNIVERSITY *of* EDINBURGH

This thesis has been submitted in fulfilment of the requirements for a postgraduate degree (e. g. PhD, MPhil, DClinPsychol) at the University of Edinburgh. Please note the following terms and conditions of use:

- This work is protected by copyright and other intellectual property rights, which are retained by the thesis author, unless otherwise stated.
- A copy can be downloaded for personal non-commercial research or study, without prior permission or charge.
- This thesis cannot be reproduced or quoted extensively from without first obtaining permission in writing from the author.
- The content must not be changed in any way or sold commercially in any format or medium without the formal permission of the author.
- When referring to this work, full bibliographic details including the author, title, awarding institution and date of the thesis must be given.

De-Risking CO_2 Sequestration in Sandstone Reservoirs Using Frequency-Dependent AVO Attributes for Enhanced Fluid Detection and Seismic Monitoring



THE UNIVERSITY
of EDINBURGH

Thesis submitted in the fulfillment of the requirements for the degree of
Master in Philosophy (MPhil) in Geology and Geophysics

School of Geosciences
Qamar Bu khamseen
2025

Declaration

I, Qamar Bu khamseen, hereby declare that this thesis has been composed solely by myself and has not been submitted, in whole or in part, for any previous degree application. The work presented herein is entirely my own, unless otherwise explicitly indicated or acknowledged.

Qamar Bu khamseen
June 2025

Abstract

Accurate seismic monitoring of subsurface CO_2 storage fundamentally depends on capturing frequency-dependent dispersion and attenuation phenomena introduced by squirt flow under partial CO_2 saturation. Traditional seismic forward-modelling approaches, which predominantly rely on low-frequency Gassmann–Biot theory, typically neglect these frequency-dependent squirt-flow effects. This omission introduces uncertainties in quantifying velocity dispersion and attenuation, consequently impacting seismic amplitudes and AVO responses that are critical for reliable reservoir characterization and effective CO_2 plume monitoring.

To address these limitations, this thesis integrates a frequency-dependent rock-physics modelling approach with deep learning techniques applied to the Jurassic Sognefjord Formation at the Smeaheia β-structure, located within the Norwegian North Sea. Elastic and petrophysical log data from the Trow 32/2-1 well are initially conditioned and upscaled to seismic resolution. Subsequently, the Papageorgiou & Chapman (2017) hybrid squirt-flow model is systematically applied to simulate the CO_2-induced dispersion and attenuation effects across relaxed, dispersive and unrelaxed frequency regimes. These simulations explore the sensitivity of the seismic attributes to varying degrees of saturation (S_w), capillary pressure (q) and seismic attenuation (Q^{-1}), allowing for the evaluation of frequency-dependent reflectivity across a comprehensive range of synthetic scenarios and offset angles.

The squirt-flow modelling results demonstrate notable frequency-dependent compressional wave softening (ΔV_p reaching up to –25%) and reductions in the compressional modulus (ΔP_{Mod} up to –46%) at intermediate to full CO_2 saturations under conditions of high attenuation (Q=10), in the dispersive state (W_c= 0), relative to the 100% brine baseline (Q=1000, W_c= –2). To illustrate these combined effects, a frequency-dependent amplitude-versus-offset (FAVO) rock-physics template was developed from the forward modelled scenarios. This template highlights increased amplitude sensitivity at lower frequencies (≤ 20 Hz) and larger offsets (30°– 40°), conditions that clearly discriminate higher CO_2 saturations, particularly under elevated attenuation levels (Q = 10). Furthermore, larger capillary pressure contrasts (q = 0.054) moderate these amplitude responses, reducing magnitudes and flattening AVO gradients, yet still preserving distinct signatures

indicative of CO_2 saturation and reservoir pressure variations. Nevertheless, the conducted feasibility study, integrating frequency-dependent reflectivity modelling, spectral decomposition and FAVO analysis, revealed that squirt-flow-related dispersive changes manifest as seismic-scale phase shifts and amplitude variations. However, the precise quantification of such CO_2-induced signatures is complicated by seismic interference from the combined effects of thin-bed tuning and frequency-dependent squirt-flow, which together mask the squirt-flow attenuation effects expected in spectral decomposition while exaggerating AVO responses in the higher-frequency range (60–90 Hz).

Given these interpretational challenges, frequency-dependent spectral amplitudes were subsequently integrated into a two-dimensional convolutional neural network (2D CNN) as a proposed mitigation strategy. This CNN was designed with multiple parallel classification outputs, enabling simultaneous inversion for CO_2 saturation, capillary pressure, and attenuation parameters. After hyperparameter optimization, the CNN demonstrated excellent predictive performance, achieving an average accuracy of 96.99%, a holistic classification accuracy of 92.6%, and an average F_1-score of 96.92% across the different S_w, q, and Q^{-1} attribute classifiers. The achieved performance indicates the model's capability in effectively distinguishing between the CO_2-induced responses and interference-related complexities, emphasizing the potential use of frequency-dependent spectral amplitudes for accurate reservoir attribute predictions.

Hence, this thesis ultimately demonstrates that integrating frequency-dependent rock-physics modelling with advanced machine-learning inversion techniques enhances the seismic monitoring and characterization of CO_2 plumes within sandstone reservoirs.

Lay Summary

Carbon Capture and Storage (CCS) is a vital strategy for reducing atmospheric carbon dioxide (CO_2) emissions. CCS involves capturing industrial CO_2, transporting it, and injecting it deep underground into suitable geological formations, such as depleted oil and gas reservoirs or saline aquifers, ensuring secure storage over extended periods.

Effective monitoring is essential to guarantee that CO_2 remains safely contained underground. To achieve this, geophysicists use rock physics, a field connecting seismic responses to the physical properties of subsurface rocks. Traditional rock physics typically employs Gassmann Fluid Substitution (GFS), which estimates how replacing original reservoir fluids with CO_2 affects the rock's elastic properties. However, this traditional method, based on Gassmann-Biot theory, overlooks important frequency-dependent effects like velocity dispersion and seismic attenuation, which arise from squirt-flow mechanisms that occur in partially CO_2-saturated reservoirs.

In simple terms, when seismic waves pass through a porous fluid saturated reservoir, they compress the rock, forcing fluids to move from narrow cracks into larger pore spaces. This movement creates internal pressure differences within the rock, changing the way seismic waves travel. Consequently, seismic velocities vary with frequency causing dispersion while the seismic waves lose energy and attenuate. Both dispersion and attenuation impact the seismic signals, affecting how accurately geophysicists can detect and monitor the CO_2 stored underground.

Recognizing these limitations, this thesis investigates a frequency-dependent rock physics modeling approach specifically applied to the potential Smeaheia CO_2 storage site, targeting the Sognefjord Formation in the North Sea. The developed modeling incorporates squirt flow mechanisms, demonstrating how variations in CO_2 saturation, capillary pressure, and attenuation affect seismic responses at different frequencies.

To further enhance the interpretation of CO_2-induced seismic responses, this research integrates machine learning methods, specifically two-dimensional convolutional neural networks (2D CNN). The CNN model developed in this study directly predicts key reservoir properties (CO_2

saturation, capillary pressure, and attenuation) from frequency-dependent seismic data. Thus, by combining advanced modeling and machine learning, the workflow presented in this thesis potentially improves the reliability of CO_2 seismic monitoring.

Acknowledgements

I would like to express my heartfelt gratitude towards my professors, Dr. Mark Chapman and Dr. Giorgos Papageorgiou, for their continuous support and unwavering patience throughout my research. Their insightful discussions and guidance have been invaluable in navigating the complexities of my studies. I am particularly grateful for their endless assistance with programming, which has significantly contributed to my progress and productivity during this MPhil program.

Furthermore, I would like to extend my sincere thanks to Dr. Kathy Whaler for her supportive and informative role as my advisor. Her input has been instrumental in shaping my research.

Equally important, I would also like to acknowledge Saudi Aramco Oil Company for their generous sponsorship, which has provided me with the financial resources and time required in order to fully dedicate myself for this academic pursuit. This opportunity has profoundly enriched my educational experience and facilitated significant technical growth and professional development.

Lastly, I want to convey my deepest appreciation to my husband and family for their consistent encouragement and reassurance, which have been a constant source of strength throughout my academic journey.

Table of Content

DECLARATION II

ABSTRACT III

LAY SUMMARY V

ACKNOWLEDGEMENTS VII

LIST OF FIGURES X

LIST OF TABLES XV

LIST OF PARAMETERS AND ABBREVIATIONS ..... **XVI**

1. INTRODUCTION 1

1.1 Carbon Capture and Storage (CCS) **1**

1.2 Implications on Seismic Velocities for Partially Saturated Reservoirs **1**

1.3 Frequency-Dependent Rock Physics: Addressing Squirt-Flow Dispersion and Attenuation **2**

1.4 Development of Squirt-Flow Models **4**

1.5 Primary Research Objective **5**

1.6 Thesis Outline **6**

2 GEOLOGICAL BACKGROUND: SOGNEFJORD FORMATION (SFJORD) 8

3 CONVENTIONAL ROCK PHYSICS FORWARD MODELLING 10

3.1 Introduction **10**

3.2 Methodology **10**

3.2.1 Well Log Analysis and Data Conditioning 10

3.2.2 Gassmann Fluid Substitution (GFS) 25

3.2.3 Synthetic Generation & AVO Analysis 37

3.3 Results & Discussion **40**

4 FREQUENCY-DEPENDENT ROCK PHYSICS FORWARD MODELLING 53

4.1 Introduction 53

4.2 Theoretical Background: Squirt-Flow Model 54

4.3 Rock Physics Forward Modelling Workflow 57
4.3.1 Well Log Analysis & Data Conditioning 58
4.3.2 Log Data Upscaling to Seismic Scale 59
4.3.3 Parameter Sampling ($\boldsymbol{Sw}$, $\boldsymbol{q}$, $\boldsymbol{Q-1}$) and Combination Sets 63
4.3.4 Squirt-Flow Modelling 66
4.3.5 Synthetics: Frequency-Dependent Convolutional Modelling and Reflectivity 74
4.3.6 Spectral Decomposition 75
4.3.7 Spectral Balancing 84
4.3.8 Frequency-Dependent (FAVO) Analysis 85

4.4 Machine Learning Workflow and Implementation 86
4.4.1 Introduction 86
4.4.2 Objective & Scope 88
4.4.3 Data Collection & Pre-Processing 90
4.4.4 Model Selection 91
4.4.5 Neural Network Architecture : (2D CNN) 92
4.4.6 Model Training and Validation 97

4.5 Results & Discussion 100
4.5.1 Frequency-Dependent Rock Physics Forward Modelling 100
4.5.2 Deep Learning : 2D CNN 128

5 CONCLUSION 132

5.1 Integrated Discussion 132

5.2 Conclusion 136

5.3 Future Recommendation 137

6 REFERENCES 139

List of Figures

FIGURE 2.1 - **(A)** LOCATION OF THE SMEAHEIA CO_2 STORAGE SITE, OFFSHORE NORWAY, WITH THE ALPHA AND BETA STRUCTURAL CLOSURES. **(B)** SW-NE INLINE OF 3D SURVEY GN1101 OVER THE SMEAHEIA REGION DISPLAYING THE LOCATION OF TROW 32/2_1, SITUATED ON THE CRESTAL DIP OF THE BETA STRUCTURAL ANTICLINE DOWNTHROWN TO THE ØYGARDEN FAULT COMPLEX (FAWAD ET AL., 2021). THE SEISMIC PROFILE IS PRESENTED IN TWO-WAY TRAVEL TIME (TWT, MS) WITH THE VERTICAL TWT SCALE DISPLAYED SCHEMATICALLY WITHOUT NUMERICAL ANNOTATIONS. THE RESERVOIR TOPS OF THE SOGNEFJORD (SFJORD) FORMATION, OF PARTICULAR INTEREST TO THIS THESIS, ARE SITUATED AT APPROXIMATELY 1200 M DEPTH AT WELL 32/4-1(ALPHA) AND 900 M DEPTH AT WELL 32/2-1 (BETA). 9

FIGURE 3.1 – COMPONENTS OF A SHALEY SANDSTONE RESERVOIR IN AN EFFECTIVE OR TOTAL POROSITY SYSTEM (SIMM & BACON, 2014B)..... 13

FIGURE 3.2 – INVESTIGATING THE DISTRIBUTION OF EFFECTIVE POROSITY BETWEEN SANDS AND SHALES WITHIN THE DIFFERENT RESERVOIR FORMATIONS ACROSS THE WELL, PARTICULARLY FOCUSING ON THE SOGNEFJORD FORMATION (SFJORD). RESULTS SHOW THAT SCENARIO 1 PROVIDES THE BEST REPRESENTATION FOR THE EFFECTIVE POROSITY DISTRIBUTION BETWEEN SANDS AND SHALES. 15

FIGURE 3.3 –ELASTIC AND PETROPHYSICAL LOGS THAT CHARACTERIZE THE DIFFERENT FORMATIONS ACROSS THE TROW 32/2_1 WELL. TRACK 1 DISPLAYS THE CALIPER AND BS TO MONITOR THE BOREHOLE CONDITIONS. TRACK 2 DISPLAYS THE GR LOG TO VERIFY THE SAND AND SHALE LITHOLOGY COMPONENTS. TRACK 3 DESCRIBES THE COMPOSITION OF THE RESERVOIR'S SOLID MATRIX. TRACK 4 DISPLAYS A POROSITY-SATURATION SET THAT QUANTIFIES THE EFFECTIVE POROSITY AT A GIVEN DEPTH AND ITS CORRESPONDING PORE FLUID CONTENT. TRACKS 5,6 AND 7 DISPLAY THE ELASTIC LOGS THAT CHARACTERIZE THE RESERVOIR (VP, VS AND P), RESPECTIVELY. 17

FIGURE 3.4 – THE P VERSUS V_P ($P - V_P$) AND V_S VERSUS V_P ($V_S - V_P$) CROSS-PLOTS FOR THE DIFFERENT SANDSTONE RESERVOIR FORMATIONS ACROSS TROW 32/2_1 CHARACTERIZED BY DIFFERENT RESERVOIR ATTRIBUTES. **(A, B AND C)** ARE V_P VS. P CROSS-PLOTS COLORED BY EFFECTIVE PORSOITY, VOLUME OF SHALE AND EFFECTIVE WATER SATURATION, RESPECTIVELY. **(D, E AND F)** ARE V_P VS. V_S CROSS-PLOTS COLORED BY EFFECTIVE PORSOITY, VOLUME OF SHALE AND EFFECTIVE WATER SATURATION, RESPECTIVELY. 18

FIGURE 3.5 – THE P VERSUS V_P ($P - V_P$) AND V_S VERSUS V_P ($V_S - V_P$) FOR THE DIFFERENT SANDSTONE RESERVOIR FORMATIONS ACROSS TROW 32/2_1 CHARACTERIZED BY DIFFERENT RESERVOIR ATTRIBUTES WITH APPLIED SATURATION AND SHALE VOLUMETRIC CUT-OFFS (VOLSH ≥ 0.8 AND SWE ≥ 0.8). THIS WAS DONE TO QC THE GC SHALE LITHOLOGY TREND AND WILL BE USED TO UPDATE THE ELASTIC PROPERTIES OF THE SHALE CONSTITUENT. PANELS **(A-C)** ALSO DISPLAY THE "UPDATED GARDNER SHALE LITHOLOGY TREND" (RED) AFTER FITTING THE CLEANER SHALE LITHOLOGY USING THE SAME CUT-OFFS. PANELS **(D-F)** SHOW THAT THE "ORIGINAL G/C SHALE TREND" (GREEN) IS A GOOD FIT OF THE CURRENT DATA AND THEREFORE, DOES NOT REQUIRE CORRECTION. 21

FIGURE 3.6 – WELL-VIEW PANEL FOR TROW 32/2_1 DISPLAYING THE ELASTIC PROPERTIES OF DRAUPNE, HEATHER AND SOGNEFJORD FORMATIONS. TRACK 1 DISPLAYS THE RESERVOIR'S MATRIX COMPOSITION. TRACKS 2 AND 4 DISPLAY THE IN-SITU V_P AND DENSITY LOGS ACROSS THE LATTER FORMATIONS. TRACK 3 COMPARES OUR PERSONAL GC PREDICTIONS VERSUS A VS PREDICTED LOG OBTAINED FROM DR. MANZAR FAWAD. BOTH VS PREDICTIONS ARE VERY SIMILAR ACROSS THE SAME FORMATIONS. 24

FIGURE 3.7 – THE V_S VERSUS V_P ($V_S - V_P$) CROSS-PLOTS OVERLAID BY GC SAND AND SHALE LITHOLOGY TRENDS. (A) COMPARES OUR GC VS PREDICTION WITH THE V_S PREDICTION FROM DR. MANZAR FAWAD FOR DRAUPNE AND HEATHER FORMATONS. (B) COMPARES THE LATTER TWO VS PREDICTIONS FOR THE SOGNEFJORD FORMATION. 25

FIGURE 3.8 – THE EFFECTIVE FLUID MODULUS FOR THE CO_2 FLUID MIXTURE IN THE SOGNEFJORD RESERVOIR, CALCULATED AT Q=1 AND q_o=0.054 FOR VARIOUS CO_2 SATURATIONS..... 35

FIGURE 3.9 – (A) ZERO-PHASE RICKER WAVELET GENERATED AT F=50 HZ. (B) POSITIVE STANDARD POLARITY (ALSO REFERRED TO AS AMERICAN POLARITY) REPRESENTS A POSITIVE REFLECTION AS A PEAK, CORRELATING TO AN INCREASE IN ACOUSTIC IMPEDANCE ACROSS A GIVEN INTERFACE. SOFT DENOTES SOFTER LITHOLOGY WHEREAS HARD REPRESENTS A STIFFER LITHOLOGY. (MODIFIED AFTER (SIMM & BACON, 2014A)). 40

FIGURE 3.10 - GASSMANN FLUID SUBSTITUTION RESULTS FOR THE SOGNEFJORD RESERVOIR AT DIFFERENT CO_2 SATURATIONS FOR UNIFORM SATURATION ($Q = 1$). THE ELASTIC RESPONSES FOR THE COMPRESSIONAL VELOCITY, DENSITY, BULK MODULUS, ACOUSTIC IMPEDANCE, THE POISSON AND VELOCITY RATIOS DECREASE WITH INCREASING CO_2 SATURATIONS. CONVERSELY, THE SHEAR-WAVE VELOCITY SLIGHTLY INCREASES..... 42

FIGURE 3.11 – THIS FIGURE IS A QC PLOT FOR THE DRY ROCK MODELLING PHASE. IT PRESENTS THE NORMALIZED BULK MODULUS KDRYKM VS. EFFECTIVE POROSITY OVERLAID BY PORE-SPACE STIFFNESS BOUNDS. THE OUTLIER POINTS FALLING ABOVE THE STIFFEST PORE SPACE STIFFNESS BOUND, AT KDRYKM > 1 WILL RESULT IN A VERY SMALL FLUID EFFECT (STIFF GFS RESPONSE). CONVERSELY, THE

outlier data points falling below, at $KdryKm < 0$ will simulate an exaggerated fluid effect (very soft response). These data points correlate to shalier non-reservoir content at relatively lower effective porosities..... 43
Figure 3.12 – The impact of uniform versus patchy saturations on the Sognefjord reservoir for different CO_2 mixtures. The lower velocity-saturation curve represents uniform distribution ($Q = 1$) that results in a soft elastic response. The upper velocity-saturation bound represents the patchy saturation ($Q = 0.054$) that results in a stiffer elastic response, for the same CO_2 concentration. 45
Figure 3.13 – **(A)** Gassmann Fluid Substitution results for the Sognefjord reservoir comparing uniform versus patchy saturations for the Brine40 fluid mixture. The results show that the change (decrease) in elastic responses produced by patchy saturation (dashed orange line) are smaller compared to the uniform saturation (solid yellow line). **(B)** Gassmann Fluid Substitution results for the Sognefjord reservoir at different CO_2 saturations under patchy saturation ($Q0 = 0.054$) conditions. The elastic responses for the compressional velocity, density, bulk modulus, acoustic impedance, the Poisson and velocity ratios decrease with increasing CO_2 saturations. Conversely, the shear-wave velocity slightly increases. 46
Figure 3.14 – Pre-stack Rock Physics Template for the Sognefjord Reservoir: AI vs. Vp/Vs Ratio for different CO_2 mixtures. **(A – B)** AI vs. Vp/Vs ratio at Uniform Saturation **(C-D)** AI vs. Vp/Vs Ratio at Patchy saturation. The linear CO_2 discriminator line is of the following representation: Vp/Vs Ratio = m*AI + b. The yellow highlighted zone indicates the data falling below the discriminator is mapping CO_2 fluids. 48
Figure 3.15 - Pre-stack Rock Physics Template: AI vs. Vp/Vs Ratio for Brine100 and Brine80. **(A)** The AI and Vp/Vs ratio responses for the Brine80 fluid mixture has been colored by volume of Quartz. **(B)** The AI and Vp/Vs ratio responses for the Brine80 fluid mixture has been colored by effective porosity. This figure demonstrates that the CO_2 discriminator line primarily targets the higher porosity CO_2-saturated sandy intervals within the Sognefjord reservoir, as highlighted by the yellow zone. 48
Figure 3.16 – **(A)** AVA seismic responses for different CO_2 mixtures, across the Sognefjord reservoir, at uniform saturation. CO_2 mixtures display a class III AVA response, stronger reflectivity and steeper gradient at larger offset angles. **(B)** AVA seismic responses for different CO_2 mixtures, across the Sognefjord reservoir, at patchy saturation. This figure shows a change in reflectivity with weaker amplitudes and shallower gradients for the Brine80 – Brine40 fluid mixtures. 50
Figure 3.17 – **(A)** AVA Pre-stack Synthetic gathers for different CO_2 mixtures at uniform saturation. Increasing CO_2 saturation results in amplitude brightening. **(B)** AVA Pre-stack Synthetic gathers for different CO_2 mixtures at patchy saturation. This figure illustrates the CO_2-induced seismic reflectivity changes across the Sognefjord (SFjord) interface between uniform and patchy saturations. Generally, the reflectivity at patchy saturations is weaker compared to the stronger reflectivity (higher amplitude) at uniform saturation. 51
Figure 4.1 – Comparison of conventional and frequency-dependent rock-physics workflows. The frequency-dependent approach reverses the traditional modelling sequence by first upscaling logs and then applying squirt-flow modelling to explicitly preserve the frequency-dependent dispersion attenuation effects. 58
Figure 4.2 – Backus-averaged in-situ elastic and petrophysical logs for Trow 32/2_1 in the depth domain. The smoother Backus-averaged logs (green), computed using a 5.5 m window, are superimposed on the original, higher-resolution in-situ logs (black). 63
Figure 4.3 – Final upscaled in-situ elastic and petrophysical logs for Trow 32/2_1, obtained by applying Backus averaging with a 5.5 m window and subsequent TWT resampling (1 ms). 63
Figure 4.4 – Probability density functions (PDFs) used for parameter sampling. **(A)** Water saturation (Sw) , represented by three normal distributions ("Low," "Mid," "High"). **(B)** Capillary pressure (Q), represented by two lognormal distributions ("Uniform," "Patchy"). **(C)** High attenuation (Q-1), represented by a lognormal distribution. Distribution parameters (mean and standard deviation) are provided in Table (8). 66
Figure 4.5 – Workflow diagram illustrating the frequency-dependent squirt flow (SQF) implementation, highlighting key steps in the modeling process. 68
Figure 4.6 – Multi-layer squirt-flow model displaying elastic inputs and dispersive outputs at Q=10, Q=0.6, and S_w=0.4. The overburden and underburden intervals are represented by upscaled in-situ logs, whereas the SFjord reservoir interval uses fully brine-saturated logs. Squirt-flow modelling is conducted exclusively within the defined dispersive zone (31 m interval at the top of the SFjord reservoir ≈ 23.1 ms). 69
Figure 4.7 – **(A)** Effective fluid modulus (KCO2_Mix) as a function of water saturation for different capillary pressure (Q) parameters, illustrating that increased capillary pressure (lower Q values) stiffens the fluid mixture at intermediate saturations. **(B)** Brooks–Corey relative permeability curves for water (blue) and CO_2 (red),

INDICATING FLUID MOBILITY ACROSS SATURATION RANGES. **(C)** DIMENSIONLESS FREQUENCY (W_C) VERSUS SATURATION, HIGHLIGHTING TRANSITIONS BETWEEN RELAXED, DISPERSIVE, AND UNRELAXED REGIMES AS INFLUENCED BY RELATIVE PERMEABILITY AND CAPILLARY FORCES..... 72
FIGURE 4.8 – DEFINED SPECTRAL DECOMPOSITION TIME WINDOW FOR THE SFJORD RESERVOIR INTERVAL (1030–1126 MS), DISPLAYING THE EMBEDDED DISPERSIVE LAYER. THIS INTERVAL WAS SPECIFICALLY CHOSEN TO INVESTIGATE HOW VARIATIONS IN KEY PARAMETERS **(S_W , Q, Q^{-1})** INFLUENCE THE SEISMIC AMPLITUDES AT BOTH THE TOP SFJORD INTERFACE AND DEEPER REFLECTORS WITHIN THE DISPERSIVE RESERVOIR ZONE. THE RIGHTMOST TRACK SHOWS A REPRESENTATIVE FREQUENCY-DEPENDENT SYNTHETIC GATHER (0–40°) GENERATED USING THE CONVOLUTIONAL REFLECTIVITY MODEL FOR 20% BRINE AT Q=10, W_C=0 AT UNIFORM PRESSURE (Q=1). 77
FIGURE 4.9 – COMPARISON OF HANN, BLACKMAN, AND BLACKMAN–HARRIS WINDOW FUNCTIONS AT VARYING NPERSEG NPERSEG , DEMONSTRATING THEIR TRADE-OFFS IN SIDELOBE SUPPRESSION AND FREQUENCY RESOLUTION. BLACKMAN–HARRIS AT NPERSEG=48 IS SELECTED FOR OPTIMAL TIME–FREQUENCY BALANCE. 80
FIGURE 4.10 – STFT SPECTROGRAMS OF A FULLY CO_2-SATURATED SEISMIC TRACE AT NORMAL INCIDENCE, GENERATED USING VARYING NOVERLAP AND NFFT PARAMETERS. PANEL **(A)** USES NFFT = 128 WITH A STANDARD OVERLAP, RESULTING IN A BLOCKY AND DISCRETE SPECTRAL REPRESENTATION. PANEL **(B)** MAINTAINS NFFT=128 BUT EMPLOYS A FINER, SAMPLE-BY-SAMPLE OVERLAP, SLIGHTLY ENHANCING TEMPORAL CONTINUITY. PANEL **(C)**, USING THE SAME FINE OVERLAP APPROACH WITH NFFT= 2048, DEMONSTRATES SIGNIFICANTLY IMPROVED SPECTRAL RESOLUTION AND SMOOTHER AMPLITUDE TRANSITIONS, CLEARLY HIGHLIGHTING SUBTLE AMPLITUDE VARIATIONS. 81
FIGURE 4.11 – STFT SPECTROGRAMS COMPUTED FOR THE DIFFERENT OFFSET TRACES (0–40°) FROM A SINGLE SYNTHETIC GATHER: (40% BRINE, Q = 20, Q = 1, $W_C = 0$). VARIATIONS IN AMPLITUDE DISTRIBUTION WITH INCREASING OFFSET HIGHLIGHT FREQUENCY-DEPENDENT SPECTRAL SHIFTS AND ENERGY REDISTRIBUTION, REFLECTING DISPERSION AND ATTENUATION EFFECTS WITHIN THE PARTIALLY CO_2-SATURATED SFJORD RESERVOIR. 83
FIGURE 4.12 – SCHEMATIC ILLUSTRATING THE OFFSET-SPECIFIC SPECTRAL BALANCING WORKFLOW. THE AMPLITUDE SPECTRA OF VARIOUS BRINE–CO_2 MIXTURES ARE NORMALIZED AGAINST A PURE-BRINE REFERENCE SPECTRUM, EFFECTIVELY REMOVING THE SOURCE WAVELET IMPRINT AND REVEALING THE UNDERLYING FREQUENCY-DEPENDENT AVO TRENDS. 85
FIGURE 4.13 – SCHEMATIC ILLUSTRATING THE EXTRACTION OF ISO-FREQUENCY SPECTRAL AMPLITUDES. MEAN SPECTRAL AMPLITUDES ARE COMPUTED ACROSS ALL TEMPORAL FRAMES AT SELECTED ISO-FREQUENCIES FOR EACH OFFSET ANGLE, WITH THIS PROCEDURE SYSTEMATICALLY REPEATED ACROSS ALL BRINE–CO_2 SATURATION MIXTURES. 86
FIGURE 4.14 – OVERVIEW OF THE MACHINE LEARNING WORKFLOW, ILLUSTRATING KEY STAGES FROM PROBLEM SCOPING THROUGH MODEL DEPLOYMENT, INCLUDING ITERATIVE HYPERPARAMETER TUNING DURING MODEL TRAINING AND VALIDATION 89
FIGURE 4.15 – ARCHITECTURE OF THE 2D CNN MODEL, CONTAINING A SHARED CONVOLUTIONAL ENCODER BLOCK THAT FEEDS INTO THREE INDIVIDUAL FULLY CONNECTED NEURAL NETWORKS (FCNN), EACH EQUIPPED WITH ITS OWN CLASSIFICATION HEAD FOR SIMULTANEOUSLY PREDICTING S_w, Q AND Q^{-1}. 93
FIGURE 4.16 – THE RECTIFIED LINEAR ACTIVATION FUNCTION (SHIVANSH, 2024). 94
FIGURE 4.17 – COMPARISON OF COMPRESSIONAL MODULUS (PMOD) LOGS FROM THE CONVENTIONAL GFS WORKFLOW (BLACK) AND THE FREQUENCY-DEPENDENT SQF MODEL (COLORED) AT THE LOW-FREQUENCY RELAXED LIMIT AT Q = 1000, Q=1, W_C= –2, CONFIRMING BASELINE AGREEMENT (GFS ≈ SQF) WITHIN THE SOGNEFJORD RESERVOIR. 101
*FIGURE 4.18 – WELL-VIEW PANELS DISPLAYING THE SQF-DERIVED RESPONSES COMPUTED AT THE RELAXED, LOW FREQUENCY CONDITION (Q = 1000, W_C= –2) FOR Q = 1 AND Q0 = 0.054. BOTH PANELS **(A) & (B)** REPRODUCE SIMILAR ELASTIC TRENDS IN VP, VS, P, PMOD AND SMOD, AS PREVIOUSLY NOTED FOR THE CORRESPONDING GFS CASES, VERIFYING THAT BOTH WORKFLOWS YIELD EQUIVALENT RESULTS UNDER LOW-FREQUENCY, NEGLIGIBLE DISPERSION CONDITIONS.* 102
*FIGURE 4.19 – RELATIVE CHANGES (%) IN ELASTIC ATTRIBUTES BENCHMARKED TO THE 100% BRINE BASELINE AT LOW-FREQUENCY, RELAXED CONDITIONS (Q = 100, W_C= –2). **(A)** BULK DENSITY (P), **(B)** COMPRESSIONAL VELOCITY (VP) AND MODULUS (PMOD), **(C)** SHEAR VELOCITY (VS) AND MODULUS (SMOD). THE DIFFERENT PANELS HIGHLIGHT THE VARYING SENSITIVITY OF THESE ELASTIC PROPERTIES TO CO_2 SATURATION AND CAPILLARY PRESSURE (Q=1 AND Q0 =0.054) CHANGES, UNDER NEGLIGIBLE DISPERSION CONDITIONS.* 103
*FIGURE 4.20 – SATURATION-DEPENDENT DISPERSIVE BEHAVIOR ILLUSTRATED BY CROSS-PLOTS OF ELASTIC ATTRIBUTES (VP, VS, PMOD, SMOD) AND THE ASSOCIATED ATTENUATIONS (QP-1 AND QS-1) AT UNIFORM CAPILLARY PRESSURE (Q=1) ACROSS DIFFERENT FREQUENCY REGIMES (W_C ∈ {–2, –1, 0, 1, 2}). PANELS **(A-D)** PROGRESSIVELY INCREASE ATTENUATION (Q^{-1}, WITH Q ∈ {1000, 30, 20, 10}), HIGHLIGHTING SIGNIFICANT DISPERSION IN COMPRESSIONAL (VP, PMOD) ATTRIBUTES AND MINIMAL SENSITIVITY IN SHEAR (VS, SMOD) ATTRIBUTES.* 106
FIGURE 4.21 – SATURATION-DEPENDENT DISPERSIVE BEHAVIOR ILLUSTRATED BY CROSS-PLOTS OF ELASTIC ATTRIBUTES (VP, VS, PMOD, SMOD) AND THE ASSOCIATED ATTENUATIONS (QP-1 AND QS-1) UNDER HIGHER CAPILLARY PRESSURE (Q_0=0.054) ACROSS

DIFFERENT FREQUENCY REGIMES ($W_C \in \{-2, -1, 0, 1, 2\}$). PANELS **(A-D)** SHOW INCREASING ATTENUATION (Q^{-1}, WITH $Q \in \{1000, 30, 20, 10\}$). COMPARED TO THE UNIFORM PRESSURE SCENARIO ($Q=1$; FIGURE (4.20)), INCREASED CAPILLARY PRESSURE STIFFENS ELASTIC RESPONSES, NOTABLY REDUCING VELOCITY DISPERSION AND ATTENUATION MAGNITUDES AT INTERMEDIATE SATURATIONS. 107

FIGURE 4.22 – RELATIVE CHANGES (%) IN COMPRESSIONAL ATTRIBUTES (V_p AND PMOD) COMPARED TO THE 100% BRINE BASELINE AT NEGLIGIBLE ATTENUATION ($Q = 1000$, $W_C = -2$) ACROSS DIFFERENT FREQUENCY REGIMES. PANELS **(A, D)** ILLUSTRATE RELATIVE CHANGES AT UNIFORM CAPILLARY PRESSURE ($Q = 1$) AND NEGLIGIBLE ATTENUATION ($Q = 1000$), HIGHLIGHTING SENSITIVITY TO CO_2 SATURATION CHANGES. PANELS **(B, E)** DISPLAY RELATIVE CHANGES AT UNIFORM CAPILLARY PRESSURE ($Q = 1$) WITH MAXIMUM ATTENUATION ($Q = 10$), EMPHASIZING SQUIRT-FLOW ATTENUATION EFFECTS. PANELS **(C, F)** DEMONSTRATE RELATIVE CHANGES AT INCREASED CAPILLARY PRESSURE ($Q_0 = 0.054$) AND MAXIMUM ATTENUATION ($Q = 10$). THESE RESULTS DEMONSTRATE THE SENSITIVITY OF COMPRESSIONAL ATTRIBUTES TO VARIATIONS IN CO_2 SATURATION, SQUIRT-FLOW ATTENUATION, AND CAPILLARY PRESSURE. 110

*FIGURE 4.23 – RELATIVE CHANGES (%) IN THE SHEAR ATTRIBUTES (VS AND SMOD) COMPARED TO THE 100% BRINE BASELINE AT NEGLIGIBLE ATTENUATION ($Q = 1000$, $W_C = -2$) ACROSS DIFFERENT FREQUENCY REGIMES. PANELS **(A, D)** ILLUSTRATE RELATIVE CHANGES UNDER UNIFORM CAPILLARY PRESSURE ($Q = 1$) AND NEGLIGIBLE ATTENUATION ($Q = 1000$). PANELS **(B, E)** DISPLAY RELATIVE CHANGES AT $Q=1$ AND MAXIMUM ATTENUATION ($Q=10$). PANELS **(C, F)** DISPLAY RELATIVE CHANGES AT INCREASED CAPILLARY PRESSURE ($Q0=0.054$) AND $Q=10$. THESE RESULTS DEMONSTRATE THAT SHEAR ATTRIBUTES EXHIBIT LOWER SENSITIVITY TOWARDS VARIATION IN CO_2 SATURATIONS, SQUIRT-FLOW DISPERSION AND CAPILLARY PRESSURE COMPARED TO THE COMPRESSIONAL ATTRIBUTES .* 111

*FIGURE 4.24 – ABSOLUTE CHANGES IN THE P- AND S-WAVE ATTENUATION CURVES (Q_P-1 AND Q_S-1) COMPARED TO THE 100% BRINE BASELINE AT NEGLIGIBLE ATTENUATION ($Q = 1000$, $W_C = -2$) ACROSS DIFFERENT FREQUENCY REGIMES. PANELS **(A, D)** CONFIRM THAT SQUIRT FLOW IS INACTIVE AT NEGLIGIBLE ATTENUATION ($Q = 1000$, $Q=1$). PANELS **(B, E)** ILLUSTRATE INCREASED ATTENUATION ($Q = 10$, $Q = 1$) EFFECTS, SHOWING PRONOUNCED BELL-SHAPED PEAKS IN THE DISPERSIVE REGIME ($W_C = 0$). PANELS **(C, F)** DEMONSTRATE THAT HIGHER CAPILLARY PRESSURE ($Q0 = 0.054$) AT THE SAME $Q = 10$) MODIFIES ATTENUATION, REDUCING MAGNITUDES AT INTERMEDIATE SATURATIONS AND ENHANCING THEM AT HIGH CO_2 SATURATIONS.* 112

FIGURE 4.25 – FREQUENCY-DEPENDENT SYNTHETIC GATHERS ILLUSTRATING SENSITIVITY TO CAPILLARY PRESSURE VARIATIONS AT NEGLIGIBLE ATTENUATION ($Q = 1000$, $W_C = -2$.) **(A)** UNIFORM CAPILLARY PRESSURE ($Q=1$), DISPLAYING AMPLITUDE BRIGHTENING WITH INCREASING CO_2 SATURATION. **(B)** INCREASED CAPILLARY PRESSURE ($Q_0=0.054$) REDUCES AMPLITUDE AT INTERMEDIATE SATURATIONS. **(C)** OVERLAY COMPARISON BETWEEN PANELS A AND B. PANEL C IMPLIES THAT IN THE ABSENCE OF ATTENUATION, CAPILLARY EFFECTS MANIFEST IN AMPLITUDE VARIATIONS ACROSS THE DESIRED TARGET WITH NO VISIBLE PHASE SHIFTS OR SQUIRT-FLOW-RELATED DISPERSION EFFECTS. 114

FIGURE 4.26 – FREQUENCY-DEPENDENT SYNTHETIC GATHERS ILLUSTRATING ATTENUATION EFFECTS ON SEISMIC AMPLITUDES. **(A)** NEGLIGIBLE ATTENUATION ($Q = 1000$) AT UNIFORM CAPILLARY PRESSURE ($Q = 1$) SHOWS MINIMAL AMPLITUDE VARIATIONS ACROSS CO_2 SATURATIONS. **(B)** HIGH ATTENUATION ($Q = 10$, $Q=1$) AT DISPERSIVE STATE ($W_C = 0$) RESULTS IN PRONOUNCED AMPLITUDE BRIGHTENING, ESPECIALLY AT INTERMEDIATE TO FULL CO_2 SATURATIONS. **(C)** OVERLAY COMPARISON HIGHLIGHTING AMPLITUDE VARIABILITY DRIVEN BY INCREASED ATTENUATION. 117

FIGURE 4.27 – FREQUENCY-DEPENDENT SYNTHETIC GATHERS ILLUSTRATING THE COMBINED EFFECTS OF HIGHER CAPILLARY PRESSURE AND ATTENUATION. **(A)** INCREASED CAPILLARY PRESSURE ($Q0=0.054$) AT NEGLIGIBLE ATTENUATION ($Q =1000$) SIGNIFICANTLY REDUCES AMPLITUDE VARIABILITY ACROSS CO_2 SATURATIONS. **(B)** HIGH ATTENUATION ($Q =10$) IN THE DISPERSIVE STATE ($W_C=0$) LIMITS AMPLITUDE BRIGHTENING PRIMARILY TO FULL CO_2 SATURATION. **(C)** OVERLAY COMPARISON HIGHLIGHTS HOW ELEVATED CAPILLARY PRESSURE REDUCES AMPLITUDE BRIGHTENING, AT INTERMEDIATE SATURATIONS, DUE TO INCREASED ROCK/FLUID STIFFNESS. 118

FIGURE 4.28 – SPECTRAL AMPLITUDE VARIATIONS ACROSS THE SFJORD REFLECTOR (PRIOR TO SPECTRAL BALANCING) FOR DIFFERENT SATURATIONS, CAPILLARY PRESSURE AND ATTENUATION SCENARIOS. **(A)** BASELINE SCENARIO WITH NEGLIGIBLE ATTENUATION ($Q=1000$, $Q=1$, $W_C=0$), SHOWING SLIGHT AMPLITUDE INCREASE AT HIGHER CO_2 SATURATIONS AND FAR OFFSETS (40°). **(B)** ATTENUATIVE, UNIFORM CAPILLARY PRESSURE SCENARIO ($Q =10$, $Q =1$, $W_C=0$), DEMONSTRATES PRONOUNCED ANGLE-DEPENDENT LOW-FREQUENCY BRIGHTENING WITH INCREASING CO_2 SATURATION. **(C)** HIGH ATTENUATION WITH INCREASED CAPILLARY PRESSURE ($Q =10$, $Q0=0.054$, $W_C=0$), SHOWING MODERATED SPECTRAL AMPLITUDES AT INTERMEDIATE SATURATIONS, YET MAINTAINING ANGLE-DEPENDENT BRIGHTENING AT HIGHER CO_2 SATURATIONS. 120

*FIGURE 4.29 – SPECTRALLY BALANCED FREQUENCY-DEPENDENT AMPLITUDES ACROSS THE SFJORD REFLECTOR. **(A)** BASELINE SCENARIO ($Q = 1000$, $Q = 1$, $W_C = 0$) EXHIBITS SUBTLE AMPLITUDE VARIATIONS WITH MINIMAL OFFSET-DEPENDENT CHANGES. **(B)** ATTENUATIVE, UNIFORM CAPILLARY PRESSURE SCENARIO ($Q = 10$, $Q = 1$, $W_C= 0$) SIGNIFICANTLY ENHANCES LOW-FREQUENCY*

BRIGHTENING (≤20 HZ), ESPECIALLY AT HIGHER OFFSETS (40°). ***(C)*** *ATTENUATIVE, HIGHER CAPILLARY PRESSURE SCENARIO (*Q *= 10,* Q0*=0.054,* WC *= 0) MODERATES AMPLITUDE RESPONSES AT INTERMEDIATE SATURATIONS WHILE MAINTAINING CLEAR ANGLE-DEPENDENT SENSITIVITY AT HIGHER* CO_2 *SATURATIONS.* 122

FIGURE 4.30 – FREQUENCY-DEPENDENT AVA (FAVA) ANALYSIS ILLUSTRATING BALANCED SPECTRAL AMPLITUDES VERSUS OFFSET ANGLE ACROSS SELECTED ISO-FREQUENCIES (5–90 HZ). ***(A)*** *NEGLIGIBLE ATTENUATION SCENARIO (*Q *= 1000,* Q*=1) SHOWING MODEST, FREQUENCY-CONSISTENT AMPLITUDE INCREASE WITH ANGLE ACROSS THE FULL 5–90 HZ BAND, CLOSELY RESEMBLING CONVENTIONAL ELASTIC AVO RESPONSES.* ***(B)*** *INCREASED ATTENUATION SCENARIO (*Q *= 10,* Q*=1), HIGHLIGHTING PRONOUNCED LOW-FREQUENCY (≤ 20 HZ) AMPLITUDE BRIGHTENING AND STEEPER ANGLE-DEPENDENT GRADIENTS, POTENTIALLY IMPROVING* CO_2*–BRINE DISCRIMINATION AT FAR OFFSETS.* 123

FIGURE 4.31 – FREQUENCY-DEPENDENT AVA (FAVA) ANALYSIS ILLUSTRATING BALANCED SPECTRAL AMPLITUDES VERSUS OFFSET ANGLE ACROSS SELECTED ISO-FREQUENCIES (5–90 HZ). ***(A)*** *NEGLIGIBLE ATTENUATION (Q=1000) AT INCREASED CAPILLARY PRESSURE (*Q0 *= 0.054) STIFFENS THE ROCK FRAME, SLIGHTLY REDUCING AMPLITUDE GRADIENTS RELATIVE TO UNIFORM-PRESSURE SCENARIOS.* ***(B)*** *AT MAXIMUM ATTENUATION (Q=10,* Q0 *= 0.054): ENERGY REDISTRIBUTES TOWARD LOWER FREQUENCIES (≤20 HZ), ENHANCING AMPLITUDE AND ANGLE-DEPENDENT GRADIENTS; HOWEVER, ELEVATED CAPILLARY PRESSURE REDUCES THIS EFFECT, MODERATING BUT NOT ELIMINATING* CO_2 *SENSITIVITY.* 125

*FIGURE 4.32 – FREQUENCY-DEPENDENT ROCK PHYSICS AVO (FAVA) TEMPLATES ILLUSTRATING SPECTRALLY BALANCED AMPLITUDES VERSUS FREQUENCY AND OFFSET ANGLE AT THE SFJORD REFLECTOR. (A) AT UNIFORM CAPILLARY PRESSURE (*Q*=1), NEGLIGIBLE ATTENUATION (*Q*=1000) EXHIBITS GENTLE, FREQUENCY-INDEPENDENT AMPLITUDE TRENDS, WHEREAS MAXIMUM ATTENUATION (*Q *=10) NOTABLY ENHANCES LOW-FREQUENCY AMPLITUDES AND STEEPENS GRADIENTS, AMPLIFYING* CO_2 *SENSITIVITY. (B) HIGHER CAPILLARY PRESSURE (*Q0*=0.054) MODERATES THE AMPLITUDE TRENDS AND REDUCES ATTENUATION-DRIVEN LOW-FREQUENCY BRIGHTENING, WHILE PRESERVING THE ANGLE-DEPENDENT FLUID SENSITIVITY.* 126

FIGURE 4.33 – FREQUENCY-DEPENDENT AVA TEMPLATES: SPECTRALLY BALANCED AMPLITUDE VERSUS FREQUENCY AND OFFSET, ILLUSTRATING HOW THE AMPLITUDE RESPONSE EXTRACTED AT THE SFJORD INTERFACE, EVOLVES ACROSS THE ENTIRE FREQUENCY SPECTRUM AND OFFSET RANGES, AS A FUNCTION OF CO_2 SATURATION AT HIGH ATTENUATION (Q = 10), SPANNING THE DIFFERENT FREQUENCY STATES (RELAXED (WC = -1), DISPERSIVE (WC = 0), UNRELAXED (WC = +1). **(A–C)** DISPLAYS FAVA TEMPLATES AT UNIFORM PRESSURE UNDER HIGH-ATTENUATION. **(D–F)** REPEAT THE SEQUENCE FOR HIGHER CAPILLARY PRESSURE (Q0= 0.054) AT THE SAME ATTENUATION. THE COLORED FITTED SURFACES SERVE PURELY AS A VISUAL AID, HIGHLIGHTING HOW THE AMPLITUDE RESPONSE EVOLVES ACROSS THE TEMPLATE SIMULATING DIFFERENT RESERVOIR SCENARIOS 127

FIGURE 4.34 – TRAINING AND VALIDATION PERFORMANCE OF THE IMPLEMENTED 2D CNN MODEL. **(A)** TOTAL TRAINING LOSS CURVE ILLUSTRATING SMOOTH, MONOTONIC CONVERGENCE OVER EPOCHS. **(B)** TOTAL VALIDATION LOSS CURVE DEMONSTRATING AN OVERALL DECREASING TREND WITH OCCASIONAL FLUCTUATIONS. **(C)** TRAINING ACCURACY CURVES FOR WATER SATURATION (S_w), CAPILLARY PRESSURE (Q), AND ATTENUATION (Q^{-1}) CLASSIFIER HEADS, PROGRESSIVELY INCREASING AND STABILIZING ABOVE 90%. **(D)** CORRESPONDING VALIDATION ACCURACY CURVES FOR S_w, Q, AND Q^{-1} HEADS CLOSELY TRACKING TRAINING ACCURACY TRAJECTORIES, DESPITE MINOR VARIABILITY. 131

List of Tables

Table 1- Trow 32/2_1 : Elastic and petrophysical logs used for rock physics analysis (Trow:32_2_1, 2020). 9
Table 2 - Modelled scenarios to investigate the distribution of effective porosity between sands and shale. 14
Table 3 – Gardner coefficients, D and F, for brine-saturated rock types (Mavko et al., 2020b). The reported Gardner Shale coefficients are updated based on the current analysis. 23
Table 4 - Greenberg-Castagna (GC) polynomial regression coefficients for pure mineral constituents (Mavko et al., 2020b)..... 24
Table 5 – Fluid properties calculated for brine, methane, and super-critical CO_2 at a pressure = 11.85 MPa and temperature = 33°C. 29
Table 6 – Elastic properties for Quartz as reported from literature (Appendices: Table A.4.1 (Mavko et al., 2020a) on behalf of Simmons (1965) and Koga et al. (1958)). The elastic properties for shales were updated based on our current Smeaheia dataset. 31
Table 7 - This table summarizes the parameter dependencies, as described in equations (3.25), (3.26), (4.1) and (4.2). 56
Table 8 - Generated class labels, ranges, typical means and variances or standard deviations assigned for each pdf distribution for the 3 defined parameters. 65
Table 9 - Selected STFT parameters and associated rationale for each parameter. 82
Table 10 - Class label definitions for the multi-class Sw classifier and binary classifiers for Q and Q-1. Each range corresponds to a discrete label used for supervised training in the CNN architecture. 91
Table 11 – Configuration for 2D convolution (CNN) block composed of 3 internal CNN Layers..... 96
Table 12 – Configuration for the independent fully connected classification neural networks. 97
Table 13 – Summary of the utilized evaluation metrics, their mathematical expressions, and their respective roles in evaluating the model performance during the training and validation phase. Metric formulations are based on standard definitions adapted from Géron (2017) and Goodfellow et al. (2016). 99
Table 14 – Quantitative performance metrics for the implemented 2D CNN model. 129

List of Parameters and Abbreviations

Term	Abbreviation
Amplitude Variation with Angle	AVA
Amplitude Variation with Offset	AVO
Angular Frequency	ω
Aspect Ratio	r
Backus Averaged Compressional Modulus	P_{Mod_Backus}
Backus Averaged Compressional Velocity	V_{p_Backus}
Backus Averaged Density	ρ_{Backus}
Backus Averaged Shear Modulus	μ_{Backus}
Backus Averaged Shear Velocity	V_{s_Backus}
Backus Window Length	$Backus\ Window$
Binary Cross-Entropy Loss	L_{BCE}
Bulk Fraction Volume of Shale	VSH
Bulk Modulus of Rock Saturated with CO_2-Brine Mixture	$K_{sat_CO2_Mix}$
Bulk Modulus of Shale Fraction	K_{shale}
Bulk Modulus of Water (Brine)	K_w
CO_2 Saturation	S_{CO2}
Capillary Pressure Parameter	q
Carbon Capture and Storage	CCS
Complex Fourier Coefficient Matrix	$Z_{xx}(f,t)$
Compressional Velocity for Rock Saturated with CO_2-Brine Mixture	$V_{p\ sat_CO2_Mix}$
Convolutional Neural Network	CNN
Crack Density	ε
Crack Radius	a
Critical Relaxation Scale	L_c
Cross-Entropy Loss	L_{CE}
Density of CO_2 Fluid	ρ_{CO2}
Density of CO_2-Brine Fluid Mixture	ρ_{CO2_Mix}
Density of Rock Saturated with CO_2-Brine Mixture	$\rho_{b_{sat_CO2_Mix}}$
‘’Density of Water (Brine) Fluid	ρ_w
Dimensionless Frequency Index	W_c
Dirac Delta Function	i_t^n
Dry Bulk Modulus	K_{dry}
Dry Shear Modulus	μ_{dry}
Effective Characteristic Frequency	ω_o

Effective Fluid Mobility	M_{eff}
Effective Fluid Modulus for CO_2-Brine Mixture	K_{CO2_Mix}
FFT Window Size	n_{fft}
Fast Fourier Transform	FFT
Fensfjord Formation	FFjord
Fluid Density	ρ_{fl}
Fluid Mobility of CO_2	M_{CO_2}
Fluid Mobility of Water	M_{w}
Frequency	f
Frequency-Dependent Amplitude Variation with Angle	FAVA
Frequency-Dependent Amplitude Variation with Offset	FAVO
Frequency-Dependent Compressional Modulus	P_{Mod_SQF}
Frequency-Dependent Compressional Velocity	Vp_{SQF}
Frequency-Dependent Reflectivity Coefficient	$R^n(\theta, \omega)$
Frequency-Dependent Shear Modulus	S_{Mod_SQF}
Frequency-Dependent Shear Velocity	Vs_{SQF}
Frequency-Dependent Synthetic Trace	$\mathrm{X}_t(\theta)$
Fully Connected Neural Network	FCNN
Gradient Term	B
Imaginary Part	$Im\{.\}$
In-Situ Fluid Bulk Modulus	K_{fl_insitu}
In-Situ Saturated Bulk Modulus	K_{sat_insitu}
Intercept Term	A
Inverse Quality Factor (Attenuation)	Q^{-1}
Krossfjord Formation	KFjord
Machine Learning	ML
Matrix Density	ρ_{ma}
Mineral Bulk Modulus	K_m
Monitoring and Verification	M&V
Normalized Bulk Modulus	$\frac{K_{dry}}{K_m}$
Normalized Shale Volume Fraction	Vol_{sh}
Overlap Window for STFT	$n_{overlap}$
P-Wave Attenuation	Q_p^{-1}
Probability Density Function	PDF
Quality Factor	Q
Real Part	$Re\{.\}$
Reflectivity	$R(\theta)$
Relative Permeability for CO_2	k_{CO_2}
Relative Permeability for Water	k_w
Relaxation Timescale Parameter	τ_m

Reuss Lower Bound Bulk Modulus	K_R
Ricker Wavelet	$w(t)$
Rock-Dependent Scaling Parameter	P_0
S-Wave Attenuation	Q_S^{-1}
Sampling Frequency	f_s
Sand Volume Fraction	Vol_{sand}
Saturated Bulk Modulus	K_{sat}
Saturation Patch Size	d
Shear Modulus of Shale Fraction	μ_{shale}
Shear Velocity for Rock Saturated with CO_2-Brine Mixture	$V_{s\ sat_CO2_Mix}$
Short-Time Fourier Transform	STFT
Sognefjord Formation	SFjord
Squirt-Flow	SQF
Standard Deviation	σ
Temporal Segment Length	n_{perseg}
Variance	σ^2
Viscosity of CO_2	η_{CO_2}
Viscosity of Water	η_w
Voigt Upper Bound Bulk Modulus	K_v
Water Saturation	S_w
Windowing Function	$window$

Parameter	Description	Unit
Acoustic Impedance	AI	m/s* g/cm^3
Bit Size	BS	inch
Bulk Density	RHOB (ρ)	g/cm^3
Caliper	CALI	API
Compressional Slowness	DTS	us/ft
Compressional Velocity	Vp	m/s
Effective Porosity	PHIE (ϕ_e)	Vol Fraction (frac.)
Effective Water Saturation	SWE	Vol Fraction (frac.)
Gamma Ray	GR	API
One-Way Time	OWT	ms
Poisson's Ratio	PR)	unitless
Shear Slowness	DT	us/ft
Shear Wave Velocity	Vs	m/s
Total Porosity	PHIT (ϕ_t)	Vol Fraction (frac.)
Two-Way Travel Time	TWT	ms
Velocity Ratio	Vp/Vs	unitless

1. Introduction

1.1 Carbon Capture and Storage (CCS)

Carbon Capture and Storage (CCS) is a key strategy employed to mitigate atmospheric carbon dioxide (CO_2) emissions, responding to the pressing challenges of climate change and global warming, as highlighted by the Intergovernmental Panel on Climate Change (IPCC) and the International Energy Agency (IEA) (Fawad et al., 2021; Gale & Wilson, 2019). CCS initiatives facilitate the process of CO_2 geosequestration in the capturing, transport and injection of CO_2 industrial emissions into deep geological reservoir formations, primarily targeting depleted hydrocarbon reservoirs or saline aquifers as potential CO_2 storage sites (Lumley, 2019).

Effective Monitoring and Verification (M&V) are pivotal requirements for ensuring the safe and reliable operation of CCS projects, maintaining proper CO_2 containment and minimizing environmental impacts (Dupuy et al., 2021; Jenkins et al., 2015). To achieve these objectives, it is crucial to monitor the evolution, migration and potential leakage pathways of the injected CO_2 plume (Eid et al., 2015). Reservoir geophysicists employ various monitoring tools, including vertical seismic profiling (VSP), downhole gravimetry, geophysical logging, microseismics and 4D seismic (time-lapse 3D surface seismic), with the latter noted particularly powerful in detecting reflectivity changes or time-shifts induced by CO_2 injection, as demonstrated in the Utsira sands at the Sleipner field and the Tubåen Formation at the Snøhvit CCS project (Jenkins et al., 2015). Nevertheless, to accurately assess the CO_2-induced changes in seismic reflectivity and ensure proper CO_2 time-lapse seismic monitoring and quantification, we must first understand the impact of CO_2 saturations on the reservoir's elastic behavior, especially the seismic wave velocities that dictate the seismic response (Caspari et al., 2011).

1.2 Implications on Seismic Velocities for Partially Saturated Reservoirs

Mavko & Mukerji (1998) state that seismic wave velocities in partially-saturated rocks are contingent on the reservoir's pore fluid saturations and the spatial distribution of various pore fluid phases within the pore spaces. In conventional hydrocarbon exploration, reservoirs typically

achieve equilibrium over extended geological timescales, resulting in homogenous and uniformly distributed hydrocarbon fluid mixtures (Eid et al., 2015). CO_2 geosequestration, however, disrupts this static equilibrium, often creating heterogeneous or non-uniform fluid distributions (Eid et al., 2015). These heterogeneities arise during high-pressure CO_2 injection, where gas does not uniformly distribute throughout the available pore spaces (Azuma et al., 2013). Consequently, CO_2-saturated reservoirs may exhibit a range of velocity-saturation profiles, bounded by two pore-fluid distribution end-members: uniform (homogeneous) and patchy (heterogeneous). These latter distributions define the static lower and upper velocity limits predicted by the low-frequency Gassmann theory (Caspari et al., 2011; Mavko & Mukerji, 1998), and thus affect the seismic velocities, reflectivity and amplitudes accordingly (Eid et al., 2015). Therefore, it becomes crucial to investigate the impact of pore fluid changes and saturation heterogeneities on the reservoir's elastic bulk (K) and shear (μ) moduli that subsequently govern the seismic response.

1.3 Frequency-Dependent Rock Physics: Addressing Squirt-Flow Dispersion and Attenuation

Conventional rock physics (RP) forward modelling workflows commonly utilize the low-frequency Gassmann-Biot theory to simulate the effect of CO_2 saturation changes on the seismic response (Dupuy et al., 2021; Eid et al., 2015; Kazemeini et al., 2010; Ma & Morozov, 2010; Maurya & Singh, 2019). Although Biot's theory provided a foundational framework for understanding seismic wave propagation within fluid-saturated porous media (Biot, 1956a, 1956b), empirical observations demonstrate that it often underestimates attenuation (Mavko et al., 2020c; Papageorgiou & Chapman, 2015), predicting negligible attenuation at seismic frequencies (Dutta & Odé, 1983), and fails to capture velocity dispersion observed in laboratory settings within such media. These shortcomings arise from the theory's assumptions of low-frequency conditions and static reservoir equilibrium, where seismic waves propagate long enough for pressure gradients to diffuse, producing uniform pore-fluid distributions (Avseth et al., 2005a; Han & Batzle, 2004; Mavko et al., 2020c). Such assumptions, however, can lead to significant misinterpretations of the CO_2 seismic response and impede effective monitoring of injected plumes.

A critical aspect underlying these inaccuracies is the inability of the Gassman-Biot framework to account for critical frequency-dependent phenomena that arise in partially saturated reservoirs

(Gurevich & Lopatnikov, 1995; King et al., 2000). In particular, the theory neglects the occurrence of squirt flow, which refers to the localized fluid movement caused by seismic wave-induced pressure gradients within the rock's microstructure (Alkhimenkov et al., 2020; Chapman et al., 2002). In the presence of gas or supercritical CO_2, partial gas saturation can trigger substantial velocity dispersion and seismic attenuation (Jin et al., 2017; W. F. Murphy, 1982; Tisato & Quintal, 2013), which lie outside the low-frequency assumptions of Gassmann theory. Consequently, classical Gassmann-Biot models omit squirt-flow affects, thus failing to capture the observed velocity dispersion and attenuation (Dutta & Odé, 1983; Mavko et al., 2020c). Nevertheless, Chapman et al. (2006) states that attenuation in gas-bearing formations can be abnormally high, emphasizing the need for advanced theoretical frameworks that incorporate squirt-flow mechanisms to explain the excess attenuation.

Hence, for accurate simulation of the velocity dispersion and seismic attenuation in partially saturated CO_2 reservoirs, an advanced frequency-dependent rock physics modelling approach becomes imperative. Laboratory measurements confirm the sensitivity of attenuation to partial gas saturation effects (Amalokwu et al., 2014; W. F. Murphy, 1982; Tisato & Quintal, 2013), demonstrating that the elastic behavior of such reservoirs can be frequency-dependent when squirt-flow mechanisms are active (Jin et al., 2017). Consequently, the frequency-dependence of seismic velocities and attenuations has become a central research focus (Lebedev et al., 2009; Müller et al., 2010), as several studies reveal that squirt-flow-induced dispersion significantly influences seismic reflectivity and amplitudes, resulting in frequency-dependent reflection coefficients (Chapman et al., 2006; Innanen, 2011; Odebeatu et al., 2006; Ren et al., 2009). Their findings further emphasize the need for employing frequency-dependent reflectivity modelling, as partial gas saturation can result in reflection coefficients that vary with frequency, highlighting the feasibility of quantifying attenuation using these frequency-dependent reflectivities (Chapman et al., 2006; Innanen, 2011; Sun et al., 2012; Wu et al., 2013; Xu et al., 2011). As a result, these studies highlight the importance of adopting a frequency-dependent modelling framework capable of capturing dispersive phenomena, ultimately facilitating a more reliable characterization and monitoring of CO_2-bearing formations.

1.4 Development of Squirt-Flow Models

The study of seismic wave propagation in poroelastic media has undergone substantial advancements, particularly in addressing the limitations of the Biot theory regarding velocity dispersion and attenuation (Chapman et al., 2002). As researchers began to explore for potential dispersive mechanisms, a series of squirt-flow models emerged. Among these, the Murphy et al. (1986) model incorporated variations in pore-space geometry and partial gas saturation, yielding results validated by experimental observations. Mavko & Jizba (1991) subsequently developed a macroscopic squirt-flow model that explores the relationship between pore geometry, particularly pore aspect ratios, and fluid mobility under seismic stress. This model primarily focused on the high-frequency unrelaxed state, assuming homogeneous pore fluid distributions. Recognizing this limitation, Gurevich et al. (2009) extended the latter model to cover the entire frequency spectrum. This extension allowed for modeling the dispersive transition between the low and high-frequency limits of the elastic moduli, providing a more comprehensive framework for understanding squirt-flow effects across different frequency ranges. Relevant literature further discusses the contributions made to squirt-flow modeling by Dvorkin et al. (1995), Dutta & Ode (1979b, 1979a) and the Biot-Squirt Flow (BISQ) model by Dvorkin & Nur (1993), among others.

With further advancements, the Chapman et al. (2002) model investigated wave-induced pressure gradients in isotropic rocks, using inclusion-based models from Le Ravalec & Guéguen (1996) and Endres & Knight (1997). The squirt-flow model addressed the time-dependent relaxation of pressure gradients in media characterized by spherical pores and randomly oriented thin ellipsoidal cracks. Their computations integrated nearest-neighbor fluid exchanges into equivalent medium calculations to derive complex-valued, frequency-dependent elastic tensors in the frequency domain (Chapman et al., 2002). Chapman (2003) extended the prior model to accommodate anisotropic, multiscale cases, maintaining consistency with Gassmann predictions at low frequencies and converging to standard equivalent medium theory at high frequencies. This extension provided a means to interpolate between the two elastic limits established by earlier works and predict dispersion under diverse conditions (Chapman, 2003; Chapman et al., 2006).

Subsequent models presented by Papageorgiou & Chapman (2015) and Papageorgiou et al. (2016, 2017) introduced additional sophistication into squirt flow modelling, particularly for partially saturated porous media. Building on the Chapman et al. (2002) framework, these

developments explored squirt-flow dynamics under varying capillary pressures and multiphase fluid saturations. Papageorgiou & Chapman (2015) developed a squirt flow model that simultaneously incorporated patchy fluid effects, enabling a more realistic representation of partially saturated reservoirs. Papageorgiou et al. (2016) further expanded the existing framework by associating the resulting patchy fluid effects with wave-induced pore pressure gradients, investigating this phenomenon at the low-frequency Gassmann limit under the assumption of negligible capillary pressure variation.

Following these developments, Papageorgiou & Chapman (2017) integrated all prior concepts into a comprehensive hybrid squirt-patch model that operates effectively across the entire frequency spectrum while accounting for various induced capillary pressure variations. This advanced model captures dispersive phenomena, with squirt-flow effects governed by a characteristic frequency dependent on fluid mobility, relative permeability and a static capillary pressure parameter (Papageorgiou & Chapman, 2017). By incorporating these elements, this advanced formulation improves predictions of squirt-flow related velocity dispersion and attenuation.

1.5 Primary Research Objective

The primary objective of this thesis is to evaluate the efficacy of the proposed frequency-dependent modelling approach in assessing squirt flow and partial saturation effects in CO_2 saturated reservoirs, with particular emphasis on velocity dispersion and seismic attenuation. To achieve this objective, we will compare the results of this advanced methodology with that of the conventional rock physics forward modelling approach, evaluating the impact of CO_2 sequestration on the resultant seismic amplitudes and associated AVO responses.

In accordance with existing literature, this thesis contends that the conventional application of Gassmann theory for fluid substitution is insufficient to model the full complexity of partially saturated reservoirs undergoing CO_2 injection. We propose that utilizing our proposed frequency-dependent approach, particularly facilitating the Papageorgiou and Chapman (2017) model, provides a comprehensive assessment of the frequency-dependent seismic responses under varying CO_2 saturations, capillary pressures and attenuation conditions, as will be demonstrated in Chapter

4. Consequently, the analysis presented in this thesis aims to provide a deeper understanding of the CO_2-induced seismic responses, as we investigate the associated frequency-dependent elastic behavior (velocities), seismic reflectivity and AVO trends This stands in contrast to the conventional RP modelling approaches, which employ standardized rock physics modelling and AVO/AVA analysis techniques conducted at singular seismic frequencies, often overlooking attenuation through purely elastic reflectivity modeling (Chapman et al., 2006).

Hence, by adopting this advanced modeling framework, we can potentially better address the challenges posed by traditional modelling techniques, allowing for improved quantification of CO_2 saturation changes, reducing uncertainty in the interpretation of seismic amplitudes and enhancing the reliability of reservoir monitoring for long-term CO_2 storage projects.

1.6 Thesis Outline

The structure of this thesis can be outlined as follows:

- **Chapter 1** presents an introduction to Carbon Capture and Storage (CCS), emphasizing the need to investigate saturation heterogeneities and squirt-flow effects while evaluating CO_2 seismic responses. This chapter further presents the relevant literature review, in the context of rock physics forward modelling for partially saturated reservoirs, with particular implication for CO_2 reservoirs.
- **Chapter 2** introduces the Smeaheia CO_2 storage site, highlighting its geological features and suitability for CCS. It also presents the Trow 32/2_1 well, which will be utilized for all proposed workflows, with specific emphasis on the Sognefjord Formation as the designated CO_2 storage reservoir throughout this report.
- **Chapter 3** applies the conventional rock physics forward modeling approach to evaluate the effects of varying CO_2 saturations and fluid patchiness on the reservoir's seismic response. It is important to note that the low-frequency Gassmann modeling conducted in this chapter simulates the reservoir's anticipated elastic behavior at the low-frequency limit (relaxed state) of the squirt-flow model to be discussed in Chapter 4.
- **Chapter 4** employs the frequency-dependent rock physics forward modeling workflow and analyzes additional squirt-flow effects under varying CO_2 saturations, capillary

pressures and attenuations across the entire frequency spectrum. The chapter then transitions into deep learning applications that utilize the rock physics constrained spectral amplitudes to classify three seismic attributes: CO_2 saturation ranges, capillary pressure regimes and attenuation conditions.

- **Chapter 5** summarizes key research findings and their implications, providing an integrative discussion on the significance of our analysis in the context of CO_2 rock physics.

In conclusion, this thesis emphasizes the necessity of integrating frequency-dependent modelling to accurately interpret and monitor seismic responses in CO_2 saturated reservoirs, thereby de-risking and enhancing the reliability of CCS project assessments.

2 Geological Background: Sognefjord Formation (SFjord)

The Smeaheia region is a potential CO_2 storage site evaluated under the Norwegian Northern Lights Carbon Capture and Storage project, as a government mitigation strategy to store industrial CO_2 emissions (Gassnova, 2013). This offshore prospective site is located in the Norwegian North Sea, on the Horda Platform and rests as a fault block sealed by two lateral fault systems: the Øygarden Fault complex in the east and the Vette Fault in the west (Rahman et al., 2020). The Smeaheia region encompasses two structural closures, Alpha and Beta, both identified as potential CO_2 sequestration sites with a storage capacity approximated at 100 Mt each (Fawad et al., 2021; Statoil, 2016). In this research, we are utilizing the Trow 32/2_1 well, drilled as a vertical hydrocarbon exploration well on the Norwegian shelf. This well is located on the crestal dip of the Beta structural anticline downthrown to the Øygarden Fault complex, 15 km east of the Troll Field, as shown in Figure (2.1) (Talisman, 2008).

The Trow 32/2_1 prospect primarily targeted the Sognefjord (SFjord), Fensfjord (FFjord) and Krossfjord (KFjord) sandstone reservoir formations separated by intra-formational shale barriers. In this research, we focus our analysis on the wet Sognefjord shaley sand reservoir unit in the Trow 32/2_1 well (Talisman, 2008). The formation reflects a shallow-marine depositional environment primarily composed of sandstones with occasional calcite cementation, interbedded claystone (argillaceous sandstones) and traces of pyrite and coal (Talisman, 2008). The Sognefjord reservoir unit is sealed by the overlying Draupne and Heather formation shales as primary and secondary caprock units, respectively, where all of the mentioned formations were deposited within the middle to upper Jurassic period as part of the Viking Group (Fawad et al., 2021; Gassnova, 2013).

The Smeaheia dataset, featuring the Trow 32/2_1 well, is a public dataset published by Equinor and Gassnova, available at the CO_2 DataShare (*Smeaheia Dataset:CO2DataShare*, 2021). This dataset encompasses crucial datatypes for various stages of our research, including elastic and petrophysical wireline log data, formation tops, stratigraphic evaluations, pressure and temperature data for deeper reservoir intervals, well reports, 2D and 3D seismic data (prior to CO_2 injection), velocity models and more (Gassnova, 2013).

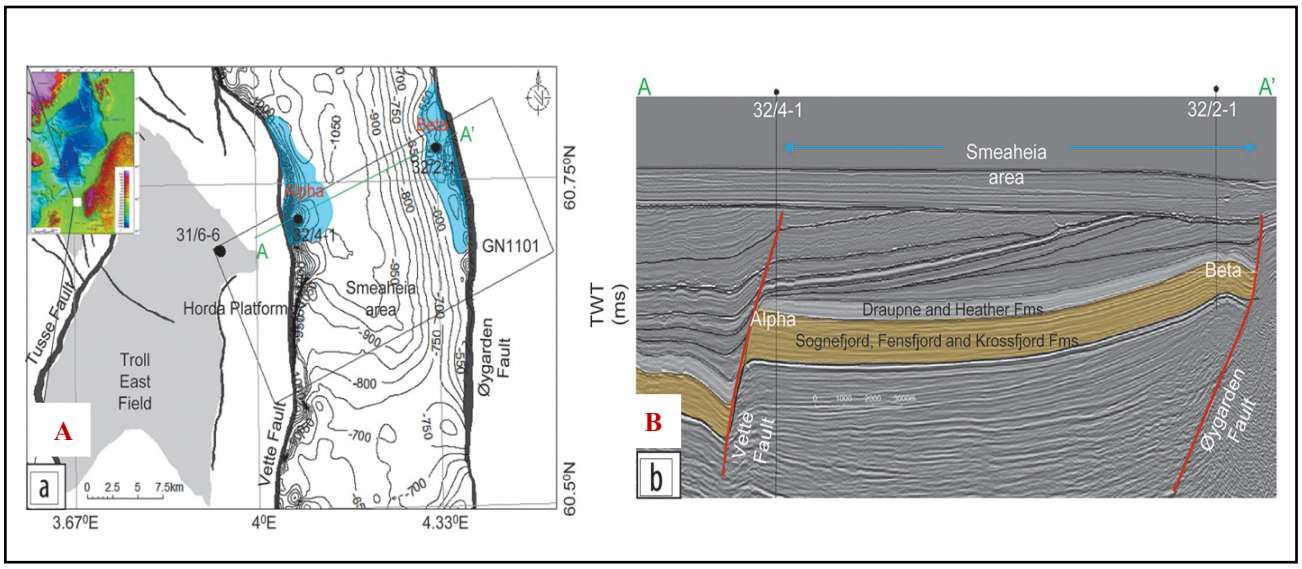


Figure 2.1 - ***(A)*** *Location of the Smeaheia CO_2 storage site, offshore Norway, with the Alpha and Beta structural closures.* ***(B)*** *SW-NE inline of 3D survey GN1101 over the Smeaheia region displaying the location of Trow 32/2_1, situated on the crestal dip of the Beta structural anticline downthrown to the Øygarden Fault Complex (Fawad et al., 2021). The seismic profile is presented in two-way travel time (TWT, ms) with the vertical TWT scale displayed schematically without numerical annotations. The reservoir tops of the Sognefjord (SFjord) formation, of particular interest to this thesis, are situated at approximately 1200 m depth at well 32/4-1(Alpha) and 900 m depth at well 32/2-1 (Beta).*

To conduct this research, we utilized the log data listed in Table (1) for the Trow 32/2_1 well (*Trow:32_2_1*, 2020). We would like to further note that no commercial software was used to generate any of the results presented in this thesis, as all coding initiatives were conducted in Python.

Table 1- Trow 32/2_1 : Elastic and petrophysical logs used for rock physics analysis *(*Trow:32_2_1*, 2020)*.

Wireline Log Data	Data Type	Measurement Unit
Depth	Depth (SSTVD)	m
CALI:1	Caliper	in
GR:1	Gamma Ray	API
BS:1	Bit size	in
PHIT:1	Total Porosity (ϕ_t)	Vol Fraction (frac.)
PHIE:1	Effective Porosity (ϕ_e)	Vol Fraction (frac.)
SWE	Effective Water Saturation	Vol Fraction (frac.)
VSH	Volume of Shale (VSH)	Bulk Vol Fraction (frac.)
DT	Compressional Slowness	us/ft
DTS	Shear Slowness	us/ft
RHOB	Bulk Density (ρ)	g/cm^3
OWT32/2-1	One-Way Travel Time	ms

3 Conventional Rock Physics Forward Modelling

3.1 Introduction

In the following chapter, we apply the conventional rock physics forward modelling approach to evaluate the effects of varying CO_2 saturations and fluid distributions (fluid patchiness) on the reservoir's seismic response. This process invokes well log analysis and conditioning to assess the petrophysical properties and seismic attributes vital for characterizing the reservoir's elastic response. We further simulate CO_2 injection using Gassmann fluid modelling and a Brie-like mixing law introduced by Papageorgiou et al. (2016), followed by synthetic generation and AVO/AVA analysis to characterize the response across the SFjord interface. We conclude this chapter by discussing the results obtained from this current forward modeling approach and present a 2D rock physics template designed for CO_2 fluid detection for enhanced mapping.

3.2 Methodology

3.2.1 Well Log Analysis and Data Conditioning

Well log analysis is an integral step of the rock physics forward modelling workflow, as this process ensures proper evaluation and conditioning of the wireline log data that describe the elastic and petrophysical behavior of the reservoir (Simm & Bacon, 2014b). Consequently, the former process is fundamentally critical for well log corrections or prediction in flawed or missing sections, petrophysical interpretation, fluid identification and avo modelling, all of which support seismic interpretation and reservoir characterization purposes (Simm & Bacon, 2014b).

In this section, we discuss the rock physics well log analysis workflow. In addressing this objective, we conduct a detailed evaluation of the petrophysical reservoir properties (porosity, saturation, lithology, etc.) and seismic attributes (seismic velocities and density). We start by analyzing the overall data across the well and later focus on the Sognefjord reservoir for fluid and AVA modelling.

In conducting the petrophysical evaluation, we consider the caliper (CALI), bit size (BS), gamma ray (GR), effective porosity (PHIE), effective water saturation (SWE) and the volume of shale (VSH) log data. The caliper and bit size logs may indicate borehole conditions, such as borehole washouts common in damaged or shaley formations and borehole mud invasion effects (Simm & Bacon, 2014b). Such poor wellbore conditions may significantly affect the quality of the density log and consequently impact the outcome of the rock physics analysis. On the other hand, the sonic wireline log is less sensitive towards poor borehole conditions, due to the position of the logging tool within the borehole, and is therefore less affected (Simm & Bacon, 2014b).

The gamma ray log is particularly useful for identifying the shale content within a formation (Buryakovsky et al., 2012). This is attributed to the higher concentrations of radioactive elements in clay minerals compared to other rock types. Consequently, elevated GR readings suggest the presence of clay minerology whereas lower GR readings indicate cleaner sandstone intervals (Buryakovsky et al., 2012). In the Sognefjord formation, the GR cut-off values to discriminate between sand and shale (55 and 105 API, respectively) were provided by the Talisman (2008) well report for Trow 32/2_1. These thresholds were subsequently employed to quantify the volume of shale within the Sognefjord formation using a combination of Density-Neutron and Gamma Ray Linear methods (Talisman, 2008). The resulting shale volumetrics was then calibrated against wellsite lithology descriptions from completion reports and core descriptions (Talisman, 2008).

Total porosity (ϕ_t), which corresponds to the PHIT log listed in Table (1), is defined as the ratio of pore volume to the total bulk volume of the rock (Buryakovsky et al., 2012). In petrophysical analysis, total porosity is conventionally estimated from the bulk density log using equation (3.1a). In shaley sand reservoirs, however, the shale or wet clay fraction contains clay minerals, silt and clay-bound water (Figure (3.1)) (Simm & Bacon, 2014b). As a result, the total porosity includes not only the interconnected pore spaces but also isolated pores and the clay-bound water within the shales, which does not contribute to fluid flow or permeability (Simm & Bacon, 2014b). To address this, the total porosity (ϕ_t), is reformulated in equation (3.1b), distinguishing the effective porosity from the non-reservoir matrix component:

$$\phi_t = \frac{\rho_{ma} - \rho_b}{\rho_{ma} - \rho_{fl}} \tag{3.1a}$$

$$\phi_t = \phi_e + VSH\left(\frac{\rho_{cl} - \rho_{sh}}{\rho_{cl} - \rho_w}\right) \tag{3.2b}$$

$$\phi_e = \phi_t - VSH\left(\frac{\rho_{cl} - \rho_{sh}}{\rho_{cl} - \rho_w}\right) \tag{3.3c}$$

where ϕ_t and ϕ_e are total and effective porosity, respectively. $\rho_{b,}$ ρ_{ma} and ρ_{fl} denote the bulk density, matrix density and fluid density, respectively. VSH is the bulk volume fraction of shale in the whole rock, while ρ_{cl}, ρ_{sh} and ρ_w are the densities of clay, shale and formation water, respectively. Equation (3.1b) indicates that total porosity consists of effective porosity and the shale porosity, with the latter representing the porosity contained within the shale fraction due to clay-bound waster.

On the other hand, effective porosity (ϕ_e), which corresponds to the PHIE log listed in Table (1), is defined in equation (3.1c) as the interconnected network of pore spaces within the rock that allows for fluid movement, and therefore excludes the additional porosity that contains the clay bound water (Buryakovsky et al., 2012). This distinction is particularly important for clastic reservoirs, where effective porosity tends to be lower than the total porosity due to the presence of shales (Buryakovsky et al., 2012). Conversely, in carbonate reservoirs, the total and effective porosity are usually equivalent due to the absence of clay minerals (Buryakovsky et al., 2012). Therefore, the concept of effective porosity becomes very critical for shaley sand reservoirs, as applicable for the Sognefjord formation, and is often employed for petrophysical evaluations and in fluid modelling (Simm & Bacon, 2014b). In this study, the PHIT and PHIE logs were already provided within the *Trow:32_2_1* (2020) dataset, where these logs were calculated in accordance with equations (3.1a-3.1c), as described in the Talisman (2008) report for Trow 32/2_1.

Hence, proceeding forward through our analysis of the shaley sand Sognefjord reservoir, we will operate within an effective porosity system. This dictates the use of a specific combination of elastic attributes to characterize the reservoir's effective solid matrix, porosity and fluid saturations. In this approach, we will employ the effective porosity, effective water saturation, the

volume of sand and volume of shale (wet clay) to characterize the different reservoir components (Dvorkin et al., 2007).

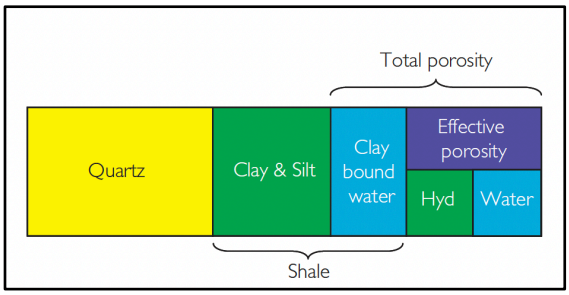


Figure 3.1 – Components of a shaley sandstone reservoir in an effective or total porosity system (Simm & Bacon, 2014b).

Given the effective porosity and water saturation log data (Table 1), we proceeded to characterize the reservoir's effective solid matrix. This required accounting for the different rock constituents, starting with the VSH log, which represents the bulk shale fraction of the total rock. Since shale includes clay-bound water and microporosity that does not contribute to fluid flow, these must be treated as part of the effective solid matrix rather than the pore space. Accordingly, the VSH log was redefined as Vol_{sh} (normalized shale volumetric log), considering shale porosity and clay-bound water as part of the non-reservoir matrix component, as expressed in equation (3.2):

$$Vol_{sh} = \frac{VSH}{(1 - \phi_e)} \tag{3.4}$$

where the denominator $(1 - \phi_e)$ denotes the effective solid matrix component of the reservoir. Thus, Vol_{sh} or equivalently, the volume of wet clay, is now defined relative to the effective solid matrix, consistent with the effective porosity system.

Based on the lithology description for the Sognefjord Formation, the reservoir is primarily composed of sandstone with interbedded claystone. Hence, as we have quantified the volume fraction of shale, the remaining part of the reservoir's effective matrix is considered the sand (quartz) component. To accurately define the volume of quartz, we investigated the distribution of effective porosity between sands and shales within our target zone. In doing that, we simulated scenarios for different porosity distributions, as listed in Table (2), assuming that the effective porosity is distributed according to equation (3.5):

$$\phi_e = VSH(\phi_{VSH}) + (1 - VSH)(\phi_{Sand}) \quad (3.5)$$

where the ϕ_{VSH} and ϕ_{Sand} are the intrinsic porosities of shale and sand while (1-VSH) denotes the volume fraction of sand.

Table 2 - Modelled scenarios to investigate the distribution of effective porosity between sands and shale.

Wireline Log Data	ϕ_{VSH} **(frac.)**	ϕ_{Sand} **(frac.)**
Scenario 1	0	0.30
Scenario 2	0.10	0.20
Scenario 3	0.20	0.10
Scenario 4	0.30	0
Scenario 5	0	0.25
Scenario 6	0.05	0.25

We initiated our modelling with presuming that we have an effective porosity of 30% (0.3 frac.) across the Sognefjord formation. In the first model, we assumed that the effective porosity is sand dominated, followed by a gradual increase in the effective porosity of the shale constituent for the remaining scenarios. The results of this modelling (Figure (3.2)) demonstrate that the effective porosity is almost entirely encapsulated within the sand component as modelled by Scenario 1, where the predicted effective porosity (magenta) correlates reasonably well with the actual provided effective porosity log (PHIE) in black. In scenarios (2-4), as we increase the porosity of shale, the simulated porosity distribution tends to either overpredict or underestimate the resulting effective porosity compared to our provided PHIE log. In the last two scenarios (5-6), we decreased the effective porosity to 25% and assumed that the larger porosity fraction is sand-dominated (Table 2). At a few depth samples within the Sognefjord formation, Scenarios 5 and 6 provided a better representation of the porosity distribution either because the effective porosity at those depths is in fact less than 30% (at depth≈933 m) or because the shale constituent slightly contributes to the effective porosity (at depth≈945 m). As a result of our analysis, the volume fraction of sand (Vol_{Sand}) in an effective porosity system was established as defined in equation (3.6):

$$Vol_{Sand} = \frac{1 - VSH - \phi_e}{(1 - \phi_e)} \tag{3.6}$$

Given the current definitions for the shale (Vol_{sh}) and sand (Vol_{Sand}) volumetrics, as outlined in equations (3.2) and (3.4), the sum of the different mineral constituents that compose the solid matrix amounts to one.

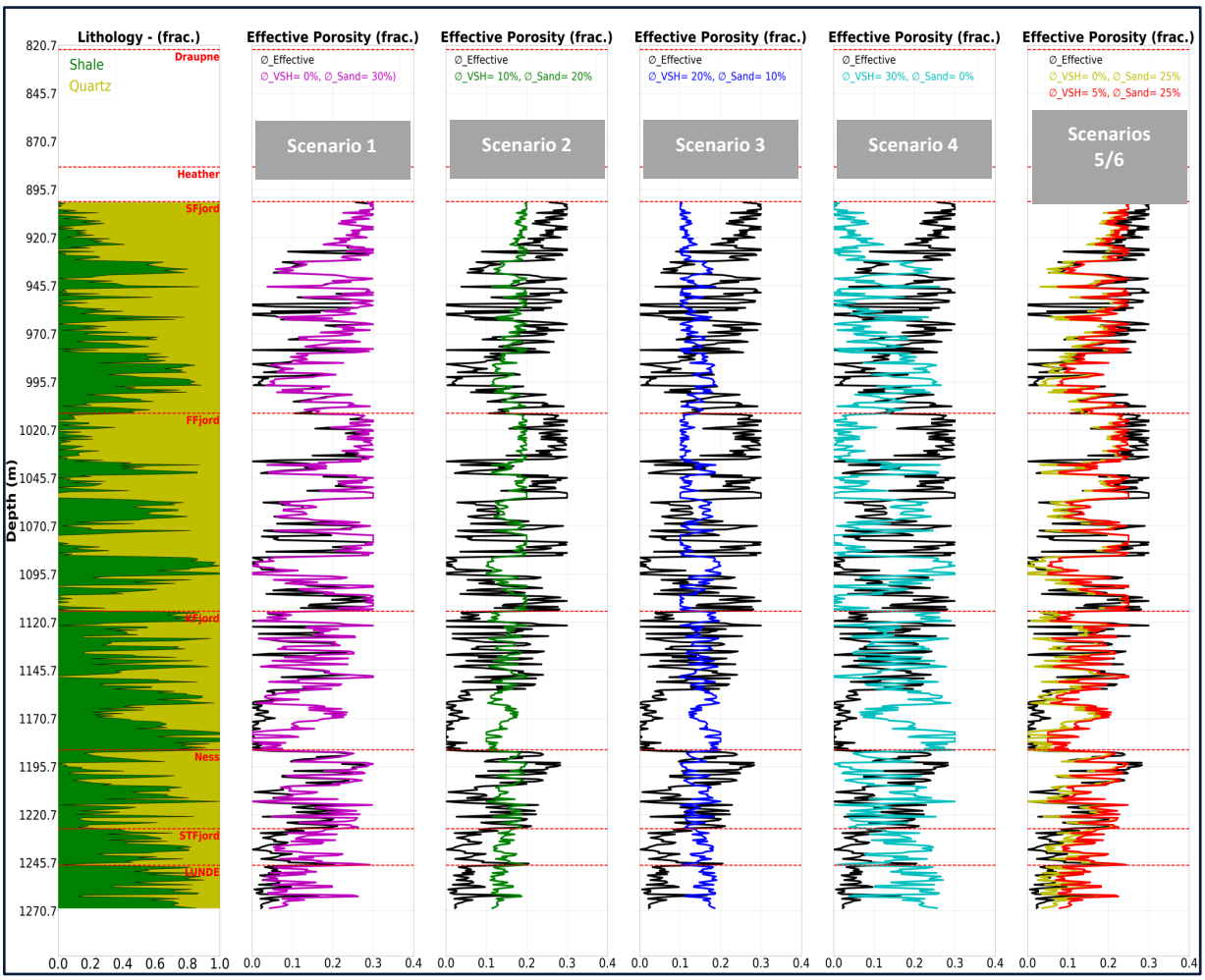


Figure 3.2 – Investigating the distribution of effective porosity between sands and shales within the different reservoir formations across the well, particularly focusing on the Sognefjord Formation (SFjord). Results show that Scenario 1 provides the best representation for the effective porosity distribution between sands and shales.

After the completion of our petrophysical analysis, we proceeded to evaluate the elastic V_p, V_s and ρ wireline log data. We were initially provided with the compressional and shear slowness or transit time curves (Table 1). To acquire the corresponding compressional and shear wave

velocities, we calculated the reciprocal of the compressional and shear slownesses, respectively, as shown by equation (3.7) and (3.8) (Buryakovsky et al., 2012):

$$V_p = \frac{1}{DT}\ , \quad \text{where } V_p \text{ is in (m/s)} \tag{3.7}$$

$$V_s = \frac{1}{DTS}\ , \quad \text{where } V_s \text{ is in (m/s)} \tag{3.8}$$

The elastic and petrophysical logs discussed above are presented in Figure (3.3) for Trow 32/2_1. For a proper understanding of the in-situ reservoir, the data was visualized in well-view tracks as a function of depth across the different reservoir formations. Looking at this well-view, we can see that the Sognefjord formation (3rd formation unit) is a clastic reservoir composed primarily of sandstones with intra-formational shale stringers (Track 3) at a depth of 900 m and a thickness of 110 m within the well. The top of Sognefjord is characterized by a sharp decrease in the GR log (Track 2). The GR drop across the Sognefjord formation reflects a clear transition from the shaley overburden caprock (Draupne and Heather formations) into a cleaner sandstone interval as illustrated by track 3 that describes the reservoir's matrix composition (shales in green and sands in yellow). Our reservoir of interest has a relatively high effective porosity average of 25% and is predominantly a wet reservoir (98.5% brine-saturated) (Talisman, 2008). This is shown in track 4 that displays an effective porosity (PHIE) log scaled by effective water saturation (SWE) (i.e. given a particular depth sample, the reservoir may have an effective porosity of 25%, where this porosity may be 99% brine-saturated and contains 1% of methane gas). However, it is worth noting that deeper reservoir targets seem to have slightly higher gas saturations. The first track displays the caliper and bit size curves, indicating small intervals of poor borehole conditions marked by the red infills at the top of the Sognefjord and Fensfjord formation units, where such badhole effects were already addressed and corrected for in the provided density (ρ) log (Talisman, 2008). Tracks 5, 6 and 7 display the reservoir's elastic response for V_p, V_s and ρ, respectively. We can directly observe that the only measured V_s log available pertains to the deeper Lunde formation (Track 6), and therefore, our primary reservoir target is missing a measured V_s log. The V_p (Track 5) and ρ (Track 7) log responses across the well for the different formations are consistent with changes in GR, lithology and porosity. The observed spikes in V_p and ρ readings are consistent and correlate to a sharp drop in the effective porosity. The occurrence of spikes in the V_p and ρ log responses may be due to an increase in the volume of shale (as observed at some depths) or

the presence of calcite cementation within some sandstone layers (noted in the core descriptions but not documented in the volumetrics) that would decrease the effective porosity accordingly (Talisman, 2008).

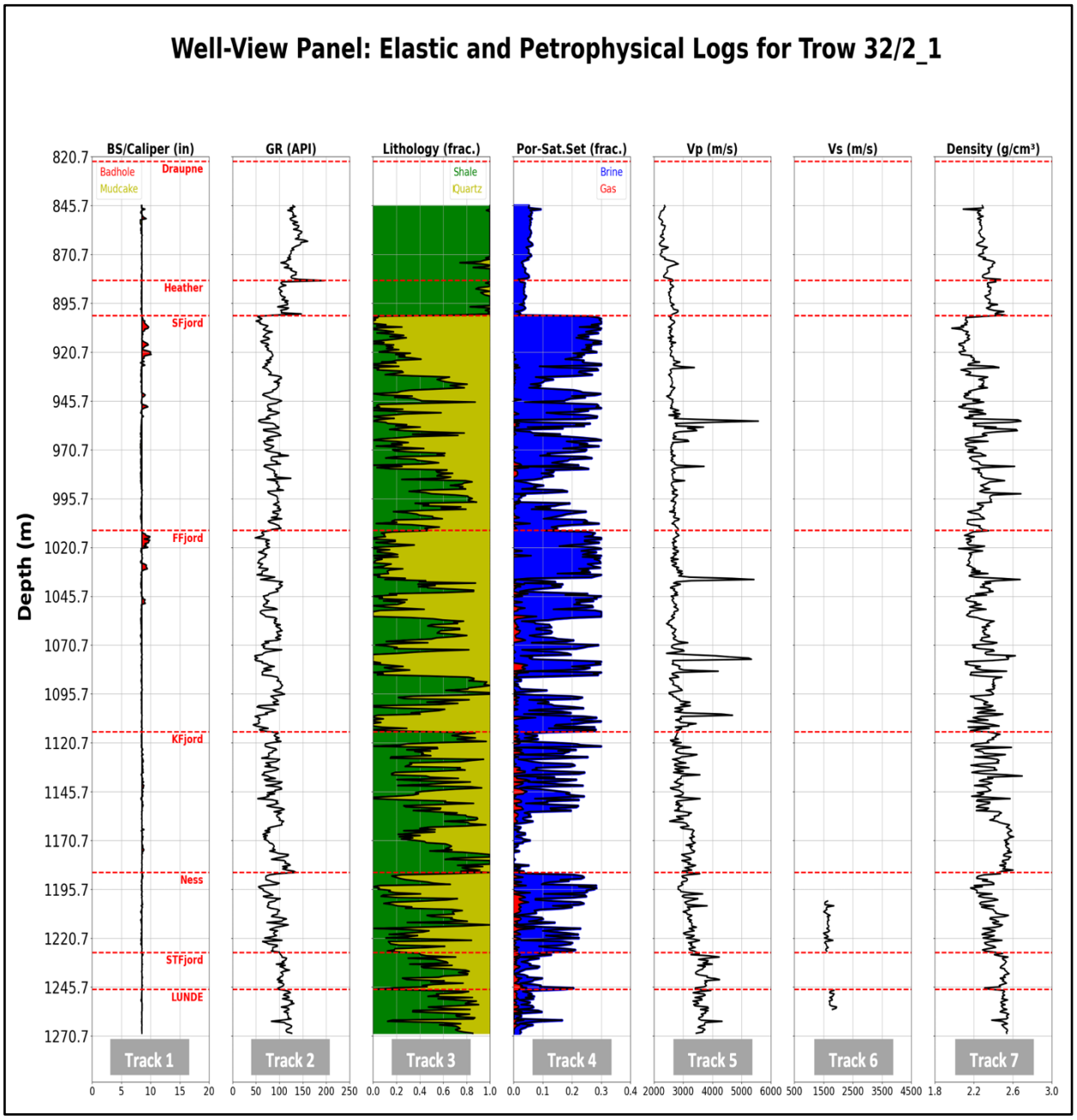


Figure 3.3 –Elastic and petrophysical logs that characterize the different formations across the Trow 32/2_1 well. Track 1 displays the caliper and BS to monitor the borehole conditions. Track 2 displays the GR log to verify the sand and shale lithology components. Track 3 describes the composition of the reservoir's solid matrix. Track 4 displays a porosity-saturation set that quantifies the effective porosity at a given depth and its corresponding pore fluid content. Tracks 5,6 and 7 display the elastic logs that characterize the reservoir (Vp, Vs and ρ), respectively.

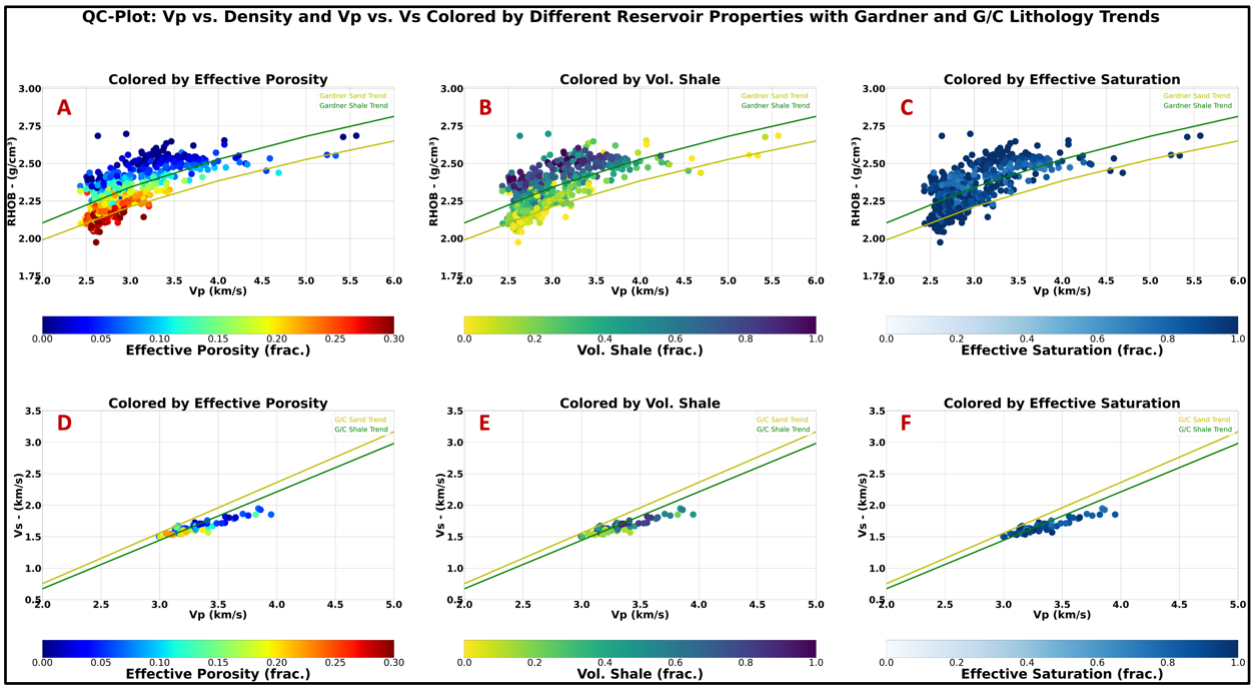


Figure 3.4 – The ρ versus V_p ($\rho - V_p$) and V_s versus V_p ($V_s - V_p$) cross-plots for the different sandstone reservoir formations across Trow 32/2_1 characterized by different reservoir attributes. ***(A, B and C)*** *are V_p vs. ρ cross-plots colored by effective porsoity, volume of shale and effective water saturation, respectively.* ***(D, E and F)*** *are V_p vs. V_s cross-plots colored by effective porsoity, volume of shale and effective water saturation, respectively.*

For a closer evaluation of V_p, ρ and the available V_s log, we generated multiple cross-plots within different elastic domains. These cross-plots asses the ρ versus V_p ($\rho - V_p$) and V_s versus V_p ($V_s - V_p$) relationships for the different sandstone formations across the well in relation to the petrophysical attributes that characterize the geological nature of these subsurface reservoirs, such as PHIE, Vol_{sh} and SWE (Figure 3.4 (A-C)). The $\rho - V_p$ and $V_s - V_p$ cross-plots are superimposed by Gardner (Gardner et al., 1974) and Greenberg-Castagna (GC) (Castagna et al., 1993) sand and shale lithology trends, respectively. This is primarily done to evaluate the overall quality of the elastic logs and the $\rho - V_p$ and $V_s - V_p$ data trends for potential anomalies. The Gardner and GC trends were derived based on empirical relationships or regressions fitted on experimental data for brine-saturated lithologies (Castagna et al., 1993; Gardner et al., 1974).

Gardner et al. (1974) presented a power law relationship between the bulk density (ρ_b) of the reservoir rock and the compressional wave velocity (V_p) , as defined by equation (3.9):

$$\rho_b = dV_p^f \,, \quad \text{where } \rho_b \text{ is in g/cm}^3, \; V_p \text{ is in km/s} \tag{3.9}$$

where d and f are the lithology-dependent scaler and exponential Gardner coefficients, as listed in Table (3) for different rock types, including shale, sandstone, limestone, dolomite and anhydrites. Consequently, to acquire Gardner's sand (yellow) and shale (green) lithology trends, we utilized the following Gardner power law representations:

$$\rho_{sand} = 1.66\, V_p^{0.261}$$
$$\rho_{shale} = 1.75\, V_p^{0.265}$$
$$\text{(using original } d \text{ and } f \text{ Gardner coefficients)} \tag{3.10}$$

Analyzing the ρ – V_p cross-plot (Figure 3.4 (A-C)), we can see that V_p increases with rising ρ. Figure 3.4 (A), colored by effective porosity, demonstrates that porosity has an inverse relationship with the latter elastic attributes. Figure 3.4 (A-C) further show that the Gardner sand lithology trend (yellow) aligns with the more porous relatively cleaner wet sandstone intervals within the reservoir. Figure 3.4 (C) also demonstrates that the well is predominantly wet (minimal residual gas) with no apparent pay zones across the well as confirmed by the well report provided (Talisman, 2008). The scattered data points observed further away from the main data trend (colored by low effective porosity and correlate to relatively higher V_p and ρ values) actually represent the data spikes that were noted previously in Figure (3.3). As these are a few datapoints that will probably be below seismic resolution, we can conclude that both the V_p and ρ logs exhibit good data quality and do not require additional conditioning across the well for the purpose of forward modelling.

Our analysis further demonstrates that the current Gardner coefficients, outlined in Table (3), used for modeling the sand lithology trend, adequately fit the cleaner, brine-saturated sandstone intervals. This observation provides additional confirmation of the dataset's reliability. Conversely, the "Original Gardner Shale" lithology trend (green), depicted in Figure 3.4 (B), shows a less reasonable fit for the cleaner shale intervals. Hence, to update Gardner's shale lithology coefficients, we utilized the ρ – V_p cross-plot, applying volumetric shale and saturation cut-offs ($Vol_{sh} \geq 0.8$ and SWE ≥ 0.8) to isolate the predominantly brine-saturated cleaner shale intervals

(Figure 3.5 (B)). The power-law fit (equation (3.7)) was then employed to derive an improved "Updated Gardner Shale" (red) trend by adjusting the associated shale coefficients (d=1.84 and f=0.26), as reported in Table (3), to better represent the targeted lithology.

To analyze the V_s – V_p cross-plots (Figure 3.4 (D-F)), we employ the GC lithology trends. Castagna et al. (1993) presented empirical polynomial relationships that approximate the shear-wave velocity (V_s) as a function of the compressional-wave velocity (V_p) for 100% brine-saturated rocks, based on monomineralic (pure) lithology trends as defined in equation (3.11):

$$V_s = a_{i2}V_p^2 + a_{i1}V_p + a_{io}\ , \qquad \text{where } V_p \text{ and } V_s \text{ are measured in (km/s)} \tag{3.11}$$

where a_{i2} , a_{i1} and a_{i0} represent the polynomial regression coefficients derived for the different monomineralic lithologies, as listed in Table (4) for sandstones , shale, limestones and dolomite (Castagna et al., 1993). As a result, we used the following linear polynomial representations to obtain the GC sand and shale lithology trends:

$$\begin{aligned} Vs_{sand} &= 0.80416\,V_p - 0.85588 \\ Vs_{shale} &= 0.76969\,V_p - 0.86735 \end{aligned} \tag{3.12}$$

Looking at the V_s – V_p cross-plots (Figure 3.4 (D-F)), we can see that the measured V_s log available is very limited in coverage and pertains to the deeper Lunde Formation (Figure 3.3 – Track 6) as noted previously. These cross-plots show that V_p increases linearly with V_s as would be expected from the modelled V_s – V_p relationships derived by Castagna et al. (1993). As elastic attributes proportionally decrease, the porosity and clay content tend to increase in that direction accordingly (Han et al., 1986). Because the porosity and clay content both impact the V_p and V_s responses similarly, we can see that the V_s – V_p data trend is tightly clustered within the sand and shale GC lithology trends (Avseth et al., 2005a). The cross-plots in Figure 3.4 (D-F) further demonstrate that the overall V_s – V_p data trend is acceptable and that the measured V_s log available is of reasonable data quality.

Considering the limited V_s log available, we evaluated the fit of the GC lithology trends through this data. Castagna et al. (1993) states that if we have proper understanding of the reservoir

lithology, then we can adjust the lithology regression coefficients for the shale content accordingly. However, in cases where the reservoir lithology is poorly understood, then the GC regression coefficients would provide reasonable lithology trends. Hence, to evaluate the GC shale lithology trend for Vs prediction, we utilized the V_s – V_p cross-plot with applied saturation and shale volumetric cut-offs ($Vol_{sh} \geq 0.8$ and SWE ≥ 0.8) to analyze the lithology trend relative to a more brine-saturated cleaner shale interval (Figure 3.5 (E)). Although GC lithology trends were derived for pure mineral brine-saturated constituents, applying the needed cut-offs was not practically possible given the limited V_s log coverage. As a result, I had to use slightly more flexible saturation and shale volumetric cut-offs to accommodate the current data available, where in this case I considered the Vol_{sh} to represent the non-reservoir matrix component ($Vol_{sh} \geq 0.8$). Given these cut-offs, we can see that the shale GC trend (green) provides a good fit for the data; and therefore, the original GC shale regression coefficients can be employed for V_s estimation across the well (Figure 3.5 (E)). Obtaining the shear-wave velocity log is critical for our rock physics forward modeling workflow, particularly in preparation for the upcoming fluid modelling and AVO analysis stages (Greenberg & Castagna, 1992). Nevertheless, measured V_s logs are frequently unavailable, as observed for this dataset.

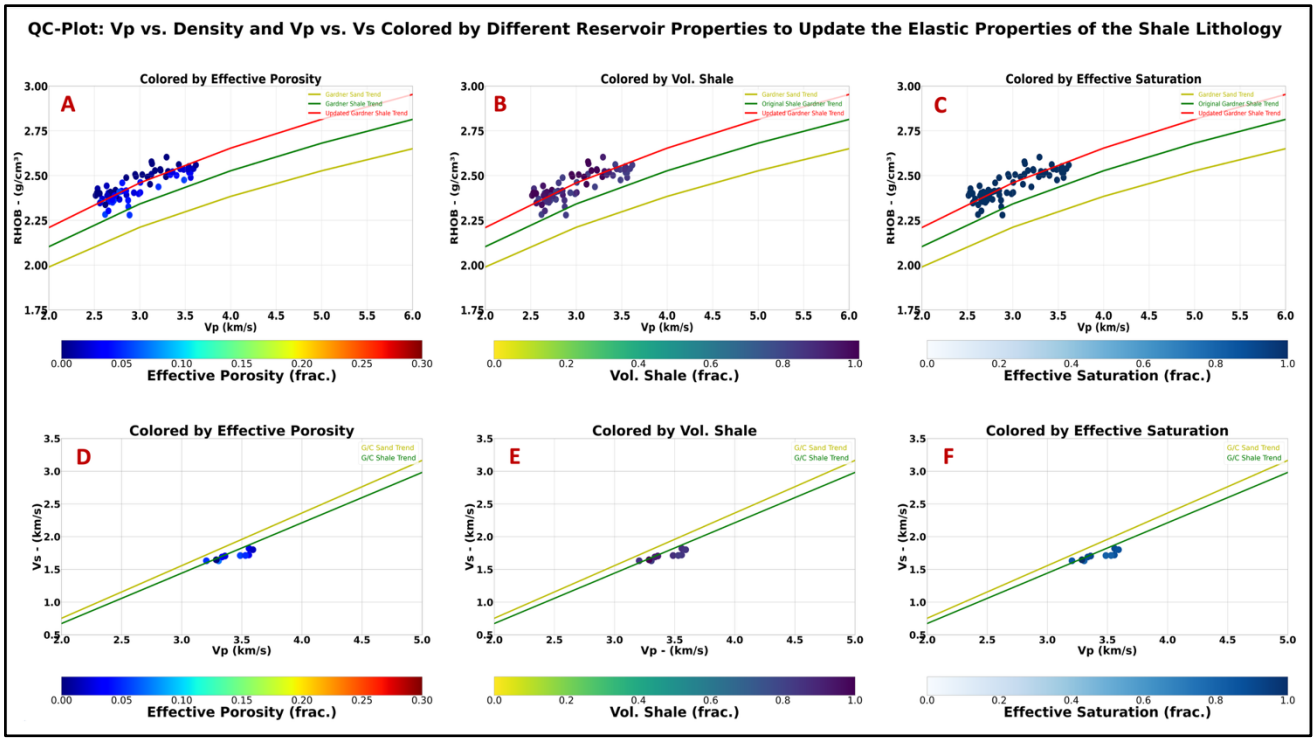


*Figure 3.5 – The ρ versus V_p ($\rho - V_p$) and V_s versus V_p ($V_s - V_p$) for the different sandstone reservoir formations across Trow 32/2_1 characterized by different reservoir attributes with applied saturation and shale volumetric cut-offs ($Vol_{sh} \geq 0.8$ and SWE ≥ 0.8). This was done to QC the GC shale lithology trend and will be used to update the elastic properties of the shale constituent. Panels **(A-C)** also display the "Updated Gardner Shale Lithology Trend" (red) after fitting the cleaner shale lithology using the same cut-offs. Panels **(D-F)** show that the "Original G/C Shale Trend" (green) is a good fit of the current data and therefore, does not require correction.*

In evaluating the measured V_s log available, we utilized the Castagna et al. (1993) empirical polynomial relationships that approximate V_s from V_p for brine-saturated pure lithology rocks. To perform our actual V_s prediction, however, we employed an extended version of that model, presented by Greenberg and Castagna (1992), to account for brine-saturated composite lithologies that contain a mixture of mineral constituents, as pertinent for our reservoir. The formulation of this modified model computes the shear-wave velocity through an average of the arithmetic and harmonic V_s means for the pure constituent minerals. Hence, the V_s prediction method, presented in equation (3.13), is closely analogous to a Voigt-Reuss-Hill (VRH) averaging mechanism that provides an effective shear velocity prediction for a composite rock (Greenberg & Castagna, 1992):

$$V_s = \frac{1}{2}\left\{\left[\sum_{i=1}^{L} X_i \sum_{j=0}^{N_i} a_{ij} V_p^{\,j}\right] + \left[\sum_{i=1}^{L} X_i \left(\sum_{j=0}^{N_i} a_{ij} V_p^{\,j}\right)^{-1}\right]^{-1}\right\} \tag{3.13}$$

$$\sum_{i=1}^{L} X_i = 1 \tag{3.14}$$

where V_p and V_s are the compressional and shear-wave velocities measured in (km/s), respectively. L is the number of the pure constituent minerals within the composite lithology. X_i is the volume fraction of a particular mineral constituent i, where the sum of the different volume fractions should equal to one, as stated by equation (3.14). N_i is the order of the polynomial equation given a particular mineral constituent. a_{ij} represents the empirical regression coefficients derived for the different monomineralic lithologies, as detailed in Table (4). The notation for the V_s prediction method, stated above, is retrieved from Mavko et al., (2020b).

The discussed V_s prediction method is applicable for brine-saturated lithologies as previously stated. As a result, we predicted V_s for the Draupne and Heather overburden caprocks and the primary Sognefjord reservoir target. This was accomplished by using the computed sand (Vol_{Sand}) and shale (Vol_{Sh}) volumetric logs in addition to the GC sand and shale regression coefficients (Table 4). The predicted Vs log for Heather, Draupne and Sognefjord formations is presented in Figures (3.6) and (3.7). In Figure (3.6), the 3rd track compares our personal GC prediction (blue) with a Vs predicted log (cyan) obtained from Dr. Manzar Fawad, a former expert on Smeaheia dataset. It was encouraging to see that the Vs predictions are very similar providing good

correlation for the different formation units. There were a few negligible discrepancies (highlighted by the black arrows in Figure (3.6) and (3.7) and Track 3) where my Vs prediction was slightly underestimated in comparison. Looking further at Figure 3.7 (A) and (B), we analyzed the overall V_p-V_s data trends obtained from the different sources for the desired formations. Overall, we can see that Vp increases linearly with Vs as expected, and that the predicted Vs data obtained from both sources are highly comparable and constrained within the GC sand and shale lithology trends.

Although Trow 32/2_1 was declared an abandoned dry exploration well, the remaining sandstone reservoir intervals below our primary target contained slightly higher residual gas saturations, as observed in Figure 3.3 (Track 4), compared to the negligible residual gas in Sognefjord formations. Consequently, V_s prediction for these deeper targets requires the application of Gassmann Fluid Substitution (GFS) (Section 3.2) To perform the prediction, we must first model the V_p response for a fully brine saturated reservoir using GFS. The GFS implementation in this cases utilizes a Vp-only fluid substitution workflow, as discussed by Mavko et al. (1995), that relies on the compressional p-wave modulus for fluid modelling rather than the bulk modulus due to the absence of the shear velocity. We then employ the brine-saturated V_p for shear prediction, as discussed in equation (3.13), to acquire a predicted V_s for a brine-saturated reservoir. Finally, we perform backward GFS to get the predicted shear velocity log for the in-situ reservoir saturation that corresponds to the original in-situ V_p log we started with (Mavko et al., 2020b). As we are currently focusing on the Sognefjord formation for our analysis, we don't need to perform V_s prediction for the remaining deeper intervals unless we decide to incorporate these formations for AVO analysis at a later stage in this research. For this reason, I could not validate the V_s prediction performed for the upper formations with the measured V_s log pertaining to the deeper Ness formation.

Table 3 – Gardner coefficients, d and f, for brine-saturated rock types (Mavko et al., 2020b). The reported Gardner Shale coefficients are updated based on the current analysis.

Lithology	$\boldsymbol{d}$	$\boldsymbol{f}$
Shale	1.84	0.264
Sandstone	1.66	0.261
Limestone	1.36	0.386

Dolomite	1.74	0.252
Anhydrite	2.19	0.160

Table 4 - Greenberg-Castagna (GC) polynomial regression coefficients for pure mineral constituents (Mavko et al., 2020b).

Lithology	a_{i2}	a_{i1}	a_{i0}
Sandstone	0	0.80416	−0.85588
Shale	0	0.76969	−0.86735
Limestone	−0.05508	1.01677	−1.03049
Dolomite	0	0.58321	−0.07775

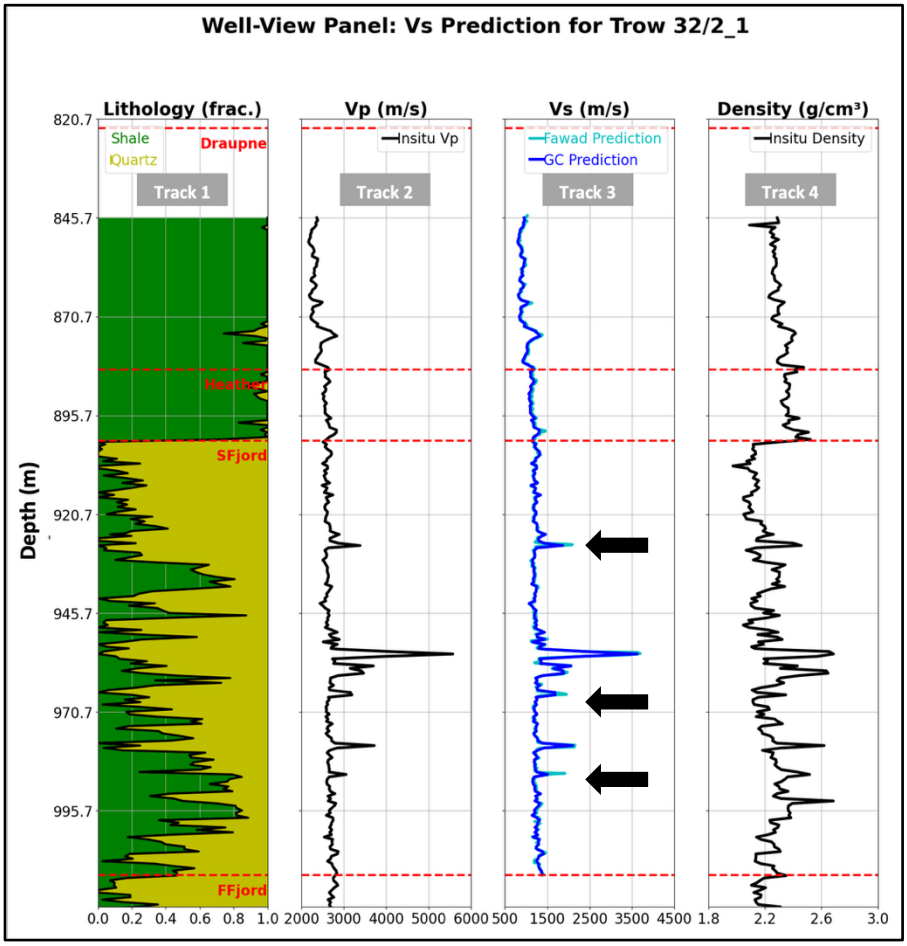


Figure 3.6 – Well-View Panel for Trow 32/2_1 displaying the elastic properties of Draupne, Heather and Sognefjord Formations. Track 1 displays the reservoir's matrix composition. Tracks 2 and 4 display the in-situ V_p and density logs across the latter formations. Track 3 compares our personal GC predictions versus a Vs predicted log obtained from Dr. Manzar Fawad. Both Vs predictions are very similar across the same formations.

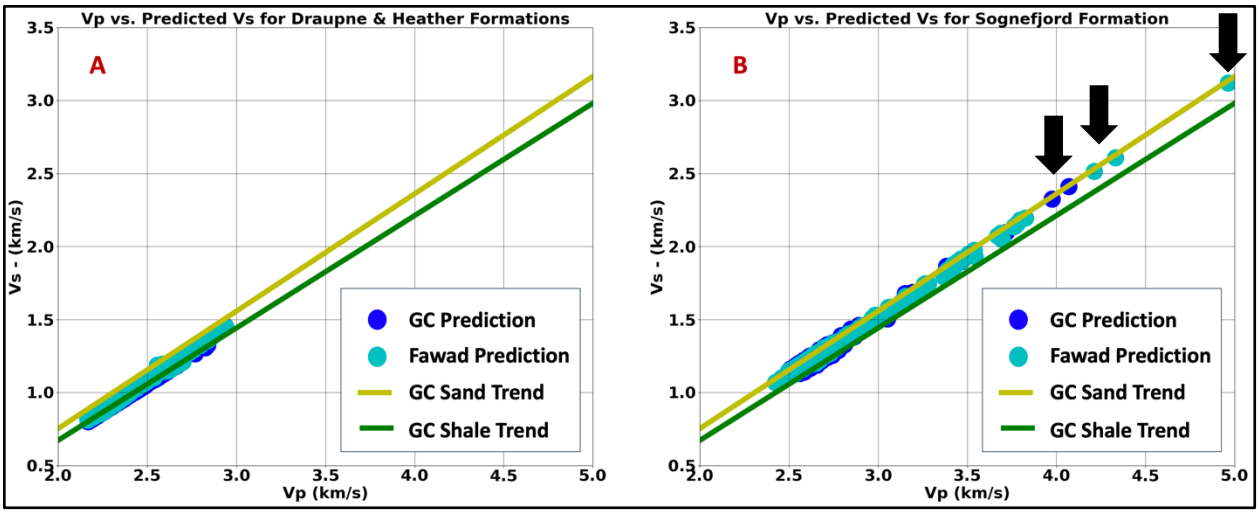


Figure 3.7 – The V_s versus V_p (V_s – V_p) cross-plots overlaid by GC sand and shale lithology trends. (A) Compares our GC Vs prediction with the V_S prediction from Dr. Manzar Fawad for Draupne and Heather Formatons. (B) Compares the latter two Vs predictions for the Sognefjord Formation.

3.2.2 Gassmann Fluid Substitution (GFS)

For proper CO_2 time-lapse seismic monitoring, it is imperative to understand the impact of pore fluid changes on the reservoir's elastic moduli (bulk K and shear μ) and properties (V_p, V_s, ρ) that govern the seismic response (Kazemeini et al., 2010; Maurya and Singh 2019). Hence, to evaluate the effect of such fluid changes on the seismic reflections and amplitudes, the low-frequency Gassmann theory is commonly employed for pore fluid substitution in the rock physics literature (Brie et al., 1995; Eid et al., 2015; Gutierrez et al., 2012; Smith et al., 2003; Z. (Zee) Wang, 2001).

Gassmann's equation establishes a link between the bulk modulus of the porous saturated reservoir rock (K_{sat}) with porosity (ϕ) and the bulk moduli of the different rock components, including its pore fluids, the solid matrix and the dry rock frame (Gassmann, 1951), as demonstrated in equation (3.15):

$$K_{sat} = K_{dry} + \frac{\left(1 - \frac{K_{dry}}{K_m}\right)^2}{\frac{\phi}{K_{fl}} + \frac{(1-\phi)}{K_m} - \frac{K_{dry}}{{K_m}^2}} \tag{3.15}$$

$$\mu_{sat} = \mu_{dry} \tag{3.16}$$

where K_{fl} is the bulk modulus of the pore fluids, K_m is the bulk modulus of the solid matrix (minerals only excluding porosity), and K_{dry} is the bulk modulus of the dry rock frame (porous solid matrix drained of pore fluids). Equation (3.15) indicates that the bulk modulus (K_{sat}) is influenced by various parameters including ϕ, K_m, K_{dry} and K_{fl} (pore fluids). Consequently, changes in fluid properties or saturations will affect K_{fl}, further impacting K_{sat} accordingly (Avseth et al., 2005a; Han & Batzle, 2004). On the contrary, equation (3.16) implies that the shear modulus is independent of such pore fluid changes, where the shear modulus of the saturated rock (μ_{sat}) remains equivalent to the shear modulus of the dry rock frame (μ_{dry}) even after pore fluid substitution (Berryman, 1999; Berryman & Milton, 1991). This is primarily because fluids possess no rigidity as shear waves do not propagate through these substances; and hence, the shear modulus of the reservoir rock is insensitive to pore fluid changes or the fluid substitution process (Berryman, 1999; Kazemeini et al., 2010).

The validity of the Gassmann equation presented above is based on a number of fundamental assumptions (Avseth et al., 2005a; Han & Batzle, 2004; Mavko et al., 2020c; Smith et al., 2003):

- The reservoir rock is elastically isotropic and homogeneous.
- The solid matrix component of the rock can be expressed by a single effective bulk modulus and density.
- The pore fluid component within the rock can be represented by a single effective fluid modulus and density.
- Gassmann is strictly viable at very low frequencies, where there is sufficient time for fluid flow to occur and equilibrate the wave-induced pore pressure gradients (arising from acoustic compression of the rock during wave propagation through a porous saturated reservoir) through an interconnected network of pore spaces. This ensures that the pore fluids remain in perfect hydraulic communication. As a result, Gassmann is most suitable and applicable for the low frequency seismic data range (<100 Hz) (Mavko et al., 2020c).

Through the implementation of the Gassmann fluid substitution workflow being discussed, we operate in an effective porosity system (PHIE, SWE, Vol_{sh} (wet clay) and Vol_{sand}) primarily due to the shaley sand reservoir lithology of the Sognefjord Formation, as suggested by Dvorkin et al. (2007) for similar (shalier) resevoirs. This is a common practice for Gassmann fluid substitution,

where we intend to replace the in-situ reservoir pore fluids with injected CO_2 mainly in the effective pore spaces associated with the higher porosity sandstones (Ma & Morozov, 2010). In shaley sand reservoirs, the effective porosity (ϕ_e) excludes the wet shale non-reservoir solid component that contains the clay bound water and is characterized by low effective porosity and very low permeability (Dvorkin et al., 2014a), as noted previously. Hence, in employing the ϕ_e for fluid substitution in equation (3.15), we ensure avoiding the immobile clay bound water that would hinder the hydraulic communication within the pore space network and consequently violate the last assumption of the Gassmann theory discussed (Dvorkin et al., 2007; Gurevich & Carcione, 2000).

In this section, we implement the Gassmann fluid substitution (GFS) workflow as described by Avseth et al. (2005a) and Smith et al. (2003) to model and evaluate the impact of varying CO_2 saturations and fluid distributions (uniform and patchy distributions) on the effective bulk modulus (K_{sat}) of the CO_2-saturated Sognefjord formation. Generally, the workflow can be subdivided into three phases: initial, dry and final phases.

In the initial phase, the GFS model requires a few preliminary input parameters including the in-situ reservoir porosity (PHIE log), mineral composition (volumetric logs: Vol_{sh} and Vol_{sand}), pore fluid saturations (SWE log) as well as the reservoir's measured in-situ elastic wireline log data for V_p, V_s and ρ. The ultimate goal is to simulate the actual in-situ Sognefjord reservoir rock and compute its associated elastic moduli. To achieve this, the reservoir and elastic properties are utilized to calculate: the shear modulus of the in-situ saturated rock (μ_{sat}), the effective bulk modulus of the in-situ saturated reservoir (K_{sat_insitu}), the effective bulk modulus of the in-situ reservoir fluid mixture (K_{fl_insitu}), and the effective bulk modulus of solid matrix (K_m).

In computing the Sognefjord's in-situ elastic moduli, equations (3.17) and (3.18) relate the in-situ bulk (K_{sat_insitu}) and shear (μ_{sat}) moduli to the Sognefjord's V_p , V_s and ρ wireline log data that characterize the reservoir's in-situ elastic behavior:

$$K_{sat_insitu} = \rho\left(V_p^2 - \frac{4}{3}V_s^2\right) \tag{3.17}$$

$$\mu_{sat} = V_s^2\rho \tag{3.18}$$

With regard to fluids, the Gassmann theory conventionally assumes fluid replacement from one single saturation phase to another (i.e. a fully brine-saturated rock would be substituted with 100% gas saturation) (Avseth et al., 2005a). With respect to the Sognefjord's formation, we

previously noted that the reservoir is primarily wet with minimal (residual) methane gas saturation. To ensure that we accurately model the reservoir's in-situ pore fluids, we employed the harmonic Reuss average (Reuss, 1929) to determine the effective bulk modulus (K_{fl_insitu}) of a fluid mixture composed of varying saturations, as elaborated by Domenico (1976). This step was necessary to maintain adherence with Gassmann's 3rd assumption discussed above.

The brine fluid properties were determined using the Batzle & Wang (1992) empirical formulas, employing the reservoir pressure (P = 11.85 MPa), temperature (T=33°C) and salinity (S=110,000 ppm NaCl) of the deeper Ness formation due to the absence of this data for the Sognefjord reservoir (Talisman, 2008). The brine density, as calculated in Table (5), matches the reported density of the fluid mixture in the Sognefjord formation (Talisman, 2008), where this serves as additional confirmation that the reservoir of interest is predominantly brine-saturated.

As the Trow 32/2_1 well was declared dry (Talisman, 2008), the fluid properties of the residual methane gas were not reported. Therefore, the properties of the methane gas were computed using a Mantis library package, under development by Dr. Giorgos Papageorgiou, that retrieves the relevant fluid properties from the National Institute of Standard and Technology (NIST) database, at the same reservoir pressure and temperature stated earlier.

Using the bulk moduli values obtained for the individual fluid components (brine and methane), we then proceed to compute the effective fluid modulus of the in-situ mixture (K_{fl_insitu}) as computed in equation (3.19):

$$K_{fl_insitu} = \left[\frac{S_w}{K_w} + \frac{(1 - S_w)}{K_{Methane}}\right]^{-1} \tag{3.19}$$

where S_w is brine saturation while K_w and $K_{Methane}$ are the bulk moduli of the individual fluid components as reported in Table (5), for brine and methane, respectively. Equation (3.19) also represents Wood's mixing law for a homogeneous fluid mixture at uniform saturation in an isostress state, where fluid flow occurs to diffuse the wave-induced pore pressure gradients (Mavko et al., 2020c). Through this process, the different pore fluid phases are mixed uniformly, at the finest scale, to create a single effective fluid. This crucial step ensures that the distinct fluid components retain equivalent induced pore pressures ensuring hydraulic communication, in

accordance with the low-frequency Gassmann assumption mentioned previously (Mavko et al., 2020c).

Table 5 – Fluid properties calculated for brine, methane, and super-critical CO_2 at a pressure = 11.85 MPa and temperature = $33°C$.

Elastic Fluid Properties	**Brine**	**Methane**	**CO_2 (super-critical)**
Density (ρ) $-$ (g/cm^3)	1.07	8.82×10^{-2}	7.76×10^{-1}
Bulk Modulus (K) - (GPa)	2.36	1.86×10^{-2}	1.26×10^{-1}
Viscosity (η) – (Pa*s)	7.34×10^{-4}	1.47×10^{-5}	6.69×10^{-5}

As with fluids, the Gassmann equation is also applicable for a monomineralic reservoir rock. To account for the multi-minerals (shale and sand) composing the solid rock frame of the Sognefjord reservoir, we compute the effective bulk modulus of the (effective) solid matrix (K_m). This is achieved through the Voigt-Reuss-Hill (VRH), as presented in equation (3.20), and detailed by Dvorkin et al. (2007) :

$$K_m = \frac{K_v + K_R}{2} \tag{3.20}$$

$$K_v = (Vol_{sand} \cdot K_{sand}) + (Vol_{sh} \cdot K_{shale}) \tag{3.21}$$

$$K_R^{-1} = \left(\frac{Vol_{sand}}{K_{sand}} + \frac{Vol_{sh}}{K_{shale}}\right) \tag{3.22}$$

Equation (3.20) computes K_m through an arithmetic average of the Voigt (arithmetic) and Reuss (harmonic) bounds, denoted by K_v and K_R, respectively (Avseth et al., 2005a). Therefore, K_v and K_R represent the upper and lower bounds that constrain the effective bulk modulus (K_m) of the solid composite, as shown by equations (3.21) and (3.22) given the Sognefjord's mineral composition. The Voigt upper bound (K_v) models the stiffest bulk modulus possible (Voigt, 1910) given the Sognefjord's mineral composition while the Reuss lower bound (Reuss, 1929) simulates

the softest bulk modulus possible given the same minerology (Avseth et al., 2005a). The Vol_{sh} and Vol_{sand} are as defined in equations (3.4) and (3.6), respectively. K_{sand} and K_{shale} are the corresponding bulk moduli of the Sognefjord's sand and shale rock components, as reported in Table (6).

It is evident that the computations for equations (3.20) through (3.22) entail precise knowledge of the reservoir's mineral composition and accurate elastic properties (ρ , V_s , V_p μ, and K) for the different constituents that compose the Sognefjord reservoir rock. Hence, updating these elastic properties based on our current dataset is of great importance because it ensures accurate calculation of K_m (dominated by the volume fractions and stiffnesses of the sand and shale components), where this input will consequently impact K_{dry} in the upcoming dry rock modelling phase.

The elastic properties of sandstones (quartz) are well investigated based on laboratory measurements (Tosaya, 1982) and published in literature (Simmons, 1965) (Table 6). On the contrary, the elastic properties of shales are highly variable. This is particularly because shales may contain different clay type constituents (i.e. illites, chlorites, kaolinites, smectites, micas) that demonstrate drastic variations in their elastic properties due to their intrinsic properties, associated clay bound water or the anisotropy resulting from the layering structure of the different clay types (Pal-Bathija et al., 2008). Such discrepancies in the elastic properties of shales are well-documented and extensively discussed in the rock physics literature (Han et al., 1986; Katahara, 1996; Pal-Bathija et al., 2008; Tosaya, 1982; Vanorio et al., 2003; Wang et al., 2001).

To update the elastic properties of the shales, we analyzed the previous cross-plots of ρ – V_p and V_s – V_p presented in Figure (3.5) with the prior saturation and shale volumetric cut-offs (Vol_{sh} $\geq$ 0.8 and SWE $\geq$ 0.8) targeting the relatively cleaner brine-saturated shale intervals available within our well (Figure 3.5 (A-F)). For this analysis, we used the measured V_s log available rather than the predicted V_s log. We then acquired average V_p, V_s and ρ readings (Table 6) for those brine-saturated shales and employed these averages to compute the bulk (K_{shale}) and shear moduli (μ_{shale}) of the shale mineral (or the non-reservoir matrix constituent) (Dvorkin et al., 2014a). To calculate K_{shale} and μ_{shale}, we used equations (3.23) and (3.24):

$$\mu_{shale} = V_s^2 \rho = 7.10 \text{ GPa} \quad (3.23)$$

$$K_{shale} = \rho \left({V_p}^2 - \frac{4}{3} {V_s}^2 \right) = 11.86 \text{ GPa} \quad (3.24)$$

and obtained the following elastic moduli values: μ_{shale}= 7 GPa and K_{shale}= 11.86 GPa. These moduli were then further employed to calculate the effective bulk modulus of the solid composite (K_m) for the Sognefjord formation as shown by equations (3.20) - (3.22).

Table 6 – Elastic properties for Quartz as reported from literature (Appendices: Table A.4.1 (Mavko et al., 2020a) on behalf of Simmons (1965) and Koga et al. (1958)). The elastic properties for shales were updated based on our current Smeaheia dataset.

Lithology	**V_p (m/s)**	**V_s (m/s)**	**ρ (g/cm3)**	**Bulk Modulus (GPa)**	**Shear Modulus (GPa)**
Quartz (Literature)	6.04×10^3	4.12×10^3	2.65	36.6	45
Shales (Calculated)	2.96×10^3	1.70×10^3	2.44	11.86	7.10

In the dry phase, the produced outputs K_{sat_insitu}, K_{fl_insitu} and K_m are incorporated with ϕ (PHIE log) to acquire the bulk modulus of the drained rock frame (K_{dry}). K_{dry} is calculated in equation (3.25) through rearranging equation (3.15) via Gassmann inversion, where this generalized formulation is suitable for the use of wireline log data (Zhu & McMechan, 1990) and is applicable for our implementation:

$$K_{dry} = \frac{K_{sat_{insitu}} \left(\frac{\phi K_m}{K_{fl_{insitu}}} + 1 - \phi \right) - K_m}{\frac{\phi K_m}{K_{fl_{insitu}}} + \frac{K_{sat_{insitu}}}{K_m} - 1 - \phi} \quad (3.25)$$

Equation (3.25) indicates that K_{dry} is a function of K_{sat_insitu}, K_{fl_insitu} , K_m , and ϕ, and will consequently be impacted by uncertainty or changes in those reservoir parameters. On the other hand, K_{dry}, is independent of the pore fluid substitution process that will occur afterwards as K_{dry} remains constant in the final phase.

In the final phase, the actual pore fluid substitution process occurs. We start with modelling a fully brine-saturated reservoir followed by a gradual increase in CO_2 saturation (super-critical state), at twenty percent increments, to analyze the following fluid substituted scenarios: 100Brine, 80Brine (S_{CO2} = 20%), 60Brine (S_{CO2} = 40%), 40Brine (S_{CO2} = 60%), 20Brine (S_{CO2} = 80%), and 100CO_2. To ensure accurate GFS implementation, we first model a fully brine-saturated Sognefjord reservoir for calibration purposes. In this scenario, the brine substituted V_p, V_s and ρ logs should align closely to the in-situ wireline log data. An exception, however, would arise in the intervals with slight gas residuals, as the GFS brine-substituted logs may exhibit higher readings compared to the in-situ data (Section 3.3).

For the CO_2 fluid properties, the reservoir pressure and temperature range dictate the phase of the injected CO_2 (Kazemeini et al., 2010). At a measured depth (MD) of 900 m with the provided pressure (P = 11.85 MPa (1719 psi)) and temperature (T=33°C) ranges, the Sognefjord reservoir is at or nearly beyond the critical point for the transition to super-critical CO_2, where supercritical conditions correlate to a P = 7.38 MPa and T=31.2°C (Span & Wagner, 1996). At the given fluid state, the super-critical CO_2 properties are also retrieved using the Mantis package mentioned earlier, from the NIST database, based on the Equation of State for Carbon dioxide (Span & Wagner, 1996) as reported in Table (5). Provided this information, the Statoil (2016) report highlighted the potential risk of the injected CO_2 transitioning into a gaseous state at Trow 32/2_1 due to reservoir depletion at shallower depths.

With the obtained CO_2 fluid properties, we can then proceed to compute the effective fluid modulus of the new substituted mixture, containing brine and CO_2 fluid components. At this point, it is worth recalling that seismic wave velocities (and therefore K_{sat} and K_{fl}) are contingent on pore fluid saturations and the spatial distribution of the different pore fluid phases within the pore structure (Mavko & Mukerji, 1998). This is evidently because K_{sat} (equation (3.15)), which directly feeds into the seismic velocity computation, is a function of pore fluid changes through the fluid modulus, as noted previously. Therefore, employing the Reuss average during GFS for the effective fluid modulus (equation (3.19)) is valid for seismic exploration purposes, where hydrocarbon accumulations have usually undergone equilibrium over extended geologic timescales, resulting in homogeneous fluid mixtures uniformly distributed (uniform saturation) (Eid et al., 2015). However, this assumption becomes invalid during CO_2 injection and migration, as this disrupts the reservoir's static equilibrium and results in heterogeneous fluid distributions or

patchy saturations (Eid et al., 2015). This patchiness occurs during injection at high pressure rates, where the CO_2 gas is incapable of uniformly distributing and equally occupying all of the available pore spaces (Azuma et al., 2013). Hence, in CO_2-saturated reservoirs, spatial saturation heterogeneities result in a range of possible velocity-saturation profiles bounded by two pore-fluid distributions: uniform (homogenous) and patchy fluid distributions or saturations (Caspari et al., 2011; Mavko & Mukerji, 1998), where such heterogeneities then consequently affect the seismic-velocities, reflectivity and seismic amplitudes accordingly (Eid et al., 2015). The difference between uniform and patchy saturations is a function of the degree or the scale at which the different fluid phases are mixed (Mavko et al., 2020c). Therefore, uniform and patchy distributions are dictated by hydraulic diffusivity and thus related to the diffusion or the critical relaxation scale (L_c), as discussed by Mavko & Mukerji (1998), and presented in equation (3.26):

$$L_c = \sqrt{\frac{\kappa K_{fl}}{f\eta}} \tag{3.26}$$

where L_c is the diffusion or critical relaxation scale, κ is permeability, K_{fl} is the fluid bulk modulus, η is the fluid viscosity and f is the seismic frequency. Uniform distributions occur when there is sufficient time for the induced pore pressure gradients to equilibrate. In other words, pore pressure gradients have sufficient time to relax when the scale of pore pressure heterogeneities or the size of the saturation patch (d) is smaller than L_c ($d < L_c$) and the seismic wavelength (Mavko et al., 2020c). Patchy distributions, on the other hand, occur when the scale of pore pressure heterogeneity or the size of the saturation patch (d) is greater than L_c ($d > L_c$). Hence, at patchy distributions, there is no sufficient time during a seismic period for pore pressure equilibration and therefore pressure gradients persist (Mavko et al., 2020c).

The Brie et al. (1995) fluid mixing law is commonly used to account for the impact of patchy saturation, to evaluate the effect of CO_2 saturation on the fluid modulus and seismic velocities in Gassmann modelling (Eid et al. 2015; Perozzi et al., 2016; Prasad et al., 2021). For our Gassmann implementation, however, we utilize a Brie-like fluid mixing law introduced by Papageorgiou et al. (2016) that attribute the spatial variation in pore fluid distributions with capillary pressure variations rather than a given patch size. Equation (3.27) presents the utilized fluid mixing law that

relates the effective fluid modulus (K_{CO2_Mix}) of the CO_2 fluid mixture to the capillary pressure parameter (q) that accounts for the differences in the induced pore-fluid pressures within each inclusion, at the microscopic scale (Papageorgiou & Chapman, 2017; Wang et al., 2021). The previous equation further implies that the effective fluid modulus is dependent on the different pore fluid saturations, their compressibility and corresponding distributions (Papageorgiou et al., 2016; Yun & Song, 2022):

$$K_{CO2_Mix} = \left[\frac{1}{\tilde{q}} \left(\frac{S_w}{K_w} + q \frac{(1 - S_w)}{K_{CO2}} \right) \right]^{-1} , \qquad \text{where } \tilde{q} = S_w + q(1 - S_w) \tag{3.27}$$

$$q_o \leq q \leq 1 \qquad , \quad \text{where} \quad q_o = \frac{K_{CO2}}{K_w} \tag{3.28}$$

where S_w is brine saturation while K_w and K_{CO2} are the bulk moduli of the brine and CO_2, as reported in Table (5), respectively.

The parameter (q) is physically constrained within the values of $q_o = K_{CO2}/K_w$ and one, which analytically simulates the arithmetic (Voigt) and harmonic (Reuss) means at the endpoints noted by equation (3.28) (Papageorgiou et al., 2016). In our GFS workflow, we calculate the reservoir's effective fluid modulus (K_{CO2_Mix}) for the various CO_2 saturations at both bounding limits: q=1 (uniform saturation) and q=q_o (patchy saturation), where the results are presented in Figure (3.8). This analysis aims to investigate the impact of capillary pressure variations, caused by wave induced pore-pressure differences during seismic wave propagation, on both the fluid mixture and the elastic response (seismic velocities, bulk, shear and compressional moduli) of the CO_2-saturated Sognefjord reservoir at both fluid distributions (uniform and patchy distributions).

At the upper limit corresponding to q=1, the fluid mixture is in an isostress condition, at equilibrated pressure gradients and uniform pore fluid pressures (uniform fluid distribution) (Papageorgiou and Chapman 2017) as noted above. Hence, evaluating equation (3.27) at q=1, illustrated in Figure (3.8), yields a relatively soft and compressible fluid mixture equivalent to the case of the Reuss (harmonic) mixing average for uniform saturation presented earlier in equation (3.19) (Papageorgiou et al., 2016; Papageorgiou & Chapman, 2017).

On the contrary, the lower q limit (q=q_o) represents the Voigt (arithmetic) upper bound (Papageorgiou et al., 2016) commonly referred to as the patchy saturation (Mavko & Mukerji,

1998) discussed above. Consequently, this yields a stiffer and less compressible CO_2 fluid mixture (Mavko et al., 2020c), where q_o= 0.054 is calculated using equation (3.29) with the brine and CO_2 bulk moduli reported in Table (5).

Looking at Figure (3.8), it is evident that substituting the saline brine with CO_2 causes significant changes in the acoustic fluid properties. As the CO_2 saturation increases (water saturation decreases) within the fluid mixture, the effective fluid modulus decreases accordingly producing a softer more compressible mix. This is because CO_2 is softer (more compressible) compared to the stiffer water fluid, as indicated by K_w and K_{CO2} in Table (5). One may also observe that within the intermediate saturation range (Brine80-Brine20), for any given CO_2 saturation, employing a smaller q (q_o = 0.054) yields a patchier stiffer fluid mixture compared to a larger q (q=1) for the same intermediate saturation. However, at full saturations (100Brine and 100CO_2), changes in q do not impact the effective fluid modulus, as the mixture at these saturation endpoints consists of a single fluid component.

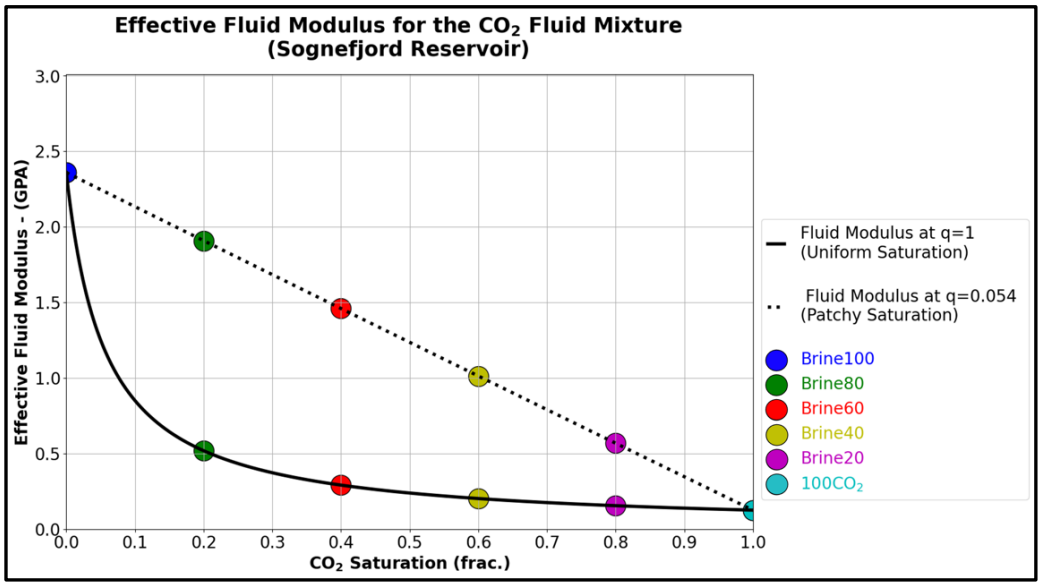


Figure 3.8 – The effective fluid modulus for the CO_2 fluid mixture in the Sognefjord reservoir, calculated at q=1 and q_o=0.054 for various CO_2 saturations.

Having obtained the effective fluid moduli for the different CO_2 mixtures, we conclude the GFS workflow by acquiring the Sognefjord's effective bulk moduli ($K_{sat_CO2_Mix}$), compressional moduli ($M_{sat_CO2_Mix}$) along with the corresponding bulk densities ($\rho_{b_{sat_CO2_Mix}}$) and seismic-

wave velocities ($V_{p\,sat_CO2_Mix}$ and $V_{s\,sat_CO2_Mix}$) associated with the different CO_2 fluid substituted scenarios, computed at both q limits for uniform and patchy saturations. $K_{sat_CO2_Mix}$ is first obtained via equation (3.15), whereas μ_{sat} remains constant through the fluid substitution process regardless of pore fluid changes, as indicated by equation (3.16). To compute the velocities, we calculate the densities (ρ_{CO2_Mix}) of the different CO_2 fluid mixtures, as presented in equation (3.29):

$$\rho_{CO2_Mix} = (S_w * \rho_w) + (S_{CO2} * \rho_{CO2}) \tag{3.29}$$

where S_w and S_{CO2} are brine and CO_2 saturations. ρ_w and ρ_{CO2} are the brine and CO_2 densities reported in Table (5). It's important to note that the densities of the various CO_2 fluid mixtures are not impacted by changes in q (i.e., the density of a fluid mixture containing 20% brine and 80% CO_2 is the same for q=1 and q_o=0.054).

The resulting products are then subsequently employed to calculate the $\rho_{b_{sat_CO2_Mix}}$, $V_{s\,sat_CO2_Mix}$ and $V_{p\,sat_CO2_Mix}$ for the various CO_2 fluid substituted scenarios, using equations (3.30) through (3.32) accordingly:

$$\rho_{b_{sat_CO2_Mix}} = \rho_{b_{Insitu_FL}} - \phi\rho_{Insitu_FL} + \phi\rho_{CO2_Mix} \tag{3.30}$$

$$V_{s\,sat_CO2_Mix} = \sqrt{\frac{\mu_{sat}}{\rho_{b_{sat_CO2_Mix}}}} \tag{3.31}$$

$$V_{p\,sat_CO2_Mix} = \sqrt{\frac{K_{sat_CO2_Mix} + \frac{4}{3}\mu_{sat}}{\rho_{b_{sat_CO2_Mix}}}} \tag{3.32}$$

where $\rho_{b_{fl_insitu}}$ is equivalent to the in-situ measured bulk density (ρ) wireline log data referred to in Table (1). The results demonstrating the impact of CO_2 fluid changes on the elastic moduli and seismic velocities are presented and discussed in the results section.

3.2.3 Synthetic Generation & AVO Analysis

Numerous studies within the CO_2 literature demonstrate the application of amplitude variation with offset/angle (AVO/AVA) analysis as a critical step of the rock physics forward modelling workflow for the detection and mapping of the injected CO_2 plume or for delineating potential CO_2 migration and leakage pathways, as required for the monitoring and verification of carbon capture and storage (CCS) projects (Dupuy et al., 2017; Fawad & Mondol, 2022; Grude et al., 2014).

Therefore, in this thesis, we intend to investigate the effect of CO_2 saturation changes, at uniform and patchy distributions, on the seismic reflectivity and corresponding seismic amplitudes. To achieve our objective, we compute reflectivity and analyze amplitude variations with offset (AVO) or angle (AVA) as we transition from the overburden caprock (Heather and Draupne shale formations) into the CO_2-saturated Sognefjord reservoir. We then conclude this analysis with generating AVA pre-stack synthetic gathers for incidence angles ranging 0-36° for the different CO_2-sautrated scenarios modelled in Section (3.2.2).

Reflectivity is fundamental for AVO or AVA analysis, which examines the change in reflectivity or seismic amplitude as a function of varying incidence angles or offsets (Castagna & Backus, 1993). The angle-dependent reflectivity provides valuable insight into the subsurface rock properties, including porosity, lithology or pore fluids, that directly impact the reservoir's elastic response dictated by density and the seismic wave velocities. Consequently, rock property variations impact the AVA/AVO response and may account for such changes in the reflectivity and seismic amplitudes (Castagna & Backus, 1993).

Reflectivity is obtained through Zoeppritz equations (Simm & Bacon, 2014a). Nevertheless, due to the complexity of the formulated equations, several researchers such as Fatti et al. (1994) and Shuey (1985), developed alternative approximations that may demonstrate the impact of reservoir and seismic properties on offset or angle-dependent reflectivity more intuitively (Simm & Bacon, 2014a). In this section, we employ a Zoeppritz formulation, as introduced by Hilterman (2001), to derive the reflectivity response across the CO_2-saturated Sognefjord reservoir. Assuming a two-layer earth model, each layer is characterized by specific elastic properties (V_p, V_s and ρ), resulting in unique acoustic impedance (AI) and Poisson ratio (σ) elastic profiles. The reflectivity $R(\theta)$ at a given incidence angle (θ) is then defined in equation (3.33) as the following:

$$R(\theta) = A(\cos\theta)^2 + B(\sin\theta)^2 \tag{3.33}$$

$$A = \frac{AI_2 - AI_1}{AI_2 + AI_1} \quad , \qquad \text{where } AI = V_p * \rho \tag{3.34}$$

$$B = \frac{\sigma_2 - \sigma_1}{(1 - \sigma_{avg})^2}, \quad \text{where } \sigma = \frac{V_p^2 - V_s^2}{2(V_p^2 - V_s^2)} \quad \text{and} \quad \sigma_{avg} = \frac{\sigma_1 + \sigma_2}{2} \tag{3.35}$$

where A and B are the intercept and gradient terms associated with the contrast of acoustic impedance and Poisson's ratio as a function of varying incidence angles across the Sognefjord interface, as expressed in equation (3.34) and (3.35), respectively. AI_1 and σ_1 represent the acoustic impedance and Poisson's ratio of the overburden caprock, maintaining its in-situ elastic response and brine-saturated fluid mixture throughout the AVA analysis, regardless of the GFS occurring in the lower layer. On the other hand, AI_2 and σ_2 correspond to the acoustic impedance and Poisson's ratio of the underburden CO_2-saturated Sognefjord reservoir.

It is important to note that the presented approximation in equation (3.33) is fairly similar to the two-term Shuey (linear) formulation of the Zoeppritz equation. However, the Shuey representation was redefined to emphasize that the angle-dependent reflectivity at an interface can be related to the contrast in two significant seismic attributes, AI and σ, as demonstrated by equations (3.34) - (3.35) (Simm & Bacon, 2014a). Knowing that the latter seismic attributes are particularly influenced by density and seismic velocities, as AI and σ are obtained through equations (3.34) and (3.35), this confirms that a change in the seismic reservoir properties will impact the AVA/AVO response at a given interface (Simm & Bacon, 2014a), as noted previously.

Hence, to acquire the desired reflectivities across the CO_2-saturated Sognefjord interface, we compute the relevant intercept and gradient terms. This computation entails employing the final GFS products ($V_{p\,sat_CO2_Mix}$, $V_{s\,sat_CO2_Mix}$ and $\rho_{b_{sat_CO2_Mix}}$) to determine the corresponding AI_2 and σ_2 profiles attributed to the various CO_2 fluid substituted scenarios for uniform and patchy saturations. For the in-situ reservoir reflectivity, we calculate AI_2 and σ_2 using the measured wireline log data (V_p , V_s and ρ) for the Sognefjord interval prior to the GFS implementation.

Proceeding forward, we generate in-situ and CO_2-substituted AVA synthetic seismic gathers for incidence angles ranging 0-36° using time-resampled reflectivities. This involves applying the convolutional model, as presented in equation (3.36):

$$s(t) = r(t) * w(t) + n(t) \tag{3.36}$$

where $s(t)$, $r(t)$, and $w(t)$ are the seismic trace, reflectivity and source wavelet as a function of time t , respectively, while n is potential noise and $*$ denotes convolution. Equation (3.36) illustrates that the computed seismic trace is the convolution of the time-reflectivity series with a source wavelet (Russell, 1988). The final seismic trace is the superposition of the individual seismic reflections generated at different subsurface interfaces (Simm & Bacon, 2014a). In this modelling scenario, we overlook the presence of noise during the generation of our synthetic seismic gathers, assuming $n(t) = 0$.

We further select a symmetrical zero-phase Ricker wavelet for the synthetic seismic generation. The Ricker wavelet $w(t)$ is originally defined in the time domain by equation (3.37):

$$w(t) = \left(1 - \frac{1}{2}{\omega_p}^2 t^2\right) e^{\left(-\frac{1}{4}{\omega_p}^2 t^2\right)} \tag{3.37}$$

where ω_p is peak angular frequency (radians/second) and t is the time in seconds (Ricker, 1953; Y. Wang, 2015). At substituting ω_p for $2\pi f$, the Ricker wavelet $w(t)$ becomes a function of the peak frequency (f) in Hz , as demonstrated by equation (3.38):

$$w(t) = (1 - 2\pi f^2 t^2) e^{(-\pi^2 f^2 t^2)} \tag{3.38}$$

In Figure 3.9 (A), we illustrate the zero-phase Ricker wavelet at a peak frequency of f=50 Hz, as reported by Blangy (1992) while analyzing the Sognefjord Formation at Troll Field, located 15 km to the west of our Trow 32/2_1 well. In constructing this wavelet, we adopt the positive standard polarity convention (also referred to as 'American' or SEG normal polarity) as discussed by Brown (2001). This convention interprets a positive reflection as a peak, indicating an increase

in acoustic impedance across a given interface, where seismic peaks are depicted in blue and troughs are displayed in red (Brown, 2001) as shown in Figure 3.9 (B).

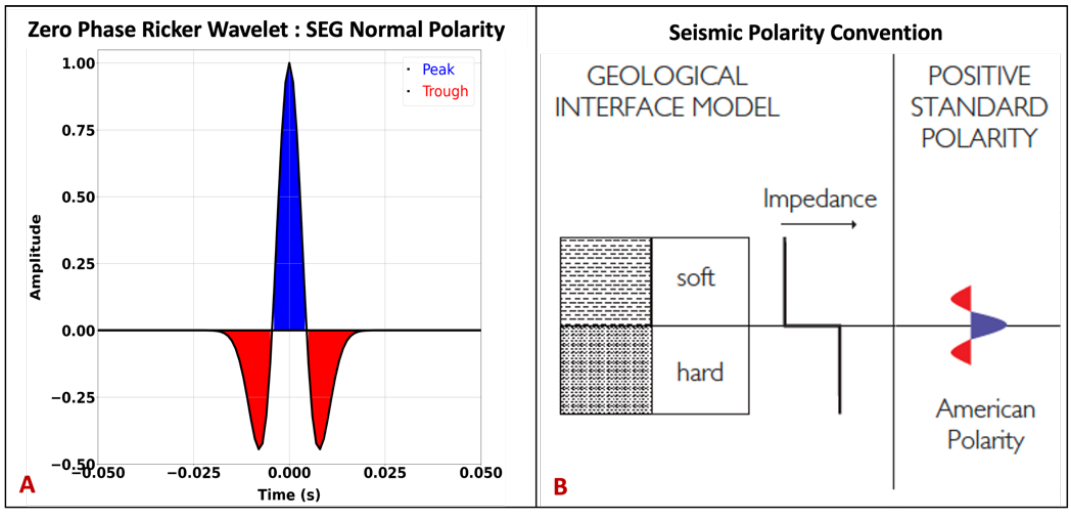


Figure 3.9 – (A) Zero-Phase Ricker wavelet generated at f=50 Hz. (B) Positive Standard Polarity (also referred to as American Polarity) represents a positive reflection as a peak, correlating to an increase in acoustic impedance across a given interface. Soft denotes softer lithology whereas hard represents a stiffer lithology. (Modified after (Simm & Bacon, 2014a)).

The generated synthetics are then evaluated to analyze the effect of varying CO_2 saturations on the seismic amplitude for uniform and patchy modelled GFS scenarios. In doing so, we investigate AVA/AVO plots for changes in the reflectivity with greater incidence angles to characterize the AVA response. The generated results will be presented and discussed in the upcoming section.

3.3 Results & Discussion

In this section, we present and discuss the results obtained from the conventional rock physics forward modelling workflow. We will particularly evaluate the impact of varying CO_2 saturations and fluid distribution patterns on the reservoir's elastic response and seismic reflectivity. To do this, we will first analyze the CO_2 fluid substituted elastic responses at uniform and patchy saturations. We will then introduce the concept of rock physics templates and discuss their implementation for CO_2 fluid detection and mapping. Finally, we will conclude this analysis with discussing the AVA responses for the different CO_2 modelled scenarios across the Sognefjord

reservoir and present the AVA pre-stack synthetic gathers to demonstrate the CO_2-induced seismic reflectivity changes across the boundary of interest.

We originally discussed that CO_2-saturated reservoirs experience spatial saturation heterogeneities that result in a spectrum of possible velocity-saturation profiles bounded by two pore-fluid distributions: uniform and patchy fluid distribution. In evaluating the GFS modelled elastic responses, Figure (3.10) illustrates the results of the CO_2-saturated Sognefjord reservoir at uniform saturation (q=1), displayed in Tracks 3 - 9. We previously mentioned that we first modelled a fully-brine saturated (dark blue) Sognefjord reservoir for calibration purposes. As anticipated, the brine substituted V_p, V_s and ρ logs correlated closely to the in-situ (black) wireline log responses, except for some intervals that contain small gas saturations. In those intervals, the GFS brine-substituted V_p and ρ displayed a higher elastic response compared to the in-situ data, while V_s remained unaffected by the CO_2 fluid changes.

Furthermore, we observe that there is a significant decrease in the Sognefjord's elastic response of V_p ($V_{p\,sat_CO2_Mix}$), ρ ($\rho_{b_{sat_CO2_Mix}}$) and the bulk modulus ($K_{sat_CO2_Mix}$) at injecting the first increment of about 20% CO_2 into the storage reservoir, modelled by the Brine80 (green log) fluid mixture across the different tracks. This decrease in the elastic response indicates a softening of the Sognefjord reservoir at injecting CO_2 due to substituting the stiff saline aquifer with a softer CO_2 fluid mixture. Conversely, the shear-wave velocity ($V_{s_{sat_CO2_Mix}}$) slightly increases (Track 4) with increasing CO_2 saturations, as this is attributed to the reduction in the bulk density of the reservoir rock. We further note that injecting the storage reservoir with larger CO_2 saturations (> 20%) yields a minimal decrease or change in the elastic properties of the Sognefjord reservoir, as demonstrated by the Brine60 (red), Brine40 (yellow), Brine20 (magenta) and 100CO_2 (cyan) fluid mixtures that contain 40% - 100% CO_2 concentrations, respectively.

The acoustic impedance (AI), Poisson's ratio (PR denoted previously as σ) and the velocity ratio (V_p/V_s) are seismic derivative attributes from the corresponding V_p, V_s and ρ logs. AI and PR (or σ) are obtained through equations (3.34) and (3.35) presented previously, whereas the velocity ratio is simply the ratio of the reservoir's compressional to shear-wave velocity. The results in Figure (3.10) illustrate that the reservoir's AI, PR and V_p/V_s ratio elastic attributes decrease with increasing CO_2 saturations accordingly, as illustrated in Tracks 7 - 9 ($\mathrm{AI_{Brine}}$, $\mathrm{PR_{Brine}}$, $\mathrm{V_p/V_{s_{Brine}}} > \mathrm{AI_{CO2}}$, $\mathrm{PR_{CO2}}$, $\mathrm{V_p/V_{s_{CO2}}}$).

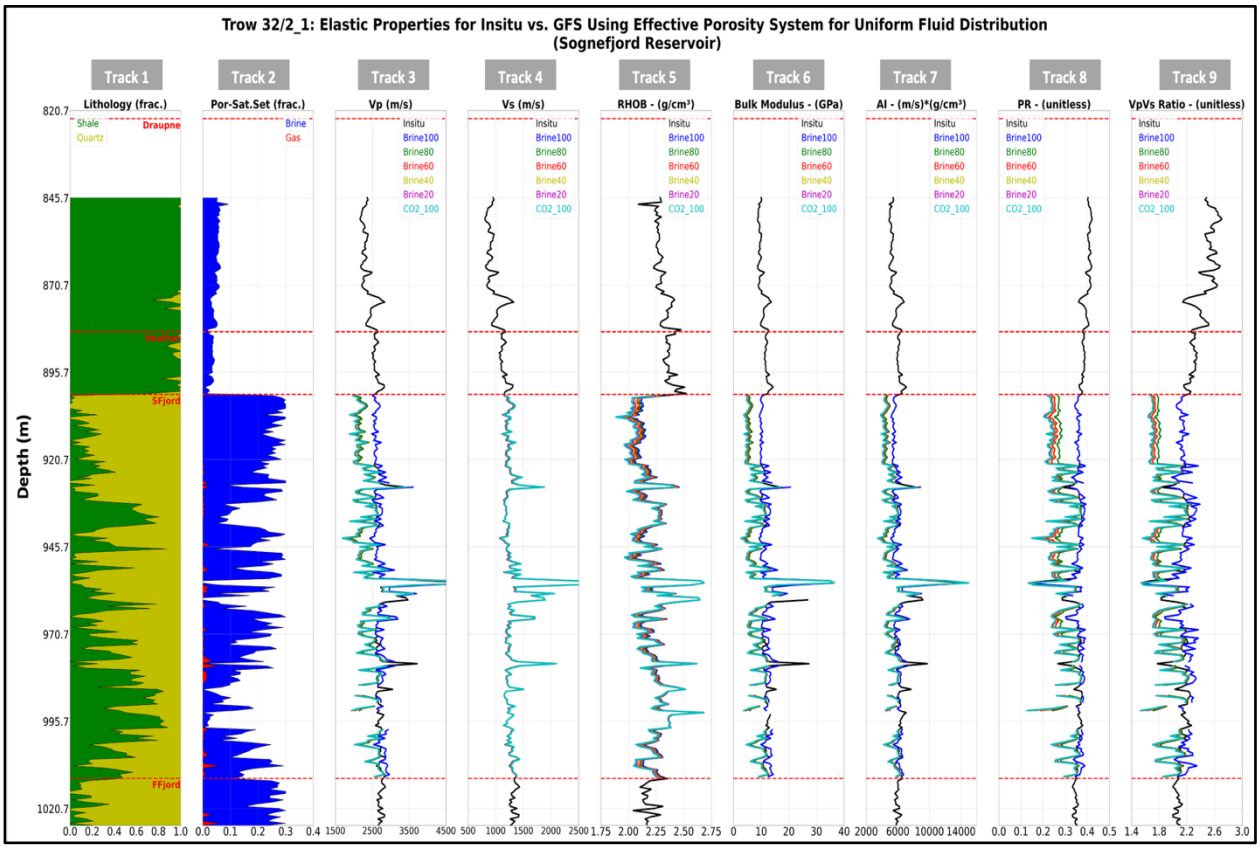


Figure 3.10 - Gassmann Fluid Substitution results for the Sognefjord reservoir at different CO_2 saturations for uniform saturation ($q = 1$). The elastic responses for the compressional velocity, density, bulk modulus, acoustic impedance, the Poisson and velocity ratios decrease with increasing CO_2 saturations. Conversely, the shear-wave velocity slightly increases.

At this stage, it is important to note that the fluctuations in the GFS response of the different elastic attributes within the reservoir correlate to variations in the effective porosity. Hence, larger effective porosity allows for a larger GFS fluid effect and vice versa. As a result, interval zones of larger porosity display a large separation between the Brine100 (blue) and the remaining CO_2 substituted GFS logs. Conversely, as effective porosity decreases (sometimes approaching zero in zones of high shale content), there is a minimal to negligible fluid effect where we observe no separation in the elastic response correlating to the different fluid mixtures. The latter observation has consequently impacted the GFS results in the lower section of the target reservoir, noted by the visible discontinuities in the produced log responses. These gaps correspond to outlier behavior that resulted during the dry rock modelling phase, as visualized in the QC plot of effective porosity vs. normalized bulk modulus (K_{dry}/K_m) in Figure (3.11). This plot illustrates that the outlier behavior occurs at relatively large ($K_{dry}/K_m > 1$) or small ($K_{dry}/K_m < 0$) normalized bulk modulus

values that correlate to relatively low effective porosity and shalier reservoir content. As discussed by Simm & Bacon (2014b), the latter challenge is noted as a common pitfall during GFS for shaley sand reservoirs. To address this issue, they recommend that we apply PHIE and Vol_{sh} cut-offs to avoid GFS in the non-reservoir matrix component. In implementing such a solution, we filtered out the outlier data points corresponding to the small and large normalized bulk modulus values while performing GFS. We would like to emphasize that this filtration process does not affect the seismic reflectivity or the AVO response at the top Sognefjord reservoir, as this pertains to a deeper section.

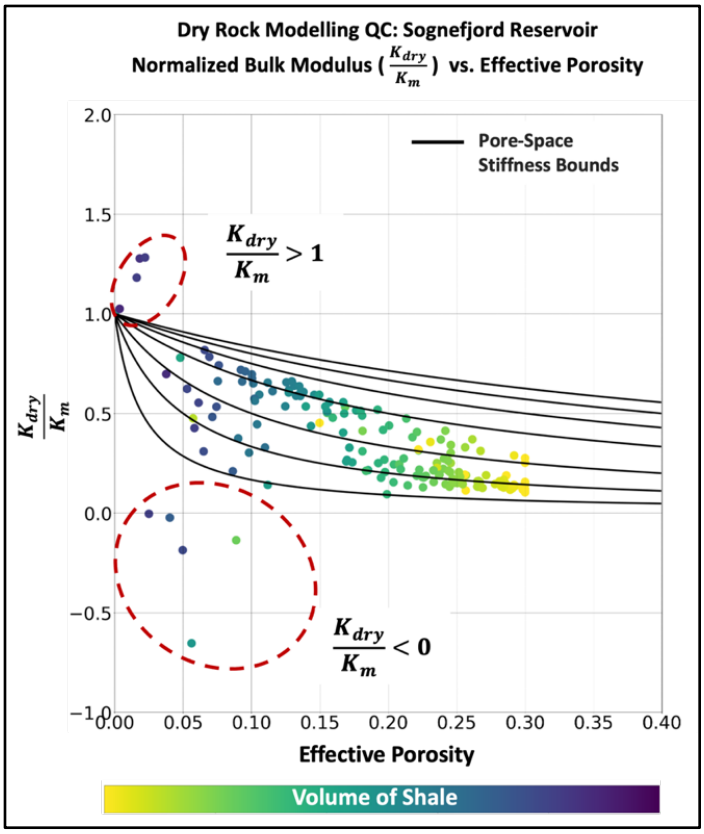


Figure 3.11 – This figure is a QC plot for the dry rock modelling phase. It presents the normalized bulk modulus $\left(\frac{K_{dry}}{K_m}\right)$ *vs. Effective Porosity overlaid by pore-space stiffness bounds. The outlier points falling above the stiffest pore space stiffness bound, at* $\left(\frac{K_{dry}}{K_m}\right) > 1$ *will result in a very small fluid effect (stiff GFS response). Conversely, the outlier data points falling below, at* $\left(\frac{K_{dry}}{K_m}\right) < 0$ *will simulate an exaggerated fluid effect (very soft response). These data points correlate to shalier non-reservoir content at relatively lower effective porosities.*

Figure (3.12) illustrates the velocity-saturation profiles associated with the uniform and patchy CO_2 distribution patterns, within the low-frequency Gassmann limit for the target reservoir. The uniform saturation profile (q =1) results in a softer (less stiff) elastic response (Mavko et al., 2020c)

due to pore-pressure equilibration. This is evident in the lower compressional velocities, bulk moduli, acoustic impedances, and the velocity ratio values obtained for the various CO_2 saturation mixtures modelled at uniform pore fluid distributions. The elastic response at uniform saturation is depicted by the lower velocity-saturation bounding curve, which abruptly decreases at injecting the first increment of 20% CO_2 followed by negligible change (slight decrease) in the elastic response for greater CO_2 saturations, as illustrated in Figure (3.12).

In contrast, the patchy saturation profile (q_o= 0.054), represented by the upper bound, exhibits an inversely linear decrease in the V_p, K, AI and V_p/V_s ratio elastic responses with increasing CO_2 saturations. At full brine and CO_2 saturations, changes in pore-fluid distributions (through changes in q) do not impact the elastic attributes. At intermediate saturations, however, the patchy saturation profile experiences persistent pore-pressure gradients that result in a stiffer reservoir response (Mavko et al., 2020c). Consequently, patchy saturation leads to higher V_p, K, AI and V_p/V_s ratio elastic readings compared to the uniform distribution, for the same CO_2 saturation. As previously noted, this figure also confirms that density decreases with increasing CO_2 saturation, while the shear-wave velocity slightly increases for reasons discussed earlier. Nevertheless, changes in pore fluid distributions do not impact the reservoir's density and shear-wave elastic responses, as observed in Figure (3.12).

In further investigating the effect of uniform versus patchy saturations on the Sognefjord's reservoir response, we take a closer look at Figures 3.13 (A-B). Figure 3.13 (A) displays the uniform and patchy modelled elastic attributes for the Brine40 GFS scenario in comparison with the in-situ reservoir log data (black), as illustrated in Tracks 3-7. Looking at this figure, it is evident that the change in elastic responses produced by patchy saturation (dashed orange line) is smaller compared to uniform saturation (solid yellow line), as observed for V_p, K, AI and the V_p/V_s ratio. This observation is also consistent for all other intermediate CO_2 saturation mixtures, as shown in Figure 3.13 (B). Consequently, this indicates that uniform saturations will yield a larger AI and PR contrast across the Sognefjord interface, generating stronger reflectivity responses. Conversely, patchy saturations will result in smaller AI and PR contrasts, affecting the seismic reflectivity accordingly. The impact of such discrepancies on reflectivity and the seismic amplitudes will be further discussed and demonstrated by the pre-stack AVA synthetics that will be presented in the subsequent discussion.

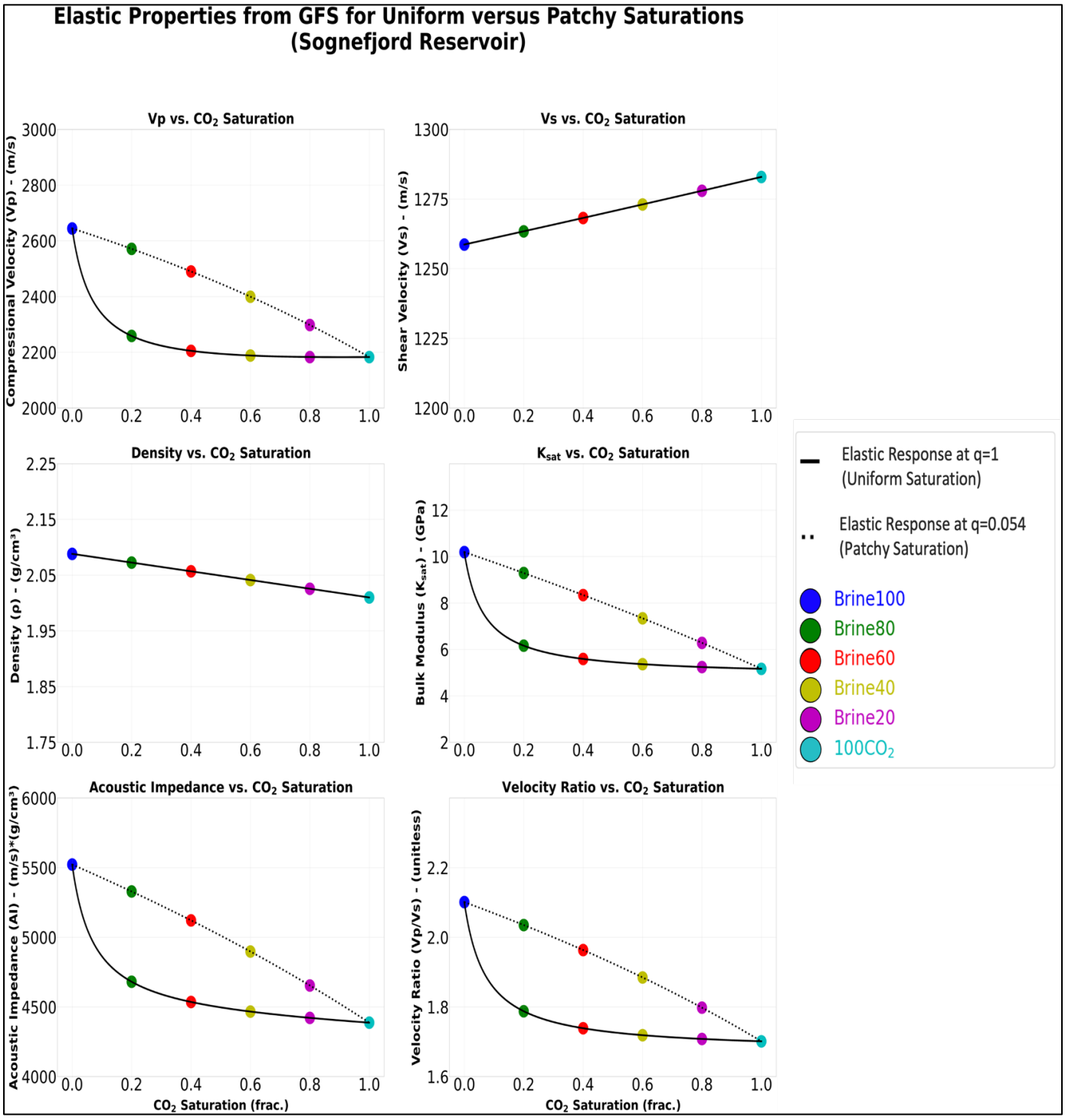


Figure 3.12 – The impact of uniform versus patchy saturations on the Sognefjord reservoir for different CO_2 mixtures. The lower velocity-saturation curve represents uniform distribution ($q = 1$) that results in a soft elastic response. The upper velocity-saturation bound represents the patchy saturation ($q = 0.054$) that results in a stiffer elastic response, for the same CO_2 concentration.

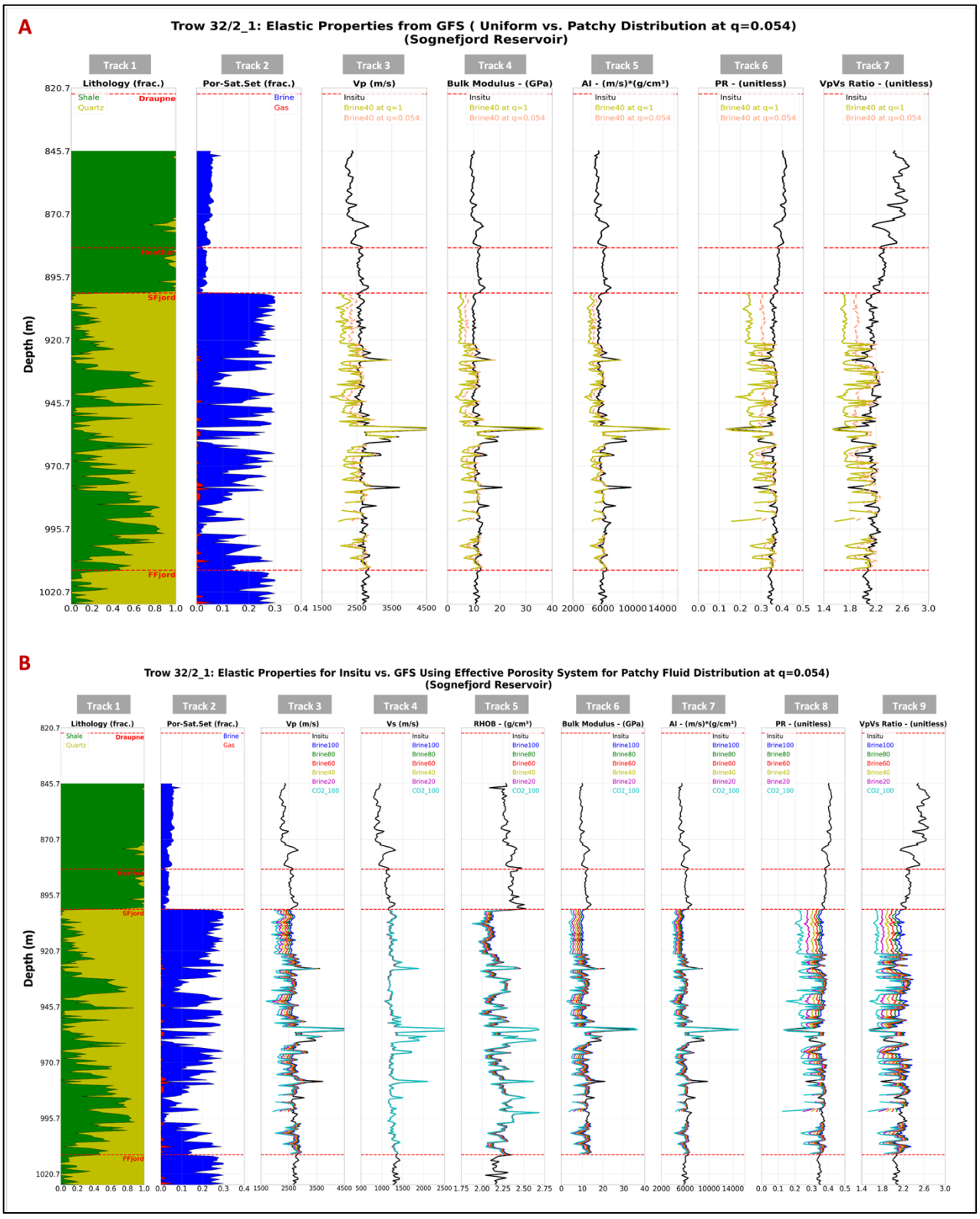


*Figure 3.13 – **(A)** Gassmann Fluid Substitution results for the Sognefjord reservoir comparing uniform versus patchy saturations for the Brine40 fluid mixture. The results show that the change (decrease) in elastic responses produced by patchy saturation (dashed orange line) are smaller compared to the uniform saturation (solid yellow line). **(B)** Gassmann Fluid Substitution results for the Sognefjord reservoir at different CO_2 saturations under patchy saturation ($q_0 = 0.054$) conditions. The elastic responses for the compressional velocity, density, bulk modulus, acoustic impedance, the Poisson and velocity ratios decrease with increasing CO_2 saturations. Conversely, the shear-wave velocity slightly increases.*

The previous analysis demonstrates that uniform and patchy saturations can have direct implications on the reservoir's elastic behavior. This introduces a degree of uncertainty in CO_2 fluid detection and mapping for reservoir characterization and seismic monitoring purposes. To address this uncertainty, we employ rock physics to establishes a link between the seismic elastic attributes and the reservoir petrophysical properties (i.e., porosity, lithology, saturation, permeability, etc.) (Fawad & Mondol, 2022). In achieving this, we utilize rock physics templates (RPT) to demonstrate the relationship between the different seismic elastic attributes with respect to various petrophysical properties, where such templates are usually constrained according to local geology and the current dataset at hand (Avseth et al., 2005b). We may utilize different templates that serve particular rock physics objectives, through cross-plotting a combination of different elastic attributes.

For our particular CO_2 fluid detection and mapping objective, we employ a particular pre-stack rock physics template by cross-plotting Acoustic Impedance (AI) versus Velocity Ratio (V_p/V_s), as discussed by Avseth et al. (2005b). In constructing this template, we utilize the pre-stack seismic attributes (AI and Vp/Vs Ratio) derived from the GFS results for the CO_2 uniform and patchy saturations, as presented in Figure 3.14 (A-B) and (C-D), respectively.

In Figure 3.14 (A), we start with plotting the Sognefjord's uniform AI and V_p/V_s ratio responses for the Brine100 and Brine80 (S_{CO2}=20%) fluid mixtures. As we anticipate, we observe the largest drop in the elastic response to occur while injecting the first increment of 20% CO_2 gas. The plot demonstrates that the reservoir's elastic response at full brine saturation exhibits higher velocity ratio compared to the softer Brine80 (S_{CO2} = 20%). Based on the observed separation in Figure 3.14 (A), we generate a linear CO_2 discriminator line that separates the brine from CO_2 using the following representation: V_p/V_s Ratio = mAI + b. We can further note that the same discriminator line is also effective for separating the Brine100 from the remaining softer CO_2 mixtures (at uniform saturations) lying at slightly lower velocity ratio values, as seen in Figure 3.14 (B). When plotting the same seismic attributes at patchy distributions using the same CO_2 fluid separation line, we can see that the discrimination between the fully brine-saturated reservoir response and the remaining CO_2 saturations is far less pronounced primarily due to the stiffer CO_2-saturated Sognefjord response, as presented in Figure 3.14 (C) and (D).

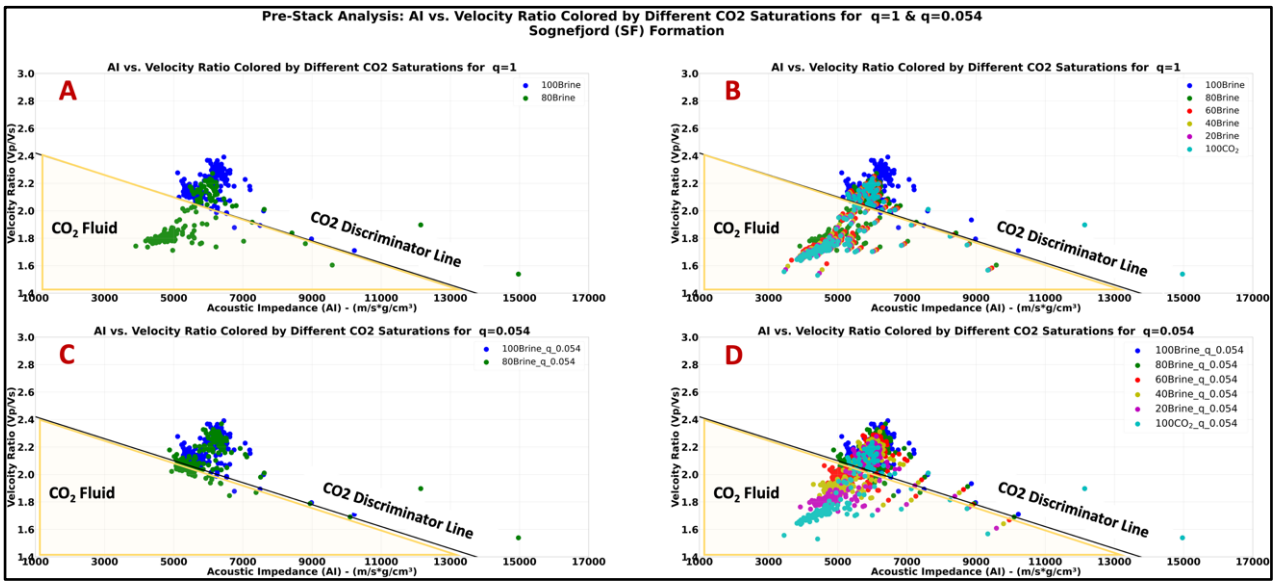


Figure 3.14 – Pre-stack Rock Physics Template for the Sognefjord Reservoir: AI vs. Vp/Vs Ratio for different CO_2 mixtures. ***(A – B)*** *AI vs. Vp/Vs ratio at Uniform Saturation* ***(C-D)*** *AI vs. Vp/Vs Ratio at Patchy saturation. The linear CO_2 discriminator line is of the following representation: Vp/Vs Ratio = m*AI + b. The yellow highlighted zone indicates the data falling below the discriminator is mapping CO_2 fluids.*

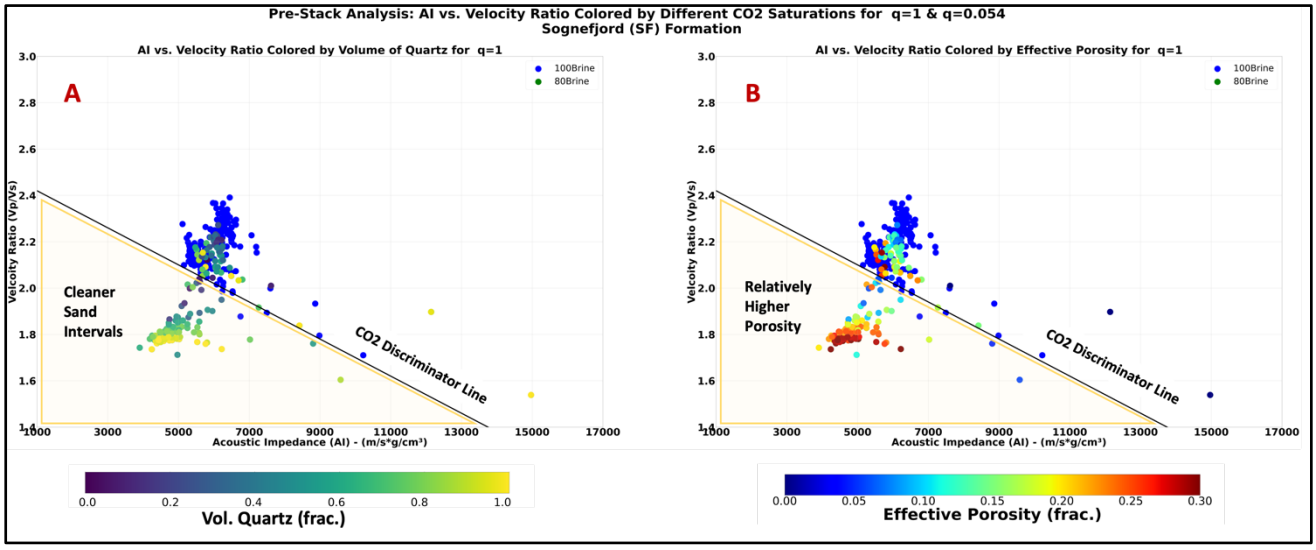


Figure 3.15 - Pre-stack Rock Physics Template: AI vs. Vp/Vs Ratio for Brine100 and Brine80. ***(A)*** *The AI and Vp/Vs ratio responses for the Brine80 fluid mixture has been colored by volume of Quartz.* ***(B)*** *The AI and Vp/Vs ratio responses for the Brine80 fluid mixture has been colored by effective porosity. This figure demonstrates that the CO_2 discriminator line primarily targets the higher porosity CO_2-saturated sandy intervals within the Sognefjord reservoir, as highlighted by the yellow zone.*

Finally, it is worth noting that the CO_2 discriminator line primarily targets the lower V_p/V_s and lower AI ranges that capture the higher porosity CO_2-saturated sandy intervals within the Sognefjord reservoir. This occurs because substituting the reservoir's in-situ brine with the lower density CO_2 gas results in a reduction of both the acoustic impedance and the velocity ratio (Fawad & Mondol, 2022), as evidently see in Figure (3.14). The desired CO_2-saturated sand bodies are indicated by the colored data points falling below the fluid line (highlighted in yellow), as opposed to the CO_2-satured shale bodies that lie above the CO_2 discriminator and overlap with the fully brine-saturated response. This observation is further confirmed when we color the corresponding data by the volume of quartz as demonstrated in Figure (3.15) (A-B). Although not implemented in this study, the generated CO_2 discriminator line can be applied on inverted acoustic impedance and velocity ratio seismic cubes to map and track the injected CO_2 plume within the Sognefjord reservoir for seismic monitoring purposes.

After evaluating the impact of CO_2 injection on the Sognefjord reservoir by examining the GFS modelled elastic log responses, we proceed to analyze the synthetics and corresponding seismic reflectivity changes through AVA/AVO analysis. In Figure 3.16 (A) and (B), we analyze the reflectivity changes across the Sognafjord's interface through the AVA plots. Simultaneously, we present the corresponding AVA pre-stack synthetic gathers for the various CO_2 fluid mixtures at uniform and patchy saturations, as shown in Figure 3.17 (A) and (B). respectively. Several observations can be made from the latter two figures.

As we transition from the shaley overburden caprock (characterized by slightly higher AI and PR) into the CO_2-saturated Sognefjord reservoir, we previously noted a decrease in the acoustic impedance and Poisson's ratio log responses with increasing CO_2 saturation, as demonstrated by Figure (3.10) and Figure 3.13 (B) for both uniform and patchy saturations. In the context of AVA analysis, the contrast in the AI and PR attributes provide the intercept and gradient terms, as previously discussed, to characterize the AVA response at the Sognefjord interface. The AVA intercept, term (A), defined in equation (3.34), determines the polarity and the amplitude of the seismic reflection at the desired interface. Hence, the decrease in acoustic impedance across this boundary indicates that the reservoir top will be represented by a negative intercept term or a trough (red) for the in-situ and different CO_2 modelled scenarios. On the other hand, the gradient term (B), as defined in equation (3.35), demonstrates the resulting changes in reflectivity with larger offset angles, ranging from 0 to 36 degrees.

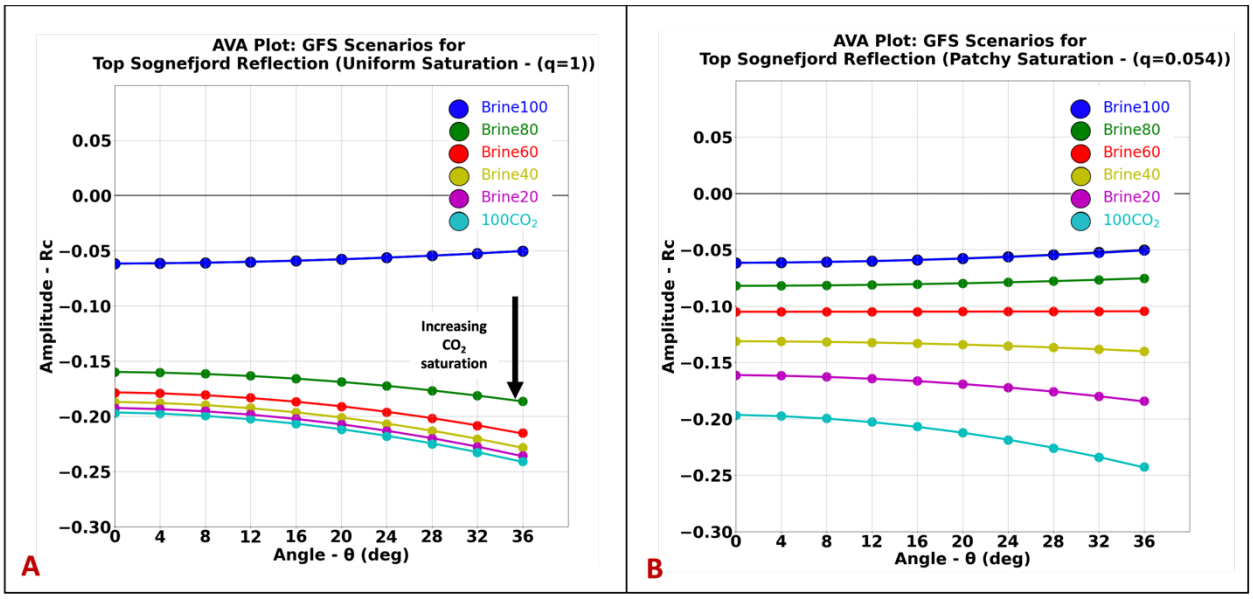


*Figure 3.16 – **(A)** AVA seismic responses for different CO_2 mixtures, across the Sognefjord reservoir, at uniform saturation. CO_2 mixtures display a class III AVA response, stronger reflectivity and steeper gradient at larger offset angles. **(B)** AVA seismic responses for different CO_2 mixtures, across the Sognefjord reservoir, at patchy saturation. This figure shows a change in reflectivity with weaker amplitudes and shallower gradients for the Brine80 – Brine40 fluid mixtures.*

Looking at Figure 3.16 (A) for uniform saturation, we can observe that the reflectivity of the in-situ and fully brine-saturated scenarios overlap as the reservoir is predominantly wet. For these scenarios, there is a very small to negligible change in reflectivity at the larger offset angles that may result in a slight dimming effect on the corresponding synthetic. The plot further demonstrates a large change in the reflectivity between the brine and the remaining CO_2 modelled scenarios, resulting in higher amplitudes for larger CO_2 concentrations. This effect can be attributed to the saturating CO_2 fluid, given that this fluid component has a lower bulk modulus compared to the brine. Consequently, this analysis reveals that while the in-situ and fully brine-saturated scenarios show a negligible AVA response across the Sognefjord interface, increasing CO_2 saturations produce stronger reflectivity that can be characterized by a more profound Class III AVA response and amplitude brightening at larger incidence angles. The discussed reflectivity changes are also observed on the reservoir's seismic response, as emphasized by the black line marking the Sognefjord's interface in the generated synthetics, shown in Figure 3.17 (A).

Analyzing the AVA plot for patchy saturations in Figure 3.16 (B), we can see that increasing CO_2 saturations still generates higher reflectivity and gradually steeper gradients that consequently produce a class III AVA response, as seen for the Brine20 (S_{CO2}=80%) and $100CO_2$ mixtures. At full saturations (brine and CO_2), there is no change in the observed seismic reflectivity or AVA

response as single fluid phase mixtures are not impacted by changing q or by uniform versus patchy distributions. Nevertheless, there is an evident change in the AVA response for Brine80 (S_{CO2}=20%), Brine60 (S_{CO2}=40%) and Brine40 (S_{CO2}=60%) patchy CO_2 mixtures. These scenarios now exhibit weaker reflectivity (lower amplitudes) and a change in gradient, attributed to the smaller AI and PR contrasts caused by increased patchiness. As a result, at forty (red) and sixty (yellow) percent CO_2, the reservoir displays a relatively flat reflectivity gradient indicating no detectable changes in the AVA seismic response and amplitude of the Sognefjord interface at these mixtures. At twenty (green) percent CO_2, the AVA response reflects a very small to negligible change in reflectivity observed at the larger offset angles which portrays a small dimming effect on the synthetic. The corresponding AVA synthetics and observed seismic responses for the Sognefjord interface at patchy distributions are displayed in Figure 3.17 (B).

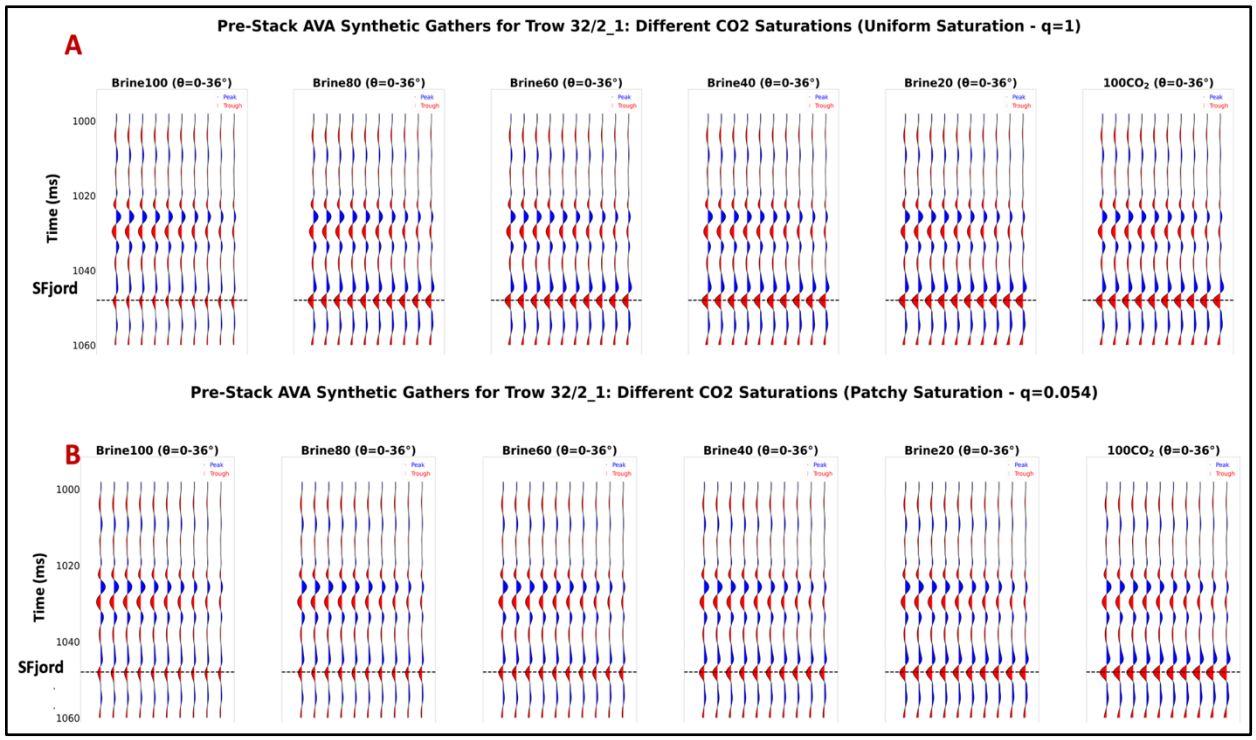


*Figure 3.17 – **(A)** AVA Pre-stack Synthetic gathers for different CO_2 mixtures at uniform saturation. Increasing CO_2 saturation results in amplitude brightening. **(B)** AVA Pre-stack Synthetic gathers for different CO_2 mixtures at patchy saturation. This figure illustrates the CO_2-induced seismic reflectivity changes across the Sognefjord (SFjord) interface between uniform and patchy saturations. Generally, the reflectivity at patchy saturations is weaker compared to the stronger reflectivity (higher amplitude) at uniform saturation.*

The conducted AVA analysis finally reveals that depending on the actual seismic data quality, detecting even small amounts of CO_2 (about 20%) at uniform saturation may be more achievable

due to the distinct reflectivity changes observed. Conversely, when patchiness increases, the detection of CO_2 in the seismic becomes more challenging unless a substantial volume of injected CO_2 (about 80% CO_2 required) is present to generate a detectable AVA seismic response. Employing the obtained observations, we can then compare the generated synthetics with the actual time-lapse data seismic data, and at identifying a seismic signature associated with a Class III AVO response, we may infer the presence of CO_2 fluids. This approach would demonstrate how we leverage the rock physics forward modelling approach in investigating the seismic response and tracking the injected CO_2 plume for seismic monitoring purposes. Nevertheless, as we don't have CO_2 injected time-lapse seismic available, we could not make this comparison for validation.

4 Frequency-Dependent Rock Physics Forward Modelling

4.1 Introduction

As seismic waves propagate through partially saturated reservoir rocks, they induce dynamic compression of the rock's pore spaces and the occupying fluids. This compression generates wave-induced pore pressure gradients, driven by variations in fluid properties and pore structure. In response to these pressure differentials, squirt flow occurs at the pore scale, facilitating fluid exchanges between cracks and pores of varying sizes, stiffnesses and orientations (Chapman et al., 2002).

The pressure equilibration process follows a frequency-dependent diffusion mechanism, during which pore fluids migrate from high-pressure, thin, compliant cracks to stiffer, lower-pressure spherical pores (W. F. Murphy et al., 1986). This squirting mechanism induces seismic dispersion and attenuation, both of which vary with frequency. Numerous studies have particularly highlighted that squirt-flow-induced dispersion results in frequency-dependent reflection coefficients, necessitating frequency-dependent convolutional modeling for accurate simulation of CO_2 seismic behavior (Innanen, 2011; Odebeatu et al., 2006; Sun et al., 2012; Wu et al., 2013; Xu et al., 2011). Given this frequency dependence, squirt flow influences seismic reflectivity by altering the dynamic moduli of partially saturated rocks (Mavko et al., 2020c). Consequently, as Chapman et al. (2006) emphasizes, there is a clear need for frequency-dependent rock physics modeling workflows that explicitly account for squirt-flow mechanisms when analyzing dispersive effects in partially saturated CO_2 reservoirs.

Within this chapter, we therefore introduce our frequency-dependent rock physics forward modelling workflow. Specifically, we employ the hybrid squirt-flow-patchy model of Papageorgiou & Chapman (2017) to simulate the SFjord reservoir under varying CO_2 saturations, capillary pressure conditions and attenuation levels. Following RP modeling, frequency-dependent convolution, as discussed by (Jin et al., 2017), is used to acquire the seismic reflectivity and generate the corresponding synthetic gathers. We then apply spectral decomposition, followed by spectral balancing and frequency-dependent AVO (FAVO) analysis, presenting our frequency-dependent AVA rock physics template designed to investigate squirt-flow effects across the Sognefjord interface. Finally, the chapter concludes by introducing our machine learning

application, illustrating how this frequency-dependent rock physics modeling approach may enhance CO_2 reservoir characterization and seismic monitoring initiatives.

In the following section, we will introduce the theoretical framework that governs our squirt flow modelling approach and its implications for modeling velocity dispersion and seismic attenuation in CO_2 partially saturated reservoirs.

4.2 Theoretical Background: Squirt-Flow Model

Chapman et al. (2002) presented a frequency-dependent rock physics model that investigates the effect of squirt flow. The squirt flow model quantifies the effective frequency-dependent bulk and shear elastic moduli, $\mathbf{K}_{\boldsymbol{eff}}(\boldsymbol{\omega})$ and $\boldsymbol{\mu}_{\boldsymbol{eff}}(\boldsymbol{\omega})$, as functions of various rock and fluid properties. This includes porosity ($\boldsymbol{\phi}$), aspect ratio ($\boldsymbol{r}$), crack radius ($\boldsymbol{a}$), crack density ($\boldsymbol{\varepsilon}$), effective fluid modulus ($\boldsymbol{K_{CO2_Mix}}$), and a relaxation timescale parameter governing the frequency range during which velocity dispersion occurs ($\boldsymbol{\tau_m}$) (Chapman et al., 2002).

Because Chapman et al. (2002) considered a single fluid phase, Papageorgiou & Chapman (2017) extended the model to address partial saturation by incorporating a two-phase fluid system. They implemented a Brie-like fluid mixing law (equation (3.25)) that accounts for the spatial variation in pore fluid distributions through a dimensionless capillary pressure ($\boldsymbol{q}$) parameter, which reflects the degree of pressure contrast between the brine and CO_2 phases (equation (3.26); (Papageorgiou et al., 2016; Papageorgiou & Chapman, 2017).

The model further emphasizes that a critical aspect of frequency-dependent dispersion is the effective characteristic frequency ($\boldsymbol{\omega_o}$), which defines the transition between two frequency regimes in porous rock: the relaxed (low-frequency) and unrelaxed (high-frequency) states. It represents the threshold where wave-induced pressure gradients drive significant squirt-flow effects, causing velocity dispersion and seismic attenuation.

The effective characteristic frequency ($\boldsymbol{\omega_o}$) of the reservoir is defined by equation (4.1):

$$\omega_o = \frac{1}{\tau_m} = \frac{P_0}{(1 + K_c)\tilde{q}} \left(\mathrm{M}_w + q\mathrm{M}_{CO_2}\right) \tag{4.1}$$

where the effective fluid mobility ($\mathbf{M}_{eff}$) is given by Equation (4.2):

$$\mathrm{M}_{eff} = \frac{1}{\tilde{q}} \left(\mathrm{M}_w + q\mathrm{M}_{CO_2}\right)$$

Here,

$$\mathrm{M}_w = \frac{k_w}{\eta_w}, \quad \mathrm{M}_{CO_2} = \frac{k_{CO_2}}{\eta_{CO_2}} \tag{4.2}$$

where $\boldsymbol{P_0}$ is a rock-dependent scaling parameter. The effective fluid mobility ($\mathbf{M}_{eff}$) is dictated by a weighted average of the individual fluid mobilities for water ($\mathbf{M}_w$) and CO_2 ($\mathbf{M}_{CO_2}$), respectively. Similarly, $\boldsymbol{k_w}$, $\boldsymbol{k_{CO_2}}$, $\boldsymbol{\eta_w}$ and $\boldsymbol{\eta_{CO_2}}$ represent the relative permeability and dynamic viscosity for the water and CO_2 fluid components in equation (4.2) (Papageorgiou & Chapman, 2017). Equation (4.1) demonstrates that the characteristic frequency ($\boldsymbol{\omega_o}$) is contingent on several factors (Table 7), including microstructural properties of the rock, capillary pressure variation, and more importantly, fluid mobility, which is governed by relative permeability and fluid viscosity.

The capillary pressure ($\boldsymbol{q}$) exerts a pronounced effect on fluid mobility and thus strongly influences $\boldsymbol{\omega_o}$. Where $\boldsymbol{q} < \mathbf{1}$ ($\boldsymbol{q} \rightarrow \boldsymbol{q_o}$), increased pressure differentials between the supercritical CO_2 and brine lowers fluid mobility, shifting $\boldsymbol{\omega_o}$ to smaller values, as relaxation takes longer. This delays pressure equilibration, broadening the frequency band over which squirt-flow effects prevail. Conversely, where $\boldsymbol{q} = \mathbf{1}$ pressure equilibrates uniformly (negligible capillary effects), increasing $\boldsymbol{\omega_o}$ (maximizing mobility) and shifting squirt-flow effects to higher frequencies.

Equations (4.1) and (4.2) further indicate that fluid mobility plays a dominant role in controlling $\boldsymbol{\omega_o}$**.** Higher mobility, resulting from low viscosity or high relative permeability, leads to faster fluid movement (Jeong et al., 2021) and pressure equilibration**,** increasing $\boldsymbol{\omega_o}$ (Papageorgiou & Chapman, 2017). In contrast, lower mobility, due to high viscosity or low relative permeability, delays fluid redistribution, reducing $\boldsymbol{\omega_o}$ (Papageorgiou & Chapman, 2017; Yin et al., 2017). However, it is important to note that in multiphase systems, relative permeability is often considered a more critical factor compared to viscosity. Relative permeability determines the available pore space for each fluid, sometimes reducing it to near-zero at certain saturations. Viscosity, while important, primarily affects flow resistance or how easily a fluid flows through

that available pore space but does not alter the space itself. Consequently, relative permeability exerts a stronger influence on flow behavior in two-phase systems (Jeong et al., 2021).

Equations (4.1) and (4.2) also emphasize that the effective fluid mobility ($\mathbf{M}_{eff}$), and consequently the characteristic frequency ($\boldsymbol{\omega_o}$), are directly saturation-dependent. This dependence primarily arises because relative permeability significantly varies with changing CO_2-brine saturations. Hence, we dynamically recompute the characteristic squirting frequency ($\boldsymbol{\omega_o}$) for each brine-CO_2 mixture as saturation changes, following the workflow detailed in the upcoming methodology discussion (Section 4.3.4).

Table 7 - This table summarizes the parameter dependencies, as described in equations (3.25), (3.26), (4.1) and (4.2).

Parameter	Dependency
Capillary Pressure Variation ($\boldsymbol{q}$)	Fluid bulk moduli, pore fluid saturations, rock wettability
Effective Fluid Modulus ($\boldsymbol{K_{CO2_Mix}}$)	Fluid bulk moduli, fluid saturations, capillary pressure variation
Characteristic Frequency ($\boldsymbol{\omega_o}$)	Rock microstructure, fluid mobility (fluid viscosity, relative permeabilities, compressibility), capillary pressure variation

Having established the significance of $\boldsymbol{q}$ and $\mathbf{M}_{eff}$ on $\boldsymbol{\omega_o}$, we can now evaluate squirt-flow effects on the reservoir's elastic response across three distinct frequency regimes: low, intermediate and high, defined with respect to a passing seismic wave at frequency ($\boldsymbol{\omega}$) (Mavko & Mukerji, 1998).

In the low frequency, relaxed ($\boldsymbol{\omega} \ll \boldsymbol{\omega_o}$) regime, wave-induced fluid flow has sufficient time to occur. This allows for pore pressure diffusion and equilibration within the seismic wavelength (Alkhimenkov et al., 2020; P. Wang et al., 2021). This results in a compliant reservoir rock, exhibiting a softer elastic response with lower seismic velocities and reduced elastic moduli, relative to the dispersive and unrelaxed states. At minimal velocity dispersion and attenuation, the rock's elastic behavior remains consistent and well-approximated by Gassmann's formulations (Alkhimenkov et al., 2020; Mavko et al., 2020c).

The intermediate, dispersive frequency regime, lies between the relaxed (low-frequency) and unrelaxed (high-frequency) states. In this transitional regime, seismic oscillations are too rapid for

complete pressure equilibration between cracks and pores within a single wave cycle. This results in partial fluid movement, where pore pressure gradients develop yet do not fully dissipate. Restricted fluid mobility within the cracks consequently stiffens the effective reservoir rock, leading to higher seismic velocities and moderately increased elastic moduli. Thus, in the dispersive state, squirt-flow effects dominate, producing maximum velocity dispersion and seismic attenuation when $\boldsymbol{\omega}_{\boldsymbol{o}}$ is highly comparable or nearly at $\boldsymbol{\omega}$ ($\boldsymbol{\omega} \approx \boldsymbol{\omega_o}$)(Alkhimenkov et al., 2020; Mavko et al., 2020c).

In the unrelaxed ($\boldsymbol{\omega} \gg \boldsymbol{\omega_o}$) high-frequency state, seismic waves propagate so rapidly that the induced pressure gradients cannot equilibrate within the seismic wavelength. As pore fluids remain trapped in high-pressure thin cracks with minimal mobility, the reservoir rock reaches its stiffest elastic state (Alkhimenkov et al., 2020; Eid et al., 2015; Mavko et al., 2020c). As a result, both attenuation and velocity dispersion are minimal in this high-frequency, unrelaxed state. (Chapman et al., 2002).

Hence, the discussed squirt flow model provides a comprehensive framework for understanding how fluid interactions and frequency-dependent processes govern attenuation and velocity dispersion in partially saturated porous rocks.

4.3 Rock Physics Forward Modelling Workflow

The primary goal of our workflow is to model dispersive behavior in a partially CO_2 saturated reservoir. Our approach involves upscaling in-situ well logs to the seismic scale, applying Gassmann fluid substitution for baseline elastic properties, and then introducing squirt-flow dispersion at various CO_2 saturations, capillary pressures and attenuations. This workflow is presented in sequential order, highlighting key theoretical concepts and equations to demonstrate our implementation, as detailed in Section (4.4). We then address our secondary goal aimed at employing machine learning applications to complement our workflow, demonstrating how ML integration can further enhance CO_2 reservoir characterization and seismic monitoring in Section (4.5).

Figure (4.1) illustrates how the conventional (Chapter 3) and frequency-dependent (Chapter 4, Section 4.4) rock physics (RP) forward modeling workflows differ as implemented in this thesis. In the conventional approach, we first perform well-log analysis and apply Gassmann fluid

substitution at the well-log scale, then upscale these results to the seismic resolution prior to synthetic generation, as conducted in typical rock physics modeling workflows. In the frequency-dependent approach, however, we partially reverse that sequence by first upscaling the in-situ well-log data to the seismic scale and then performing squirt-flow modeling to simulate dispersive (frequency-dependent) behavior. This ordering ensures that any attenuation introduced via squirt-flow remains fully accounted for rather than being averaged out during the upscaling process. In doing so, we introduce the dispersion and attenuation conditions in a thick, porous reservoir unit at the top of the SFjord reservoir (31 m in thickness ≈ 23.1 ms in time) to ensure its resolvability at the seismic scale.

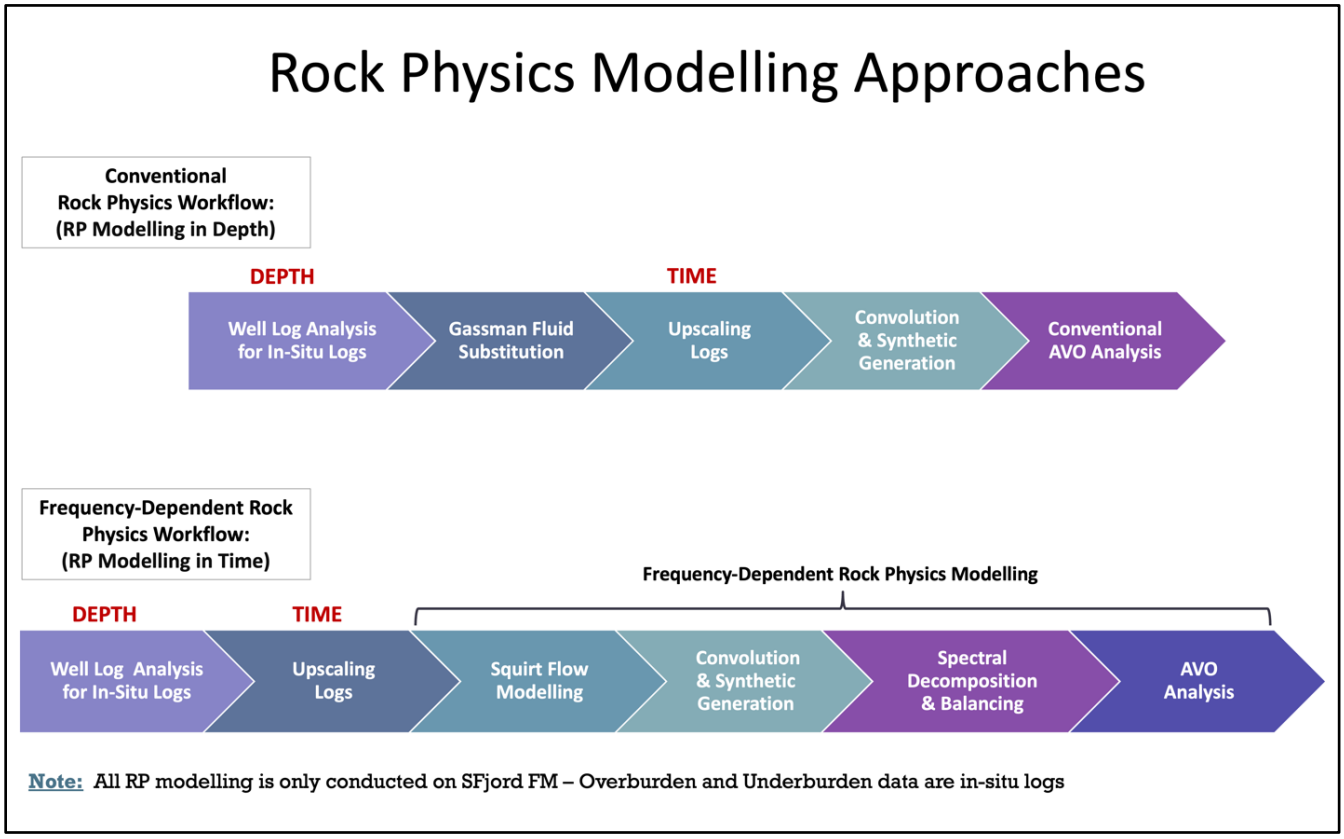


Figure 4.1 – Comparison of conventional and frequency-dependent rock-physics workflows. The frequency-dependent approach reverses the traditional modelling sequence by first upscaling logs and then applying squirt-flow modelling to explicitly preserve the frequency-dependent dispersion attenuation effects.

4.3.1 Well Log Analysis & Data Conditioning

The current workflow being implemented in this chapter builds on the well log analysis and data conditioning procedures documented in Chapter 3, (Section 3.2.1). In particular, we will utilize the in-situ elastic logs (**V_p**, **V_s** and $\boldsymbol{\rho}$) in conjunction with the petrophysical logs (effective porosity, saturation and volumetrics) as key inputs for subsequent modeling steps.

4.3.2 Log Data Upscaling to Seismic Scale

After confirming the suitability of our input log data, we upscale the logs using Backus averaging (a convolution-based procedure). This technique reduces the high-resolution depth sampling into an effective medium more suitable for seismic-scale analysis, where individual thin reservoir layers are blocked together and treated as a single isotropic unit over specified depth windows. The resulting effective properties represent the bulk elastic response at the low-frequency limit, consistent with the seismic band (Lindsay & Van Koughnet, 2001; C. Liner & Fei, 2007).

To accomplish this task as conducted in common practice (Lindsay & Van Koughnet, 2001; C. Liner & Fei, 2007; C. L. Liner, 2014), we first compute the in-situ compressional ($\boldsymbol{P_{Mod}}$) and shear moduli ($\boldsymbol{\mu}$), via equations (4.3) and (4.4):

$$P_{Mod} = V_p^2 \rho \tag{4.3}$$

$$\mu = V_s^2 \rho \tag{4.4}$$

We then define a depth window for the Backus moving average based on a dominant frequency ($\boldsymbol{F_{Dominant}}$) of 50 Hz and the minimum shear velocity ($\boldsymbol{V_{s_{min}}}$) within our reservoir, as demonstrated in equation (4.5) (C. Liner & Fei, 2007; Simm & Bacon, 2014b):

$$Backus\ Window = \frac{V_{s_{min}}}{3\ F_{Dominant}} \tag{4.5}$$

With regards to the Backus window, compliance with the dual requirements of Backus averaging is essential (Dvorkin et al., 2014b; Lindsay & Van Koughnet, 2001). Specifically, this

averaging window must be longer than the thickness of individual laminae so that multiple thin layers are combined into an effective medium yet remain significantly smaller than the seismic wavelength so that the layered reservoir strata appear homogeneous to the propagating wavefield. Given the in-situ properties of the SFjord reservoir, equation (4.5) yields a Backus window length of approximately 5.5 m. This fulfils the first requirement by ensuring that multiple thin laminae (typically ~1 m thick in SFjord) are effectively blocked within each Backus averaging window, as the selected window length corresponds to about 5.5 times the thickness of an individual thin layer.

Equally important, the size of the Backus window must be evaluated relative to the dominant seismic wavelength across the frequency range of interest. For the SFjord reservoir, a representative compressional velocity is $V_p \approx 3000$ m/s. At 50 Hz, this corresponds to a seismic wavelength of approximately 60 m ($\lambda = V_p/F_{Dominant}$= 3000/50). To remain within the effective medium regime, the Backus window should be smaller than the full wavelength of 60 m, typically constrained to be less than $\lambda/10$ = 6 m. Hence, the selected Backus window of 5.5 m (< 6m) , therefore, lies just below this threshold, ensuring that thin layering is effectively invisible to the seismic wavefield and maintaining consistency with the assumptions of the effective medium theory.

Proceeding forward, we implement the moving average by sliding the 5.5 m depth window sample by sample along our reservoir interval, ensuring that the elastic moduli are adequately averaged at each step. As a result, within each Backus window, $\boldsymbol{P_{Mod}}$ and $\boldsymbol{\mu}$ are upscaled using harmonic averaging (equations (4.6) and (4.7)), whereas ρ is upscaled via an arithmetic mean (equation (4.8)):

$$P_{Mod_Backus} = \left(\frac{1}{N}\sum_{i=1}^{N}\frac{1}{P_{Mod_i}}\right)^{-1} \tag{4.6}$$

$$\mu_{Backus} = \left(\frac{1}{N}\sum_{i=1}^{N}\frac{1}{\mu_i}\right)^{-1} \tag{4.7}$$

$$\rho_{Backus} = \frac{1}{N}\sum_{i=1}^{N}\rho_i \tag{4.8}$$

where $\boldsymbol{N}$ is the total number of layers in the Backus window and $\boldsymbol{P_{Mod_i}}$, $\boldsymbol{\mu_i}$ and $\boldsymbol{\rho_i}$ are the consecutive individual values of the compressional modulus, shear modulus and density in layer $\boldsymbol{i}$, respectively. Likewise, $\boldsymbol{P_{Mod_Backus}}$, $\boldsymbol{\mu_{Backus}}$ and $\boldsymbol{\rho_{Backus}}$ are the Backus averaged elastic attributes.

The above Backus-averaged moduli are then used to calculate the upscaled P-wave and S-wave velocities in equations (4.9) and (4.10), respectively:

$$V_{p_Backus} = \sqrt{\frac{P_{Mod_Backus}}{\rho_{Backus}}} \tag{4.9}$$

$$V_{s_Backus} = \sqrt{\frac{\mu_{Backus}}{\rho_{Backus}}} \tag{4.10}$$

where Figure (4.2) shows the Backus-averaged in-situ elastic and petrophysical logs for Trow 32/2_1 in the depth domain, displaying the smoother Backus-averaged logs in green overlying our original (depth) in-situ elastic logs (black), computed with a Backus window = 5.5 m.

Finally, we interpolate the upscaled logs from depth into two-way time (TWT), maintaining a 1 ms resampling rate to align the depth logs with the seismic domain. In this study, we utilize the TWT log scale provided as part of our dataset (Talisman, 2008; *Trow:32_2_1*, 2020), in which the TWT log is index-matched to the depth scale such that each depth sample corresponds directly to a matching time sample. It is important to emphasize, however, that while the 1 ms sampling in time is uniform, the corresponding sampling in depth is inherently irregular due to velocity variations with depth.

Proceeding forward, we then resample the TWT log together with the upscaled petrophysical and elastic logs at 1 ms intervals. As a result, the Backus-averaged logs in TWT are now properly upscaled (Figure (4.3)), preserving the low-frequency character necessary for the subsequent forward seismic modeling workflow (Lindsay & Van Koughnet, 2001).

In the context of Backus averaging, adherence to the Shannon–Nyquist criterion (Nyquist, 1928; Shannon, 1949) which requires a sampling rate at least twice the highest frequency present in a band-limited signal, is essential for preserving seismic frequencies of interest. Specifically, both the depth and time sampling must be fine enough to capture relevant higher frequencies without introducing aliasing. If sampling is too coarse, higher-frequency energy can overlap with lower-frequency bands, leading to amplitude and phase distortion that may undermine the accuracy of our forward seismic modeling workflow.

Hence, given the above discussion, our workflow that employs a 5.5 m Backus window in combination with a 1ms time sampling interval, satisfies the theoretical requirements of Backus averaging and the Shannon-Nyquist criterion. Since 1 ms corresponds to a 1,000 Hz sampling rate, the resulting 500 Hz Nyquist limit is well beyond the frequency range (50-90 Hz) of interest. Similarly, the selected Backus window length of 5.5 m respects the relevant theoretical constraints: it avoids aliasing at the 1 ms sampling interval and simultaneously ensures that the Backus-averaged logs provide a valid homogenized representation of the medium for subsequent seismic-scale forward modelling. Consequently, the upscaled logs retain critical high-frequency information, ensuring accurate seismic analysis.

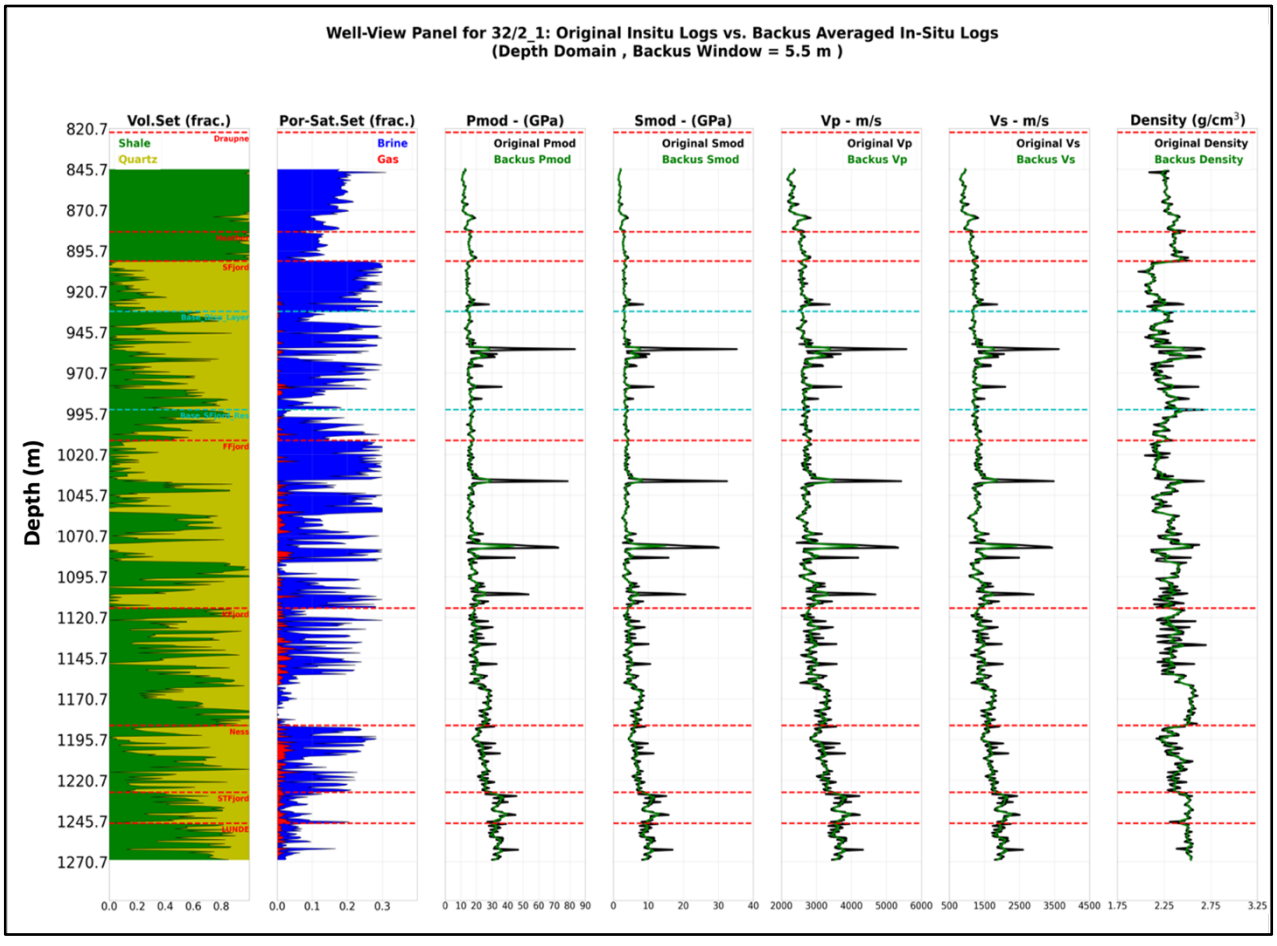


Figure 4.2 – Backus-averaged in-situ elastic and petrophysical logs for Trow 32/2_1 in the depth domain. The smoother Backus-averaged logs (green), computed using a 5.5 m window, are superimposed on the original, higher-resolution in-situ logs (black).

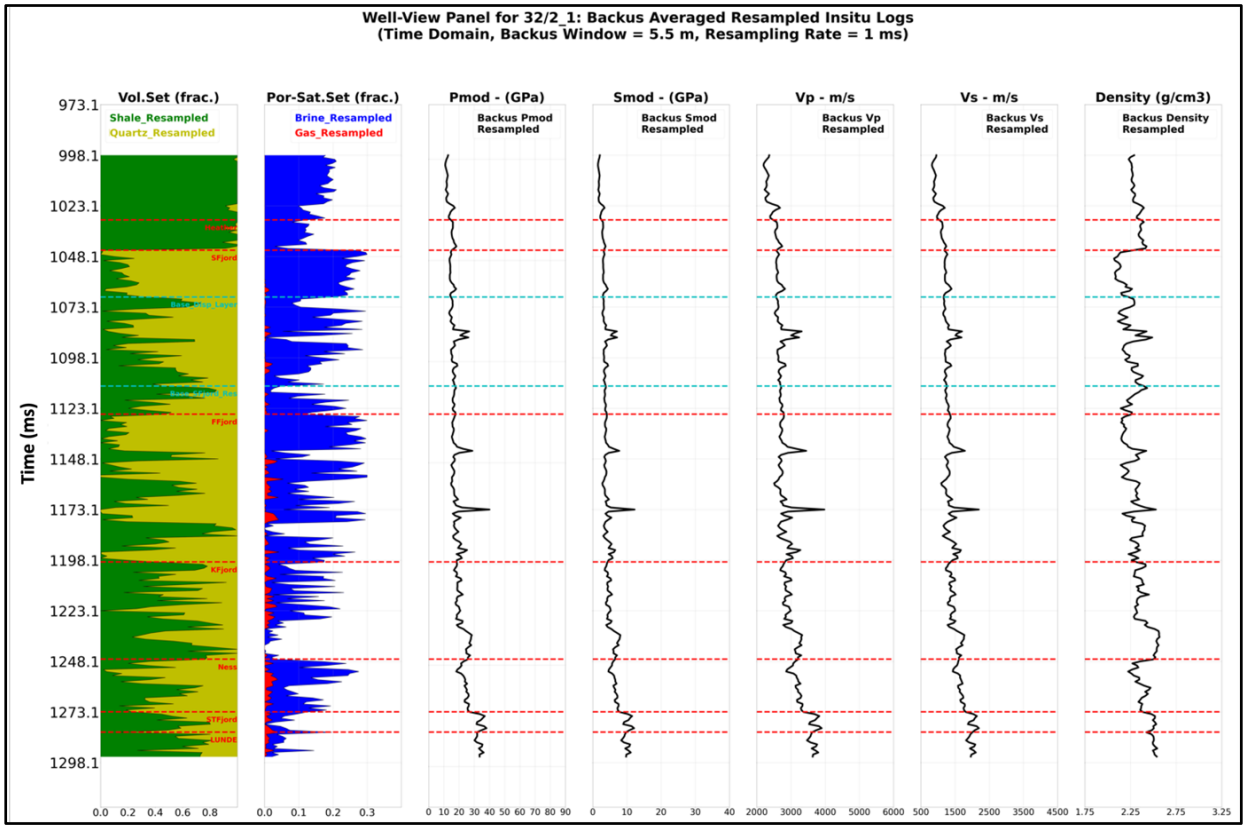


Figure 4.3 – Final upscaled in-situ elastic and petrophysical logs for Trow 32/2_1, obtained by applying Backus averaging with a 5.5 m window and subsequent TWT resampling (1 ms).

4.3.3 Parameter Sampling (S_w, q , Q^{-1}) and Combination Sets

In this task, we begin by defining the key input parameters that will later drive the squirt-flow simulations. Specifically, three primary parameters are targeted: water saturation ($\boldsymbol{S_w}$), capillary pressure variation ($\boldsymbol{q}$) and attenuation ($\boldsymbol{Q^{-1}}$). By comprehensively sampling the full range of $\boldsymbol{S_w}$, $\boldsymbol{q}$ and $\boldsymbol{Q^{-1}}$, we aim to generate an unbiased machine learning (ML) dataset that accurately captures CO_2 dispersive behavior and the corresponding physical variability. We believe that such broad coverage is essential for robust model training, allowing the learning algorithm to recognize underlying patterns and generalize to diverse reservoir conditions.

To generate our ML dataset, we start by constructing probability density functions (pdf) for each of the three parameters. Starting with $\boldsymbol{S_w}$, we opted for normal distribution, split into "Low", "Mid" and "High S_w" ranges as summarized in (Table (8)), since water saturation is inherently bounded between 0 and 1. The normal distribution is centered around our selected input mean ($\boldsymbol{\mu}$), whereas the pdf spread is influenced by the input variance ($\boldsymbol{\sigma^2}$) parameter chosen to help us constrain the values within the bounding limits (Table (8)). To ensure that the sampled values actually remain within our desired finite ranges, we apply additional clipping at the bounding limits.

As discussed by Papageorgiou and Chapman (2017), the parameter $\boldsymbol{q}$ essentially represents a ratio of fluid pressures in a partially saturated pore system, varying between values much smaller than one (q_o = 0.054) and one, as per equation (3.26). Because $\boldsymbol{q}$ is a multiplicative factor and is always positive, it can vary over several orders of magnitude, particularly when transitioning from near-uniform pressures ($q \approx 1$) down to much larger pressure gradients ($q \approx q_o \approx 0.054$). Such variation is more accurately captured by a lognormal distribution rather than a normal distribution. The same reasoning applies to both $\boldsymbol{q}$ and $\boldsymbol{Q^{-1}}$, since these parameters exhibit skewed distributions and must remain strictly positive. Consequently, we adopt lognormal distributions for $\boldsymbol{q}$ and $\boldsymbol{Q^{-1}}$, each defined by our selected input means and standard deviations ($\boldsymbol{\sigma}$) provided in Table (8).

We consider two classifications for $\boldsymbol{q}$: "Uniform" ($q \approx 1$) reflecting negligible capillary pressure differences, and "Patchy" ($q \approx q_o \approx 0.054$) , indicating a significant pressure differential between fluids. We then specify the bounding ranges, means and standard deviation values that simulate these uniform and patchy pdfs, accordingly, ensuring coverage of intermediate values, as presented in Table (8) and Figure (4.4).

For the attenuation parameter ($\boldsymbol{Q^{-1}}$) , we bounded the range from Q =10, stated in the literature as a reasonable observed value for attenuation in gas-saturated reservoirs (Klimentos, 1995), up to Q =1000, representing the Gassmann baseline with negligible attenuation. Studies of dry or nearly dry rock often report relatively high $\boldsymbol{Q}$ implying minimal attenuation (Toksoz et al., 1979), whereas partially saturated reservoirs, particularly those containing gas or CO_2 in patchy mixtures, can exhibit $\boldsymbol{Q}$ values as low as 5–15 indicative of high attenuation (Ekanem et al., 2016; Lei & Xue, 2009). Initially, we experimented with $\boldsymbol{Q}$ values lower than 10 (i.e., $Q = 5$ or $3 \rightarrow$ high attenuation), but these values resulted in an unrealistically large dispersion effect. Consequently,

we confined our final range, in light of our particular field dataset and its in-situ conditions, to $Q =$ (10 -1000). Within this range, additional trials at intermediate attenuation values (i.e., $Q = 50$, 70, 100, 250, 500) showed that any $Q < 30$ leads to a negligible dispersive response. As a result, we defined two attenuation classes: a single "No-Attenuation" value at $Q =$1000 (no distribution required), and a " High-Attenuation" class randomly sampling from $Q =$ (10 – 30) (Table (8)). This approach ensured adequate coverage of meaningful $\boldsymbol{Q^{-1}}$ values while eliminating unrealistic extremes. All pdf distributions are plotted in Figure (4.4).

To ensure reproducibility, we specify a fixed seed before drawing 100 random samples from each defined distribution. Because simply combining every possible $\boldsymbol{S_w}$, $\boldsymbol{q}$, and $\boldsymbol{Q^{-1}}$ value would result in an excessively large set, we select a total of 1,440 parameter combination sets that contain an equal distribution of classes across these three parameters. Each combination set is then assigned three distinct labels: one $\boldsymbol{S_w}$, label ("Low", "Mid", or "High"), a $\boldsymbol{q}$ label ("Uniform" or "Patchy") and a $\boldsymbol{Q^{-1}}$ label ("No Attenuation" or "High Attenuation"), yielding 12 categorical classes or labels ($3\, S_w \times 2q \times 2\, Q^{-1}$) in total, thereby framing our problem as a multi-label classification task. In multi-label classification, an instance can belong to multiple categories or labels, recognizing the overlapping characteristics that often arise in real-world data (Zhang & Zhou, 2014). This approach offers a more comprehensive perspective than single-label classification by enabling the model to learn a function mapping inputs to sets of relevant labels, rather than a single label. We then store these 1,440 combinations sets for subsequent squirt-flow modeling and machine learning applications.

Table 8 - Generated class labels, ranges, typical means and variances or standard deviations assigned for each pdf distribution for the 3 defined parameters.

Parameter	Distribution	Class Label & Range	Mean (μ)	Standard Deviation (σ) / Variance (σ^2)
$\boldsymbol{S_w}$	Normal	Low S_w = (0–0.3)	0.15	$\sigma^2 = 0.05$
		Mid S_w = (0.4–0.6)	0.5	$\sigma^2 = 0.05$
		High S_w = (0.7–1.0)	0.85	$\sigma^2 = 0.05$
$\boldsymbol{q}$	Lognormal	Uniform = (0.14 – 1.0)	0.57	$\sigma = 0.4$
		Patchy = (0.054 - 0.1)	0.077	$\sigma = 0.3$

Q^{-1}	Lognormal	High Attenuation = (10–30)	20	σ = 0.3
	No Distribution required	No Attenuation = (1000)	-	-

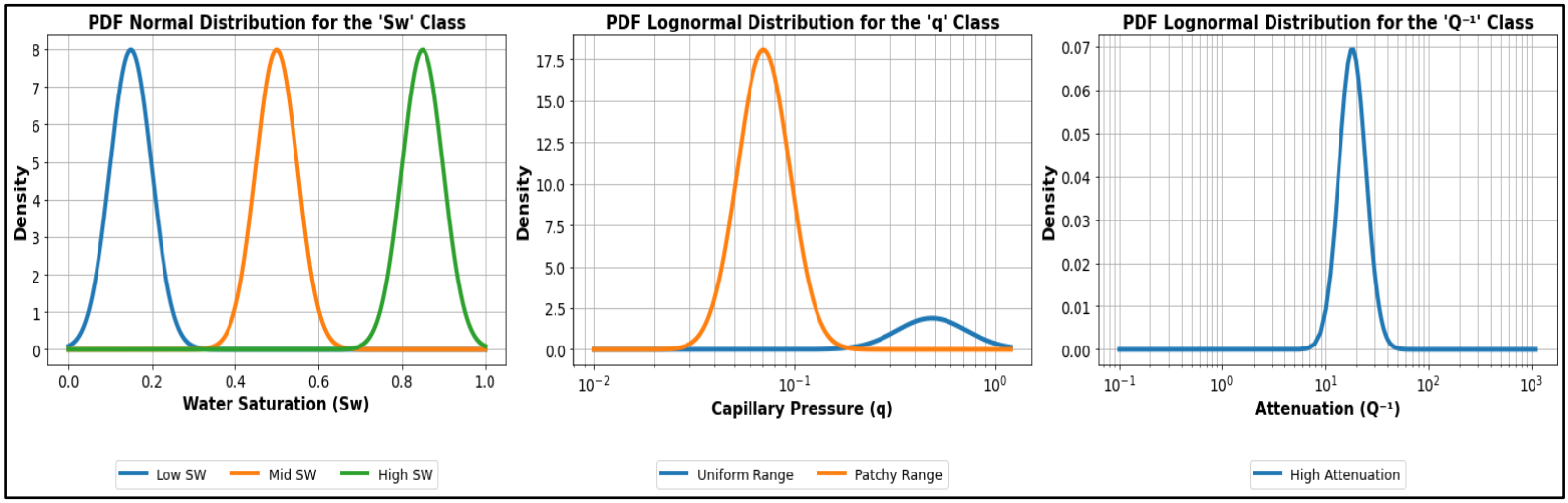


Figure 4.4 – Probability density functions (PDFs) used for parameter sampling. ***(A)*** *Water saturation (**S_w**) , represented by three normal distributions ("Low," "Mid," "High").* ***(B)*** *Capillary pressure (**q**), represented by two lognormal distributions ("Uniform," "Patchy").* ***(C)*** *High attenuation (**Q^{-1}**), represented by a lognormal distribution. Distribution parameters (mean and standard deviation) are provided in Table (8).*

4.3.4 Squirt-Flow Modelling

With the upscaled logs in place, we perform squirt flow (SQF) modeling following Papageorgiou and Chapman (2017), employing the Mantis rock physics library developed by Giorgos Papageorgiou. Our implemented workflow is illustrated in Figure (4.5). Within this implementation, we adopt a multi-layer model (Figure (4.6)) that includes an elastic overburden (caprock formations: Draupne and Heather) represented by in-situ elastic logs (upscaled V_p, V_s, ρ) without fluid modeling, a dispersive SFjord reservoir interval characterized by 100% brine-saturated upscaled logs, and an in-situ elastic underburden covering the remaining formations without additional modeling. In our current SQF scenario, we investigate the reservoir's dispersive behavior as a function of three primary variants, each varied within the pre-defined ranges, according to the parameter combination sets (S_w, q, Q^{-1}) generated in Section (4.3.3):

- Water saturation ($\boldsymbol{S_w}$) : (0 → 1) (frac.)
- Capillary parameter ($\boldsymbol{q}$) : (0.054 → 1) (dimensionless)
- Attenuation ($\boldsymbol{Q^{-1}}$) with $Q \in \{10, 20, 30, 1000\}$

We specifically introduce dispersion and attenuation by applying these parameter combination sets ($\boldsymbol{S_w}$, $\boldsymbol{q}$, $\boldsymbol{Q^{-1}}$) uniformly only within the thick, porous interval at the top of the SFjord reservoir (31 m in thickness ≈ to 23.1 ms in time) ensuring seismic resolvability. This means that saturations, capillary pressures and attenuation values are held constant for the entire interval during each SQF iteration. By adopting this approach, we preserve non-dispersive behavior in the overburden and underburden zones, allowing us to investigate how the frequency-dependent AVO responses change across the SFjord interface as the rock transitions from an elastic layer into a dispersive zone.

Before discussing our methodology, we first outline our model inputs along with several key assumptions. Important model inputs include elastic log data (upscaled brine saturated $\boldsymbol{V_p}, \boldsymbol{V_s}, \boldsymbol{\rho}$), petrophysical data ($\phi$, pore fluids, mineralogy), and fluid/mineral properties (Tables (5) and (6)) utilized to compute the effective fluid ($\boldsymbol{K_{CO2_Mix}}$) and mineral ($\boldsymbol{K_m}$) moduli, both of which are derived from in-situ reservoir petrophysical properties based on well log analysis, as detailed in Chapter 3. Utilizing the latter inputs, we characterize the reservoir's pore geometry in terms of stiff spherical pores along with more compliant needle-like cracks. In doing so, our python code internally inverts the elastic logs and the input attenuation parameter ($\boldsymbol{Q^{-1}}$) to derive the reservoir's pore geometry features, including aspect ratio and crack density, which govern the fluid redistribution within this cracked medium.

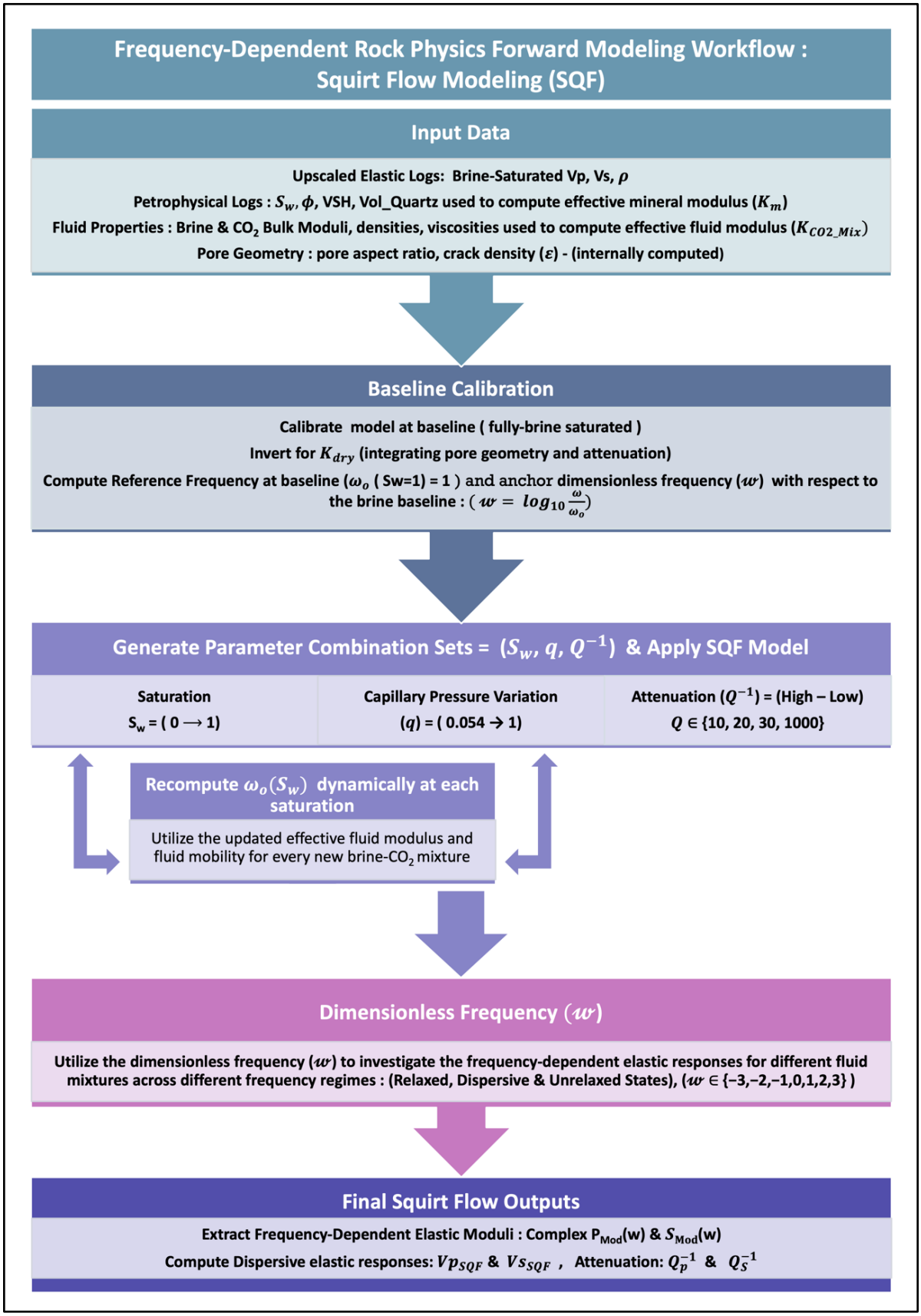


Figure 4.5 – Workflow diagram illustrating the frequency-dependent squirt flow (SQF) implementation, highlighting key steps in the modeling process.

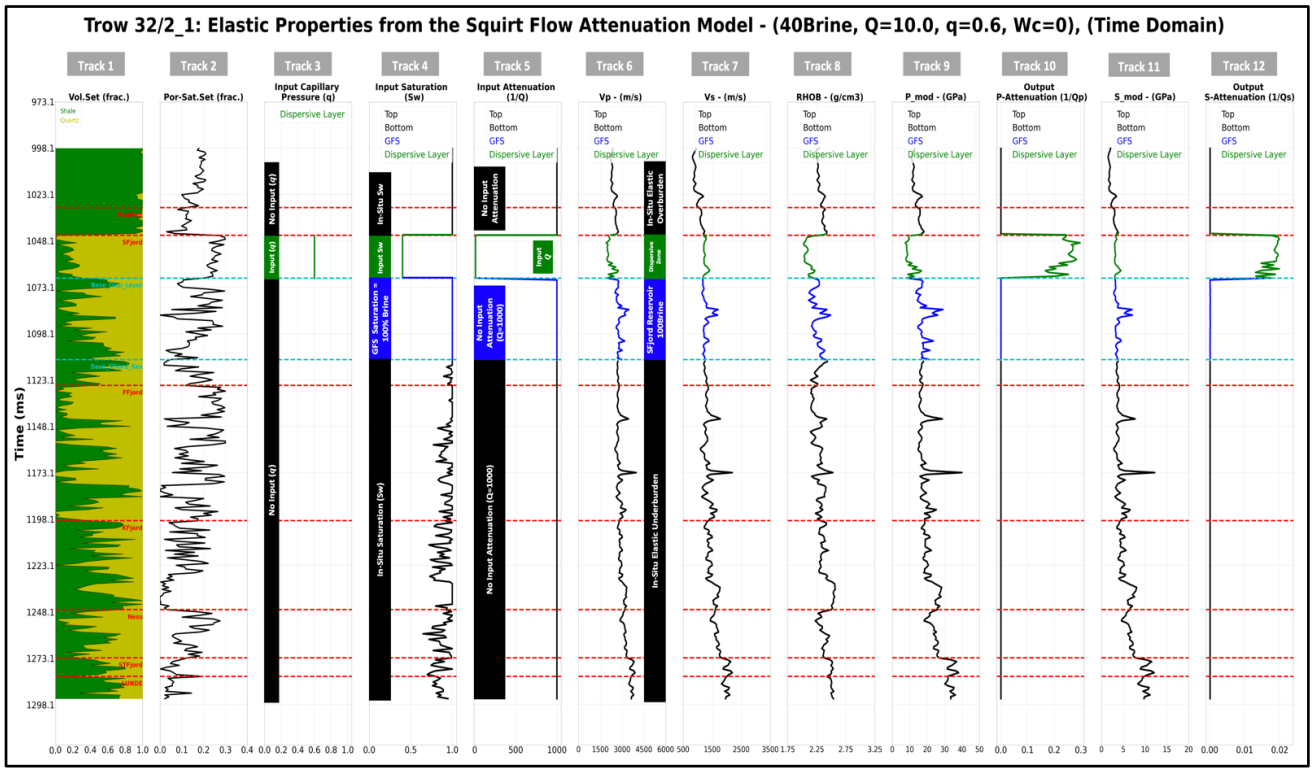


Figure 4.6 – Multi-layer squirt-flow model displaying elastic inputs and dispersive outputs at Q=10, q=0.6, and S_w=0.4. The overburden and underburden intervals are represented by upscaled in-situ logs, whereas the SFjord reservoir interval uses fully brine-saturated logs. Squirt-flow modelling is conducted exclusively within the defined dispersive zone (31 m interval at the top of the SFjord reservoir ≈ 23.1 ms).

To initialize the squirt-flow model, we calibrate it to the baseline reservoir condition of 100% brine saturation, effectively removing all fluid effects at this reference state. At this stage, it is important to highlight a key modification in our implementation, introduced by Papageorgiou, which uses the upscaled brine-saturated $\boldsymbol{V_p}$, $\boldsymbol{V_s}$, $\boldsymbol{\rho}$ logs to invert for the dry-frame bulk modulus ($\boldsymbol{K_{dry}}$) via Gassmann's formulation. This inversion incorporates a crack-density parameter ($\boldsymbol{\varepsilon}$) and an attenuation quality factor ($\boldsymbol{Q^{-1}}$) to account for dispersive effects in the dry rock frame. Rather than assuming a fixed dry frame, the model dynamically recalculates $\boldsymbol{K_{dry}}$ at each depth point, as this calibration step ensures that, even in the presence of microcracks, the low-frequency elastic response remains consistent with Gassmann's predictions for a brine-saturated rock. The resulting $\boldsymbol{K_{dry}}$ is then embedded into the squirt-flow model, enabling simulation of the full frequency-dependent elastic response across different saturation and frequency conditions.

A third key assumption entails defining a reference characteristic frequency for our fully brine-saturated baseline (second assumption) by normalizing the timescale parameter, as per Papageorgiou and Chapman (2017). Specifically, we set the reference frequency ($\boldsymbol{\omega_o}$) in equation (4.11):

$$\omega_o\ (S_w{=}1\ ) = \frac{2\pi}{\tau_m} = 1 \tag{4.11}$$

since the rock dependent scaling parameter ($\boldsymbol{P_0}$), introduced in equation (4.1), cannot be easily computed nor directedly measured, yet still depends on the reservoir's microstructure. By selecting the fully brine-saturated case (ω_o=1) as our reference, the model consistently reverts to this baseline when evaluating squirt-flow dispersive effects for partial saturations. Because both fluid viscosity and relative permeability are well defined at full brine saturation, normalizing to this reference simplifies comparisons among different fluid mixtures across various frequency regimes. Therefore, our squirt-flow modeling approach not only aligns with the Gassmann limit at low frequencies but also clarifies how introducing CO_2 partial saturations shifts the characteristic frequency and elastic response relative to the brine-saturated reference.

We define a dimensionless frequency ($\boldsymbol{W_c}$) index to evaluate how partial saturations modify the squirting frequency ($\boldsymbol{\omega_o}$) relative to the established brine-saturated baseline. This parameter is expressed by equation (4.12):

$$W_c = \log_{10}\frac{\omega}{\omega_o} \tag{4.12}$$

where $\boldsymbol{\omega}$ is the seismic wave frequency. We then model the squirt-flow dispersive behavior at $\boldsymbol{W_c} \in \{-2,-1,0,1,2\}$, reflecting the three distinct frequency regimes. At highly negative values (i.e., $\boldsymbol{W_c} = -2$) the wave frequency is 100 times slower than the squirting threshold ($\boldsymbol{\omega} \ll \boldsymbol{\omega_o}$), placing the reservoir in a relaxed regime that matches Gassmann's low-frequency limit. Conversely, positive values ($\boldsymbol{W_c} \in \{1,2\}$) imply unrelaxed behavior ($\boldsymbol{\omega} \ll \boldsymbol{\omega_o}$), where the wave frequency surpasses the squirting threshold by factors of 10 or 100. At $\boldsymbol{W_c = 0}$, we observe intermediate dispersive behavior ($\boldsymbol{\omega \approx \omega_o}$).

In our implementation, the characteristic squirting frequency $\boldsymbol{(\omega_o)}$ is dynamically recomputed for each brine–CO_2 mixture as a function of saturation, following equations (4.1) and (4.2). For every saturation mixture, we update both the effective fluid modulus ($\boldsymbol{K_{CO2_Mix}}$) and effective fluid mobility ($\mathbf{M}_{\boldsymbol{eff}}$). Partial saturation is modelled using the capillary parameter ($\boldsymbol{q}$), which enables fluid mixing across the full saturation range ($\boldsymbol{S_w}$: $0 \rightarrow 1$). To compute fluid mobility, we

employ the Brooks–Corey model for saturation-dependent relative permeabilities, combining these with their respective fluid viscosities (Table (5)) to acquire the $\mathbf{M}_{eff}$ for each mixture.

Although $\boldsymbol{\omega_o}$ is recalculated at each saturation to reflect changing fluid properties, we would like to emphasize that the dimensionless frequency ($\boldsymbol{W_c}$) remains anchored to the fully brine-saturated reference. This enables a clear evaluation of how saturation-dependent mobility influences elastic dispersion, while maintaining a consistent reference for comparing different fluid mixtures across frequency regimes. Ultimately, the coupling between fluid mixing, viscosity, relative permeability and characteristic frequency is essential for capturing the saturation-dependent nature of squirt-flow dispersion, which in turn governs the reservoir's frequency-dependent elastic response.

Figures 4.7 (A–C) illustrate the key concepts of this approach. Figure 4.7(A) reflects the impact of capillary pressure variations on the effective fluid modulus across all brine–CO_2 saturations. Consistent with earlier observations in Figure (3.8), we find that, at full saturations (brine or CO_2), changing $\boldsymbol{q}$ does not alter the effective fluid modulus, since only a single fluid phase is present. In contrast, at intermediate saturations, lower $\boldsymbol{q}$ (implying stronger capillary pressure contrasts) produces a stiffer or patchier mixture, resulting in a higher fluid modulus for the same brine–CO_2 mixture than would be obtained at a higher (more uniform pressure gradient) $\boldsymbol{q}$ value.

Figure 4.7(B) shows the Brooks–Corey relative permeability curves for water (blue) and CO_2 (red), indicating that each fluid's relative permeability approaches unity at near-pure saturation and diminishes as the other fluid becomes dominant. Near full brine saturation, water flows freely while CO_2 mobility effectively reduces to zero, and vice versa. At intermediate saturations, however, capillary forces can create a patchy effect, where both fluids coexist yet exhibit different mobilities due to their respective relative permeability behavior.

As Figures 4.7 (A–B) individually illustrate how both the relative permeability model and the capillary parameter drive dispersive effects within the seismic band, Figure 4.7(C) further confirms these observations by plotting the dimensionless frequency ($\boldsymbol{W_c}$) against water saturation for various capillary pressure gradients. This figure reflects how wave-induced pore-fluid pressures equilibrate relative to the reference brine-saturated baseline: $\boldsymbol{W_c} < 1$ indicates the relaxed regime, $\boldsymbol{W_c} > 1$ corresponds to the unrelaxed (high-frequency) regime, and values near $\boldsymbol{W_c} \approx 1$ mark the dispersive state. Near pure water or CO_2 saturations, the viscosity of the dominant fluid dictates the overall mobility. Water's higher viscosity lowers the overall mobility (thus

lowering $\boldsymbol{W_{c_{(water)}}}$), whereas CO_2's lower viscosity increases mobility, raising $\boldsymbol{W_{c_{(CO2)}}}$, thereby $\boldsymbol{W_{c_{(water)}} < W_{c_{(CO2)}}}$. At intermediate saturations, both fluids exhibit finite relative permeabilities, and stronger capillary forces stiffen the mixture within the pore spaces, reducing the effective mobility compared to a single-phase condition, thereby decreasing $\boldsymbol{W_c}$. These findings align with the relative permeability curves and emphasize how fluid viscosity, partial saturation, and capillary pressure collectively shape frequency-dependent behavior.

Having computed the fluid moduli and characteristic frequencies for each brine–CO_2 mixture, we next evaluate the frequency-dependent elastic responses by feeding the parameters sets $(\boldsymbol{S_w, q, Q^{-1}, W_c})$ into SQF model. Each combination yields a unique dispersion and attenuation profile characterized by a complex stiffness matrix $\boldsymbol{(C_{ij})}$ (6×6 tensor), from which the compressional $(\boldsymbol{P_{Mod_SQF}})$ and shear $(\boldsymbol{S_{Mod_SQF}})$ moduli are extracted as complex quantities.

Specifically, in the relaxed regime, we employ GFS to establish the baseline elastic responses, varying CO_2 saturations and capillary effects $(\boldsymbol{q})$ according to the combination sets, while maintaining negligible attenuation (Q^{-1}=1/1000). We then derive the dry rock frame modulus, compute the saturated-rock moduli, and extract final seismic attributes (V_p, V_s, ρ, $etc.$) , following the workflow established in Chapter 3.

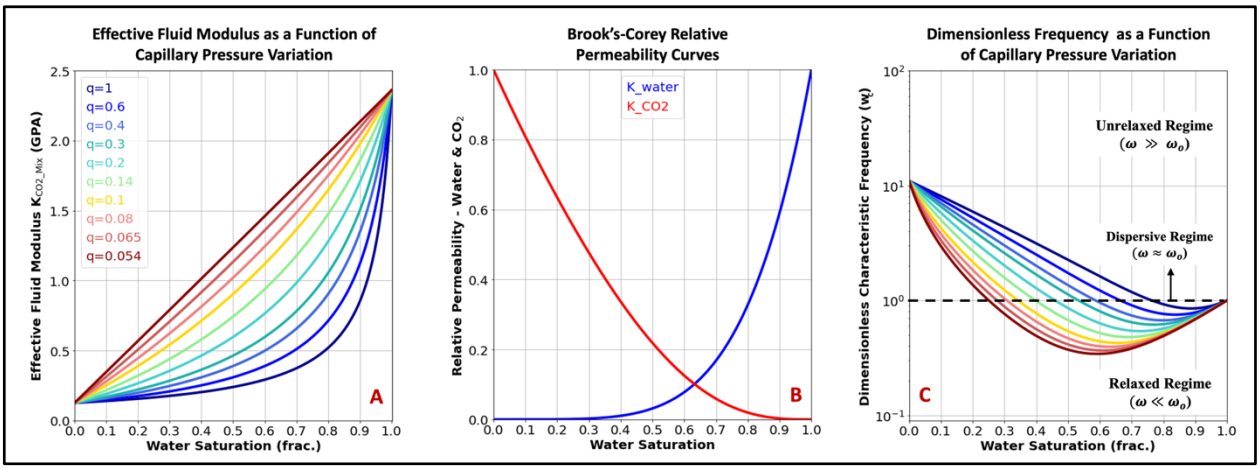


*Figure 4.7 – **(A)** Effective fluid modulus (K_{CO2_Mix}) as a function of water saturation for different capillary pressure $(\boldsymbol{q})$ parameters, illustrating that increased capillary pressure (lower q values) stiffens the fluid mixture at intermediate saturations. **(B)** Brooks–Corey relative permeability curves for water (blue) and CO_2 (red), indicating fluid mobility across saturation ranges. **(C)** Dimensionless frequency $(\boldsymbol{W_c})$ versus saturation, highlighting transitions between relaxed, dispersive, and unrelaxed regimes as influenced by relative permeability and capillary forces.*

In the dispersive and unrelaxed regimes, however, we apply the full squirt-flow model over all the specified saturation, capillary and attenuation ranges across the entire frequency spectrum. For each combination, we extract the real parts of the compressional ($\boldsymbol{Re}\left[\boldsymbol{P_{Mod_SQF}}\right]$) and shear ($\boldsymbol{Re}\left[\boldsymbol{S_{Mod_SQF}}\right]$) moduli to compute the reservoir's dispersive P-wave ($\boldsymbol{Vp_{SQF}}$) and S-wave ($\boldsymbol{Vs_{SQF}}$) velocities, as presented in equations in (4.13) and (4.14):

$$Vp_{SQF} = \sqrt{\frac{Re\left[P_{Mod_SQF}\right]}{\rho}} \tag{4.13}$$

$$Vs_{SQF} = \sqrt{\frac{Re\left[S_{Mod_SQF}\right]}{\rho}} \tag{4.14}$$

Finally, attenuation factors ($\boldsymbol{Q^{-1}}$) are calculated as the ratio of the imaginary to the real parts of each complex modulus. Therefore, we compute the resulting saturation-dependent P-wave ($\boldsymbol{Q_p^{-1}}$) and S-wave ($\boldsymbol{Q_S^{-1}}$) attenuations, which reflect the dissipative effects associated with changing reservoir properties. These latter attenuations are computed using the following expressions (4.15) and (4.16):

$$Q_p^{-1} = \frac{Im\left[P_{Mod_SQF}\right]}{Re\left[P_{Mod_SQF}\right]} \tag{4.15}$$

$$Q_S^{-1} = \frac{Im\left[S_{Mod_SQF}\right]}{Re\left[S_{Mod_SQF}\right]} \tag{4.16}$$

Given the implemented workflow, we have constructed a comprehensive dictionary or catalog of rock physics constrained dispersive responses (given our particular reservoir conditions and modelling scenario). This catalog contains P-wave and S-wave velocity, advanced seismic attributes (AI, V_p/V_s Ratio, PR, LambdaRho, etc.) and attenuation profiles for each combination set, all labeled uniquely for subsequent analyses, including AVO modeling or machine-learning applications. Last but not least, we would like to highlight that although we initially input a uniform attenuation parameter within the dispersive zone, the resulting P-wave attenuation logs exhibit heterogeneity at each time sample (Figure (4.6), Track (10)) due to variations in porosity and lithology.

4.3.5 Synthetics: Frequency-Dependent Convolutional Modelling and Reflectivity

To construct our synthetic seismograms, we adopt a workflow that incorporates frequency-dependent reflectivity into convolutional modelling, as proposed by (Wu et al., 2014a) for a single interface and extended by Jin et al. (2017) to accommodate isotropic, muti-layer (flat) reservoir models. The final reflectivity is formulated using the Schoenberg and Protazio approach to Zoeppritz equations (Jin et al., 2017).

Following Jin et al. (2017), the frequency-dependent synthetic seismic trace $\mathbf{X_t(\theta)}$ at a given incidence angle $\boldsymbol{\theta}$, is computed via the following equation (4.17):

$$\mathrm{X}_t(\theta) = \sum_{n=1}^{K} i_t^n * F^{-1}[W(\omega) \cdot R^n(\theta, \omega)]$$

$$i_t^n = \delta(t - n\Delta t) \tag{4.17}$$

where $\boldsymbol{t}$ is the time depth, $\boldsymbol{\Delta t}$ is the sampling interval, $\boldsymbol{K}$ is the total number of interfaces. The $\boldsymbol{i_t^n}$ term is a shifted Dirac delta "spike" in the time domain, centered at the time sample corresponding to the nth interface. This spike positions the reflection at the correct two-way travel time ($\boldsymbol{t = n\Delta t}$) in the synthesized seismogram. $\boldsymbol{W(\omega)}$ is the Fourier transform of the source wavelet at angular frequency ($\boldsymbol{\omega}$), while $\boldsymbol{R^n(\theta, \omega)}$ is the frequency-dependent reflectivity coefficient at the nth interface. The $*$ symbol indicates convolution, $\boldsymbol{F^{-1}}$ represents the inverse Fourier transform and $\cdot$ represents multiplication.

According to equation (4.17), reflectivity at each interface is first computed in the frequency domain by multiplying the wavelet spectrum $\boldsymbol{W(\omega)}$ with the frequency-dependent reflection coefficient $\boldsymbol{R^n(\theta, \omega)}$ **.** Noting that convolution in the time domain corresponds to multiplication in the frequency domain (Onajite, 2014), the reflectivity is then transformed back into the time domain by an inverse Fast Fourier transform (FFT), yielding a reflectivity wavelet whose amplitude and phase have been shaped by dispersion and attenuation at the nth interface. Convolving this wavelet with the Dirac delta function ($\boldsymbol{i_t^n}$) subsequently places the reflections at

the correct arrival time for each interface. The final reflectivities are then summed over all interfaces to produce the complete synthetic seismic trace (Jin et al., 2017).

In this scheme, $\boldsymbol{W(\omega)}$ corresponds to the frequency domain expression of our source wavelet, specifically the 50 Hz Ricker wavelet $\boldsymbol{w(t)}$ derived in Section (3.2.3), equation (3.35). Following Y. Wang (2015), the Fourier transform of the Ricker wavelet can be written as:

$$W(\omega) = \frac{2\omega^2}{\sqrt{\pi}\omega_p^3} e^{\frac{-\omega^2}{\omega_p^2}} \tag{4.18}$$

where $\boldsymbol{\omega_p}$ is the dominant angular frequency (radians/second).

To implement this workflow, we employ Mantis library packages (courtesy of my advisor Giorgos Papageorgious), using dispersive P-wave and S-wave velocities, P-wave attenuations and density logs obtained from the squirt-flow modeling in Section (4.3.4) as inputs for the frequency-dependent reflectivity. In practice, we discretize the SFjord reservoir into finite, isotropic layers at distinct time depths, then iterate over each pair of consecutive layers, employing their respective elastic properties and attenuations, to generate the frequency-dependent and shifted reflection/transmission responses at multiple angles (0° to 40°, in 10° increments). We then apply the inverse FFT and time-window summation approach described above to produce a single stacked trace per angle, ultimately generating pre-stack synthetic gathers for all ($\boldsymbol{S_w, q, Q^{-1}}$) sets, to be presented in the results section. It is also important to note that no noise was introduced during the synthetic gather modeling process.

4.3.6 Spectral Decomposition

Seismic signals typically exhibit nonstationary behavior, as their frequency content and amplitude vary over time while propagating through the subsurface. This occurs because subsurface heterogeneities (e.g., layers with contrasting acoustic properties) alter the wave's frequency characteristics, causing amplitude decay, phase shifts and frequency-dependent attenuation (Y. Wang, 2022a). Consequently, real seismic traces cannot be fully described by a single time-

invariant wavelet. To address this limitation, time–frequency analysis, also referred to as spectral decomposition, becomes necessary (Y. Wang, 2022b).

Spectral decomposition transforms seismic amplitudes ($\boldsymbol{D}$) as a function of time ($\boldsymbol{t}$) at receiver ($\boldsymbol{n}$) from the time domain into spectral amplitudes ($\boldsymbol{S}$) as a function of time ($\boldsymbol{t}$) and frequency ($\boldsymbol{f}$) in the frequency domain (Wu et al., 2014a) :

$$D(t,n) \leftrightarrow S(t,n,f) \tag{4.19}$$

In the frequency domain, the seismic signal is characterized by both amplitude and phase spectra. The amplitude spectrum describes the magnitude of the seismic signal at discrete frequency components, whereas the phase spectrum defines the signal's phase at those frequencies (Y. Wang, 2022a). Together, these spectral profiles, examined across time, reveal how frequency content varies within the subsurface, exposing geological or reservoir-scale attributes that might otherwise remain hidden in the time-domain representation. As a result, spectral decomposition can illuminate stratigraphic and depositional features near or below seismic resolution and is widely employed in seismic processing, interpretation and reservoir characterization (Khonde & Rastogi, 2013), including CCS projects where mapping CO_2 channels is a key objective.

Various spectral decomposition methods have been implemented in CCS initiatives to highlight unique subsurface features. For instance, the continuous wavelet transform (CWT) was employed to delineate thin shallow reservoir channels in 3D seismic data from the southern North Sea basin (Kenneth Samuel & Righteous, 2019), whereas the Wigner-Ville distribution (WVD**)** was used at the Sleipner field to assess temporal thickness and velocity changes in an injected CO_2 plume (Williams & Chadwick, 2012). Other approaches include the short-time Fourier transform (STFT), applied for imaging temporal bed thickness and geologic discontinuities (Partyka et al., 1999), and matching pursuit decomposition (MPD) to detect carbonate gas reservoirs (Y. Wang, 2007). Among these methods, STFT offers a practical balance between time localization and frequency resolution while remaining conceptually straightforward and computationally efficient (Y. Wang, 2022b). Consequently, in this study, we employ STFT to examine dispersive behavior in the SFjord reservoir under varying fluid saturations, capillary pressures, and attenuation parameters.

The STFT decomposes each seismic trace into smaller, quasi-stationary segments via a sliding window function, and then performs Fourier transform on the individual segments accordingly. Mathematically, STFT is represented by equation (4.20) :

$$S_{STFT}(t,f) = \int_{-\infty}^{+\infty} w(t-\tau)x(\tau)e^{-i2\pi f\tau}\,d\tau \tag{4.20}$$

where $\boldsymbol{S_{STFT}(t,f)}$ is the time-frequency spectrum, $\boldsymbol{x(\tau)}$ is the original seismic trace, and $\boldsymbol{w(t-\tau)}$ is the sliding window function centered at time $\boldsymbol{t}$ (Y. Wang, 2022b).

In our workflow, we focus on a seismic time window from 1,030 ms to 1,126 ms, containing 96 samples at 1 ms intervals, primarily focusing on the overburden seal and SFjord reservoir (Figure (4.8)). Each pre-stack incidence trace within this time window is individually spectrally decomposed to investigate frequency-content variations induced by the modelled dispersive effects.

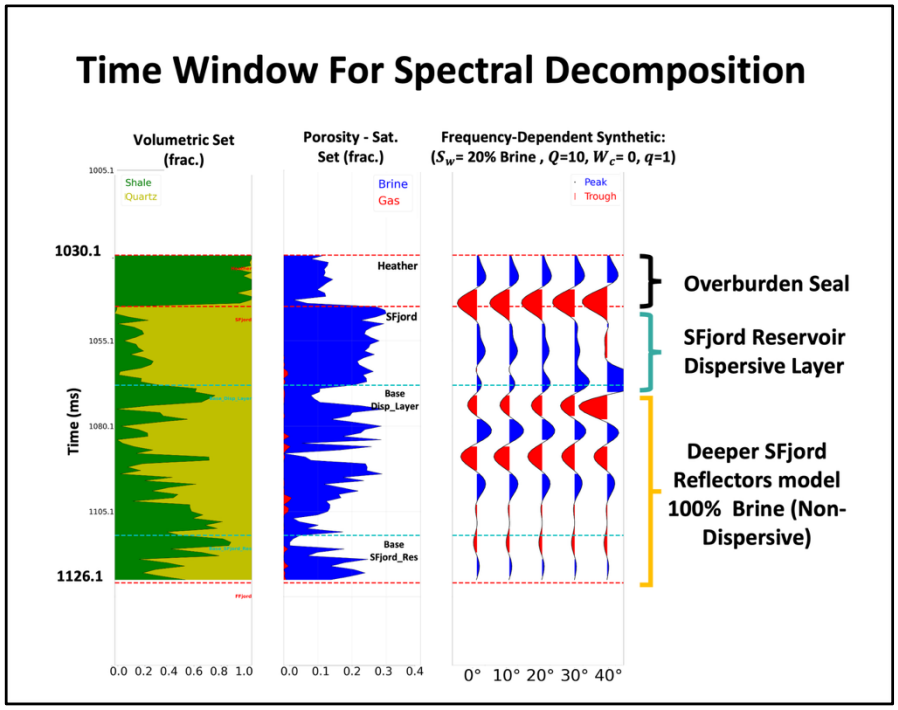


Figure 4.8 – Defined spectral decomposition time window for the SFjord reservoir interval (1030–1126 ms), displaying the embedded dispersive layer. This interval was specifically chosen to investigate how variations in key parameters ***(S_w , q, Q^{-1})*** *influence the seismic amplitudes at both the top SFjord interface and deeper reflectors within the dispersive reservoir zone. The rightmost track shows a representative frequency-dependent synthetic gather (0–40°) generated using the convolutional reflectivity model for 20% Brine at Q=10, W_c=0 at uniform pressure (q=1).*

We use SciPy's STFT function, which specifies an input sampling frequency ($\boldsymbol{f_s}$), a windowing function ($\boldsymbol{window}$), segment length ($\boldsymbol{n_{perseg}}$), an overlap between consecutive segments ($\boldsymbol{n_{overlap}}$) and the FFT window size ($\boldsymbol{n_{fft}}$), as summarized in Table (9). These parameters must be carefully chosen to balance time and frequency resolution, acknowledging that enhanced frequency resolution generally compromises temporal detail and vice versa (Y. Wang, 2022b).

Throughout this task, we begin by experimenting with various windowing functions (Hann, Blackman, Blackman-Harris, etc.), each having a particular shape in the time domain and a unique frequency-domain response, at various $\boldsymbol{n_{perseg}}$ window sizes (Figure 4.9 (A-C)). This allows us to assess how different tapering windows can mitigate spectral leakage, defined as energy bleeding from strong frequencies into adjacent frequency bins, thus influencing the spectral detail captured by the STFT.

When selecting a window function for STFT analysis, one must balance sidelobe minimization (to reduce leakage) against maintaining a suitably narrow main lobe (to resolve closely spaced frequencies) (Y. Wang, 2022b). We initially tested the Hann windowing function (Figure 4.9 (A)), mathematically expressed by $\boldsymbol{w(n)}$:

$$w(n) = 0.5\left[1 - \cos\left(\frac{2\pi n}{N-1}\right)\right], \qquad \text{N =0,1, ……. , N-1} \tag{4.21}$$

where **N** is the total number of samples in the window. This two-term structure tapers the edges smoothly, producing a relatively narrow main lobe but only moderate sidelobe suppression, allowing some leakage when large-amplitude frequencies dominate. In contrast, the Blackman–Harris window employs four cosine terms, offering stronger sidelobe suppression and reduced leakage from strong frequencies into neighboring bins (Figure 4.9 (C)), a key advantage for highlighting weak spectral variations in fluid-sensitive reservoir analyses. Although its slightly broader main lobe may complicate distinguishing very closely spaced frequencies, we ultimately favor Blackman–Harris in this implementation because it minimizes spectral leakage while maintaining sufficient resolution (Y. Wang, 2022b).

The $\boldsymbol{n_{perseg}}$ parameter specifically defines the number of samples in each time segment, effectively defining the width of the windowing function and thus dictating temporal resolution. Hence, in this workflow, we tested different segment sizes ($\boldsymbol{n_{perseg}} \in$ [16, 32, 48, 64, 80, 96]) in to optimize time–frequency balance. Our observations indicate that a smaller $\boldsymbol{n_{perseg}}$ implies

shorter segments that adapt more rapidly to abrupt changes in the seismic signal, thus improving time resolution at the expense of coarser frequency bins. In contrast, increasing $\boldsymbol{n_{perseg}}$ spans more cycles of the wavelet in each segment, providing better frequency resolution yet degrading temporal resolution, as illustrated in Figure 4.9 (A-C) for various $\boldsymbol{n_{perseg}}$ spanning different windowing functions. This figure demonstrates that selecting an $\boldsymbol{n_{perseg} = 48}$ achieves a balance, ensuring that the main lobe isn't excessively broad (as it might be at very large segment sizes) and that time resolution isn't overly compromised (as it would be for significantly higher $\boldsymbol{n_{perseg}}$). The figure further supports this choice, illustrating how Blackman–Harris at 48 samples achieves strong sidelobe suppression and manageable main-lobe width for reliable STFT analysis.

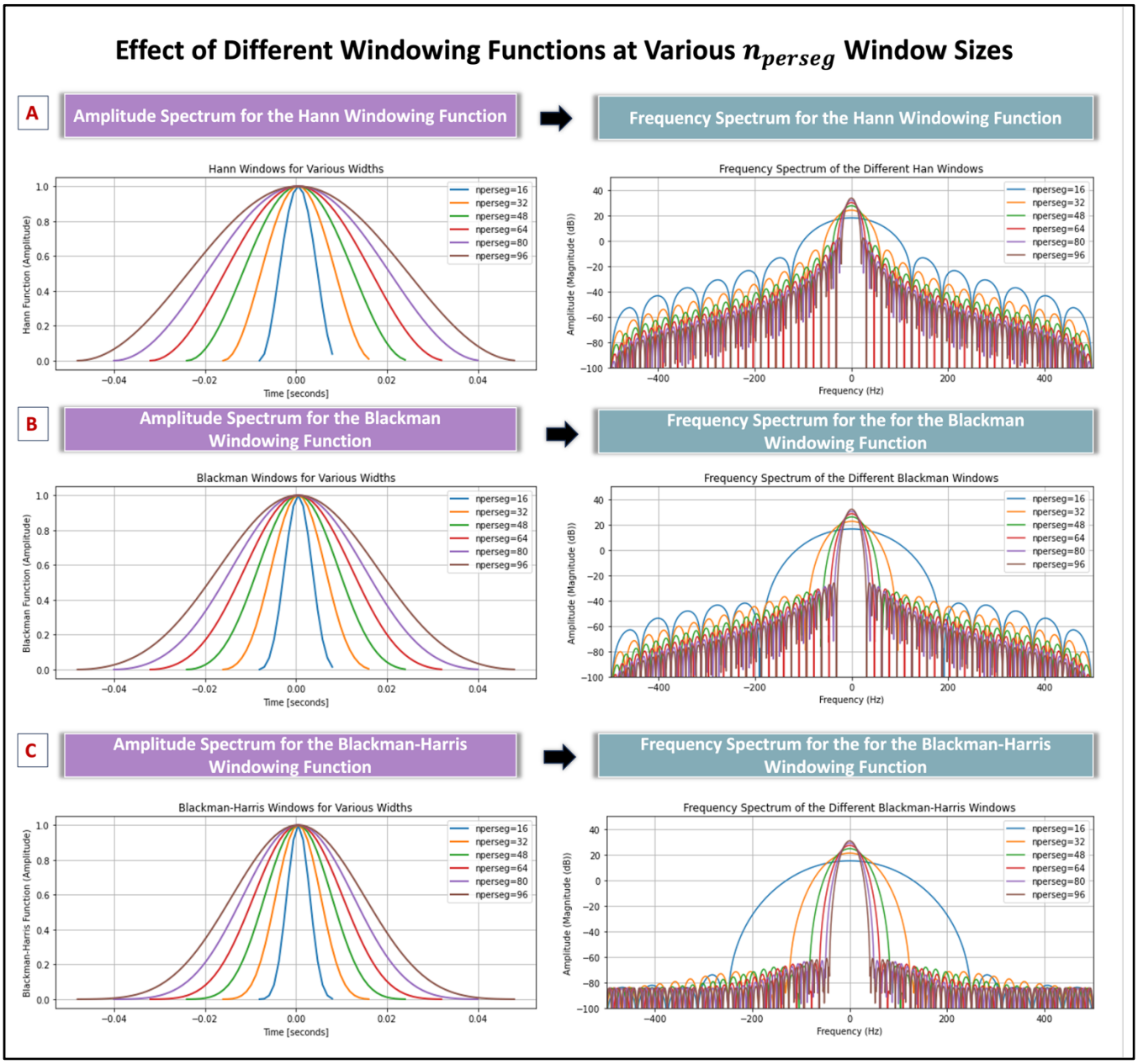


Figure 4.9 – Comparison of Hann, Blackman, and Blackman–Harris window functions at varying nperseg $\boldsymbol{n_{perseg}}$, demonstrating their trade-offs in sidelobe suppression and frequency resolution. Blackman–Harris at $\boldsymbol{n_{perseg}}$=48 is selected for optimal time–frequency balance.

The $\boldsymbol{n_{fft}}$ input parameter determines the length of the Fast Fourier transform applied to each windowed segment, thereby influencing frequency resolution (Figure 4.10 (A-C)). A larger $\boldsymbol{n_{fft}}$ window produces a denser grid of frequency bins with finer increments, creating a smoother, more detailed spectrum without introducing new frequency content. In our workflow, we evaluated $\boldsymbol{n_{fft}}$ values at powers of two (i.e., 128, 256, 512, 1024, 2048) and ultimately selected $n_{fft} = 2048$, as it yields a smoother time–frequency representation that enhances small-amplitude spectral variations (Figure 4.10 (C)). Because the selected $\boldsymbol{n_{fft}}$ exceeds $\boldsymbol{n_{perseg}}$, any extra samples are zero-padded, refining the visibility of peak frequencies at the cost of increased computational runtime. Nevertheless, given our relatively short time window for spectral decomposition, the runtime remains manageable, making 2,048 an acceptable choice for this analysis.

We also investigated the $\boldsymbol{n_{overlap}}$ input parameter. We initially adopted a 50% overlap (Figure 4.10 (A)):

$$n_{overlap} = \frac{n_{perseg}}{2} \tag{4.22}$$

as a common guideline for the short-time Fourier transform, ensuring sufficient continuity to avoid abrupt changes in amplitude or phase. However, upon testing different possible overlaps, $\boldsymbol{n_{overlap}} \in [8, 16, 24, 32, 40, 48]$ corresponding to different $\boldsymbol{n_{perseg}}$ window sizes, we still observed noticeable transitions between consecutive segments. As a result, we employed the following overlap approach (Figure 4.10 (B)):

$$n_{overlap} = n_{perseg} - 1 \tag{4.23}$$

effectively sliding the windowing function on a sample-by-sample basis, thereby achieving the desired STFT resolution within our spectral window, as shown in Figure 4.10 (C).

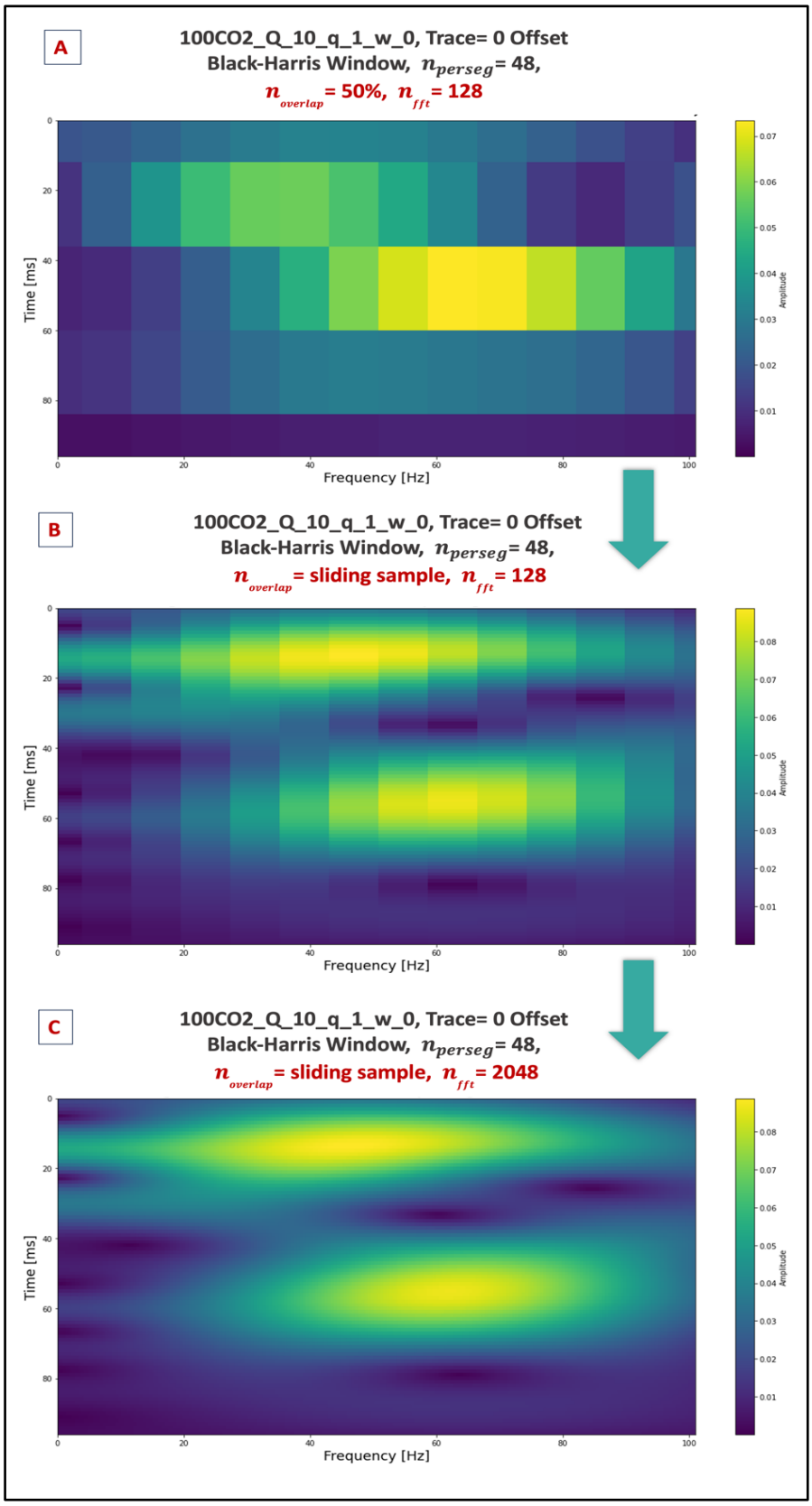


*Figure 4.10 – STFT spectrograms of a fully CO_2-saturated seismic trace at normal incidence, generated using varying $\mathbf{n_{overlap}}$ and $\mathbf{n_{fft}}$ parameters. Panel **(A)** uses $\mathbf{n_{fft}}$ = 128 with a standard overlap, resulting in a blocky and discrete spectral representation. Panel **(B)** maintains $\mathbf{n_{fft}}$=128 but employs a finer, sample-by-sample overlap, slightly enhancing temporal continuity. Panel **(C)**, using the same fine overlap approach with $\mathbf{n_{fft}}$= 2048, demonstrates significantly improved spectral resolution and smoother amplitude transitions, clearly highlighting subtle amplitude variations.*

Based on the above experimentation, we determined that the STFT input parameters in Table (9) provide an acceptable balance between time and frequency resolution, ensuring sufficiently clear time localization while preserving detailed spectral content. Using these parameters, we then generated an STFT output for each incidence trace. Each trace was decomposed into a two-dimensional matrix of complex Fourier coefficients, $\boldsymbol{Z_{xx}(f,t)}$, spanning 1,025 frequency bins from 0 to the 500 Hz Nyquist limit at ~0.48 Hz increments (governed by 1 ms sampling), across 96 temporal frames. In total, this process yielded a dictionary of (21,600) 2D data frames that encompass complex coefficients ($\boldsymbol{Z_{xx}}$) for all the incidence traces that compose our synthetic gathers, as this latter output will be utilized in subsequent analysis steps .

Table 9 - Selected STFT parameters and associated rationale for each parameter.

STFT Input Parameter	Value	Justification
Sampling Frequency (f_s)	1/(1ms) = 1000 Hz	Derived from the 1 ms sampling interval (fs = 1 / dt). This provides a 0–500 Hz range, ensuring adequate coverage for the targeted wavelet band.
Window Function	Blackman-Harris	Reduces sidelobe leakage more effectively, highlighting subtle amplitude changes.
n_{perseg}	48	With a dominant wavelet at ~50 Hz, a 48 ms window accommodates sufficient cycles for frequency clarity (period ~20 ms) while retaining reasonable time resolution over the short spectral decomposition window of 298 samples.
$n_{overlap}$	47	Slides the window nearly sample-by-sample, yielding a smoother STFT output and reduced abrupt segment transitions, important for tracking subtle events in the reservoir zone.
n_{fft}	2048	Offers finer frequency increments (~0.48 Hz) and produces a smoother spectral map without significant computational overhead.

To visualize spectral amplitudes, we generated spectrograms (Figure (4.11)), providing two-dimensional time-frequency maps of each incidence trace , allowing us to analyze variation in the frequency content with time and angle. In these plots, color intensity encodes spectral amplitude, with brighter colors indicating stronger energy. For each STFT time frame $\boldsymbol{t}$, the spectral amplitude is the magnitude of the complex spectrum $\boldsymbol{Z_{xx}(f,t)}$,using equation (4.24):

$$A(f,t) = |Z_{xx}(f,t)| = \sqrt{[Re\{Z_{xx}(f,t)\}]^2 + [Im\{Z_{xx}(f,t)\}]^2} \quad (4.24)$$

where $\boldsymbol{Re}\{.\}$ and $\boldsymbol{Im}\{.\}$ refer to the real and imaginary parts of $\boldsymbol{Z_{xx}(f,t)}$, respectively. Physically, $\boldsymbol{A(f,t)}$ is proportional to the signal's energy at frequency $\boldsymbol{f}$ and time $\boldsymbol{t}$ (Y. Wang, 2022b). In the results section, we compare these spectrograms across saturations, capillary pressures and attenuations to assess how dispersive behavior redistributes spectral energy.

The spectrogram panels in Figure (4.11) illustrate STFT results for individual offset traces (0–40°), extracted from a single synthetic gather (40% Brine, Q = 20, q = 1, W_c=0) covering the SFjord reservoir interval. These panels reveal a bimodal spectral pattern characterized by two distinct spectral lobes. The upper, weaker spectral lobe corresponds to the SFjord-top reflector, where modest impedance contrast produces a relatively subdued, broadband spectral response. Approximately 15 ms deeper, a second, stronger lobe emerges at the base of the dispersive zone. This deeper horizon marks a significant porosity reduction coupled with a shalier and stiffer lithology, resulting in a stronger elastic contrast and consequently a more pronounced spectral response. This deeper lobe becomes increasingly dominant at higher offset angles, exhibiting a clear spectral shift toward lower frequencies. Such behavior indicates frequency dependence and highlights the impact of squirt-flow in the partially CO_2-saturated SFjord reservoir.

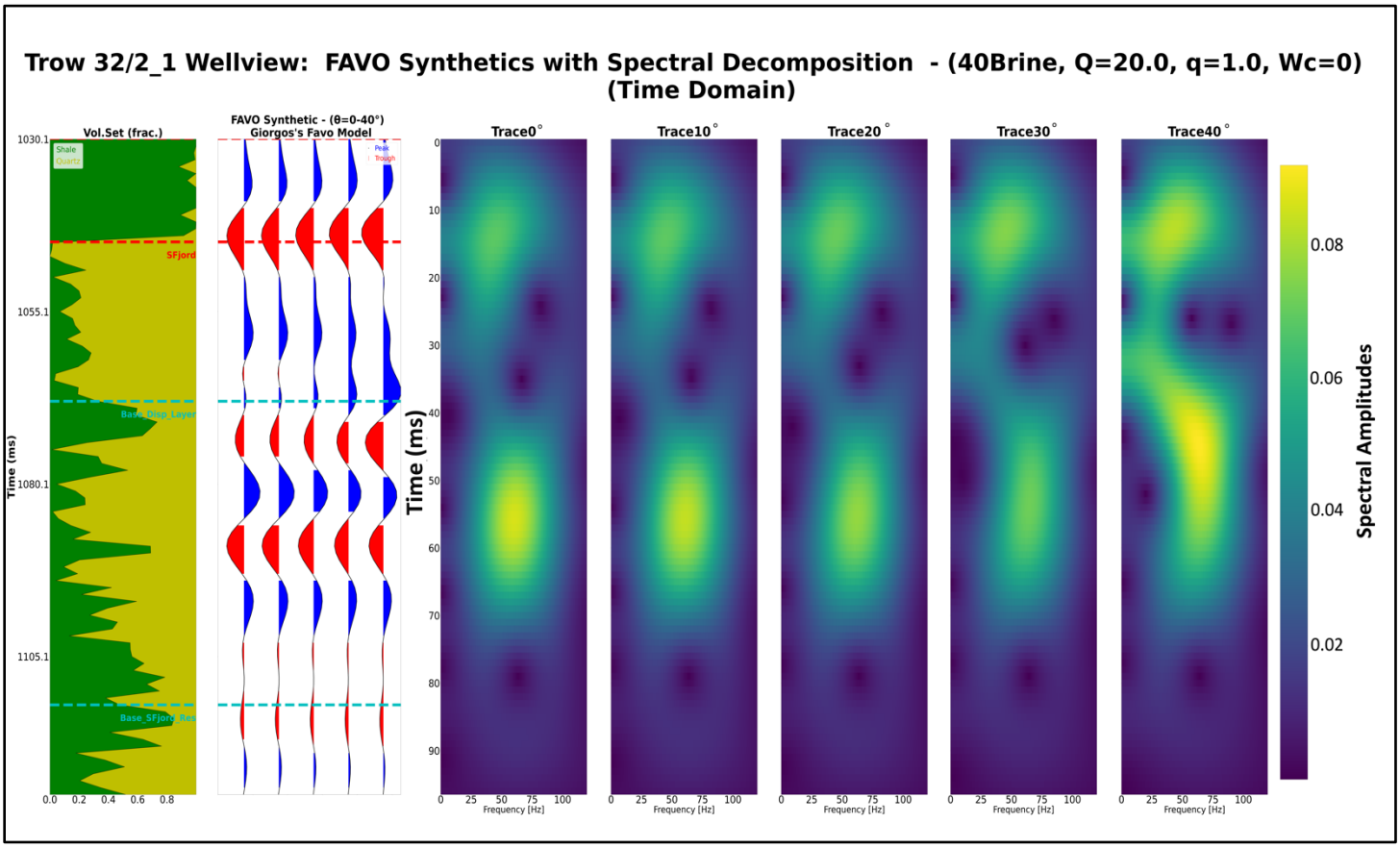


Figure 4.11 – STFT spectrograms computed for the different offset traces (0–40°) from a single synthetic gather: (40% Brine, Q = 20, q = 1, W_c = 0). Variations in amplitude distribution with increasing offset highlight frequency-dependent spectral shifts and energy redistribution, reflecting dispersion and attenuation effects within the partially CO_2-saturated SFjord reservoir.

4.3.7 Spectral Balancing

After spectral decomposition, we perform spectral balancing to remove the overprint of the source wavelet and evaluate the true spectral behavior of the geology and saturating fluids (Partyka et al., 1999). This corrective step compensates for natural amplitude decay or amplification across frequencies, ensuring any observed frequency-dependent variation reflects reservoir properties rather than the source signal. By normalizing all amplitude spectra consistently, we obtain an unbiased perspective that highlights squirt-flow dispersive effects across a range of frequencies and offset angles.

In this study, we initially considered two spectral balancing methods. The first, a single-offset normalization technique, normalizes all brine-CO_2 saturation traces modeled at different offsets by the reference amplitude of 100 % brine only at normal incidence. In doing so, amplitudes at different frequencies or offsets become comparable, effectively standardizing them relative to the chosen reference. This uniform scaling, however, removes any offset-dependent variability that might be diagnostic for our analyses. Consequently, we selected an offset-specific normalization approach because it better aligns with our objective of highlighting frequency-dependent offset trends and resolving amplitude variations driven by saturation changes, capillary pressure contrsasts, and increasing attenuation.

In this scheme, the amplitude spectra of the different brine-CO_2 saturation mixtures at a given offset are divided by the amplitude spectrum of 100 % brine at the same offset, at negligible attenuation ($Q = 1000$) to provide a relatively frequency-independent baseline reference. The resulting ***Balanced Amplitude Ratio*** is given by equation (4.25):

$$Balanced\ Amplitude\ Ratio = \frac{Amplitude\ Spectrum\ (Brine - CO_2\ Mixture(S_w)_Q_q_OffsetAngle}{Amplitude\ Spectrum\ (100Brine_Q(1000)_OffsetAngle)} \tag{4.25}$$

To compute this ratio, we use the STFT-derived $\boldsymbol{Z_{xx}}$ dataframes and apply an element-wise division operation to acquire the balanced amplitude for each brine-CO_2 saturation mixture accordingly. The discussed workflow is illustrated in Figure (4.12). Once these balanced

amplitudes are generated, we check the results by examining the amplitude spectra and verify 5that the ratio plots capture realistic frequency trends, as will be presented and discussed in the results section.

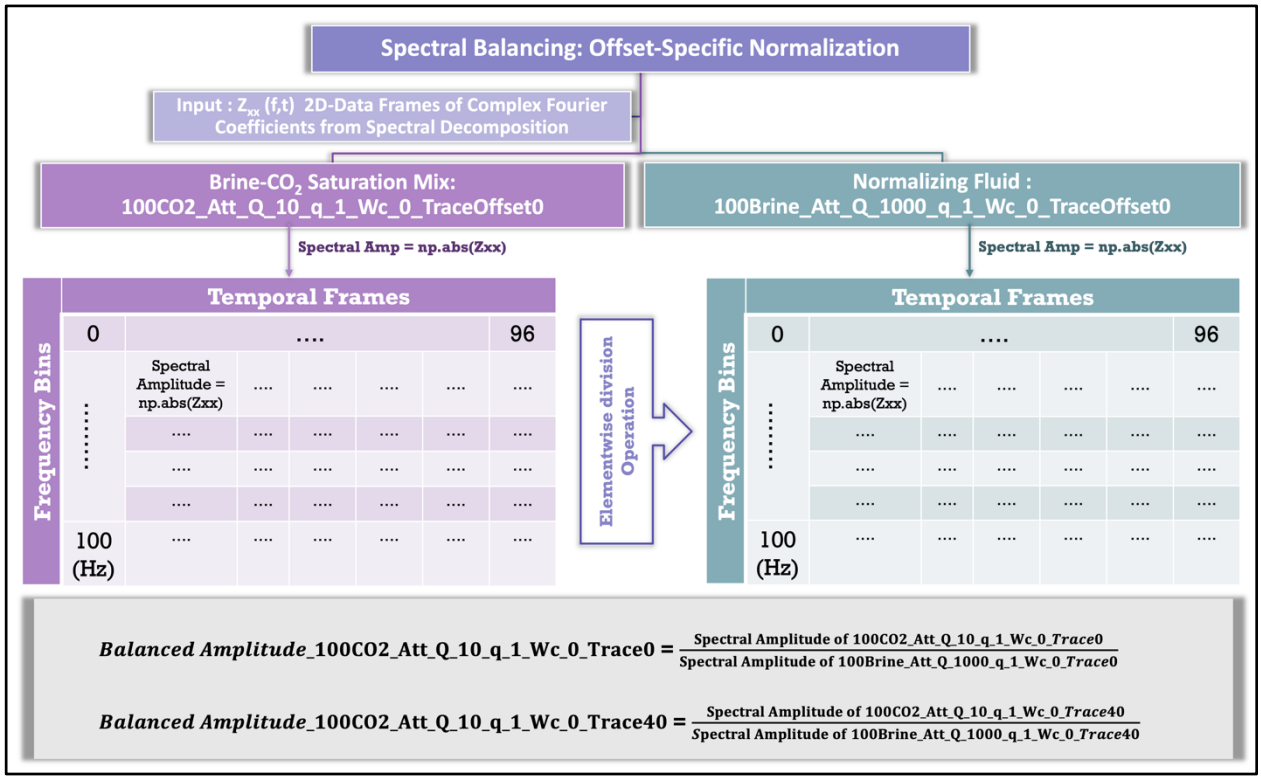


Figure 4.12 – Schematic illustrating the offset-specific spectral balancing workflow. The amplitude spectra of various brine–CO_2 mixtures are normalized against a pure-brine reference spectrum, effectively removing the source wavelet imprint and revealing the underlying frequency-dependent AVO trends.

4.3.8 Frequency-Dependent (FAVO) Analysis

Following spectral balancing, we perform frequency-dependent AVO analysis to investigate amplitude variations across different offsets and frequencies. This allows us to evaluate the effects of CO_2 saturation, capillary pressure, and attenuation on the frequency-dependent seismic responses across the SFjord interface.

To achieve this, we extract spectrally balanced amplitudes at selected iso-frequencies (5, 10, 15, 20, 30, 40, 45, 50, 60, 70, 80, and 90 Hz) and compute the mean amplitudes across predefined temporal frames. The procedure is systematically repeated for all modeled synthetic gathers to

ensure analytical consistency, yielding a single mean amplitude value for each offset trace at each iso-frequency, as illustrated in Figure (4.13).

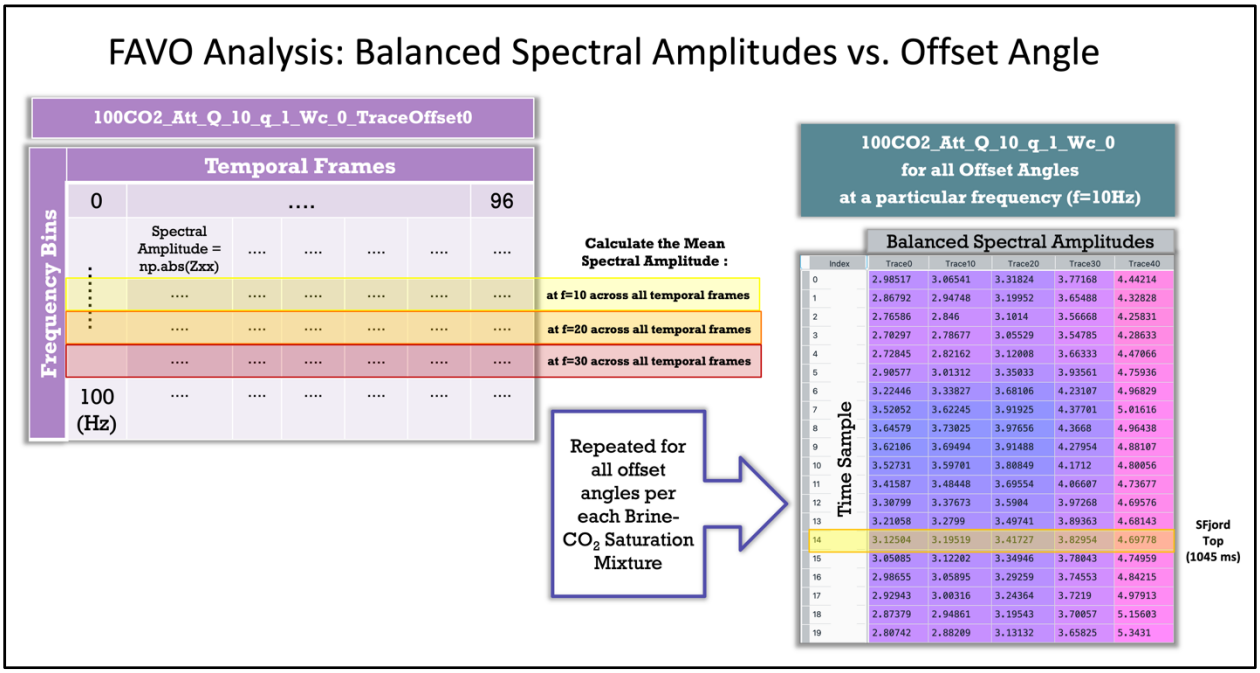


Figure 4.13 – Schematic illustrating the extraction of iso-frequency spectral amplitudes. Mean spectral amplitudes are computed across all temporal frames at selected iso-frequencies for each offset angle, with this procedure systematically repeated across all brine–CO_2 saturation mixtures.

We next employ these frequency-dependent amplitudes to generate key attributes for AVO interpretation. Specifically, we extract mean spectral amplitudes at the SFjord interface (1,045 ms) and compare amplitude-versus-offset trends to examine how varying CO_2 saturations and attenuation conditions influence reflection characteristics. The workflow concludes by developing a frequency-dependent AVO rock-physics template, highlighting amplitude trends across multiple frequencies and offsets. The detailed findings and their broader implications are presented and discussed further in the results section.

4.4 Machine Learning Workflow and Implementation

4.4.1 Introduction

Machine learning is a widely employed tool in artificial intelligence, encompassing a broad range of algorithms and techniques designed for automatically uncovering data trends, extracting insights and generating predictions from diverse datasets (Rashid & Kausik, 2024). Tom Mitchell provides a well-known, engineering-oriented definition: "A computer program is said to learn from experience E with respect to some task T and some performance measure P, if its performance on T, as measured by P, improves with experience E" (Shute et al., 2023). Likewise, Géron, (2017) characterizes machine learning as "the science of programming computers so they can learn from data."

The integration of machine learning (ML) has seen a significant surge across various industries, driven by advancements in technology and computational power, especially during this era of rapid digital transformation. ML offers enhanced data processing capabilities, improved predictive analytics, and valuable insights that facilitate informed decision-making and optimized resource allocation, leading to increased efficiency and productivity (Rashid & Kausik, 2024). In the geoscience domain, ML has been instrumental in addressing complex challenges, from mineral exploration to environmental monitoring, by enabling the analysis of large and complex datasets that were previously intractable with traditional methods (Zhao et al., 2024).

The application of machine learning in geophysics has evolved significantly over the decades. Early implementations in the 1970s and 1980s explored pattern recognition techniques, including the use of shallow neural networks for seismic signal classification and geophysical data interpretation (Dowla et al., 1990). These foundational efforts laid the groundwork for more advanced applications in the 2000s, such as support vector machines and decision trees, for lithology prediction and seismic facies classification (Dramsch, 2020). The emergence of deep learning in the 2010s further transformed the field, introducing convolutional neural networks (CNNs) for seismic image analysis and recurrent neural networks (RNNs) for modeling time-series geophysical data, including well logs and petrophysical properties. This progression reflects a transition from the traditional physics-based models to data-driven approaches (Dramsch, 2020).

In more recent development, machine learning (ML) has been increasingly adopted in carbon capture and storage (CCS) projects, particularly to improve seismic monitoring and the detection or mapping of subsurface CO_2 plumes (Yan et al., 2021). Li & Li (2021) developed a deep learning U-net convolutional neural network for automatic detection and delineation of the CO_2 plume at the Sleipner storage site using time-lapse (4D) seismic data. The model was trained on baseline

and post-injection seismic volumes, achieving results consistent with expert interpretations while significantly reducing processing time. Similarly, Gonzalez & Misra (2022) applied unsupervised ML techniques such as K-means and agglomerative clustering, utilizing seismic tomography and well log data for qualitative CO_2 plume mapping. Their approach demonstrated successful plume characterization, tracking the spatial extent of the CO_2 plume over time. At the Illinois Basin Decatur Project (IBDP), Iyegbekedo et al. (2024) further combined injection rates, well-log attributes, and microseismic events in a gradient-boosted-tree (XGBoost) model to predict the 3-D extent of the CO_2 plume after each monitoring interval. Their supervised ML workflow produced near-real-time plume maps that matched seismic inversions while cutting interpretation time and improving spatial accuracy by ~30 %, illustrating the value of data-driven monitoring in CCS operations. Hence, the latter examples all highlight the significance of machine learning in CCS applications, providing data-driven approaches that may improve subsurface monitoring, reduce interpretation uncertainty, and enhance the management of CO_2 storage sites.

4.4.2 Objective & Scope

There are different machine learning algorithms that can be categorized as: supervised, unsupervised, semi-supervised and reinforcement learning (Goodfellow et al., 2016). Of these algorithms, we are focusing on supervised learning that entail providing the algorithm with a clearly "labelled" dataset that includes the desired input data and corresponding outputs. The algorithm is then expected to learn a relationship that maps the inputs to the outputs through identifying data trends and learning from observations to improve the algorithm's predictive performance. Supervised learning addresses regression, classification and forecasting tasks through several algorithms, such as support vector machines, decision trees, random forests and neural networks (Goodfellow et al., 2016).

In this thesis, the primary objective of this milestone is to develop and validate a supervised two-dimensional convolutional neural network (2D CNN) explicitly designed to mitigate the interference-related amplitude artifacts observed in the synthetic seismic data and associated spectral amplitudes. The CNN model is therefore trained directly on the frequency-dependent spectral amplitudes, which inherently capture the squirt-flow related dispersive responses. By leveraging these spectral amplitudes, the CNN is expected to internalize and accurately distinguish

genuine CO_2-induced seismic responses from interference-dominated spectral patterns. To achieve this task, the CNN architecture incorporates multiple parallel classification outputs, facilitating simultaneous inversion for the key desired reservoir attributes: saturation ($\boldsymbol{S_w}$) , capillary pressure ($\boldsymbol{q}$), and attenuation ($\boldsymbol{Q^{-1}}$) conditions.

Rigorous quantitative evaluation of the CNN model is essential to confirm its ability in overcoming the interference-related effects. Model performance will be assessed using a dedicated validation dataset and standard classification metrics, including maintaining a stable, low validation loss, high validation accuracy, and a balanced F_1-score. Additionally, we introduce a holistic accuracy metric, defined as the simultaneous correct prediction of all three reservoir attributes for each validation sample. Meeting these defined performance thresholds would demonstrate the CNN's robustness and reliability in correctly inverting for the defined reservoir attributes, validating its applicability as an effective diagnostic tool for enhanced CO_2 seismic monitoring.

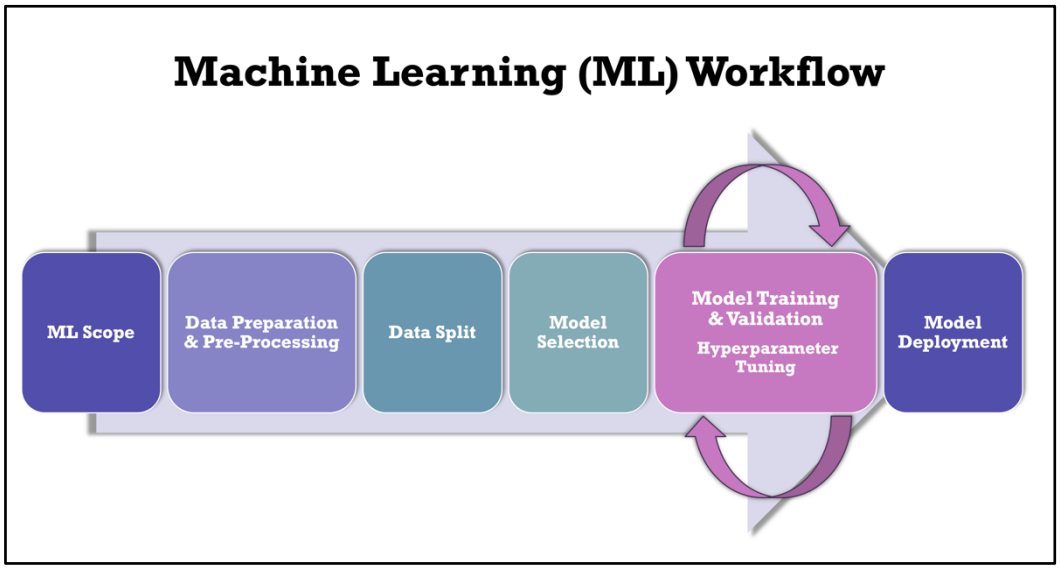


Figure 4.14 – Overview of the machine learning workflow, illustrating key stages from problem scoping through model deployment, including iterative hyperparameter tuning during model training and validation

To accomplish this objective, we adopt the generic machine learning workflow illustrated in Figure (4.14). The process begins by clearly defining the project scope or ML objective, as discussed earlier in this section, followed by comprehensive data collection and preparation. The dataset is then split into subsets for model training and testing. Subsequently, we perform model selection and engage in an iterative cycle of training and validation prior to final model

deployment (Géron, 2017; Goodfellow et al., 2016; Rashid & Kausik, 2024). The following sections detail each of these steps and introduce our selected model accordingly.

4.4.3 Data Collection & Pre-Processing

In this section, we address the data collection and preparation phase of the machine learning workflow. Our input features are the frequency-dependent spectral amplitudes computed as a function of the different parameter combination sets ($\boldsymbol{S_w, q, Q^{-1}}$). These spectral amplitudes have been preserved in their pre-balancing state to avoid introducing potential biases or errors that might arise during the latter step. By maintaining these original amplitudes, this allows the model to make the necessary internal adjustments based on underlying data trends or patterns (spectral characteristics) that might otherwise be masked by balancing.

Although data preparation often includes multiple preprocessing steps, such as data cleaning and feature scaling or selection, we did not employ these methods in our workflow for two reasons. First, we aim to determine whether our model can accurately classify the targeted reservoir attribute ranges ($\boldsymbol{S_w, q, Q^{-1}}$) using only spectral seismic amplitudes as model inputs. Second, all input features were generated and subjected to quality control during the rock physics constrained modeling stage (Section 4.4), thereby ensuring a comprehensive check on the model inputs.

The RP forward modeling stage generated 3,240 synthetic seismic gathers of dimension (48, 5), each containing five seismic traces recorded at incidence angles ranging from 0° to 40°, at 10° increments. The resulting data were then spectrally decomposed into amplitude representations stored as two-dimensional matrices of complex Fourier coefficients, $\boldsymbol{Z_{xx}(f,t)}$, spanning a 48 ms time window and covering frequencies from 0 to 100 Hz (207 frequency bins), with a focus on the overburden caprock seal and the dispersive SFjord reservoir layer.

Because supervised learning requires labelled targets, we adopt the classification scheme introduced in Section (4.4.3). Each spectral-amplitude input is mapped to three output labels, each handled by its own fully connected classifier head: water saturation ($\boldsymbol{S_w}$) range discretized into three classes, capillary-pressure variation ($\boldsymbol{q}$) binarized into two classes, and attenuation ($\boldsymbol{Q^{-1}}$) also binarized into two classes. The numerical limits defining each class are listed in Table (10).

Table 10 - Class label definitions for the multi-class S_w classifier and binary classifiers for q and Q^{-1}. Each range corresponds to a discrete label used for supervised training in the CNN architecture.

Classifier Head	Range	Class Label
1st Classifier Head: Water Saturation	$0 \leq \text{Low } S_w \leq 0.3$	0
	$0.4 \leq \text{Mid } S_w \leq 0.6$	1
	$0.7 \leq \text{High } S_w \leq 1.0$	2
2nd Classifier Head: Capillary Pressure	$0.14 \leq Uniform\,(q) \leq 1.0$	0
	$0.054 \leq Patchy\,(q) \leq 0.1$	1
3rd Classifier Head: Attenuation	$No\ Attenuation\,(Q = 1000)$	0
	$High\ Attenuation\,(Q \geq 30)$	1

4.4.4 Model Selection

In the model selection stage, multiple algorithms are typically evaluated based on the specific machine learning objective. Accordingly, for this implementation, we assessed a range of neural network architectures, including Transformers, Recurrent Neural Networks (RNNs) such as Long Short-Term Memory (LSTM) and Gated Recurrent Unit (GRU) and Convolutional Neural Networks (CNN), in order to identify the approach that best meets our requirements.

While Transformers have gained prominence for their ability to model long-range dependencies and parallelize computations effectively, they are computationally intensive because their self-attention mechanism has a time complexity that grows quadratically with input length (Duan et al., 2023). This requirement for substantial computational resources and large datasets renders them less suitable for scenarios constrained by limited data or hardware, as in our case. In contrast, RNN architectures (e.g., LSTM and GRU) process sequential data by preserving a form of state or memory across inputs. Despite this advantage, RNNs are inherently sequential, limiting parallelization and resulting in slower training and inference times. They are also susceptible to the vanishing gradient problem, where gradients diminish during backpropagation through time, hindering the learning of long-term dependencies (Zucchet & Orvieto, 2024). Although LSTM and GRU architectures were developed to mitigate this issue, RNNs still face challenges when dealing with lengthy sequences and can be computationally demanding.

Hence, given the limitations of Transformers and RNNs for our particular implementation, CNNs present a favorable alternative, especially considering the structure of our input features (2D time–frequency arrays of spectral amplitudes with five channels, each channel representing a distinct trace at incidence angles from 0° to 40°). Hence, by leveraging convolutional operations, CNNs efficiently capture local patterns, making them well-suited for spatially structured data (Goodfellow et al., 2016; Lecun et al., 1998). In particular, 2D CNNs can model the spatial relationships in our 2D time–frequency datasets, where each channel corresponds to a different offset angle. Furthermore, CNNs offer parallel processing capabilities, resulting in faster training and inference compared to RNNs. This efficiency, combined with their capacity to learn hierarchical features, makes them particularly suitable for our seismic analysis tasks.

4.4.5 Neural Network Architecture : (2D CNN)

After model selection, we delve into designing a suitable 2D CNN architecture. This architecture consists of a shared convolutional "encoder" block that extracts hierarchical feature representations, followed by three independent fully connected (FC) classifier heads. These FC heads individually map the encoded spectral-amplitude patterns into categorical predictions for the three classified reservoir properties: water saturation $(\boldsymbol{S_w})$, capillary-pressure variation ($\boldsymbol{q}$), and attenuation ($\boldsymbol{Q^{-1}}$), as illustrated in Figure (4.16) and Table (10). The model operates on spatially structured 2D inputs and is designed to learn spectral, temporal, and spatial patterns present within the time–frequency dataset.

The CNN architecture starts with an input layer of shape (5, *H*, *W*) that receives a 5-channel (*H*×*W*) array, where each channel represents a distinct seismic trace at a particular offset angle, while H and W represent the height and width of the time-frequency representation. The input layer then feeds into the convolutional block consisting of 3 individual CNN layers. The first CNN layer applies 32 convolutional filters with a kernel size of 3, stride of 1 and no padding, which results in an output feature map where both the height and width are reduced by 2 pixels. This step allows the network to detect local patterns in the data, such as frequency variations over time. A max pooling layer with a kernel size of 2 and a stride of 2 is then applied, which reduces both the height and width of the feature map by a factor of 2, reducing the computational load and ensuring that deeper layers focus on higher-level features rather than fine-scale noise.

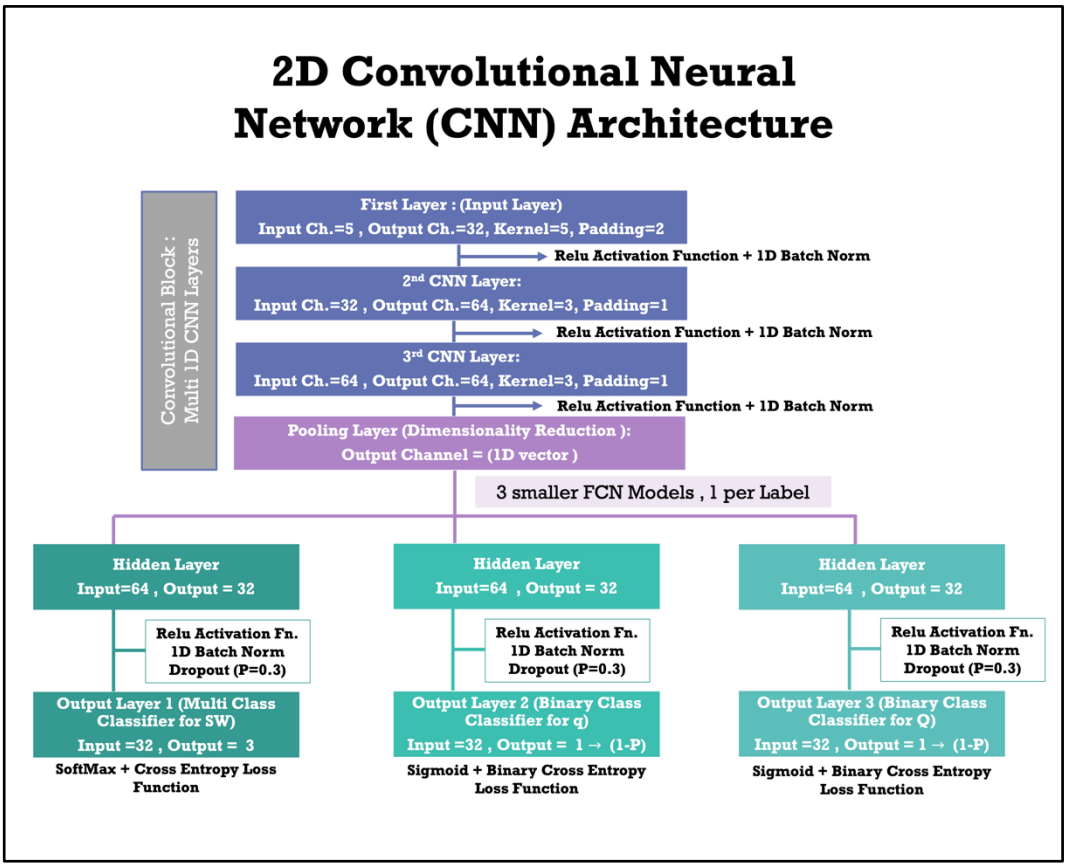


Figure 4.15 – Architecture of the 2D CNN model, containing a shared convolutional encoder block that feeds into three individual fully connected neural networks (FCNN), each equipped with its own classification head for simultaneously predicting S_w, q and Q^{-1}.

The second CNN layer increases the number of filters to 64, applying (3 × 3) kernels with the same previous configuration. Since there is no padding, the convolution once again reduces both the height and width by 2 pixels, further refining the feature representation. A second max pooling layer follows, again reducing the spatial resolution by a factor of 2. The purpose of these pooling operations is to ensure that deeper layers focus on more abstract, high-level features rather than fine-grained details, which improves generalization and reduces overfitting.

The third and final CNN layer applies 128 filters, maintaining the same (3×3) kernel configuration. As with previous CNN layers, the current configuration further reduces both the height and width by 2 pixels. At this stage, the feature maps are smaller but contain richer, more abstract representations of the spectral amplitudes. We incorporate an adaptive average pooling layer, which automatically partitions the feature map into equal regions and computes the

average within each region, producing a fixed (1×1) output vector, This latter step ensures that the entire sequence is reduced to a single value per feature channel, before being flattened and passed to the three individual classification heads (Goodfellow et al., 2016). The output of the pooling layer is computed in equation (4.26):

$$y[i] = \frac{1}{k} \sum_{j=0}^{k-1} x[i+j] \tag{4.26}$$

where $\boldsymbol{y[i]}$ is the pooled output at index $\boldsymbol{i}$. $\boldsymbol{x[i+j]}$ is the original input values being pooled, as $\boldsymbol{j}$ iterates over the kernel size or window length $\boldsymbol{k}$ over which the average is computed (Hutchison et al., 2010). Each CNN layer is internally followed by 2D batch normalization, which normalizes the feature maps (or layer inputs) to stabilize training and accelerate convergence through batch statistics (Ioffe & Szegedy, 2015). This is followed by a Rectified Linear Unit (ReLU) activation function, which is widely used in deep neural networks due to its computational efficiency and its ability to mitigate the vanishing gradient problem (Goodfellow et al., 2016; Nair & Hinton, 2010).

The vanishing gradient problem arises during training when the gradients used to update weights become extremely small as they are backpropagated through the network, making it especially difficult for earlier layers to learn effectively. This is commonly observed with activation functions like sigmoid and tanh, which saturate for large input values, resulting in near-zero derivatives and diminished gradient flow. ReLU addresses this issue by avoiding saturation in the positive domain and maintaining a constant, non-zero gradient for positive inputs (Figure (4.16)). This property preserves gradient magnitude across layers, enabling more stable and efficient training in deep architectures (Goodfellow et al., 2016).

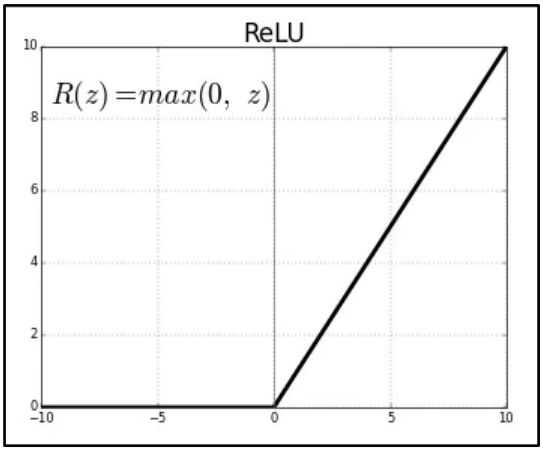


Figure 4.16 – The rectified linear activation function (Shivansh, 2024).

The convolutional block then feeds into 3 independent classification "heads" for classifying $\boldsymbol{S_w}$, $\boldsymbol{q}$, and $\boldsymbol{Q^{-1}}$. Each classification head consists of a fully connected (FC) layer that transforms the 128-dimensional feature vector into a 64-dimensional vector (weight matrix of shape **(***output_dim*×*input_dim***)** = (128, 64)), through a linear transformation, as will be discussed in Section (4.5.6). The output of this operation is then normalized using 1D batch normalization, followed by ReLU activation, and dropout with a probability of 0.5 to mitigate overfitting by randomly deactivating neurons during training.

The final layer of each classifier head then maps the processed features to their respective label outputs. The $\boldsymbol{S_w}$ classifier, as shown in Table (10), is a multi-class classifier that predicts one of three categories, and therefore outputs a vector of length 3 corresponding to the "**Low"**, "**Mid"**, and "**High"** $\boldsymbol{S_w}$ classes (encoded as labels 0, 1, and 2), which is subsequently passed through a SoftMax activation function, as defined in Equation (4.27):

$$\sigma(x_i) = \frac{e^{x_i}}{\sum_j e^{x_j}} \tag{4.27}$$

where $\boldsymbol{\sigma(x_i)}$ represents the predicted probability of class $\boldsymbol{i}$, $\boldsymbol{x_i}$ is the score output by the final neuron corresponding to class $\boldsymbol{i}$, $\boldsymbol{e^{x_i}}$ is the exponential of that score, and $\boldsymbol{\sum_j e^{x_j}}$ is the sum of exponentials across all j classes in the output vector, serving as a normalization factor. The SoftMax is the standard choice for multi-class classification tasks (Bridle, 1989), as it produces a normalized probability distribution over a mutually exclusive class, ensuring that the predicted values sum to 1, effectively transforming them into class probabilities, as addressed in our CNN architecture.

The corresponding loss function used is the cross-entropy loss ($\boldsymbol{L_{CE}}$), which measures the divergence between the predicted probability distribution ($\boldsymbol{\hat{y}_i}$) and the true class labels ($\boldsymbol{y_i}$) as expressed in equation (4.28):

$$L_{CE} = -\sum y_i \log(\hat{y}_i) \tag{4.28}$$

Cross-entropy is the preferrable loss function commonly used for classification tasks (Goodfellow et al., 2016), as it directly measures the penalty for deviating from the correct probability distribution.

For the $\boldsymbol{q}$ classifier, the final layer produces a single output neuron, which is passed through a sigmoid activation function in equation (4.29):

$$\sigma(x) = \frac{1}{1 + e^{-x}} \tag{4.29}$$

where **σ(x)** is the output of the sigmoid function, representing a probability value in the range [0,1] making it suitable for binary classification. $\boldsymbol{e^{-x}}$ represents the exponential decay of the input value $\boldsymbol{x}$, as this parameter determines the curvature of the sigmoid function. The model is then trained using binary cross-entropy loss ($\boldsymbol{L_{BCE}}$), which measures the error in binary classification tasks via the following equation (4.30):

$$L_{BCE} = -[ylog(\hat{y}) + (1 - y)\log(1 - \hat{y})] \tag{4.30}$$

where $\boldsymbol{y}$ is the true label (0 or 1), and $\hat{\boldsymbol{y}}$ is the predicted probability. The attenuation ($\boldsymbol{Q^{-1}}$) classifier adopts the same structure set for the $\boldsymbol{q}$ classifier, using sigmoid activation and binary cross-entropy loss**.** Binary cross-entropy is analogous to cross-entropy but specialized for two-class or binary (0/1) problems, making it appropriate for tasks where each label is either present or absent (Géron, 2017; Goodfellow et al., 2016; K. P. Murphy, 2012).

Thus, the presented 2D CNN architecture handles spatially organized time–frequency data, extracting hierarchical features before branching into three parallel classification heads providing a flexible multi-task framework within a single CNN. All relevant layer configurations and input parameters are summarized in Tables (10), (11) and (12).

Table 11 – Configuration for 2D convolution (CNN) block composed of 3 internal CNN Layers

Layer	Input Channels	Output Channels	Kernel Size	Stride	Padding	Bias
First Layer	5	32	5	1	2	True

Second Layer	32	64	3	1	1	True
Third Layer	64	128	3	1	1	True

Table 12 – Configuration for the independent fully connected classification neural networks.

Layer	Input Size	Output Size	Bias
First Layer	128	64	True
Second Layer	64	3	True

4.4.6 Model Training and Validation

The selected 2D CNN is trained through a iterative cycle of forward and backward propagation, allowing the model to progressively optimize its learnable parameters for accurate classification across the three target labels (Géron, 2017; Goodfellow et al., 2016). Training is conducted over 350 epochs, using a dataset split of 80% for model training and 20% for blind validation.

During the forward propagation cycle, the model computes predicted outputs by transforming the input features (frequency-dependent spectral amplitudes) through successive convolutional and fully connected layers. The CNN predicted output is then compared to the actual target label using an appropriate loss function: categorical cross-entropy is used for the multi-class classification of $\boldsymbol{S_w}$ (equation (4.30)), while binary cross-entropy is applied to the binary classification tasks for $\boldsymbol{q}$ and $\boldsymbol{Q^{-1}}$ (equation (4.32)), producing a residual loss that is then propagated backward through the network (Géron, 2017; Goodfellow et al., 2016).

During backward propagation, this loss is propagated through both convolutional and FC layers using the chain rule of calculus, to calculate how the loss function changes with respect to each learnable parameter (weights and biases). These gradients quantify the contribution of each parameter to the overall loss and are used iteratively to update and optimize the parameters during training in order to minimize prediction error (Goodfellow et al., 2016). Parameter optimization is performed using the Adam optimizer, an adaptive learning algorithm that adjusts the learning rate for each parameter based on the first and second moments of the gradient history, applying the default Adam parameter settings: $\beta_1 = 0.9$, $\beta_2 = 0.999$, and $\varepsilon = 10^{-8}$ (Kingma & Ba, 2017).

The learning rate ($\boldsymbol{\alpha}$) is a key hyperparameter governing the step size of each update which directly dictates the rate at which the model learns (Goodfellow et al., 2016). Empirical or manual tuning revealed that higher learning rates led to unstable convergence and signs of overfitting. In contrast, the selected learning rate (α =0.00002) resulted in more stable training and no apparent overfitting across the training and validation loss trajectories.

To further mitigate overfitting, dropout regularization was employed within the fully connected layers of the classification heads. This regularization technique randomly deactivates a fraction of the neurons during training (Srivastava et al., 2014). Various dropout rates were explored as part of the tuning process, and the observed performance across different configurations led us to adopt a shallow FC architecture, as deeper configurations exhibited overfitting, while excessively shallow models underfit the training data. Based on these evaluations, we selected a dropout rate of $\boldsymbol{p}$=0.5 as a suitable compromise between model complexity and generalization capacity.

Throughout the training process, model performance was monitored at each epoch using both training and validation sets. The validation samples were not exposed during training, enabling an unbiased evaluation of the model's generalization performance (Goodfellow et al., 2016). The model's performance is further assessed using a set of quantitative metrics, including per-label accuracy for each classifier head, (equation (4.31)) as well as a custom metric that we introduce and refer to as holistic accuracy (equation (4.32)). This stricter evaluation measure considers a prediction correct only if all three labels ($\boldsymbol{S_w}$, $\boldsymbol{q}$, $\boldsymbol{Q^{-1}}$) are simultaneously classified correctly for a given sample, making it particularly suitable for our multi-label classification task. We additionally assess the average ***F_1-score*** (equation (4.33)) across all classifier heads, offering a balanced evaluation of ***precision*** (equation (4.34)) and ***recall*** (equation (4.35)) into a single value. Specifically, ***precision*** quantifies the accuracy of positive predictions (the proportion of predicted positives that are correct), while ***recall*** measures the model's sensitivity (the proportion of actual positives correctly identified). Therefore, a high F_1-score signifies balanced performance, indicating that the model effectively maintains accuracy while correctly capturing most positive instances. The definitions and formulations of all evaluation metrics are summarized in Table (13).

We would like to finally note that our hyperparameter tuning approach was performed manually via trial-and-error, with configurations validated based on their impact on accuracy and loss behavior. In future work, however, we plan to adopt systematic hyperparameter

optimization strategies, such as grid search, to identify optimal hyperparameter settings. Nonetheless, the current training yields a good model with stable convergence and good generalization behavior, supporting the model's ability to infer key reservoir attributes directly from frequency-dependent spectral amplitude inputs.

The model's classification performance and evaluation metrics will be presented and thoroughly discussed in the Results section accordingly.

Table 13 – Summary of the utilized evaluation metrics, their mathematical expressions, and their respective roles in evaluating the model performance during the training and validation phase. Metric formulations are based on standard definitions adapted from Géron (2017) and Goodfellow et al. (2016).

Metric	Expression	What it measures
Cross Entropy	$-\sum y_i \log(\hat{y}_i)$	Loss function used to train the $\boldsymbol{S_w}$ classification head (equation (4.28))
Binary Cross Entropy	$-[y log(\hat{y}) + (1-y)\log(1-\hat{y})]$	Loss function used to train the $\boldsymbol{q}$ and $\boldsymbol{Q^{-1}}$ classification heads (equation (4.30))
Accuracy	$\frac{Number\ of Correct\ Predictions}{Size\ of\ Dataset}$	Used separately for $\boldsymbol{S_w}$, $\boldsymbol{q}$ and $\boldsymbol{Q^{-1}}$ classification. Indicates the proportion of correctly predicted labels out of the total samples (equation (4.31))
Holistic Accuracy	$\frac{Num.\ samples\ with\ all\ labels\ Correct}{Size\ of\ Dataset}$	A stricter metric that only considers a sample as correct if all three labels ($\boldsymbol{S_w}$, $\boldsymbol{q}$, $\boldsymbol{Q^{-1}}$) are predicted correctly (equation (4.32))
F_1 score	$2 \cdot \frac{Precision \cdot Recall}{Precision + Recall}$	Harmonic mean of precision and recall for binary classifiers. Especially useful when classes are imbalanced (equation (4.33))
Precision	$\frac{True\ Positives}{True\ Positives + False\ Positives}$	Measures the proportion of positive predictions that are actually correct. Useful when the cost of false positives is high (equation (4.34))

Recall	$\frac{True\ Positives}{True\ Positives + False\ Negatives}$	Measures the proportion of actual positives that were correctly identified. Important when missing a positive instance is costly (equation (4.35))

4.5 Results & Discussion

This section presents the results of the frequency-dependent forward-modelling and the subsequent machine learning analysis. For simplicity and clarity, we share a representative subset of results, consistently evaluating the dispersive responses and seismic signatures for identical parameter combinations across various frequency regimes:

- $\boldsymbol{S_w} \in \{0.0 \rightarrow 1.0\}$, at 0.20 (20 %) CO_2 increments
- $\boldsymbol{q} \in \{1, 0.054\}$
- $\boldsymbol{Q} \in \{1000, 30, 20, 10\}$
- $\boldsymbol{W_c} \in \{-2, -1, 0, 1, 2\}$

4.5.1 Frequency-Dependent Rock Physics Forward Modelling

To establish a baseline for evaluating dispersive effects, we first verify that our SQF model accurately converges to the classical Gassmann behavior at negligible dispersion and attenuation. This validation is clearly illustrated in Figure (4.17), comparing the conventional GFS results (Chapter 3) to the SQF outputs (Chapter 4) computed in the low-frequency, relaxed limit (Q = 1000, q = 1, W_c= –2). The well-view panels of the compressional modulus (P_{Mod}) logs demonstrate a precise match across the entire Sognefjord reservoir interval, with colored SQF elastic logs perfectly overlaying their black GFS counterparts for all brine–CO_2 mixture. Baseline equivalence testing further quantifies this convergence, revealing negligible residuals ($\Delta V_p \approx -0.05$ %, $\Delta P_{Mod} \approx -0.09$ %), computed as the percentage difference between the 100 % brine GFS baseline and the corresponding 100 % brine SQF baseline at Q = 1000 and W_c = –2. This convergence further confirms that frequency-dependent dispersion effects actually vanish at sufficiently low frequencies. Figure 4.18 (A-B) extends this comparison by displaying the complete suite of SQF-derived elastic responses at Q = 1000, in the relaxed state (W_c= –2) for both q = 1 and q_o = 0.054. Both panels reproduce the elastic trends in V_p, V_s, ρ, P_{Mod} and S_{Mod} observed in the corresponding

GFS scenarios (Figures (3.10) and (3.12)), confirming that the two modelling workflows yield equivalent results under low-frequency, negligible attenuation conditions.

With this equivalence established, Figure (4.19) quantifies the relative change (Δ %) in each elastic attribute with respect to the 100 % brine baseline (Q = 1000 , with the corresponding q). Employing these low-frequency results provides a frequency-independent baseline, against which the dispersive effects, caused by variations in capillary pressure or attenuation, can be subsequently evaluated. Panel (A) illustrates that CO_2 substitution progressively lowers the ρ, reaching a 3.5 % reduction at 100 % CO_2 relative to the baseline reference. Panel (B) highlights greater fluid sensitivity in V_p and P_{Mod}, as both attributes decrease substantially (~16% and 32%, respectively) with increasing CO_2 content at uniform pressure (q=1). Increasing capillary pressure yields smaller incremental reductions in V_p and P_{Mod} at intermediate saturations, compared to the uniform-pressure scenario. In contrast, panel (C) demonstrates a significantly lower sensitivity in shear properties (V_s and S_{Mod}), varying by 1.4% in V_s and less than 1 % in S_{Mod} across the entire saturation sweep.

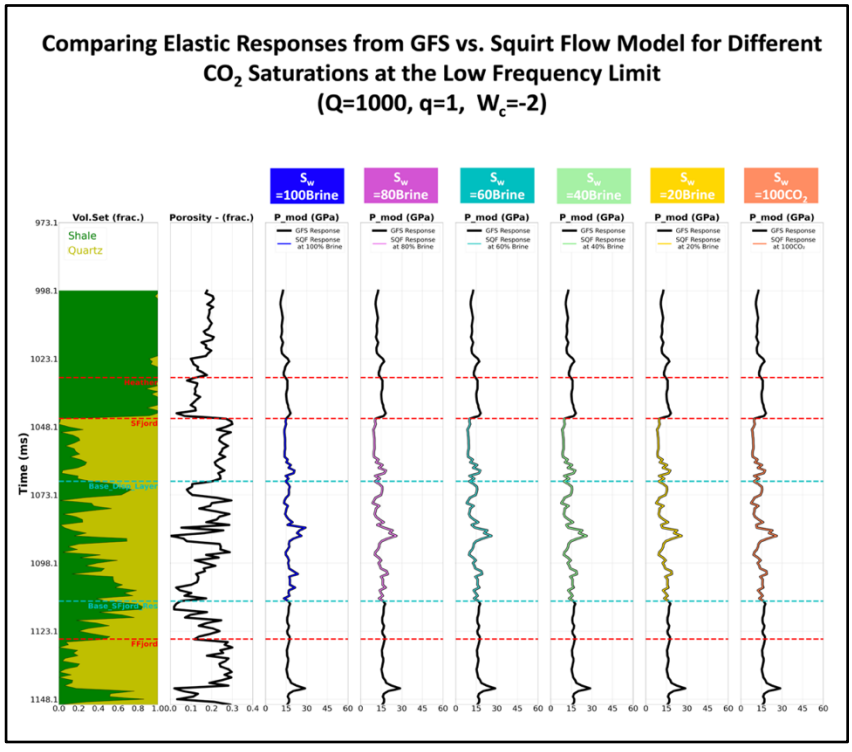


Figure 4.17 – Comparison of compressional modulus (P_{Mod}) logs from the conventional GFS workflow (black) and the frequency-dependent SQF model (colored) at the low-frequency relaxed limit at Q = 1000, q=1, W_c= –2, confirming baseline agreement (GFS ≈ SQF) within the Sognefjord reservoir.

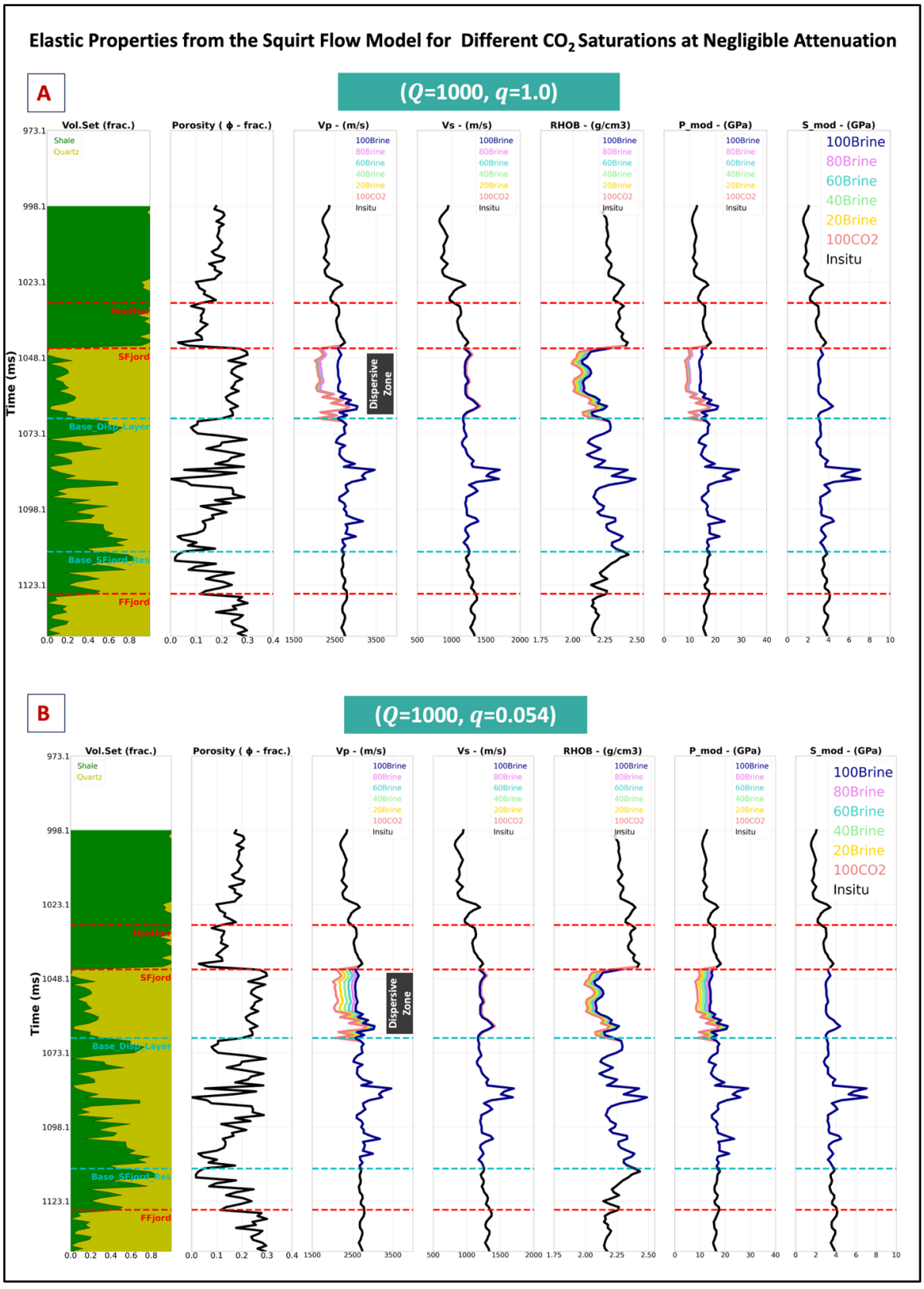


*Figure 4.18 — Well-view panels displaying the SQF-derived responses computed at the relaxed, low frequency condition ($Q = 1000$, $W_c = -2$) for $q = 1$ and $q_o = 0.054$. Both panels **(A)** & **(B)** reproduce similar elastic trends in V_p, V_s, ρ, P_{Mod} and S_{Mod}, as previously noted for the corresponding GFS cases, verifying that both workflows yield equivalent results under low-frequency, negligible dispersion conditions.*

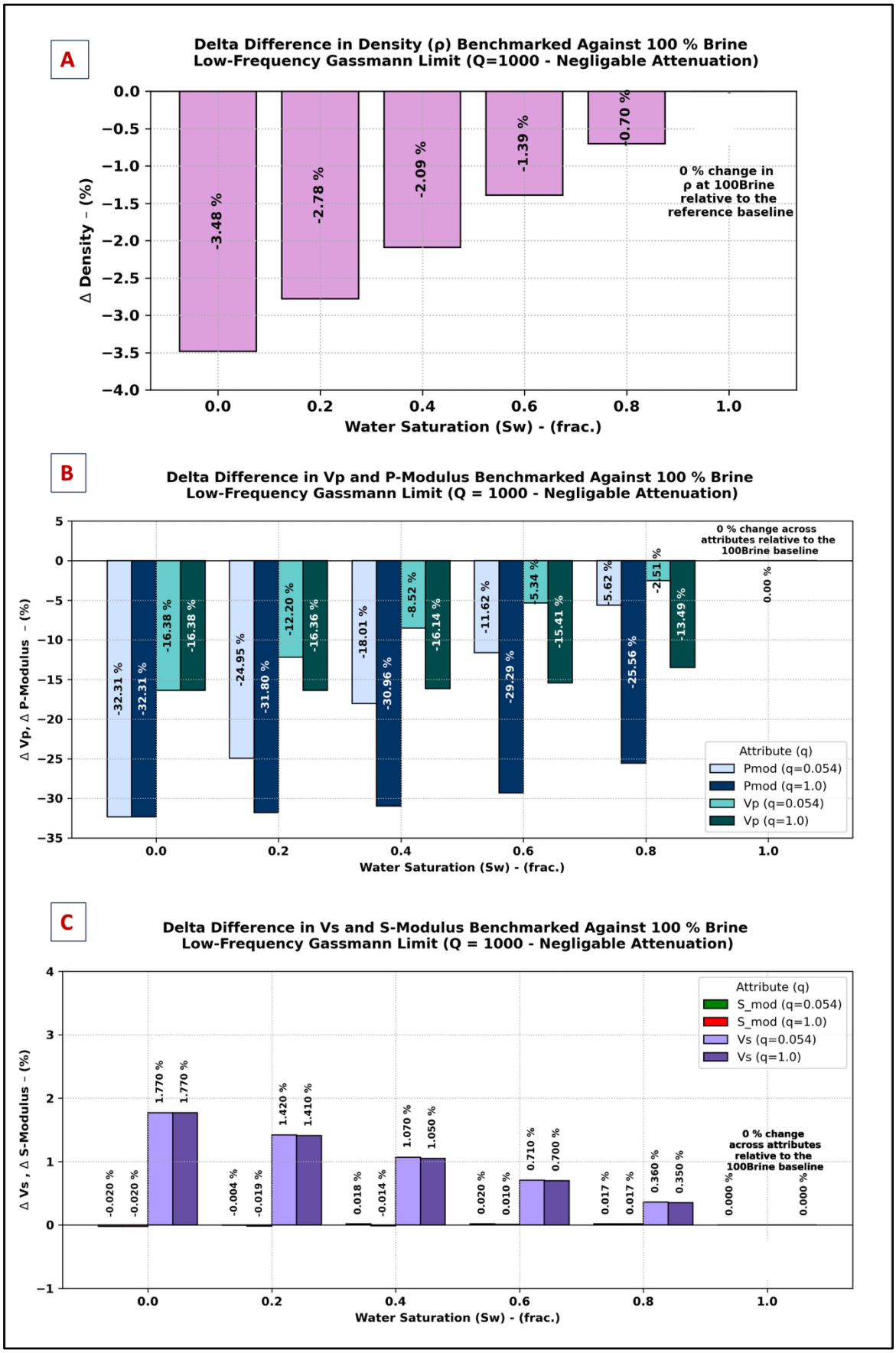


*Figure 4.19 – Relative changes (%) in elastic attributes benchmarked to the 100% brine baseline at low-frequency, relaxed conditions (Q = 100, $W_c = -2$). **(A)** Bulk Density (ρ), **(B)** Compressional velocity (V_p) and modulus (P_{Mod}), **(C)** Shear velocity (V_s) and modulus (S_{Mod}). The different panels highlight the varying sensitivity of these elastic properties to CO_2 saturation and capillary pressure ($q=1$ and $q_0 = 0.054$) changes, under negligible dispersion conditions.*

The preceding well-view panels demonstrated how variations in CO_2 saturation and capillary pressure impact the elastic log responses within the Sognefjord reservoir, relative to two-way travel time, given the in-situ porosity and lithological framework. We now further investigate the saturation-dependent dispersive behavior under varying capillary pressures, attenuation conditions and frequency regimes, as illustrated in Figures (4.20) and (4.21). For consistency, all dispersive responses are sampled at 1,048 ms within the reservoir's dispersive layer, characterized by relatively clean and highly porous sands ($Vol_{sh}\approx 0.12$, $\phi \approx 0.30$). The results are displayed through a matrix cross-plot view that evaluates how squirt-flow alters the seismic attributes (V_p, V_s, P_{Mod}, S_{Mod}) and their associated attenuations (Q_p^{-1} and Q_s^{-1}).

Figure 4.20 (A) establishes the baseline reference at uniform capillary pressure and negligible attenuation (q=1, Q=1000), effectively representing the low-frequency Gassmann limit. Here, the plotted elastic curves show no velocity dispersion or frequency dependence, consistent with the negligible attenuation magnitudes ($Q_p^{-1}\approx 2.7\times10^{-3}$, $Q_s^{-1}\approx 2.5\times10^{-4}$). Maintaining uniform pressure (q=1) while systematically increasing attenuation ($Q = 30 \rightarrow 10$) in panels (B-D), induces stronger velocity dispersion and larger attenuation peaks, directly proportional to the inverse of Q. Consequently, the spread between the relaxed (W_c= –2) and unrelaxed (W_c=2) states substantially increases in V_p and P_{Mod}, whereas the shear properties (V_s and S_{Mod}) remain largely unaffected. At intermediate saturations (S_w= 0.5), the V_p spread increases from ~200 m/s at Q = 30 to greater than 450 m/s at Q = 10, whereas V_s experiences a marginal reduction (<15m/s), and S_{Mod} remains essentially unchanged. Correspondingly, peak P-wave attenuation (Q_p^{-1}) at $S_w = 0.5$ significantly increases from ~0.09 at Q = 30 to ~0.27 at Q = 10 and W_c=0 (dispersive state = maximum attenuation). This emphasizes that the input attenuation factor primarily governs the rate of squirt-flow-induced dispersion and the associated magnitude of peak attenuation without shifting the characteristic frequency or the saturation level at which maximum attenuation occurs, provided that capillary pressure and saturation remain constant.

The cross-plots presented in panels (A–C) further highlight two complementary aspects of squirt-flow dispersion. The first concerns the effective squirt-flow frequency, $\boldsymbol{\omega_o}(S_w)$, which is intrinsically controlled by fluid mobility, as a function of relative permeability and saturation. Accordingly, each brine–CO_2 mixture exhibits a distinct $\boldsymbol{\omega_o}$, producing saturation-dependent velocity dispersion and attenuation profiles. This is particularly because at a fixed seismic

frequency ($\boldsymbol{\omega}$), the dimensionless frequency index (W_c), defined in equation (4.12), systematically varies with saturation, placing different brine–CO_2 mixtures into different squirt-flow dispersive regimes. For instance, panel (D) at q=1, Q=10 shows that a mixture with 20% brine saturation lies within the relaxed state ($W_c = -1$), a 50% brine mixture occupies the dispersive state (W_c = 0), while brine-rich mixtures with saturations above $\sim$ 80% transition into the unrelaxed regime (W_c = +1).

Additionally, Figure (4.20) demonstrates that for a fixed brine–CO_2 mixture at constant capillary pressure and attenuation conditions, an increase in the dimensionless frequency index, W_c, similarly transitions this mixture from relaxed to unrelaxed regimes, thereby modulating the dispersive responses accordingly.

Moreover, Figure 4.20 (D) illustrates a unique twin-peak behavior in the attenuation curves, particularly at W_c= 0 (cyan) across the different attenuation conditions (Q = 1000 → 10). This phenomenon is evident as the Q_p^{-1} curve peaks at two separate saturations ($S_w \approx 0.50$ and $S_w \approx$ 0.95), due to the non-monotonic dependence of the squirt-flow frequency $\boldsymbol{\omega_o(S_w)}$. This is because, initially, the $\boldsymbol{\omega_o(S_w)}$ increases with brine substitution, reflecting a stiffening bulk modulus, and subsequently decreases at higher brine fractions due to increased fluid viscosity. Consequently, a fixed seismic wave frequency can therefore intersect two distinct saturation mixtures across the reservoir, positioning these mixtures simultaneously in highly dispersive states.

Introducing higher capillary pressures (q_o= 0.054) in Figure 4.21 (A–D) stiffens the compressional attributes at intermediate saturations, lowering velocity dispersion and attenuations relative to the uniform pressure scenario (q=1). Correspondingly, the peak P-wave and S-wave attenuations, previously reported (at $S_w \approx 0.50$, Q=10 and W_c= 0), are now notably reduced after introducing higher capillary pressure: $Q_p^{-1} \approx 4\times10^{-2}$ and $Q_s^{-1} \approx 6\times10^{-3}$. Although end-member saturations remain unaffected, the intermediate saturation mixtures ($S_w \approx 0.80 \rightarrow 0.20$) now exhibit a stiffer, more linear decline in V_p and P_{Mod} compared to the uniform pressure scenario, consistent with the patchy-saturation behavior explained in Chapter 3 (Figure (3.12)). In conclusion, the noted observations from Figures (4.20) and (4.21) theoretically align with the hybrid squirt-flow model of Papageorgiou & Chapman (2017) and the expected mechanics of squirt-flow dispersion.

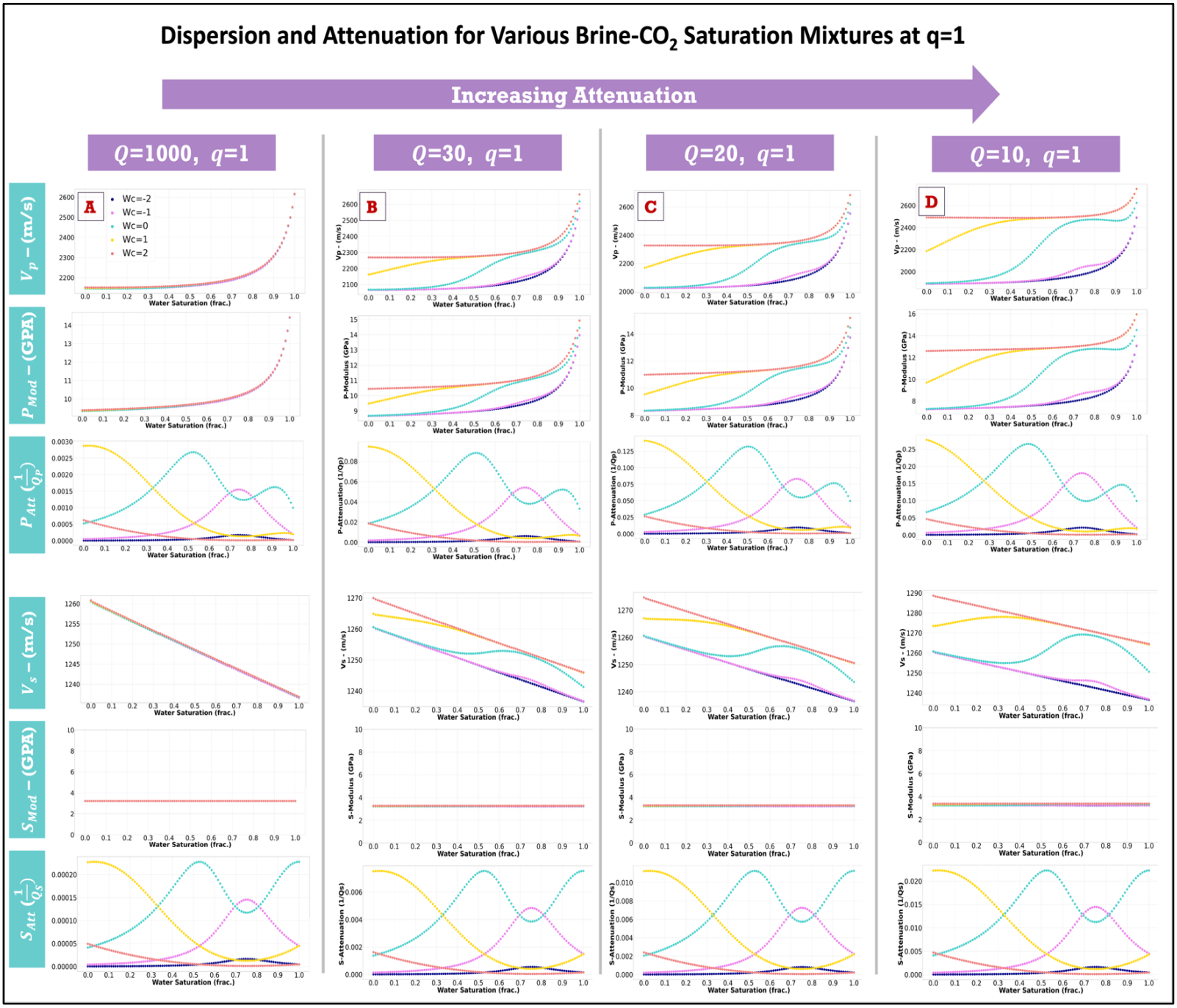


*Figure 4.20 – Saturation-dependent dispersive behavior illustrated by cross-plots of elastic attributes (V_p, V_s, P_{Mod}, S_{Mod}) and the associated attenuations (Q_p^{-1} and Q_s^{-1}) at uniform capillary pressure (q=1) across different frequency regimes ($W_c \in \{-2, -1, 0, 1, 2\}$). Panels **(A-D)** progressively increase attenuation (Q^{-1}, with $Q \in \{1000, 30, 20, 10\}$), highlighting significant dispersion in compressional (V_p, P_{Mod}) attributes and minimal sensitivity in shear (V_s, S_{Mod}) attributes.*

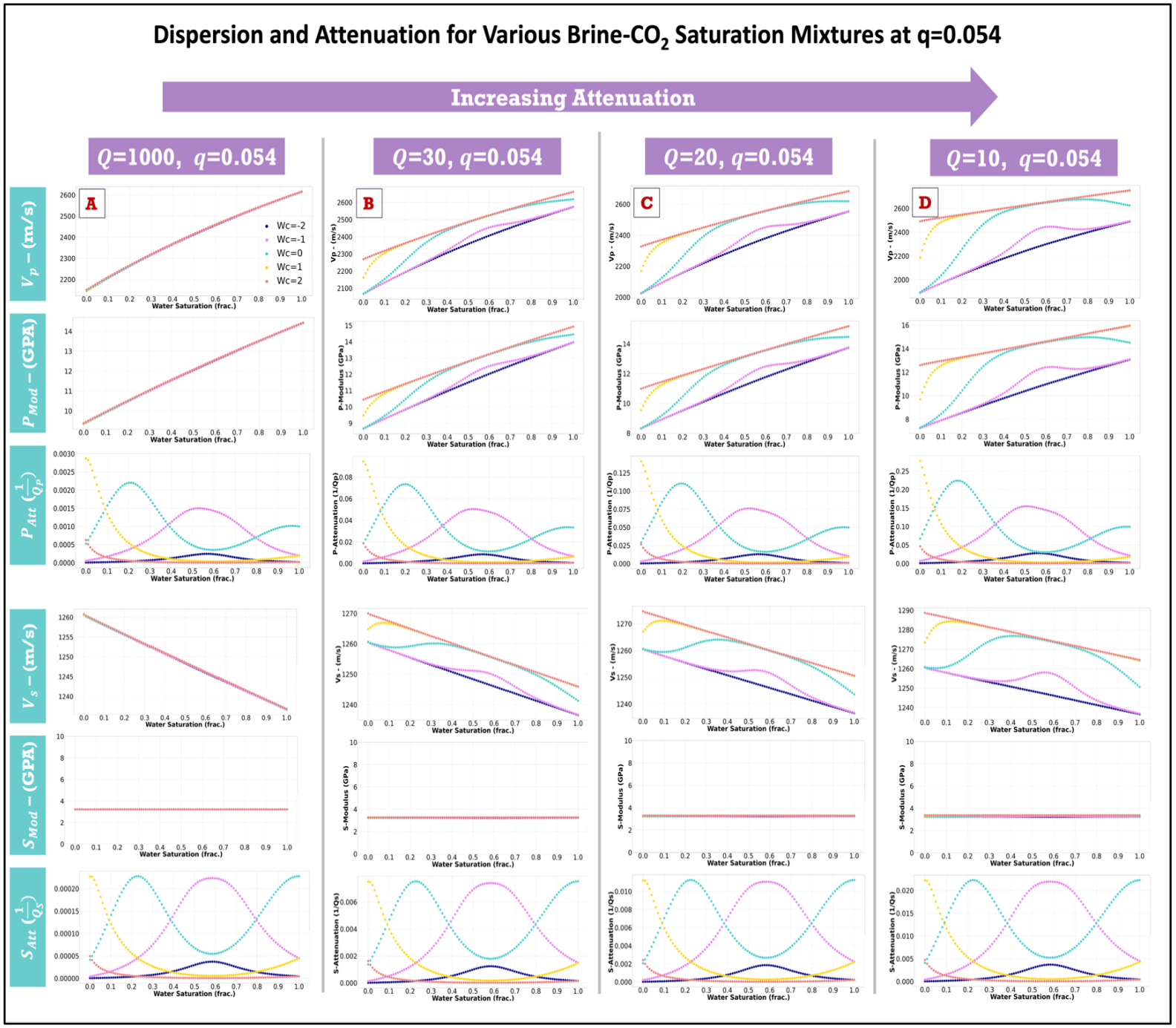


*Figure 4.21 – Saturation-dependent dispersive behavior illustrated by cross-plots of elastic attributes (V_p, V_s, P_{Mod}, S_{Mod}) and the associated attenuations (Q_p^{-1} and Q_s^{-1}) under higher capillary pressure (q_0=0.054) across different frequency regimes ($W_c \in \{-2, -1, 0, 1, 2\}$). Panels **(A-D)** show increasing attenuation (Q^{-1}, with $Q \in \{1000, 30, 20, 10\}$). Compared to the uniform pressure scenario (q=1; Figure (4.20)), increased capillary pressure stiffens elastic responses, notably reducing velocity dispersion and attenuation magnitudes at intermediate saturations.*

Building on the qualitative insights from the previous section, we now quantify the effects of squirt-flow dispersion on seismic attributes within the reservoir. These effects are presented as relative (%) and absolute differences referenced to the established baseline conditions (100%

brine, Q=1000, W_c = −2, at their respective q values). These baseline references effectively remove lithological and depth-related variability, isolating the impact of changing CO_2 saturation, capillary pressure, and attenuation across different frequency regimes. The results are systematically illustrated using Δ-histograms in Figures (4.22) - (4.24) and discussed accordingly.

Relative to the 100% brine reference at negligible attenuation, the compressional attributes (V_p and P_{Mod}) exhibit significant sensitivity to squirt-flow dispersion, collectively influenced by our key parameters, as shown in Figure 4.22 (A-F). Water saturation dictates the general softening direction: increasing CO_2 consistently decreases both V_p and P_{Mod}, increasing the delta differences at fixed q, Q, and W_c. At higher attenuation (Q=10), the dimensionless frequency index (W_c) then modulates the magnitude of elastic softening and dispersion. Specifically, in the relaxed state (Q=10, W_c = –2; panels (B) and (E)), elastic softening intensifies, resulting in pronounced reductions at intermediate to full CO_2 saturations ($\Delta V_p \approx$ –24 to –26 % and $\Delta P_{Mod} \approx$ – 43 to – 47%). In the dispersive state (W_c= 0), where attenuation and dispersion peak, this softening is partially reduced, ($\Delta V_p \approx$ –9 to –25 % and $\Delta P_{Mod} \approx$ – 17 to – 46%) at the same saturation ranges, reflecting partial stiffness recovery due to maximum dispersion effects. Progressing to the fully unrelaxed state (W_c= +2; panels (B) and (E)), the softening further diminishes resulting in even smaller reductions ($\Delta V_p \approx$ –3 to –4% and $\Delta P_{Mod} \approx$ – 8 to –10%), indicative of the stiffer compressional responses typical of this high frequency regime.

Introducing higher capillary pressure (q_0 = 0.054, Q=10), as shown in Figure 4.22 (C) and (F), partially mitigates the elastic losses, resulting in approximately 8–12% smaller reductions compared to the uniform pressure scenario (q=1; panels (B) and (E)) . Collectively, these observations illustrate the interaction between our key parameters in governing the reservoir's dispersive behavior.

On the other hand, the shear attributes (V_s and S_{Mod}), depicted in Figure 4.23 (A-D), exhibit relatively lower sensitivity to CO_2 fluid substitution and squirt-flow dispersion when compared to compressional attributes. Transitioning from Figure 4.23 (A) to (B), the observed ΔV_s trend demonstrates relatively small increases of approximately 2 – 4% , apparent at higher-frequency and higher attenuation conditions (W_c= 0 → +2, Q = 10). Similarly, transitioning from Figure 4.23 (D) to (E), the ΔS_{Mod} attribute displays comparable incremental increases ($\approx +4\%$). Increasing capillary pressure (q_0 = 0.054 at Q=10, W_c= 0 ; panels (C) and (F)) slightly increases the latter ΔV_s

and ΔS_{Mod} responses by approximately 1-2%, at intermediate saturations, compared to the uniform pressure scenario (q=1; panels (B) & (E)). These latter observations indicate that shear properties are primarily influenced by attenuation and dispersion effects, whereas variations in CO_2 saturation and capillary pressure exert relatively minor impacts on the reservoir's shear behavior.

Lastly, to quantify attenuation effects, Figure 4.24 (A–F) illustrates the absolute changes in P-wave (ΔQ_p^{-1}) and S-wave (ΔQ_s^{-1}) histograms, relative to their brine-saturated baselines. At relaxed, low-frequency baseline conditions (Q = 1000, W_c= –2, q=1), attenuation values are negligible for both $\Delta\ Q_p^{-1}$ (Figure 4.24 (A)) and $\Delta\ Q_s^{-1}$ (Figure 4.24 (D)), indicating that squirt flow is inactive at these conditions.

Under higher attenuation conditions (Q = 10), the ΔQ_p^{-1} *and* $\Delta\ Q_s^{-1}$ trends display a characteristic bell-shaped trend: attenuation is minimal in the relaxed state (W_c= –2), increases sharply in the dispersive state (W_c= 0), and decreases toward the unrelaxed regime (W_c = +2). Specifically, at uniform capillary pressure (q = 1), maximum attenuation occurs at the dispersive state (Q = 10, W_c = 0), with histograms peaking at approximately 2.2 × 10^{-1} for ΔQ_p^{-1} (Figure 4.24 (B)) and 2.1 × 10^{-2} for $\Delta\ Q_s^{-1}$ (Figure 4.24 (E)). This indicates that the magnitude of the S-wave attenuation is notably smaller, approximately an order of magnitude less than the noted P-wave attenuation.

Increasing capillary pressure to q_0 = 0.054 (Figure 4.24 (C) and (F)) leaves end-member saturations largely unaffected but significantly influences intermediate saturations. At brine-rich saturations (S_w = 1.0 – 0.6), higher capillary pressure stiffens both the rock frame and fluid, reducing fluid mobility and consequently attenuation relative to the uniform pressure scenario. Conversely, at higher CO_2 saturations ($S_w \leq 0.4$), the increased compressibility and mobility of CO_2 enhance fluid-induced attenuation, overriding the stiffening effect. Thus, intermediate saturations reflect a balance between capillary pressure induced stiffening and CO_2-driven fluid mobility, with a transition occurring around $S_w \approx 0.4$.

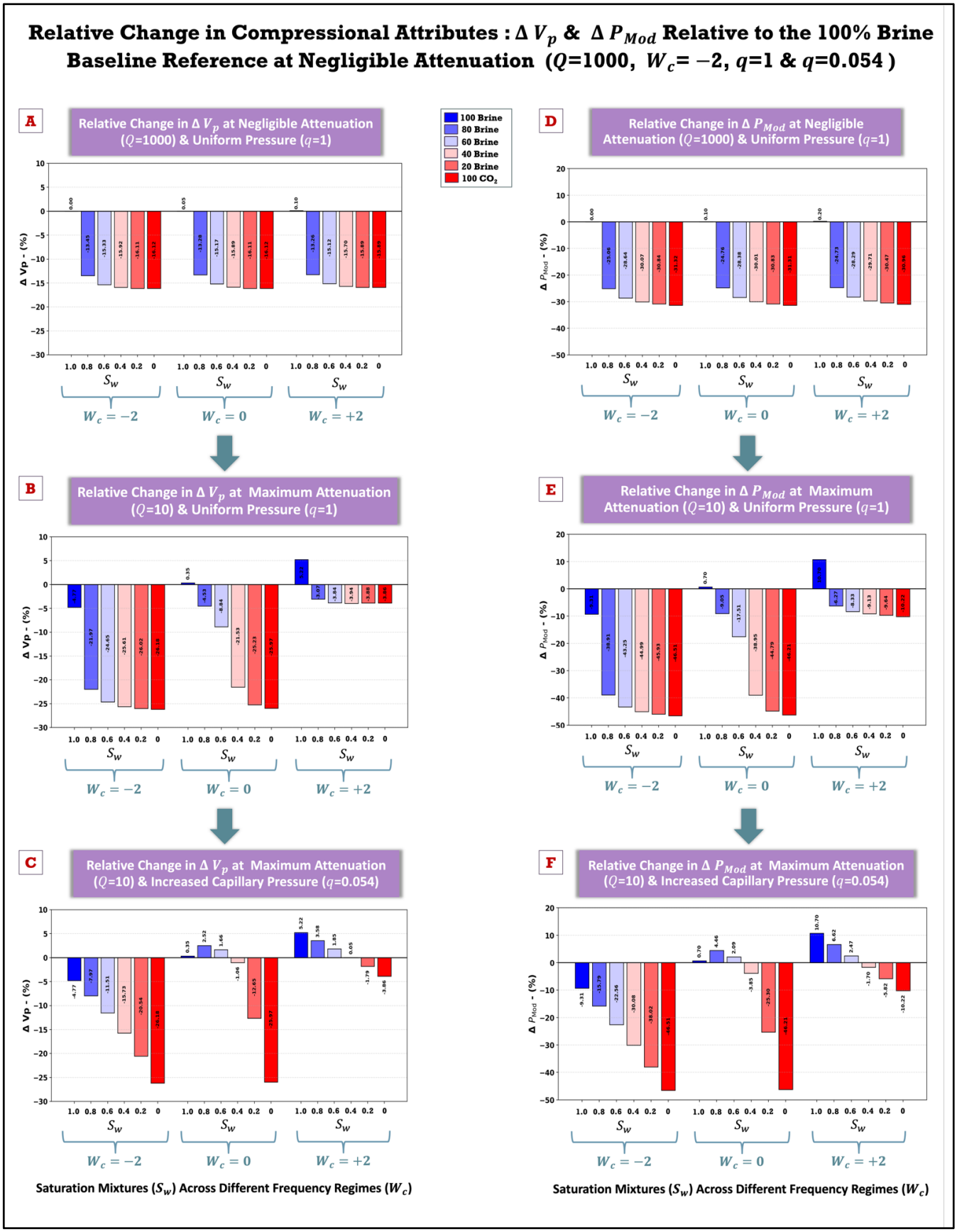


*Figure 4.22 – Relative changes (%) in compressional attributes (V_p and P_{Mod}) compared to the 100% brine baseline at negligible attenuation (Q = 1000, Wc = –2) across different frequency regimes. Panels **(A, D)** illustrate relative changes at uniform capillary pressure (q = 1) and negligible attenuation (Q = 1000), highlighting sensitivity to CO_2 saturation changes. Panels **(B, E)** display relative changes at uniform capillary pressure (q = 1) with maximum attenuation (Q = 10), emphasizing squirt-flow attenuation effects. Panels **(C, F)** demonstrate relative changes at increased capillary pressure (q_0 = 0.054) and maximum attenuation (Q = 10). These results demonstrate the sensitivity of compressional attributes to variations in CO_2 saturation, squirt-flow attenuation, and capillary pressure.*

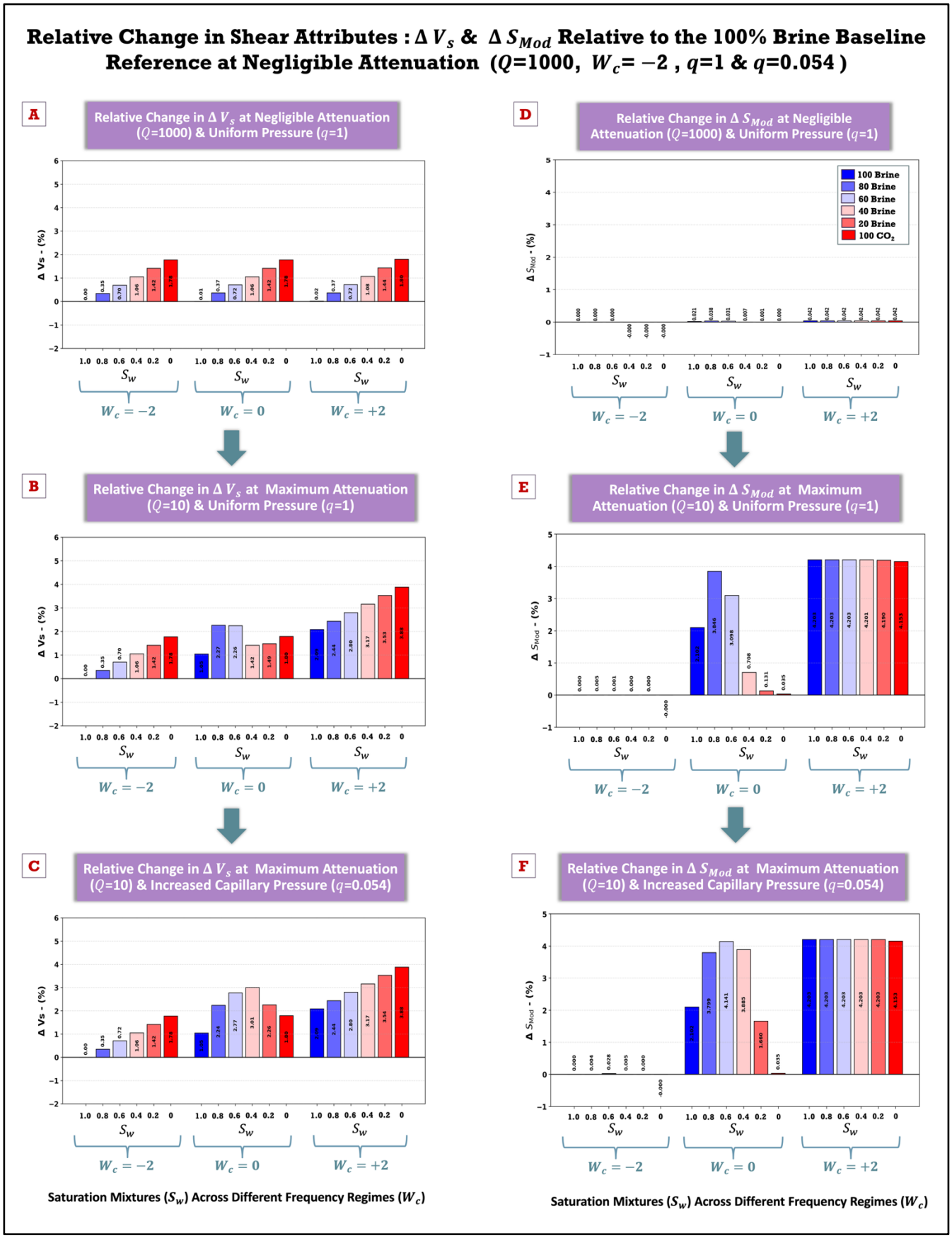


*Figure 4.23 – Relative changes (%) in the shear attributes (V_s and S_{Mod}) compared to the 100% brine baseline at negligible attenuation (Q = 1000, Wc = –2) across different frequency regimes. Panels **(A, D)** illustrate relative changes under uniform capillary pressure (q = 1) and negligible attenuation (Q = 1000). Panels **(B, E)** display relative changes at q=1 and maximum attenuation (Q=10). Panels **(C, F)** display relative changes at increased capillary pressure (q_0=0.054) and Q=10. These results demonstrate that shear attributes exhibit lower sensitivity towards variation in CO_2 saturations, squirt-flow dispersion and capillary pressure compared to the compressional attributes .*

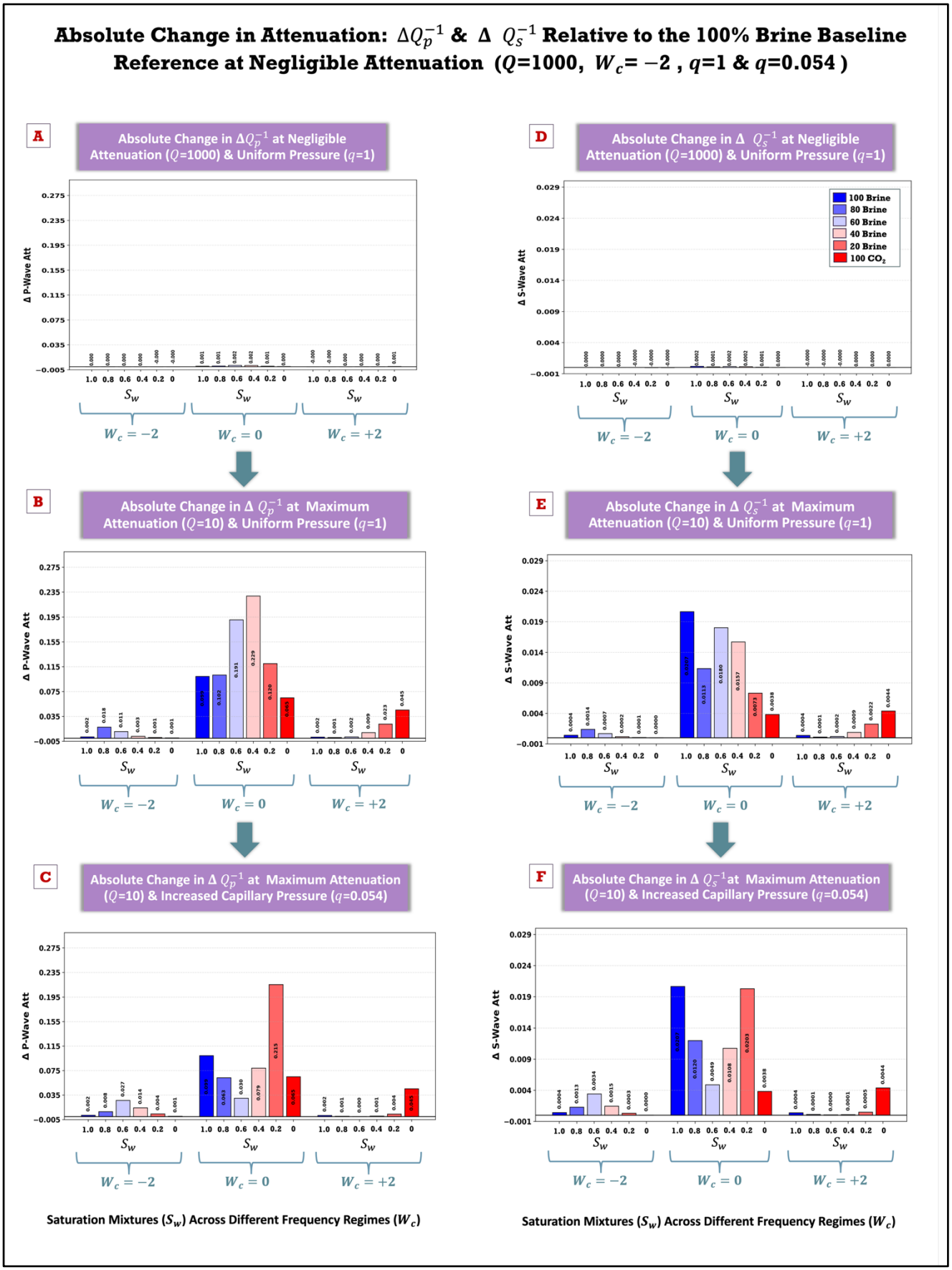


*Figure 4.24 – Absolute changes in the P- and S-wave attenuation curves (Q_p^{-1} and Q_s^{-1}) compared to the 100% brine baseline at negligible attenuation (Q = 1000, W_c= –2) across different frequency regimes. Panels **(A, D)** confirm that squirt flow is inactive at negligible attenuation (Q = 1000, q=1). Panels **(B, E)** illustrate increased attenuation (Q = 10 , q = 1) effects, showing pronounced bell-shaped peaks in the dispersive regime (W_c = 0). Panels **(C, F)** demonstrate that higher capillary pressure (q_0 = 0.054) at the same Q = 10) modifies attenuation, reducing magnitudes at intermediate saturations and enhancing them at high CO_2 saturations.*

The presented statistical analysis emphasizes the critical importance of incorporating squirt-flow dispersion and attenuation, and thus, the need for adopting the current frequency-dependent forward modelling approach. This necessity is evident given the sensitivity of compressional elastic attributes (V_p and P_{Mod}) to variations in CO_2 fluid substitution, dispersion, and attenuation. At intermediate to full CO_2 saturation and high attenuation (Q = 10), elastic responses reflected considerable variability between the fully relaxed and fully unrelaxed frequency states. Such substantial variations directly influence the seismic reflectivity and amplitude responses, emphasizing the risk of seismic misinterpretations if frequency-dependent dispersion is not explicitly accounted for during CO_2 reservoir characterization and seismic monitoring.

Building upon these observations, we proceed to investigate the influence of our governing parameters (S_w, q, Q^{-1}) on the frequency-dependent synthetic seismic gathers, specifically targeting the SFjord interface and the underlying dispersive layer. In Figure 4.25 (A-B), the frequency-dependent synthetics at negligible attenuation (Q=1000, W_c= –2 for q=1 and q_o= 0.054) display elastic trends and seismic variations consistent with those previously documented for the frequency-independent (Gassmann) cases in Chapter 3 (Figure 3.17(A-B)). Increasing CO_2 saturation progressively softens the compressional impedance, steepening the AVO gradient (Class III) and brightening the negative trough at the SFjord reflector. Additionally, increasing capillary pressure ($q_o \rightarrow$ 0.054) partially counteracts this softening effect at intermediate saturations (smaller $\Delta\ AI$ and ΔPR), producing flatter, lower-amplitude seismic responses, as similarly noted in Chapter 3. In contrast, the end-member fluid saturations (100% brine or CO_2) remain largely unaffected.

Panel C further highlights capillary effects by displaying an overlay comparison of the uniform pressure synthetics (q = 1) and their patchy counterparts (q_0= 0.054) at negligible attenuation (Q = 1000, W_c = –2). The amplitude difference observed between the overlaid gathers at the SFjord interface visually highlights the additional stiffening introduced by patchiness. At uniform capillary pressure (q = 1), the reservoir rock remains relatively softer than it does under higher capillary pressure conditions (q_0= 0.054), yielding larger impedance contrasts across the interface and thus, stronger amplitudes at intermediate brine saturations. As more CO_2 replaces brine, both capillary regimes progressively soften toward the same CO_2 end-member, steadily reducing the residual difference, which ultimately diminishes at 100% CO_2. The residual remains zero at full brine and CO_2 saturation, as single-fluid phase mixtures remain unaffected by differences in

capillary pressure. As a result, we see that in the absence of attenuation, capillary effects manifest as amplitude variations across the desired target with no visible phase shifts or squirt-flow-related dispersion effects.

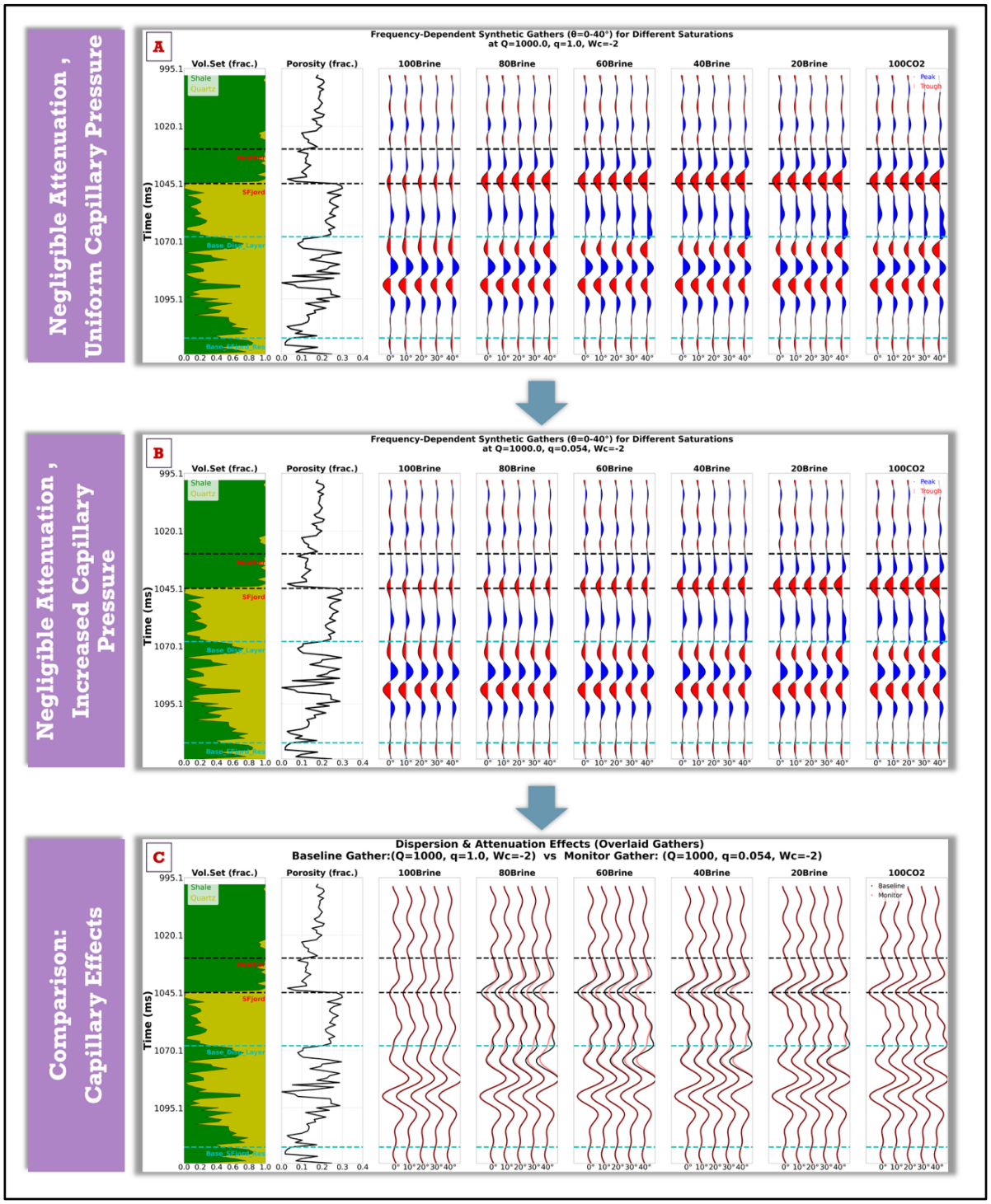


*Figure 4.25 – Frequency-dependent synthetic gathers illustrating sensitivity to capillary pressure variations at negligible attenuation (Q = 1000, W_c = –2.) **(A)** Uniform capillary pressure (q=1), displaying amplitude brightening with increasing CO_2 saturation. **(B)** Increased capillary pressure (q_0=0.054) reduces amplitude at intermediate saturations. **(C)** Overlay comparison between panels A and B. Panel C implies that in the absence of attenuation, capillary effects manifest in amplitude variations across the desired target with no visible phase shifts or squirt-flow-related dispersion effects.*

The subsequent synthetic example focuses on evaluating the additional frequency-dependent dispersive and attenuation effects that influence the synthetic seismic responses in the current modeling scenario. In Figure 4.26 (A-C), we compare frequency-dependent synthetic gathers generated under conditions of low attenuation (Q = 1000) versus high attenuation (Q = 10) for various saturation mixtures at uniform capillary pressure. This comparison specifically targets the dispersive state (W_c = 0), where velocity dispersion and attenuation effects are maximized. Panel (A) at negligible attenuation (Q = 1000), shows minimal evidence of velocity dispersion or amplitude alteration, while comparison with panel (B) clearly demonstrates that higher attenuation at Q = 10 affects the seismic amplitudes.

Panel C highlights these effects through an overlay comparison of baseline gathers (Q = 1000) and their high-attenuation counterparts (Q = 10), at q=1 and W_c= 0. The comparison reveals that there is an amplitude brightening, occurring at increased attenuation and higher CO_2 saturations at far offset angles. This brightening arises primarily from the increased elastic contrast between the highly dispersive, attenuative, CO_2-saturated reservoir and the elastic, brine-saturated overburden caprock. Panel (C) further demonstrates that attenuation amplifies amplitude variability, particularly at intermediate to full CO_2 saturation compared with the fully brine-saturated case. Such observations, therefore, highlight the sensitivity of CO_2-saturated reservoir rocks to frequency-dependent squirt-flow and attenuation effects.

Repeating this analysis at higher capillary pressure (q_0 = 0.054) in the dispersive state (W_c = 0) yields a different response. The increased capillary pressure stiffens the effective fluid mixture, which in turn increases the saturated bulk modulus, resulting in lower impedance contrast across the interface. As a result, this diminishes the amplitude brightening previously observed under uniform capillary pressure conditions (q = 1). Consequently, amplitude brightening becomes prominent only at full CO_2 saturation (100% CO_2), as depicted in Figure 4.27 (C).

Given the detailed analysis presented, it is clear that frequency-dependent dispersion and attenuation arising from squirt-flow mechanisms are visible at both log and seismic scales. Figures (4.25) – (4.27) illustrate these squirt-flow-related phenomena, primarily manifested as amplitude variations and subtle phase shifts. Specifically, under conditions of high attenuation, progressive amplitude brightening is evident at the primary CO_2 reflector (SFjord Top), accompanied by complementary amplitude dimming and phase delays at the base of the underlying dispersive layer. Close inspection of the seismic panels further reveals subtle wavelet broadening, consistent with

frequency-dependent attenuation in the dispersive frequency state. Collectively, these seismic signatures become prominent at partial to full CO_2 saturations, emphasizing the necessity of incorporating squirt-flow mechanisms into rock physics forward modelling workflows for reliable CO_2 reservoir characterization.

Nevertheless, accurate quantification of these amplitude variations and subtle phase shifts remains challenging in realistic multi-layer reservoir scenarios. Unlike idealized single-layer reservoir models, where isolated reflections enable clear and direct quantification, the multi-layered Sognefjord reservoir inherently introduces complex interference effects. Intra-formational shale stringers within the reservoir's matrix generates thin bed tuning, while frequency-dependent squirt-flow produces dispersion (phase shifts) and attenuation (wavelet broadening and amplitude redistribution). At far offsets, these lithological and frequency-dependent effects overlap, causing reflections from closely spaced geological layers to interfere and smear amplitudes, which complicates conventional techniques used to quantify these amplitude variations and phase shifts. Such complications are well discussed in CO_2-related literature, with seismic studies from multi-layered reservoirs, such as Sleipner and Snøhvit fields, consistently reporting interference-induced ambiguities in amplitude and phase interpretations (Izadian, 2024; White et al., 2018; Williams & Chadwick, 2012). To mitigate these complexities, established workflows commonly integrate rock physics modeling, spectral decomposition, and seismic inversion techniques to improve the interpretability of CO_2-induced seismic signatures.

In line with these established methodologies, this thesis therefore addresses the limitations posed by interference effects through the integration of a supervised machine-learning inversion component, as detailed in Chapter 5. Specifically, the developed ML model is trained on a comprehensive synthetic catalogue, systematically varying fluid saturation, capillary pressure, and attenuation, capturing the associated CO_2-induced seismic signatures, including amplitude variations, subtle phase shifts, and frequency-dependent wavelet shape changes across multiple frequency regimes. Consequently, the employed machine-learning approach is designed to handle the complex interference patterns and overlapping seismic signatures that traditional manual methods find challenging to resolve, supporting more reliable seismic reservoir characterization despite the complexities associated with multi-layer interference.

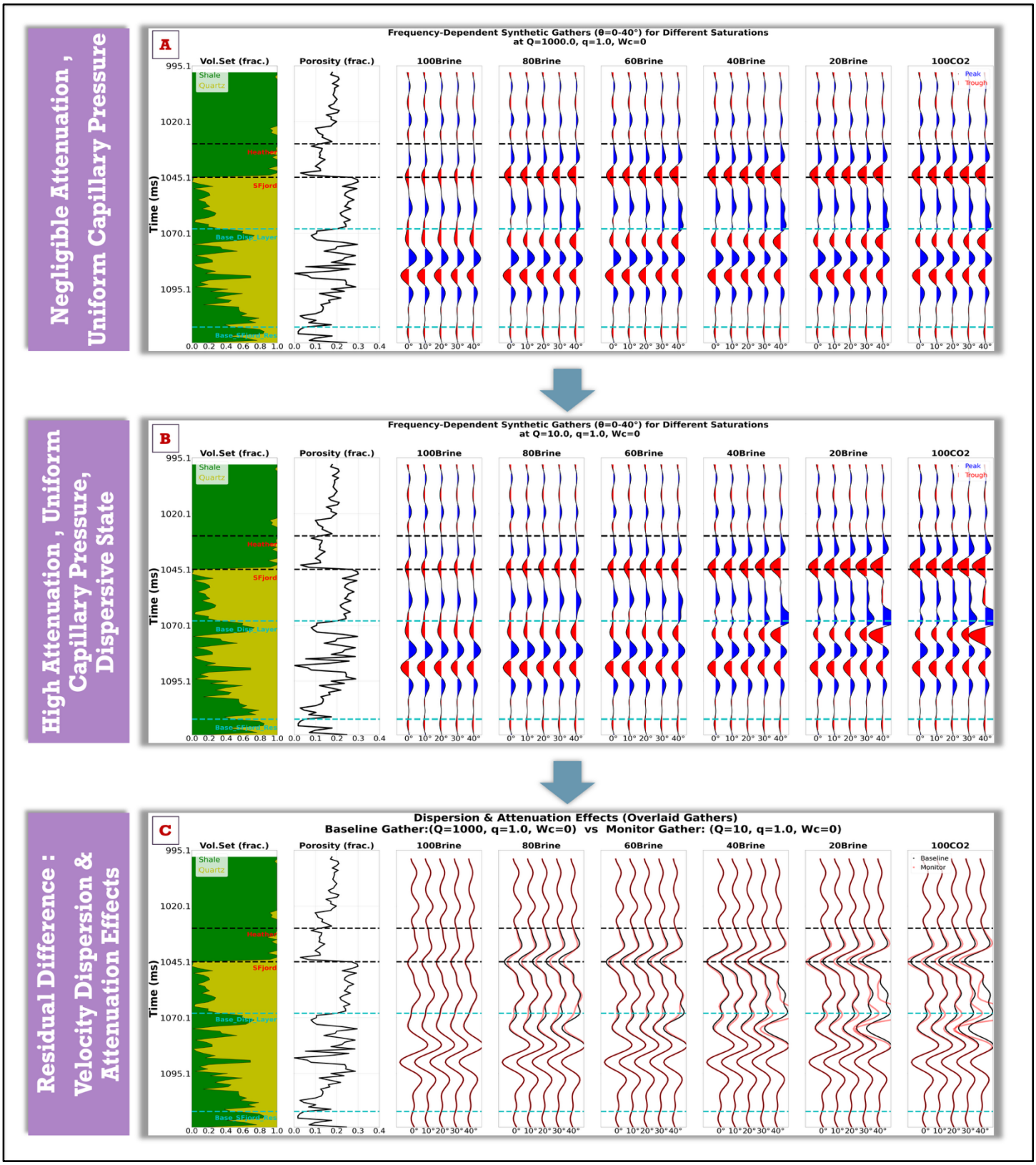


Figure 4.26 – Frequency-dependent synthetic gathers illustrating attenuation effects on seismic amplitudes. ***(A)*** *Negligible attenuation (Q = 1000) at uniform capillary pressure (q = 1) shows minimal amplitude variations across CO_2 saturations.* ***(B)*** *High attenuation (Q = 10, q=1) at dispersive state (W_c = 0) results in pronounced amplitude brightening, especially at intermediate to full CO_2 saturations.* ***(C)*** *Overlay comparison highlighting amplitude variability driven by increased attenuation.*

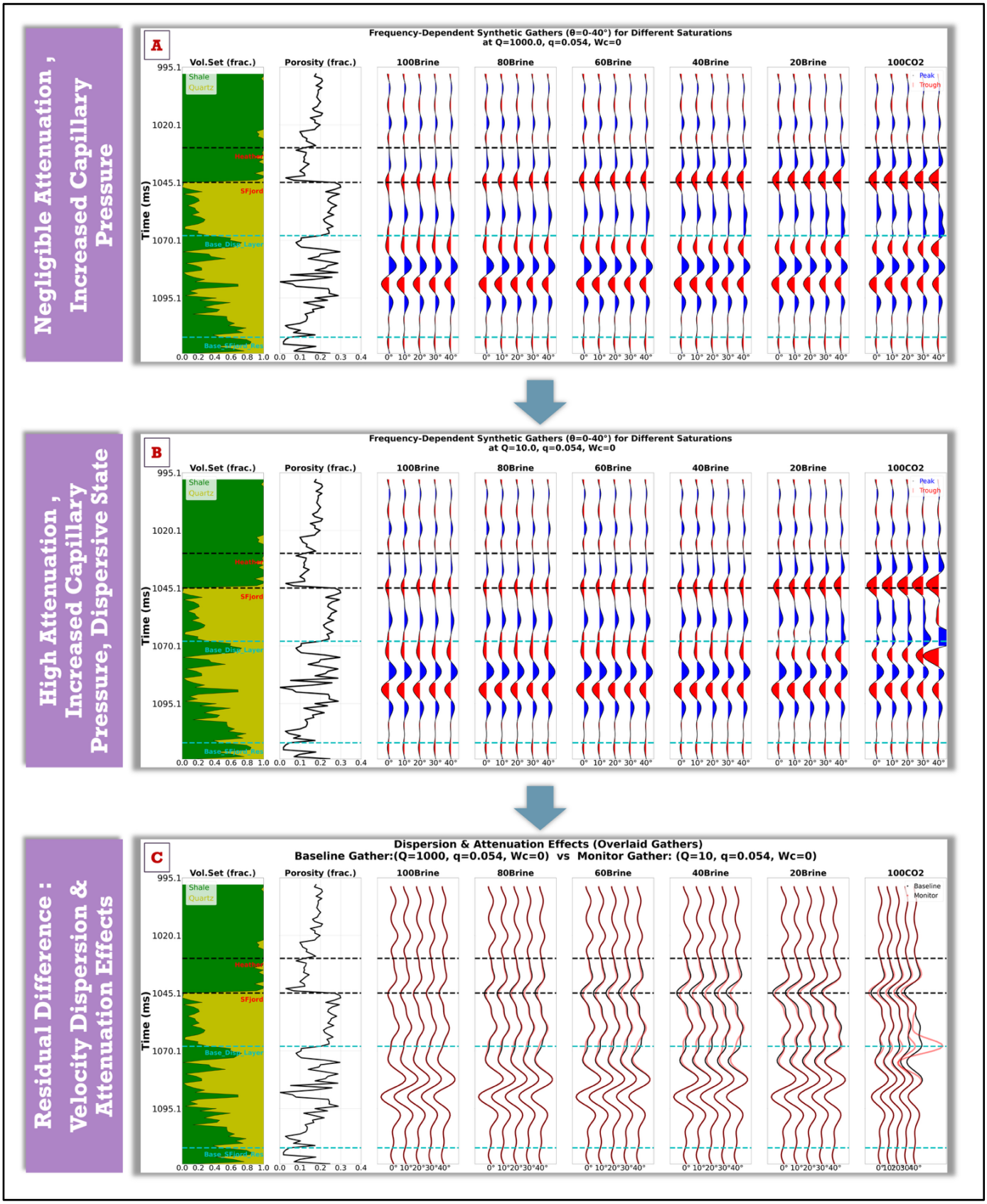


Figure 4.27 – Frequency-dependent synthetic gathers illustrating the combined effects of higher capillary pressure and attenuation. ***(A)*** *Increased capillary pressure (q_0=0.054) at negligible attenuation (Q =1000) significantly reduces amplitude variability across CO_2 saturations.* ***(B)*** *High attenuation (Q =10) in the dispersive state (W_c=0) limits amplitude brightening primarily to full CO_2 saturation.* ***(C)*** *Overlay comparison highlights how elevated capillary pressure reduces amplitude brightening, at intermediate saturations, due to increased rock/fluid stiffness.*

Following our analysis of the frequency-dependent synthetics, we transition into time-frequency analysis to examine spectral amplitude variations as a function of CO_2 saturation, capillary pressure, and attenuation. Figure 4.28 (A-C) presents the unbalanced time-frequency responses extracted at the SFjord interface with increasing CO_2 saturations and offset angles under progressively more dispersive and higher capillary pressure conditions.

Panel (A) displays the elastic baseline reference scenario at negligible attenuation (Q = 1000, q = 1, W_c = 0), depicting a relatively weak spectral lobe broadly distributed around the 50 Hz Ricker band. With increasing CO_2 saturation, we see a slight increase in the spectral energy that becomes more gradually apparent at the far-offset angles (40°) due to the modest impedance contrast across the interface.

Transitioning to panel (B) (Q = 10, q = 1, W_c = 0), increased attenuation reshapes the spectral energy distribution, clearly narrowing the amplitude spectrum. Specifically, the high-frequency components (≥60 Hz) experience notable attenuation, resulting in spectral amplitudes becoming more concentrated within the intermediate to low frequency range (10–40 Hz). This attenuation-driven energy redistribution leads to pronounced low-frequency amplitude brightening at larger incidence angles (40°) with increasing CO_2 saturation, clearly highlighting the angle-dependent fluid sensitivity. As a result, CO_2-rich mixtures exhibit enhanced low-frequency amplitudes, whereas brine-rich mixtures remain comparatively muted, displaying dimmer spectral responses under higher attenuation conditions.

It is important to note the presence of high-frequency (60-90 Hz) spectral peaks, observed in panel (B) particularly at larger offsets and higher CO_2 saturations, that mask the squirt-flow attenuation effects described earlier. In particular, these observed high-frequency spectral peaks primarily result from the interference effects previously noted, rather than indicating enhanced CO_2-related fluid sensitivity within this higher frequency band. Such spectral behavior has been similarly observed at Sleipner and Snøhvit fields, highlighting the presence of such high-frequency spectral components due to thin-bed tuning and interference within the injected CO_2 plumes (White et al., 2015; Williams & Chadwick, 2012).

Figure 4.28 (C) maintains high attenuation conditions (Q = 10) while introducing elevated capillary pressure (q_0= 0.054). The increased capillary forces stiffen the rock frame at intermediate saturations, consequently moderating the influence of squirt-flow dispersion previously observed in panel (B), slightly dimming the overall spectral amplitudes at those particular saturation ranges.

Nonetheless, the angle-dependent low-frequency amplitude brightening persists, especially at higher CO_2 saturations, demonstrating that capillary pressure reduces, but does not entirely suppress, the characteristic fluid-sensitive spectral response identified under uniform capillary pressure conditions. Hence, these findings offer valuable insights into how squirt-flow mechanisms influence frequency-dependent seismic amplitudes in partially saturated reservoirs, highlighting the relevance of the squirt-flow modeling framework adopted in this thesis.

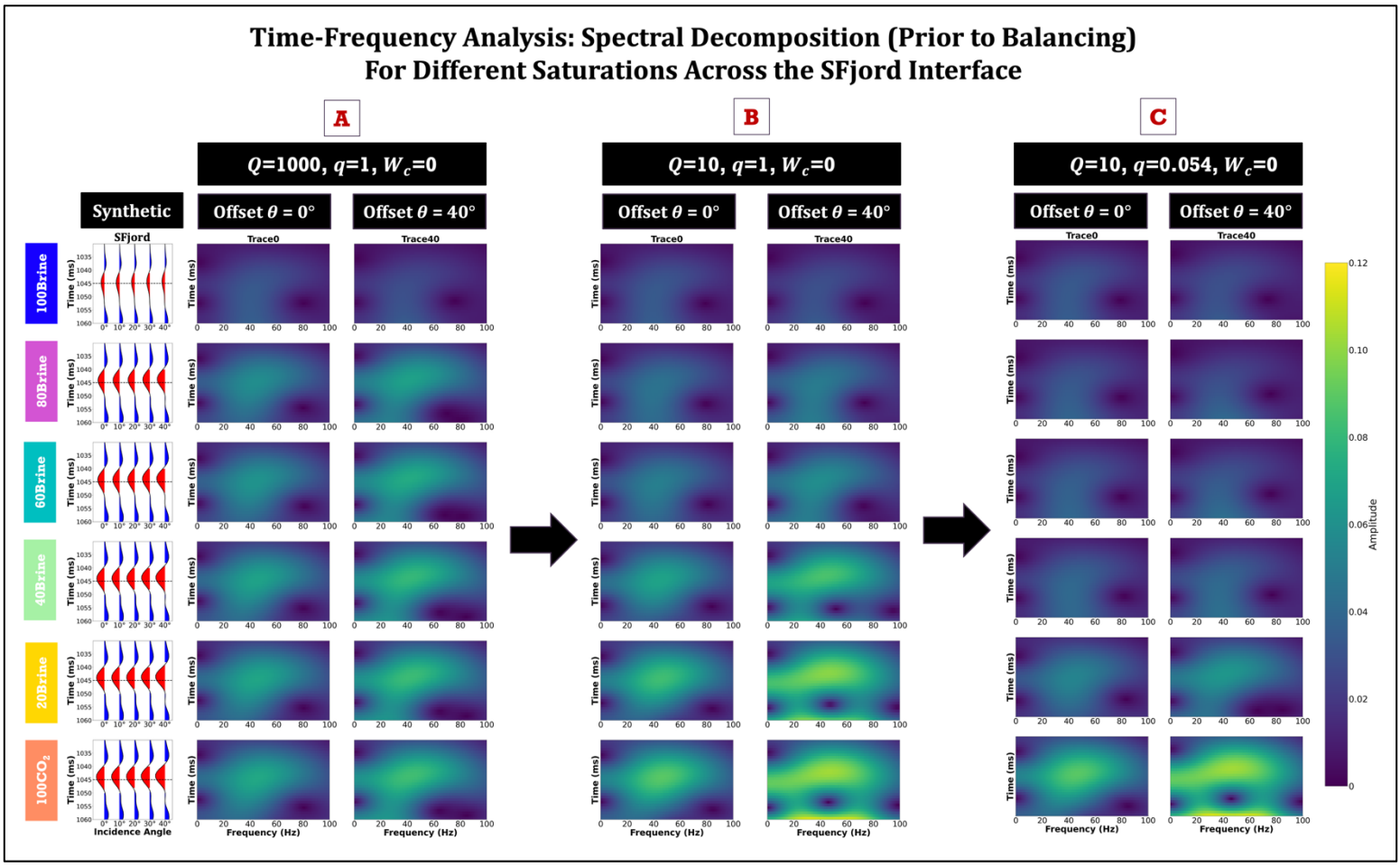


Figure 4.28 – Spectral amplitude variations across the SFjord reflector (prior to spectral balancing) for different saturations, capillary pressure and attenuation scenarios. ***(A)*** *Baseline scenario with negligible attenuation (Q=1000, q=1, W_c=0), showing slight amplitude increase at higher CO_2 saturations and far offsets (40°).* ***(B)*** *Attenuative, uniform capillary pressure scenario (Q =10, q =1, W_c=0), demonstrates pronounced angle-dependent low-frequency brightening with increasing CO_2 saturation.* ***(C)*** *High attenuation with increased capillary pressure (Q =10, q_0=0.054, W_c=0), showing moderated spectral amplitudes at intermediate saturations, yet maintaining angle-dependent brightening at higher CO_2 saturations.*

Having established a comprehensive understanding of the spectral behavior across the attenuative interface and within the underlying dispersive layer, we now focus on the spectrally balanced amplitude spectra extracted specifically at the primary SFjord reflector. By applying the

offset-specific normalization method described in Section (4.4.7), we remove the influence of the source wavelet, isolating the true reflectivity response and reducing wavelet-induced bias in the AVO amplitudes extracted at the target interface. Consequently, the resulting balanced amplitude spectra (Figure 4.29 (A-B)) illustrate the frequency-dependent signatures associated with variations in CO_2 saturation, capillary pressure and attenuation.

Collectively, the balanced spectra in Figure 4.29 (A–C) reinforce our three primary observations: (i) frequency-dependent attenuation redistributes energy towards lower frequencies, resulting in distinct CO_2-induced low-frequency amplitude brightening (≤ 20 Hz); (ii) interference effects locally enhance amplitudes within specific high-frequency bands (60–90 Hz), partially masking the underlying squirt-flow attenuation effect, as clearly indicated by the prominent high-frequency peaks (yellow peaks) consistently evident across panels (A–C); and (iii) angle-dependent fluid sensitivity intensifies systematically with increasing CO_2 saturation. Consequently, the characteristic low-frequency brightening associated with higher CO_2 saturation remains clearly evident and becomes progressively more pronounced as attenuation increases. Hence, the spectral complexities observed in Figure 4.29 (A–C), arising from interference-related effects, reinforce the value of integrating a supervised machine-learning approach to mitigate these challenges.

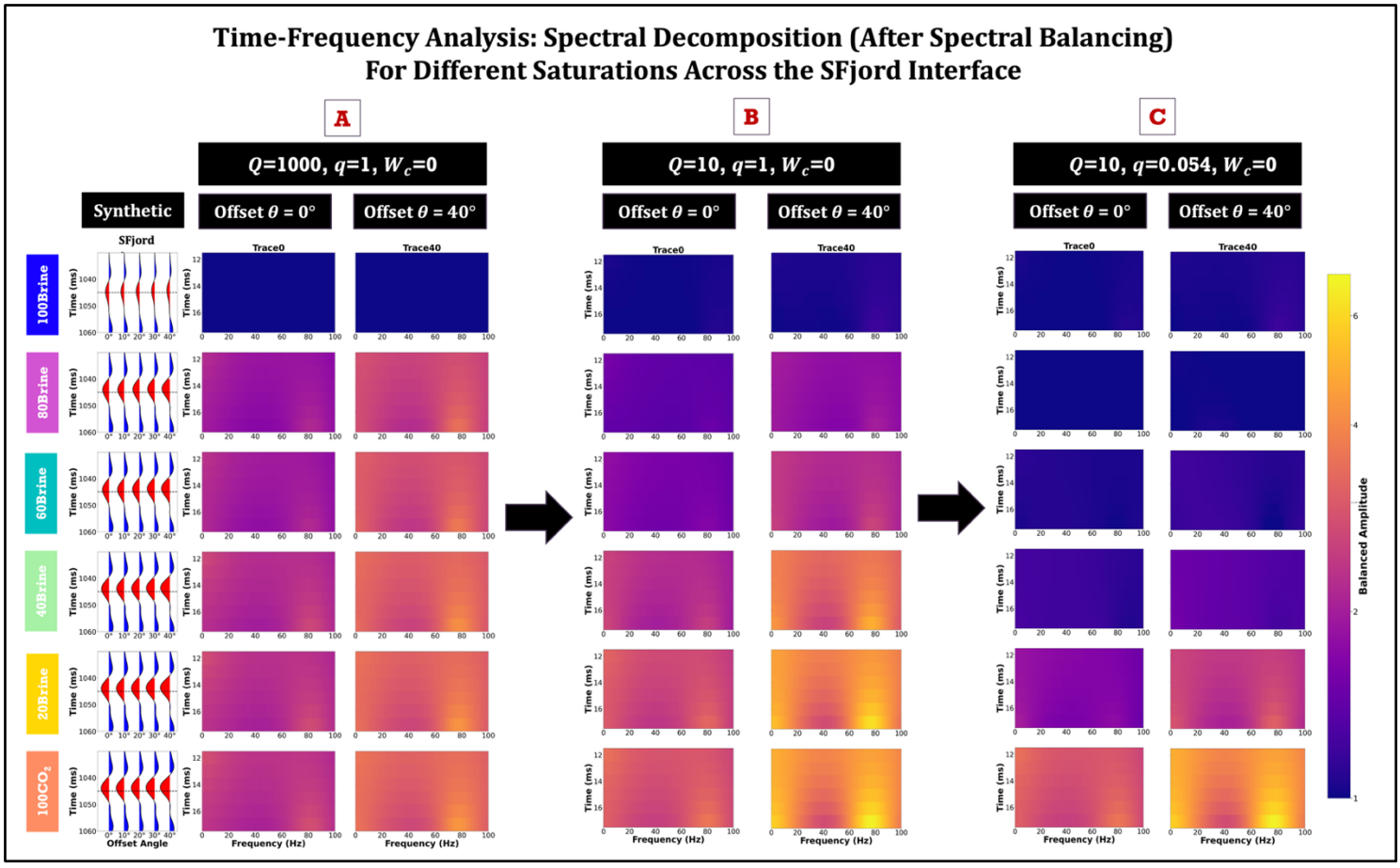


Figure 4.29 – Spectrally balanced frequency-dependent amplitudes across the SFjord reflector. ***(A)*** *Baseline scenario (Q = 1000, q = 1, W_c = 0) exhibits subtle amplitude variations with minimal offset-dependent changes.* ***(B)*** *Attenuative, uniform capillary pressure scenario (Q = 10, q = 1, W_c= 0) significantly enhances low-frequency brightening (≤20 Hz), especially at higher offsets (40°).* ***(C)*** *Attenuative, higher capillary pressure scenario (Q = 10, q_0=0.054, W_c = 0) moderates amplitude responses at intermediate saturations while maintaining clear angle-dependent sensitivity at higher CO_2 saturations.*

The iso-frequency AVO cross-plots presented in Figure 4.30 (A–B) further reinforce and expand the preceding spectral analyses. These figures illustrate balanced spectral amplitudes plotted against offset angles for discrete frequency slices ranging from 5 Hz to 90 Hz, extracted at the SFjord reflector and normalized relative to the 100% brine scenario. Consistently across all frequency subplots, balanced spectral amplitudes systematically increase with rising CO_2 saturation, displaying stronger reflectivity and steeper AVO gradients at larger offset angles (angle-dependent fluid sensitivity), characterized by a Class III AVO response. Given that the reflectivity is now represented by spectral amplitude magnitudes, these Class III AVO responses naturally plot entirely within the positive quadrant, contrary to the typically negative domain representation adopted in conventional AVO analysis. At 100% brine saturation, the normalized amplitude remains consistently at unity across all offsets, exhibiting a flat AVO gradient.

At negligible attenuation (Q = 1000 , Figure 4.30 (A)), the reflectivity and associated AVO gradients exhibit minimal frequency-dependent variations, with little distinction between varying CO_2 saturation responses. As attenuation increases (Q = 10 ; Figure 4.30 (B)), however, we observe pronounced low-frequency brightening, notably amplifying the absolute amplitude intercept terms at lower frequencies (5–20 Hz). This low-frequency brightening confirms the attenuation-induced energy redistribution, resulting in steeper AVO gradients at higher CO_2 saturations and larger offsets, particularly evident below 20 Hz. On the contrary, intermediate saturations (60–80% brine mixtures) exhibit relatively subdued reflectivity and flatter gradients compared to the CO_2-rich mixtures, while the 100% brine baseline maintains a flat AVO gradient across the entire frequency spectrum. Consequently, these findings suggest that CO_2 fluid discrimination is particularly effective in the low-frequency band (≤ 20 Hz) at larger incidence angles (30°– 40°) , where differentiation of CO_2-rich mixtures (≤ 40 % brine, ≥ 60 % CO_2) appears most pronounced. These results highlight the notable angle-dependent fluid sensitivity enhanced by increased attenuation.

Although conventional responses at 50 Hz (Chapter 3, Figure 3.17 (A-B)) already illustrate a consistent Class III AVO trend across the saturation range, the current multi-frequency analysis exposes a far richer spectrum of offsets and frequencies where the CO_2 signature is enhanced, potentially improving CO_2 fluid discrimination for seismic monitoring

purposes. Specifically examining Figure 4.30 (A), we observe that the conventional elastic AVO responses modelled at 50 Hz yield relatively modest fluid-related AVO variations, as it inherently neglects attenuation and frequency-dependent dispersion effects. In contrast, introducing higher attenuation (Q = 10, Figure 4.30 (B)) distinctly increases the intercept reflectivity and steepens the AVO gradients, amplifying amplitude separation at larger offsets and lower frequencies. Consequently, this comparison indicates that neglecting squirt-flow-induced attenuation can result in an underestimation of amplitude variations associated with CO_2 saturation in frequency-dependent AVO analysis.

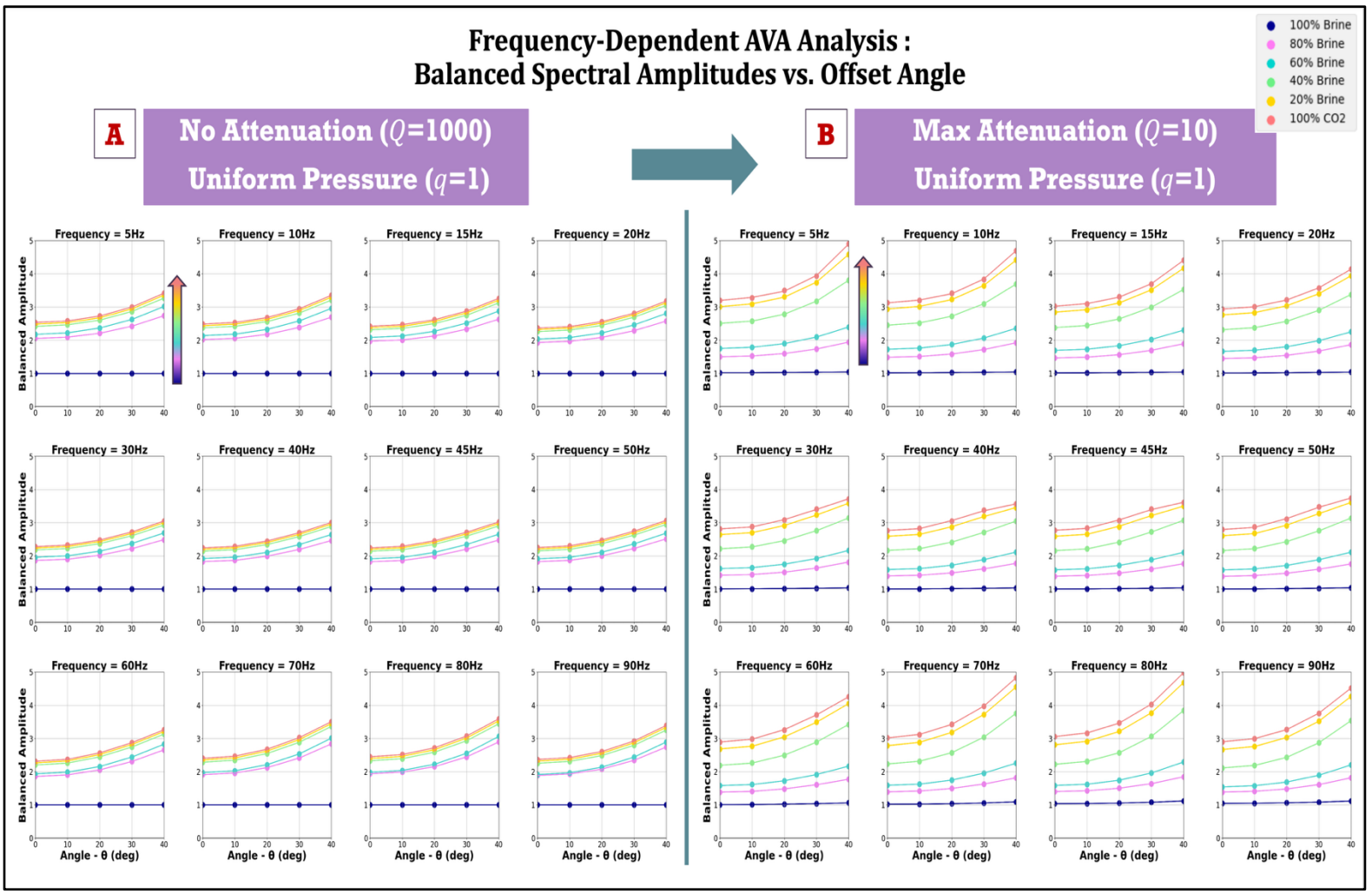


*Figure 4.30 – Frequency-dependent AVA (FAVA) analysis illustrating balanced spectral amplitudes versus offset angle across selected iso-frequencies (5–90 Hz). **(A)** Negligible attenuation scenario (Q = 1000, q=1) showing modest, frequency-consistent amplitude increase with angle across the full 5–90 Hz band, closely resembling conventional elastic AVO responses. **(B)** Increased attenuation scenario (Q = 10, q=1), highlighting pronounced low-frequency (≤ 20 Hz) amplitude brightening and steeper angle-dependent gradients, potentially improving CO_2–brine discrimination at far offsets.*

Examining the effects of increased capillary pressure (q_0 = 0.054) in Figure 4.31 (A-B), we observe that the low-frequency amplitude brightening, and angle-dependent offset amplification remain apparent, but with notably reduced magnitudes. Consequently, the spectral amplitudes exhibit smaller reflectivity and flatter AVO gradients compared to uniform capillary pressure (q = 1). This observation confirms that elevated capillary pressures moderate the squirt-flow-induced attenuation and dispersion effects, yet the fundamental fluid sensitivity and associated spectral signatures remain clearly preserved.

Lastly, the previously identified interference effects remain distinctly visible within the iso-frequency AVO slices across both capillary pressure scenarios (q=1 and q_0=0.054), particularly as attenuation increases to Q=10 (Figures 4.30 (B) and 4.31 (B)). Specifically, interference manifests as amplitude brightening within the high-frequency band (60–90 Hz), marked by increased intercept reflectivity and steeper AVO gradients. These interference-driven features closely resemble the genuine Class III AVO responses observed at lower frequencies (≤ 20 Hz), which are directly attributed to CO_2 saturation changes. Therefore, careful differentiation of interference-driven anomalies from true CO_2-related signatures becomes critical to avoid misinterpretation during the seismic reservoir characterization phase.

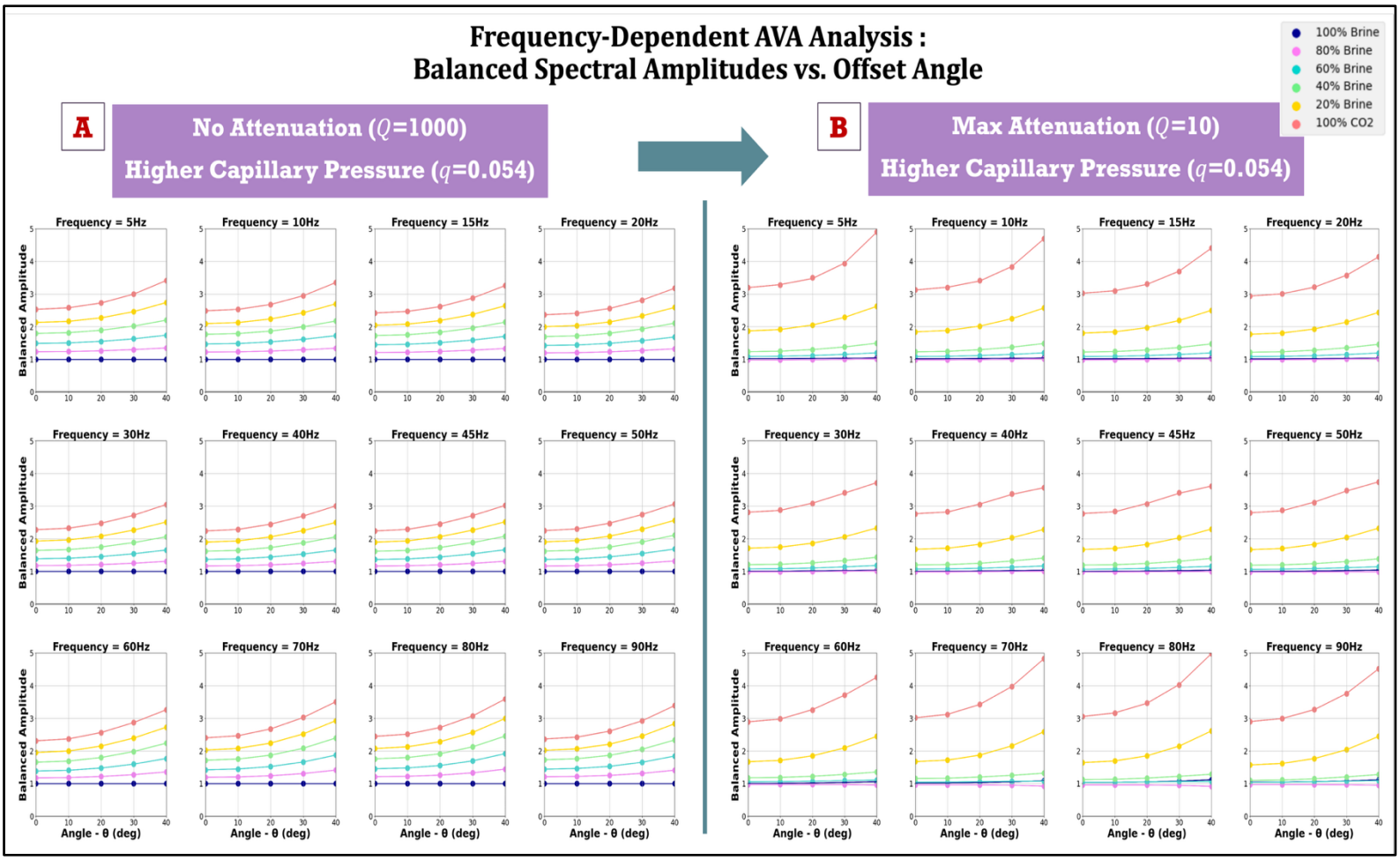


Figure 4.31 – Frequency-dependent AVA (FAVA) analysis illustrating balanced spectral amplitudes versus offset angle across selected iso-frequencies (5–90 Hz). ***(A)*** *Negligible attenuation (Q=1000) at increased capillary pressure (q_0 = 0.054) stiffens the rock frame, slightly reducing amplitude gradients relative to uniform-pressure scenarios.* ***(B)*** *At maximum attenuation (Q=10, q_0 = 0.054): energy redistributes toward lower frequencies (≤20 Hz), enhancing amplitude and angle-dependent gradients; however, elevated capillary pressure reduces this effect, moderating but not eliminating CO_2 sensitivity.*

While individual iso-frequency AVO slices offer valuable insights, clearly visualizing simultaneous amplitude variations across frequency and offset remains challenging. To address this, we introduce a comprehensive frequency-dependent AVO (FAVO) template (Figures (4.32) and (4.33)) that illustrates spectrally balanced amplitudes across a continuous frequency spectrum and offset range. This integrated representation captures key observed trends, including low-frequency amplitude brightening, angle-dependent amplitude steepening, and enhanced fluid sensitivity at higher CO_2 saturations. Additionally, the template highlights how attenuation reshapes amplitude responses, evolving from relatively flat surfaces under negligible attenuation (Q=1000) to more pronounced frequency- and angle-dependent amplitude ridges at higher attenuation levels (Q=10), where this curvature is particularly noticeable at lower frequencies (≤ 20 Hz) and larger offsets (30°–40°), highlighting dispersion and attenuation effects (Figure 4.32 (A)). This template further demonstrates that under elevated capillary pressure conditions (Figure 4.32 (B)), these effects are notably moderated, resulting in flatter AVO gradients and generally lower amplitude magnitudes, although the underlying frequency- and angle-dependent trends remain evident.

Thus, the primary advantage of this frequency-dependent template is its ability in simultaneously capturing the combined effects of CO_2 saturation, capillary pressure, and attenuation providing insight that is difficult to access using conventional single-frequency modelling (as shown previously in Figure 3.17 (A-B)). By integrating these factors into a unified framework, this template assists in identifying suitable frequency-angle combinations or cut-offs for effective fluid discrimination, especially within the lower-frequency (≤ 20 Hz) and larger-offset (≥ 30°) ranges relevant to our SFjord reservoir scenario. Consequently, this template can serve as a potential diagnostic tool guiding seismic acquisition design, frequency-selective processing, and scenario-based reservoir simulations, feasibly improving CO_2 reservoir characterization and seismic monitoring precision.

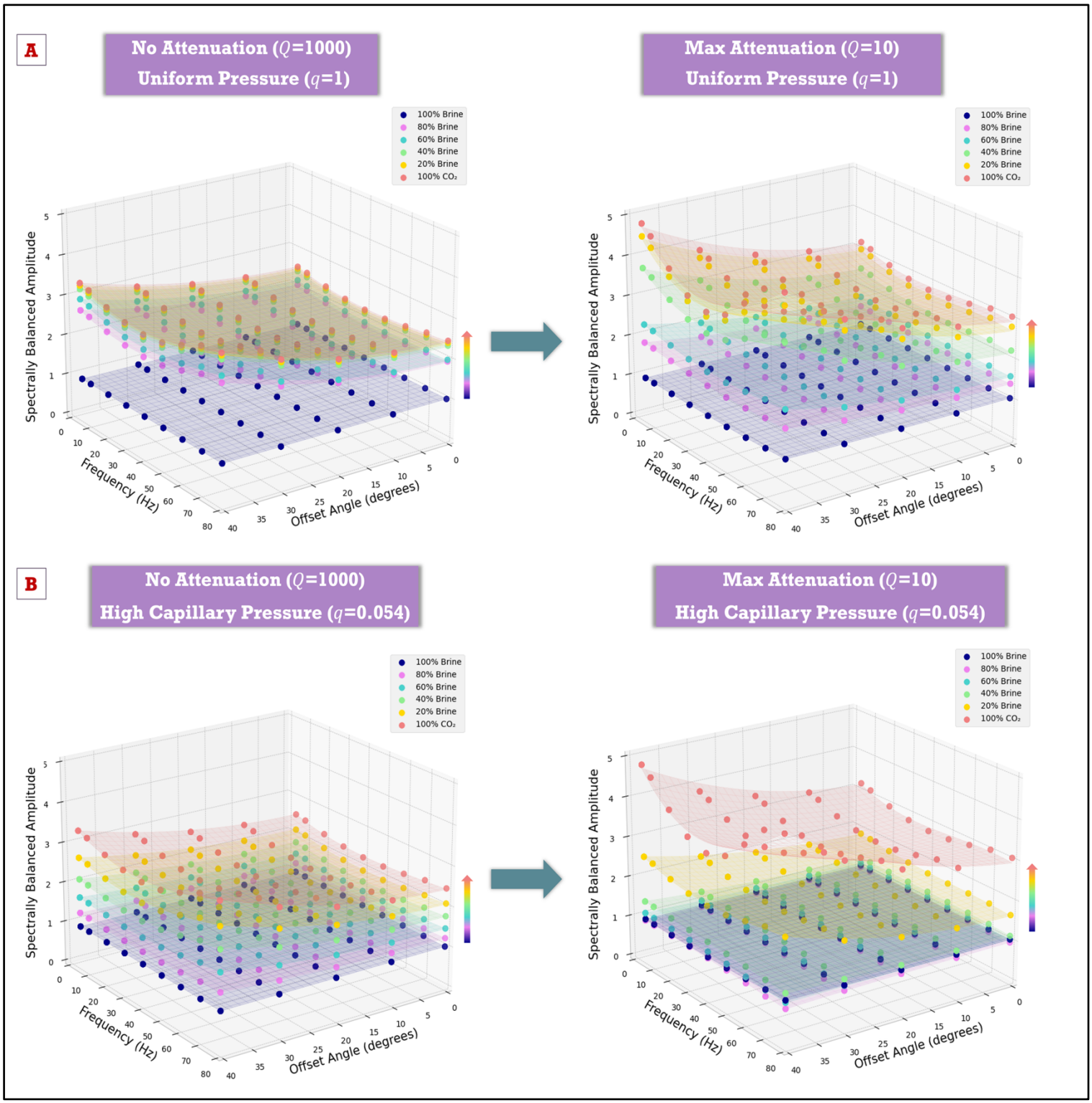


Figure 4.32 – Frequency-dependent Rock Physics AVO (FAVA) templates illustrating spectrally balanced amplitudes versus frequency and offset angle at the SFjord reflector. (A) At uniform capillary pressure (q=1), negligible attenuation (Q=1000) exhibits gentle, frequency-independent amplitude trends, whereas maximum attenuation (Q =10) notably enhances low-frequency amplitudes and steepens gradients, amplifying CO_2 sensitivity. (B) Higher capillary pressure (q_0=0.054) moderates the amplitude trends and reduces attenuation-driven low-frequency brightening, while preserving the angle-dependent fluid sensitivity.

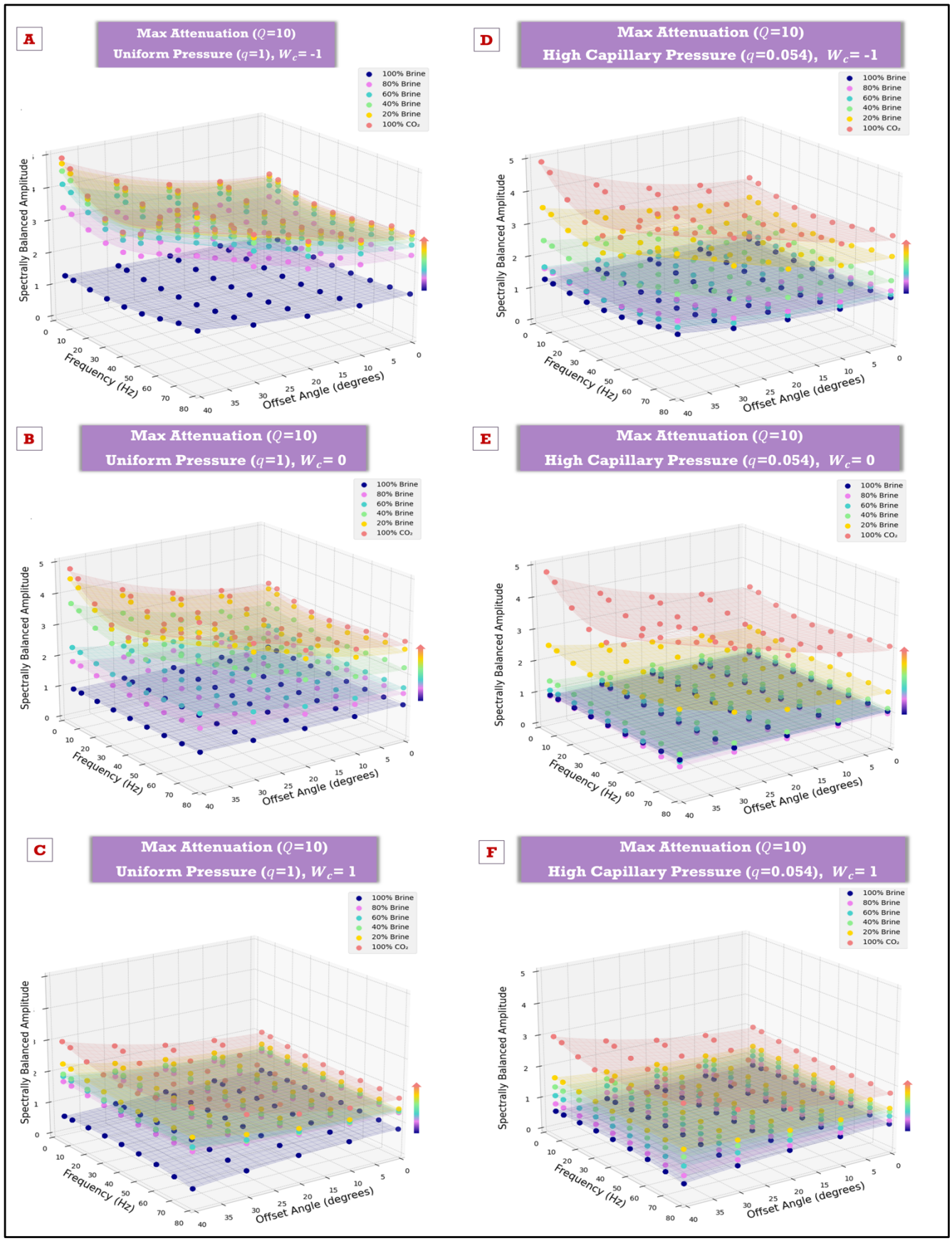


*Figure 4.33 – Frequency-Dependent AVA templates: spectrally balanced amplitude versus frequency and offset, illustrating how the amplitude response extracted at the SFjord interface, evolves across the entire frequency spectrum and offset ranges, as a function of CO_2 saturation at high attenuation (Q = 10), spanning the different frequency states (relaxed (W_c = -1), dispersive (W_c = 0), unrelaxed (W_c = +1). **(A–C)** Displays FAVA templates at uniform pressure under high-attenuation. **(D–F)** repeat the sequence for higher capillary pressure (q_0= 0.054) at the same attenuation. The colored fitted surfaces serve purely as a visual aid, highlighting how the amplitude response evolves across the template simulating different reservoir scenarios .*

4.5.2 Deep Learning : 2D CNN

In this section, we evaluate the predictive capability and performance of the 2D CNN developed in Section (4.5), marking the transition into the deep learning component of this thesis. Analyzing our CNN model, we observe smooth convergence throughout the training epochs. As illustrated in Figure 4.34 (A), the training-loss trajectory demonstrates a steady and monotonic decrease, indicative of efficient optimization and effective learning. The validation-loss curve similarly shows an overall downward trend, despite some variable fluctuations. We attribute these fluctuations to inherent variability within the validation dataset, suggesting the presence of particularly challenging examples rather than evidence of model overfitting. This interpretation is further supported by the validation accuracy curves (Figure 4.34 (D)), which remain consistently high and closely track the corresponding training accuracy curves despite these fluctuations. Each classification head progressively improved its training accuracy, surpassing 90% within approximately 100 epochs. The minimal divergence between training and validation accuracies further reinforces the model's robust generalization capability, indicating minimal concerns regarding underfitting or overfitting problems.

Having evaluated the training history and established stable convergence behavior, we now proceed to examine the quantitative performance metrics evaluating our model. The 2D CNN demonstrates strong predictive performance across all target labels, effectively classifying water saturation, capillary pressure and attenuation, as quantitatively summarized in Table (14). The average accuracy for the multi-class CNN was 96.99% with an average loss of 0.289, further reinforced by an average F_1-score of 96.92%, across all three classification heads. Particularly, the latter F_1-score value indicates that the current model does not sacrifice precision for recall, or vice versa, thus demonstrating reliability and balanced classification performance across all three reservoir attributes.

Taking a closer look at the performance of the individual classification heads, the S_w classifier achieved an accuracy of 95.37% and an F_1-score of 95.38%, demonstrating reliable differentiation between low, intermediate and high water saturations. The capillary pressure (q) classifier attained an excellent performance with 99.88% accuracy and a corresponding F_1-score of 99.92%, clearly indicating the model's effectiveness in distinguishing uniform from increased capillary pressure conditions. Meanwhile, the attenuation (Q^{-1}) classifier scored an accuracy of 95.72% with an F_1-

score of 95.46%, showing slightly greater variability in validation performance relative to the other two heads. Notably, the holistic accuracy of 92.6% is particularly significant, as it reflects the stringent capability of the model to simultaneously classify all three reservoir properties accurately for individual samples. More importantly, the consistently high accuracy and robust F_1-scores indicate that the CNN model successfully accommodated the interference effects embedded within the spectrally unbalanced amplitude inputs. Despite these complexities, the model effectively learned to distinguish the CO_2-related saturation variations, capillary-pressure conditions, and varying attenuation levels. Thus, the presence of interference driven spectral variations did not hinder the model's ability to classify the reservoir attributes accurately.

Table 14 – Quantitative performance metrics for the implemented 2D CNN model.

Metric	Individual Classifier Heads		
	Water Saturation (S_w)	**Capillary Pressure** (q)	**Attenuation** (Q^{-1})
Total Loss	**0.289**		
Holistic Accuracy	**92.59%**		
Individual Accuracy per Classifier Head	**95.37%**	**99.88%**	**95.72%**
Average Accuracy	**96.99%**		
Individual F1 Score per classifier Head	**95.38%**	**99.92%**	**95.46%**
Average F1 Score	**96.92%**		

Despite the model's strong overall performance, minor limitations were identified. Occasional spikes observed in the validation-loss curve indicate that the model encountered difficulties with certain challenging validation samples. Furthermore, the slight instability observed in the validation accuracy for the attenuation (Q^{-1}) classification head indicates that attenuation features may present greater complexity for the current CNN architecture. To further enhance model stability and robustness, future work could incorporate advanced training techniques such as label smoothing or focal loss. Nevertheless, the obtained results confirm the effectiveness of the developed 2D CNN architecture and the selected hyperparameters. The designed model

successfully identified discriminative features embedded within frequency-dependent spectral amplitudes, enabling reliable predictions and robust generalization to previously unseen data. Overall, these results support that the presented CNN model effectively mitigated the interference-related amplitude effects previously identified in seismic panels and spectral amplitude spectrograms.

In conclusion, this exercise demonstrates that frequency-dependent rock physics forward modelling can be effectively integrated with a supervised, multi-label 2D CNN approach to infer key reservoir attributes directly from spectral seismic amplitudes. The curated catalogue generated in Section (4.4), systematically covering variations in S_w, q, and Q^{-1} at the Trow 32/2_1 wellsite, provides a comprehensive training dataset that enables accurate classification of spectral inputs into their respective water-saturation, capillary-pressure, and attenuation categories. Although the current implementation is specifically calibrated for Sognefjord reservoir conditions, we anticipate that the developed CNN model provides a transferable framework that can be potentially applied at nearby locations lacking sufficient well control, provided that the geological conditions remain broadly analogous to those considered here. Moreover, by expanding the training dataset to incorporate additional geological settings, broader parameter ranges and further synthetic realizations, this foundational approach could be progressively generalized into a comprehensive diagnostic tool, greatly enhancing CO_2 reservoir monitoring across diverse geological scenarios and reservoir conditions.

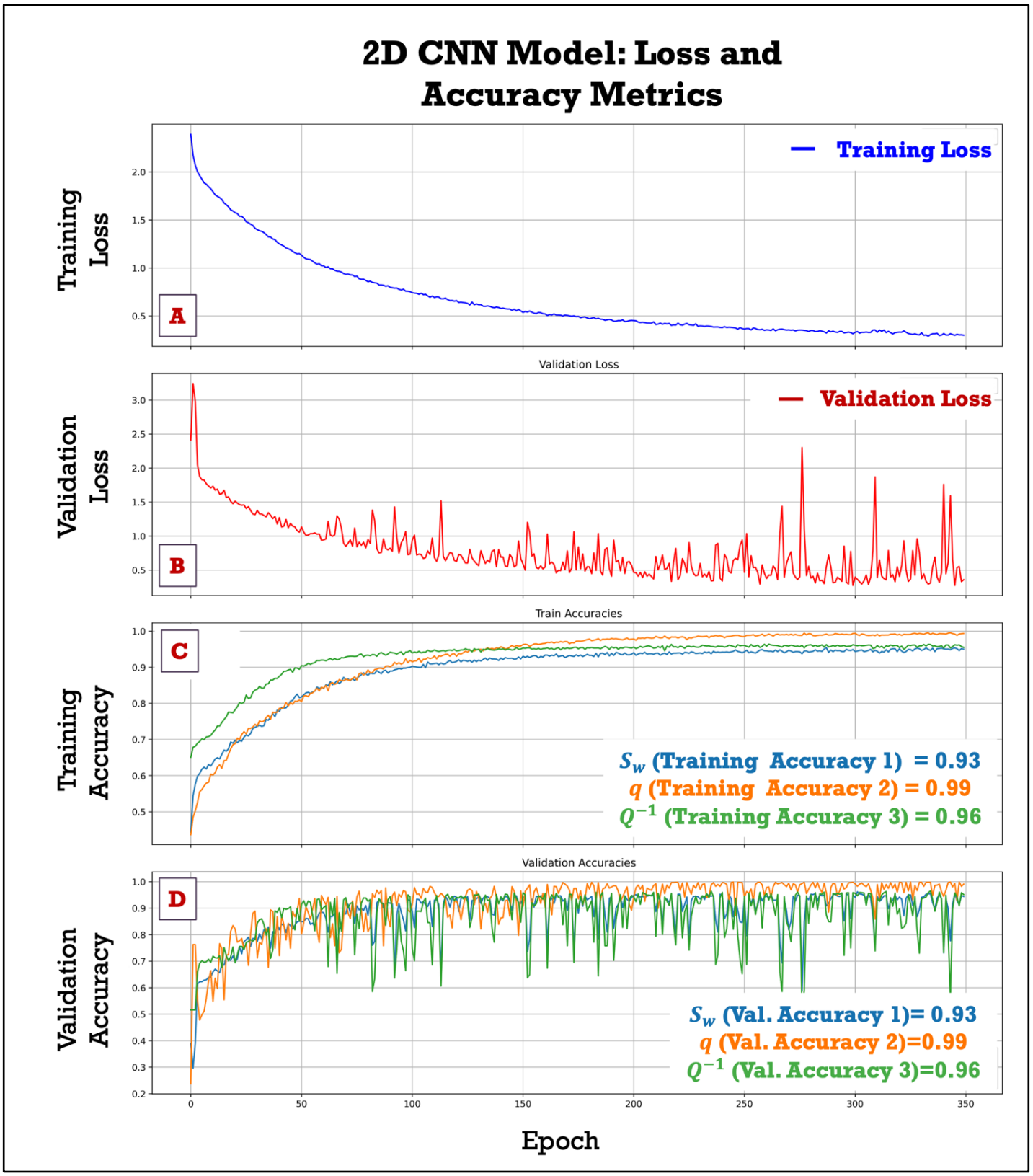


Figure 4.34 – Training and validation performance of the implemented 2D CNN model. ***(A)*** *Total training loss curve illustrating smooth, monotonic convergence over epochs.* ***(B)*** *Total validation loss curve demonstrating an overall decreasing trend with occasional fluctuations.* ***(C)*** *Training accuracy curves for water saturation (S_w), capillary pressure (q), and attenuation (Q^{-1}) classifier heads, progressively increasing and stabilizing above 90%.* ***(D)*** *Corresponding validation accuracy curves for S_w, q, and Q^{-1} heads closely tracking training accuracy trajectories, despite minor variability.*

5 Conclusion

5.1 Integrated Discussion

Accurate seismic monitoring of subsurface CO_2 storage fundamentally depends on capturing the frequency-dependent dispersion and attenuation phenomena introduced by partial CO_2 saturation and capillary pressure variation. Traditional seismic forward-modelling approaches, predominantly reliant on low-frequency Gassmann–Biot theory, typically neglect these crucial frequency-dependent squirt-flow effects. This omission introduces uncertainties in quantifying velocity dispersion and attenuation, consequently impacting seismic amplitudes and AVO responses that are critical for reliable reservoir characterization and effective CO_2 plume monitoring.

To address these limitations, this thesis investigates whether explicitly incorporating squirt-flow dispersion, attenuation, and capillary pressure within a frequency-dependent rock-physics (RP) framework could enhance seismic characterization of CO_2 storage reservoirs compared to the conventional low-frequency Gassmann–Biot modelling. This research specifically targets the Jurassic Sognefjord Formation at the Smeaheia CO_2 potential storage site, located in the Norwegian North Sea, utilizing the Trow 32/2_1 well log data available on the CO_2 DataShare website.

To achieve this objective, both conventional (Chapter 3) and frequency-dependent (Chapter 4) rock-physics forward modelling approaches begin with rigorous well-log analysis and data conditioning. This process includes updating in-situ fluid properties, computing supercritical CO_2 fluid-phase properties, recalibrating shale elastic moduli, and verifying the elastic data trends within $V_p - \rho$ and $V_p - V_s$ domains, using Gardner and Greenberg-Castagna lithology trends required for later V_s prediction in missing intervals. Chapter 3 further discussed the impact of total porosity (PHIT) versus effective porosity (PHIE), emphasizing that the latter captures only hydraulically connected pore spaces crucial for fluid flow and elastic deformation, a distinction particularly relevant for the shaley-sand reservoir conditions of the Sognefjord formation. The frequency-dependent approach (Chapter 4) later inherited this conditioned log suite, subsequently upscaling it to seismic resolution via Backus averaging and two-way-time resampling. This

analytical task was integral to both workflows, ensuring acquisition of reliable log data for the forward modelling phase.

Applying the conventional RP forward modelling approach, we established baseline elastic trends and AVO responses at the low-frequency Gassmann limit. We examined the impacts of varying CO_2 saturations under different capillary-pressure conditions, simulating both uniform and patchy saturation distributions, while excluding dispersive attenuation effects. Conventional Gassmann fluid substitution predicted clear elastic softening with increasing CO_2 saturation, governed by saturation heterogeneities or the fluid distribution patterns (q=1 or q_o= 0.054). Uniform (Reuss-bound) saturation results in pronounced reductions in V_p, K_{sat} and AI, producing Class III AVO responses even at moderate saturations (~20%). Conversely, patchy (Voigt-bound) distributions yield stiffer elastic responses, reducing amplitude contrasts and relatively flattening intercept–gradient trajectories, narrowing the detectability envelope at intermediate saturations, implying potential uncertainty in 4D seismic interpretation if saturation heterogeneity patterns are ignored.

In Chapter 4, we transitioned into the frequency domain by incorporating the Papageorgiou & Chapman (2017) squirt-flow model, explicitly capturing fluid flow-induced velocity dispersion and attenuation effects across relaxed, dispersive, and unrelaxed states. Model integrity was validated through baseline equivalence testing, demonstrating negligible residual differences relative to the conventional Gassmann model ($\Delta V_p \approx$ –0.05%, $\Delta P_{Mod} \approx$ –0.09%) at the 100% brine baseline reference. Under relaxed conditions with negligible attenuation (Q = 1000, W_c = –2), CO_2 substitution resulted in substantial elastic softening, notably reducing the compressional velocity and modulus ($\Delta V_p \approx$ –16% ; $\Delta P_{Mod} \approx$ –32%), while shear attributes remained largely unaffected. Transitioning to the dispersive regime, at maximum attenuation and dispersion (Q = 10, $W_c \approx 0$) this softening effect further intensified (ΔV_p up to –25 %; ΔP_{Mod} up to –47%) with respect to the same baseline. This significantly steepened AVO gradients and enhanced amplitude sensitivity (amplitude brightening). Increased capillary pressure (q_o = 0.054) further moderated these elastic responses at intermediate saturations, partially stiffening the fluid mixtures, reducing amplitude brightening effects, and flattening AVO gradients.

Further frequency-dependent spectral and AVO analysis revealed that dispersion and attenuation reshaped seismic amplitude responses. In the dispersive state, at maximum attenuation (Q = 10, $W_c \approx 0$), seismic energy shifted toward lower frequencies, amplified amplitude sensitivity, and

yielded steeper amplitude-versus-offset (AVO) trends. Consequently, the developed frequency-dependent AVO (FAVO) template identified optimal windows for potential CO_2 discrimination, most notably below 20 Hz at larger offset angles (30°–40°). Unlike conventional low-frequency methods, this feasibility study, integrating squirt-flow modelling, frequency-dependent reflectivity, spectral decomposition, and FAVO analysis, comprehensively characterized squirt-flow-induced dispersion, revealing seismic-scale phase shifts and amplitude variations. However, precise quantification of these CO_2-induced signatures was complicated by seismic interference arising from the combined effects of thin-bed tuning caused by intra-formational shale stringers and frequency-dependent squirt-flow, which produces dispersion-related phase shifts and attenuation-driven wavelet broadening.

Specifically, interference effects manifested as amplitude brightening within the high-frequency band (60–90 Hz), characterized by increased intercept reflectivity and steeper AVO gradients, closely resembling genuine Class III AVO responses observed at lower frequencies ($\leq$ 20 Hz) directly related to CO_2 saturation changes. Therefore, careful differentiation between interference-driven anomalies and true CO_2-related signatures is essential to avoid misinterpretation during time-lapse monitoring and reservoir characterization.

Given these interpretational challenges posed by interference-related effects, frequency-dependent spectral amplitudes were subsequently integrated into a two-dimensional convolutional neural network (2D CNN) as a proposed mitigation strategy. This CNN was designed with multiple parallel classification outputs, enabling simultaneous inversion for the simulated saturation (S_w) ranges, capillary pressure (q) regimes, and attenuation (Q^{-1}) conditions. After hyperparameter optimization, the CNN demonstrated strong predictive performance, achieving an average accuracy of 96.99%, a holistic classification accuracy of 92.6%, and an average F_1-score of 96.92% across the different S_w, q, and Q^{-1} attribute classifiers. Hence, the achieved performance indicates the model's inherent capability in effectively distinguishing between the CO_2-induced responses and interference-related complexities, demonstrating the utility of frequency-dependent spectral amplitudes for potential reservoir attribute prediction.

While the results presented throughout this thesis demonstrate clear potential, we do acknowledge that the proposed workflow poses several limitations. Currently, the integrated approach remains conceptual and requires validation using actual time-lapse seismic data from active CO_2 injection projects. Consequently, our findings depend on assumed model parameters,

including capillary pressure values constrained theoretically following Papageorgiou and Chapman (2017), rather than direct core or field calibration. Similarly, our selection of attenuation (Q^{-1}) conditions involved employing a plausible range of low, medium, and high attenuation scenarios drawn from literature, further validated via preliminary sensitivity analyses (Section 4.3.3), ensuring physically reasonable dispersive responses. However, actual attenuation values remain uncertain without direct measurement or calibration, potentially achievable through vertical seismic profiling (VSP) at the borehole location, enabling direct measurement of seismic attenuation by analyzing the amplitude decay and frequency changes with depth.

In addition to parameter uncertainties, the accuracy of our forward modelling predictions relies on the extent to which our synthetic responses realistically mimic the wavelet properties and noise conditions observed in the actual seismic data. Currently, as a proof of concept, we used a synthetic Ricker wavelet with a 50 Hz dominant frequency, consistent with previous studies from the nearby Troll field, neglecting the presence of potential noise conditions. Therefore, future validation and simulation models should use wavelets extracted directly from the existing baseline seismic data at Smeaheia and incorporate realistic noise scenarios. These factors are critical to ensure comparability with actual time-lapse seismic monitoring data, particularly as noise and wavelet mismatches can obscure or alter predicted dispersion features.

Finally, the current workflow employs 1D forward modelling at the well location, utilizing elastic logs upscaled to seismic resolution via Backus averaging combined with TWT resampling. Despite these measures, upscaled logs may still retain finer vertical detail and higher-frequency content compared to actual 3D seismic volumes, making some predicted dispersion features difficult to seismically detect. Furthermore, the 1D forward modeling approach does not explicitly account for lateral or spatial heterogeneity naturally present within the reservoir. Consequently, the amplitude and detectability of the modelled frequency-dependent effects may differ when transitioning from the simplified 1D well-based modelling to practical 3D seismic applications. Hence, addressing these uncertainties by leveraging baseline and future time-lapse seismic data will ultimately improve workflow reliability and applicability.

The appraisal wells recently drilled by Equinor at Smeaheia (32/7_1 and 32/4_4) will provide critical field datasets for validating the modelling approach developed in this thesis (well data pending public release; *SODIR*, 2025). Preliminary injection tests and reservoir analyses from these wells confirm the geological suitability of the targeted Sognefjord Formation for CO_2

storage, directly highlighting the relevance and potential impact of this research. If publicly available, the data from these wells will enable validation of the frequency-dependent modelling workflow by verifying whether the currently modelled dispersive trends can be replicated. Successful replication would substantiate the validity of our approach, confirm key findings, and enhance our existing training dataset. Such expansion could potentially improve the CNN model's generalization capabilities and allow a rigorous assessment of the workflow's viability and applicability to CCS monitoring at Smeaheia and geologically analogous sites.

In summary, this thesis demonstrates that explicitly incorporating squirt-flow effects and realistic capillary pressure scenarios into frequency-dependent rock physics modelling provides an enhanced framework for seismic reservoir characterization relative to conventional methods. By integrating this latter approach with deep-learning inversion, the proposed workflow facilitates direct inference of reservoir properties from spectral seismic amplitudes. Although specifically calibrated for the geological conditions of the Sognefjord reservoir (a shallow, highly porous, unconsolidated sandstone under super-critical CO_2 conditions), the underlying methodology presented remains adaptable. Consequently, it holds potential for deployment at analogous CCS sites, particularly at locations with limited well control, possibly reducing interpretational uncertainties and improving reservoir monitoring reliability.

5.2 Conclusion

This thesis demonstrates that explicitly incorporating squirt-flow dispersion, attenuation, and capillary pressure within a frequency-dependent rock-physics modelling workflow enhances seismic characterization of subsurface CO_2 storage reservoirs compared to conventional low-frequency Gassmann–Biot modelling. By capturing dispersion and attenuation effects, the frequency-dependent approach identifies phase shifts, amplitude variations, and frequency-dependent AVO signatures critical for reservoir diagnostics. Integrating this forward-modelling framework with supervised machine learning inversion further mitigates interpretational challenges, providing accurate reservoir attribute predictions and enhanced monitoring reliability.

Hence, the workflow presented, specifically calibrated for the Jurassic Sognefjord Formation at the Smeaheia CO_2 storage site, offers practical methodology suitable for deployment at analogous CCS sites. To further establish the workflow's reliability and generalization capability,

future research should therefore focus on validating the model with field seismic data incorporating realistic geological variability and noise conditions.

5.3 Future Recommendation

There are several practical improvements and recommendations for future work stemming from the presented workflow. Firstly, the dimensionless capillary-pressure parameter (q) is currently treated as depth-invariant. Given that capillary pressure typically varies with porosity and effective stress, adopting a depth-dependent function ($q(z)$), supported by core data or empirical relationships, would better reflect reservoir heterogeneity and produce more realistic patchy-saturation elastic predictions. Furthermore, the present modelling workflow assumes an isotropic, purely viscoelastic medium with idealized pore geometries, omitting stress-induced anisotropy and fracture-related attenuation effects. Incorporating anisotropic effects would enhance amplitude predictions, dispersion trends, and velocity pull-up estimates, thus increasing the credibility and performance of our modelling workflow for seismic interpretation.

For further validation of the proposed frequency-dependent squirt-flow modelling approach, a critical next step would involve applying the developed model and associated FAVO templates using actual time-lapse seismic data from established North Sea CO_2 storage sites, such as Sleipner or Snøhvit. This validation step would help confirm the squirt-flow related effects observed or identified in our current modelling results. Additionally, using these validated templates to optimize seismic acquisition could potentially support determining ideal survey parameters, such as azimuth, offset, and frequency ranges, to maximize CO_2 plume detectability, improve reservoir monitoring effectiveness, and minimize monitoring uncertainties.

Regarding improvements to the CNN workflow, expanding the training dataset beyond the current idealized, noise-free synthetic gathers, generated for specific parameter combinations (S_w q, Q^{-1}), would improve the model's generalization capabilities when applied to real seismic data. To address this concern, we can pre-train the developed CNN on synthetic or real time-lapse datasets representative of the diverse geological settings and reservoir conditions typical of the North Sea CO_2 storage sites. Blind validation and testing could be subsequently conducted using the synthetic dataset specifically modeled for the targeted Smeaheia CO_2 storage site, as presented in this thesis. This approach would effectively enhance the model's robustness across varying

lithological and noise conditions, reducing subsequent data-volume requirements at future site applications. Finally, replacing the manual hyperparameter tuning process with systematic optimization methods, such as grid search techniques, or exploring alternative neural network architectures or loss functions (e.g., focal loss or class-balanced objectives) could further enhance the model's classification stability and accuracy.

6 References

Alkhimenkov, Y., Caspari, E., Gurevich, B., Barbosa, N. D., Glubokovskikh, S., Hunziker, J., & Quintal, B. (2020). Frequency-dependent attenuation and dispersion caused by squirt flow: Three-dimensional numerical study. *GEOPHYSICS*, *85*(3), MR129–MR145. https://doi.org/10.1190/geo2019-0519.1

Amalokwu, K., Best, A. I., Sothcott, J., Chapman, M., Minshull, T., & Li, X.-Y. (2014). Water saturation effects on elastic wave attenuation in porous rocks with aligned fractures. *Geophysical Journal International*, *197*(2), 943–947. https://doi.org/10.1093/gji/ggu076

Avseth, P., Mukerji, T., & Mavko, G. (Eds.). (2005a). Introduction to rock physics. In *Quantitative Seismic Interpretation: Applying Rock Physics Tools to Reduce Interpretation Risk* (pp. 1–47). Cambridge University Press. https://doi.org/10.1017/CBO9780511600074.002

Avseth, P., Mukerji, T., & Mavko, G. (Eds.). (2005b). Rock physics interpretation of texture, lithology and compaction. In *Quantitative Seismic Interpretation: Applying Rock Physics Tools to Reduce Interpretation Risk* (pp. 48–110). Cambridge University Press. https://doi.org/10.1017/CBO9780511600074.003

Azuma, H., Konishi, C., & Xue, Z. (2013). Introduction and Application of the Modified Patchy Saturation for Evaluating CO2 Saturation by Seismic Velocity. *Energy Procedia*, *37*, 4024–4032. https://doi.org/10.1016/j.egypro.2013.06.302

Batzle, M. L., & Wang, Z. (1992). Seismic properties of pore fluids. *Geophysics*, *57*(11), 1396–1408. https://doi.org/10.1190/1.1443207

Berryman, J. G. (1999). Origin of Gassmann's equations. *Geophysics*, *64*(5), 1627–1629. https://doi.org/10.1190/1.1444667

Berryman, J. G., & Milton, G. W. (1991). Exact results for generalized Gassmann's equations in composite porous media with two constituents. *Geophysics*, *56*(12), 1950–1960. https://doi.org/10.1190/1.1443006

Biot, M. A. (1956a). Theory of Propagation of Elastic Waves in a Fluid-Saturated Porous Solid. I. Low-Frequency Range. *The Journal of the Acoustical Society of America*, *28*(2), 168–178. https://doi.org/10.1121/1.1908239

Biot, M. A. (1956b). Theory of Propagation of Elastic Waves in a Fluid-Saturated Porous Solid. II. Higher Frequency Range. *The Journal of the Acoustical Society of America*, *28*(2), 179–191. https://doi.org/10.1121/1.1908241

Bridle, J. (1989). Training Stochastic Model Recognition Algorithms as Networks can Lead to Maximum Mutual Information Estimation of Parameters. *Advances in Neural Information Processing Systems*, *2*. https://proceedings.neurips.cc/paper/1989/hash/0336dcbab05b9d5ad24f4333c7658a0e-Abstract.html

Brie, A., Pampuri, F., Marsala, A. F., & Meazza, O. (1995, October 22). *Shear Sonic Interpretation in Gas-Bearing Sands*. SPE Annual Technical Conference and Exhibition. https://doi.org/10.2118/30595-MS

Brown, A. R. (2001). Color in seismic display. *The Leading Edge*, *20*(5), 549. https://doi.org/10.1190/1.1438992

Buryakovsky, L., Chilingar, G. V., Rieke, H. H., & Shin, S. (2012). *Fundamentals of the Petrophysics of Oil and Gas Reservoirs*. John Wiley & Sons, Incorporated. http://ebookcentral.proquest.com/lib/ed/detail.action?docID=947733

Caspari, E., Müller, T. M., & Gurevich, B. (2011). Time-lapse sonic logs reveal patchy CO_2 saturation in-situ: IN-SITU CO_2 PATCH SIZE ESTIMATION. *Geophysical Research Letters*, *38*(13), n/a-n/a. https://doi.org/10.1029/2011GL046959

Castagna, J. P., & Backus, M. M. (1993). Principles—Knovel. In *Offset-Dependent Reflectivity—Theory and Practice of AVO Analysis*. Society of Exploration Geophysicists (SEG). https://app-knovel-com.ezproxy.is.ed.ac.uk/web/view/khtml/show.v/rcid:kpODRTPAV1/cid:kt011IJJQ1/viewerType:khtml//root_slug:offset-dependent-reflectivity/url_slug:principles?b-toc-cid=kpODRTPAV1&b-toc-root-slug=offset-dependent-reflectivity&b-toc-title=Offset-Dependent%20Reflectivity%20-%20Theory%20and%20Practice%20of%20AVO%20Analysis&b-toc-url-slug=principles&kpromoter=marc&view=collapsed&zoom=1&page=2

Castagna, J. P., Batzle, M. L., & Kan, T. K. (1993). Rock physics – The link between rock properties and AVO response. In *In Offset-Dependent Reflectivity – Theory and Practice of AVO Analysis, Investigations in Geophysics.* (8th ed., pp. 135–171). SEG Books. https://books.google.co.uk/books?id=F0aShbgvDWgC

Chapman, M. (2003). Frequency-dependent anisotropy due to meso-scale fractures in the presence of equant porosity. *Geophysical Prospecting*, *51*(5), 369–379. https://doi.org/10.1046/j.1365-2478.2003.00384.x

Chapman, M., Liu, E., & Li, X.-Y. (2006). The influence of fluid sensitive dispersion and attenuation on AVO analysis. *Geophysical Journal International*, *167*(1), 89–105. https://doi.org/10.1111/j.1365-246X.2006.02919.x

Chapman, M., Zatsepin, S. V., & Crampin, S. (2002). Derivation of a microstructural poroelastic model. *Geophysical Journal International*, *151*(2), 427–451. https://doi.org/10.1046/j.1365-246X.2002.01769.x

Domenico, S. N. (1976). Effect of brine-gas mixture on velocity in an unconsolidated sand reservoir. *Geophysics*, *41*(5), 882–894. https://doi.org/10.1190/1.1440670

Dowla, F. U., Taylor, S. R., & Anderson, R. W. (1990). Seismic discrimination with artificial neural networks: Preliminary results with regional spectral data. *Bulletin of the Seismological Society of America*, *80*(5), 1346–1373. https://doi.org/10.1785/BSSA0800051346

Dramsch, J. S. (2020). 70 years of machine learning in geoscience in review. In *Advances in Geophysics* (Vol. 61, pp. 1–55). Elsevier. https://doi.org/10.1016/bs.agph.2020.08.002

Duan, G., Zhang, J., Zheng, X., Zhu, Y., & Chang, V. (2023). *Bitformer: An efficient Transformer with bitwise operation-based attention for Big Data Analytics at low-cost low-precision devices* (No. arXiv:2311.13502). arXiv. https://doi.org/10.48550/arXiv.2311.13502

Dupuy, B., C., V. A. T., Ghaderi, A., Querendez, E., & Mezyk, M. (2017). Constrained AVO for CO2 Storage Monitoring at Sleipner. *Energy Procedia*, *114*, 3927–3936. https://doi.org/10.1016/j.egypro.2017.03.1524

Dupuy, B., Romdhane, A., Eliasson, P., & Yan, H. (2021). Combined geophysical and rock physics workflow for quantitative CO2 monitoring. *International Journal of Greenhouse Gas Control*, *106*, 103217. https://doi.org/10.1016/j.ijggc.2020.103217

Dutta, N. C., & Ode, H. (1979a). Attenuation and dispersion of compressional waves in fluid-filled porous rocks with partial gas saturation (White model); Part I, Biot theory. *Geophysics*, *44*(11), 1777–1788. https://doi.org/10.1190/1.1440938

Dutta, N. C., & Ode, H. (1979b). Attenuation and dispersion of compressional waves in fluid-filled porous rocks with partial gas saturation (White model); Part II, Results. *Geophysics*, *44*(11), 1789–1805. https://doi.org/10.1190/1.1440939

Dutta, N. C., & Odé, H. (1983). Seismic reflections from a gas-water contact. *Geophysics*, *48*(2), 148–162. https://doi.org/10.1190/1.1441454

Dvorkin, J., Gutierrez, M. A., & Grana, D. (2014a). Rock physics models and transforms. In *Seismic Reflections of Rock Properties* (pp. 13–42). Cambridge University Press. https://doi.org/10.1017/CBO9780511843655.004

Dvorkin, J., Gutierrez, M. A., & Grana, D. (2014b). Rock-physics-based workflow in oil and gas exploration. In *Seismic Reflections of Rock Properties* (1st ed.). Cambridge University Press. https://doi.org/10.1017/CBO9780511843655

Dvorkin, J., Mavko, G., & Gurevich, B. (2007). Fluid substitution in shaley sediment using effective porosity. *Geophysics*, *72*(3), 01–08. https://doi.org/10.1190/1.2565256

Dvorkin, J., Mavko, G., & Nur, A. (1995). Squirt flow in fully saturated rocks. *Geophysics*, *60*(1), 97–107. https://doi.org/10.1190/1.1443767

Dvorkin, J., & Nur, A. (1993). Dynamic poroelasticity; a unified model with the squirt and the Biot mechanisms. *Geophysics*, *58*(4), 524–533. https://doi.org/10.1190/1.1443435

Eid, R., Ziolkowski, A., Naylor, M., & Pickup, G. (2015). Seismic monitoring of CO2 plume growth, evolution and migration in a heterogeneous reservoir: Role, impact and importance of patchy saturation. *International Journal of Greenhouse Gas Control*, *43*, 70–81. https://doi.org/10.1016/j.ijggc.2015.10.019

Ekanem, A. M., Li, X. Y., Chapman, M., & Main, I. G. (2016). Effects of CO2 on P-wave attenuation in porous media with micro-cracks: A synthetic modelling study. *Journal of Applied Geophysics*, *135*, 309–316. https://doi.org/10.1016/j.jappgeo.2016.10.025

Endres, A. L., & Knight, R. J. (1997). Incorporating pore geometry and fluid pressure communication into modeling the elastic behavior of porous rocks. *Geophysics*, *62*(1), 106–117. https://doi.org/10.1190/1.1444110

Fatti, J. L., Smith, G. C., Vail, P. J., Strauss, P. J., & Levitt, P. R. (1994). Detection of gas in sandstone reservoirs using AVO analysis: A 3-D seismic case history using the Geostack technique. *GEOPHYSICS*, *59*(9), 1362–1376. https://doi.org/10.1190/1.1443695

Fawad, M., & Mondol, N. (2022). Monitoring geological storage of CO2 using a new rock physics model. *Scientific Reports*, *12*. https://doi.org/10.1038/s41598-021-04400-7

Fawad, M., Rahman, M. J., & Mondol, N. H. (2021). Seismic-derived geomechanical properties of potential CO2 storage reservoir and cap rock in Smeaheia area, northern North Sea. *The Leading Edge*, *40*(4), 254–260. https://doi.org/10.1190/tle40040254.1

Gale, J., & Wilson, M. (2019). Climate Change and the Role of Carbon Capture and Storage in Mitigation. In M. Wilson, M. Landrø, & T. L. Davis (Eds.), *Geophysics and Geosequestration* (pp. 1–10). Cambridge University Press. https://doi.org/10.1017/9781316480724.002

Gardner, G. H. F., Gardner, L. W., & Gregory, A. R. (1974). Formation velocity and density; the diagnostic basics for stratigraphic traps. *Geophysics*, *39*(6), 770–780. https://doi.org/10.1190/1.1440465

Gassmann, F. (1951). *Uber die elastizitat poroser medien. Vierteljahrsschrift der Naturforschenden Gesellschaft in Zurich*. *96*, 1–23.
Gassnova, S. (2013). *Rapport:Troll Kystnaer subsurface evaluation report*. https://doi.org/10.11582/2021.00012
Géron, A. (2017). *Hands-On Machine Learning with Scikit-Learn and TensorFlow: Concepts, Tools, and Techniques to Build Intelligent Systems*. O'Reilly Media, Incorporated. http://ebookcentral.proquest.com/lib/ed/detail.action?docID=4822582
Gonzalez, K., & Misra, S. (2022). *Monitoring the CO2 Plume Migration during Geological Carbon Storage using Spatiotemporal Clustering*. Geophysics. https://doi.org/10.1002/essoar.10510855.1
Goodfellow, I., Bengio, Y., & Courville, A. (2016). *Deep Learning*. MIT Press. https://www.deeplearningbook.org/
Greenberg, M. L., & Castagna, J. P. (1992). Shear-Wave Velocity Estimation in Porous Rocks: Theoretical Formulation, Preliminary Verification and Applications1. *Geophysical Prospecting*, *40*(2), 195–209. https://doi.org/10.1111/j.1365-2478.1992.tb00371.x
Grude, S., Landrø, M., White, J. C., & Torsæter, O. (2014). CO2 saturation and thickness predictions in the Tubåen Fm., Snøhvit field, from analytical solution and time-lapse seismic data. *International Journal of Greenhouse Gas Control*, *29*, 248–255. https://doi.org/10.1016/j.ijggc.2014.08.011
Gurevich, B., & Carcione, J. M. (2000). Gassmann Modeling of Acoustic Properties of Sand-clay Mixtures. *Pure and Applied Geophysics*, *157*(5), 811–827. https://doi.org/10.1007/PL00001119
Gurevich, B., & Lopatnikov, S. L. (1995). Velocity and attenuation of elastic waves in finely layered porous rocks. *Geophysical Journal International*, *121*(3), 933–947. https://doi.org/10.1111/j.1365-246X.1995.tb06449.x
Gurevich, B., Makarynska, D., & Pervukhina, M. (2009). Ultrasonic moduli for fluid-saturated rocks: Mavko-Jizba relations rederived and generalized. *Geophysics*, *74*(4), N25–N30. https://doi.org/10.1190/1.00V7414
Gutierrez, M., Katsuki, D., & Almrabat, A. (2012). Effects of CO₂ Injection on the Seismic Velocity of Sandstone Saturated with Saline Water. *International Journal of Geosciences*, *03*(05), 908–917. https://doi.org/10.4236/ijg.2012.325093
Han, D., & Batzle, M. L. (2004). Gassmann's equation and fluid-saturation effects on seismic velocities. *Geophysics*, *69*(2), 398–405. https://doi.org/10.1190/1.1707059
Han, D., Nur, A., & Morgan, D. (1986). Effects of porosity and clay content on wave velocities in sandstones. *Geophysics*, *51*(11), 2093–2107. https://doi.org/10.1190/1.1442062
Hilterman, F. J. (2001). *Seismic Amplitude Interpretation: 2001 Distinguished Instructor Short Course*. SEG Books.
Hutchison, D., Kanade, T., Kittler, J., Kleinberg, J. M., Mattern, F., Mitchell, J. C., Naor, M., Nierstrasz, O., Pandu Rangan, C., Steffen, B., Sudan, M., Terzopoulos, D., Tygar, D., Vardi, M. Y., Weikum, G., Scherer, D., Müller, A., & Behnke, S. (2010). Evaluation of Pooling Operations in Convolutional Architectures for Object Recognition. In K. Diamantaras, W. Duch, & L. S. Iliadis (Eds.), *Artificial Neural Networks – ICANN 2010* (Vol. 6354, pp. 92–101). Springer Berlin Heidelberg. https://doi.org/10.1007/978-3-642-15825-4_10

Innanen, K. A. (2011). Inversion of the seismic AVF/AVA signatures of highly attenuative targets. *Geophysics*, *76*(1), R1–R14. https://doi.org/10.1190/1.3518816

Ioffe, S., & Szegedy, C. (2015). *Batch Normalization: Accelerating Deep Network Training by Reducing Internal Covariate Shift* (No. arXiv:1502.03167). arXiv. https://doi.org/10.48550/arXiv.1502.03167

Iyegbekedo, I., Fathi, E., Carr, T. R., & Belyadi, F. (2024). Machine Learning-Driven Quantification of CO2 Plume Dynamics at Illinois Basin Decatur Project Sites Using Microseismic Data. *Energies*, *17*(17), 4421. https://doi.org/10.3390/en17174421

Izadian, S. (2024). Tuning effect in time-lapse seismic inversion for CO2 plume monitoring at Sleipner field. *International Journal of Greenhouse Gas Control*, *137*, 104224. https://doi.org/10.1016/j.ijggc.2024.104224

Jenkins, C., Chadwick, A., & Hovorka, S. D. (2015). The state of the art in monitoring and verification—Ten years on. *International Journal of Greenhouse Gas Control*, *40*, 312–349. https://doi.org/10.1016/j.ijggc.2015.05.009

Jeong, G. S., Ki, S., Lee, D. S., & Jang, I. (2021). Effect of the Flow Rate on the Relative Permeability Curve in the CO2 and Brine System for CO2 Sequestration. *Sustainability*, *13*(3), Article 3. https://doi.org/10.3390/su13031543

Jin, Z., Chapman, M., Wu, X., & Papageorgiou, G. (2017). Estimating gas saturation in a thin layer by using frequency-dependent amplitude versus offset modelling: Estimating gas saturation in a thin layer. *Geophysical Prospecting*, *65*(3), 747–765. https://doi.org/10.1111/1365-2478.12437

Kazemeini, S. H., Juhlin, C., & Fomel, S. (2010). Monitoring CO2 response on surface seismic data; a rock physics and seismic modeling feasibility study at the CO2 sequestration site, Ketzin, Germany. *Journal of Applied Geophysics*, *71*(4), 109–124. https://doi.org/10.1016/j.jappgeo.2010.05.004

Kenneth Samuel, O., & Righteous, O. (2019). Application of Spectral Decomposition and Seismic Attributes For Channel Geometry and Infill Lithology Determination: A Case Study from The Southern North Sea Basin. *International Journal of Earth Science and Geophysics*, *5*(1). https://doi.org/10.35840/2631-5033/1823

Khonde, K., & Rastogi, R. (2013). *Recent Developments in Spectral Decomposition of Seismic Data (Techniques and Applications): A Review*. https://www.semanticscholar.org/paper/Recent-Developments-in-Spectral-Decomposition-of-(-Khonde-Rastogi/d8819da86364152a368797707beb67baaf2b29c8

King, M. s., Marsden, J. r., & Dennis, J. w. (2000). Biot dispersion for P- and S-wave velocities in partially and fully saturated sandstones. *Geophysical Prospecting*, *48*(6), 1075–1089. https://doi.org/10.1111/j.1365-2478.2000.00221.x

Kingma, D. P., & Ba, J. (2017). *Adam: A Method for Stochastic Optimization* (No. arXiv:1412.6980). arXiv. https://doi.org/10.48550/arXiv.1412.6980

Klimentos, T. (1995). Attenuation of P- and S-waves as a method of distinguishing gas and condensate from oil and water. *Geophysics*, *60*(2), 447–458. https://doi.org/10.1190/1.1443782

Koga, I., Aruga, M., & Yoshinaka, Y. (1958). Theory of Plane Elastic Waves in a Piezoelectric Crystalline Medium and Determination of Elastic and Piezoelectric Constants of Quartz. *Physical Review*, *109*(5), 1467–1473. https://doi.org/10.1103/PhysRev.109.1467

Le Ravalec, M., & Guéguen, Y. (1996). High- and low-frequency elastic moduli for a saturated porous/cracked rock-Differential self-consistent and poroelastic theories. *Geophysics*, *61*(4), 1080–1094. https://doi.org/10.1190/1.1444029

Lebedev, M., Toms-Stewart, J., Clennell, B., Pervukhina, M., Shulakova, V., Paterson, L., Müller, T. M., Gurevich, B., & Wenzlau, F. (2009). Direct laboratory observation of patchy saturation and its effects on ultrasonic velocities. *The Leading Edge*, *28*(1), 24–27. https://doi.org/10.1190/1.3064142

Lecun, Y., Bottou, L., Bengio, Y., & Haffner, P. (1998). Gradient-based learning applied to document recognition. *Proceedings of the IEEE*, *86*(11), 2278–2324. https://doi.org/10.1109/5.726791

Lei, X., & Xue, Z. (2009). Ultrasonic velocity and attenuation during CO2 injection into water-saturated porous sandstone: Measurements using difference seismic tomography. *Physics of the Earth and Planetary Interiors*, *176*(3), 224–234. https://doi.org/10.1016/j.pepi.2009.06.001

Li, B., & Li, Y. E. (2021). Neural Network-Based CO2 Interpretation From 4D Sleipner Seismic Images. *Journal of Geophysical Research: Solid Earth*, *126*(12), e2021JB022524. https://doi.org/10.1029/2021JB022524

Lindsay, R., & Van Koughnet, R. (2001). Sequential Backus Averaging: Upscaling well logs to seismic wavelengths. *The Leading Edge*, *20*(2), 188–191. https://doi.org/10.1190/1.1438908

Liner, C., & Fei, T. (2007). The Backus number. *The Leading Edge*, *26*(4), 420–426. https://doi.org/10.1190/1.2723204

Liner, C. L. (2014). Long-wave elastic attenuation produced by horizontal layering. *The Leading Edge*, *33*(6), 634–638. https://doi.org/10.1190/tle33060634.1

Lumley, D. (2019). The Role of Geophysics in Carbon Capture and Storage. In M. Wilson, M. Landrø, & T. L. Davis (Eds.), *Geophysics and Geosequestration* (pp. 11–53). Cambridge University Press. https://doi.org/10.1017/9781316480724.003

Ma, J., & Morozov, I. (2010). AVO modeling of pressure-saturation effects in Weyburn CO2 sequestration. *The Leading Edge*, *29*, 178–183. https://doi.org/10.1190/1.3304821

Maurya, S. P., & Singh, N. P. (2019). Seismic modelling of CO2 fluid substitution in a sandstone reservoir: A case study from Alberta, Canada. *Journal of Earth System Science*, *128*, 236. https://doi.org/10.1007/s12040-019-1263-x

Mavko, G., Chan, C., & Mukerji, T. (1995). Fluid substitution; estimating change in V p without knowing V s. *Geophysics*, *60*(6), 1750–1755. https://doi.org/10.1190/1.1443908

Mavko, G., & Jizba, D. (1991). Estimating grain-scale fluid effects on velocity dispersion in rocks. *Geophysics*, *56*(12), 1940–1949. https://doi.org/10.1190/1.1443005

Mavko, G., & Mukerji, T. (1998). Bounds on low-frequency seismic velocities in partially saturated rocks. *Geophysics*, *63*(3), 918–924. https://doi.org/10.1190/1.1444402

Mavko, G., Mukerji, T., & Dvorkin, J. (Eds.). (2020a). Appendices. In *The Rock Physics Handbook* (3rd ed., pp. 613–672). Cambridge University Press. https://www.cambridge.org/core/books/rock-physics-handbook/appendices/E2BA72BAA31042FF17CFE7D3F3447AF5

Mavko, G., Mukerji, T., & Dvorkin, J. (Eds.). (2020b). Empirical Relations. In *The Rock Physics Handbook* (3rd ed., pp. 474–524). Cambridge University Press. https://doi.org/10.1017/9781108333016.008

Mavko, G., Mukerji, T., & Dvorkin, J. (2020c). Fluid Effects on Wave Propagation. In *The Rock Physics Handbook* (3rd ed., pp. 367–473). Cambridge University Press. https://doi.org/10.1017/9781108333016.007

Müller, T. M., Gurevich, B., & Lebedev, M. (2010). Seismic wave attenuation and dispersion resulting from wave-induced flow in porous rocks—A review. *GEOPHYSICS*, *75*(5), 75A147-75A164. https://doi.org/10.1190/1.3463417

Murphy, K. P. (with Internet Archive). (2012). *Machine learning: A probabilistic perspective*. Cambridge, Mass. : MIT Press. http://archive.org/details/machinelearningp0000murp

Murphy, W. F. (1982). Effects of partial water saturation on attenuation in Massilon sandstone and Vycor porous glass. *The Journal of the Acoustical Society of America*, *71*(6), 1458–1468. https://doi.org/10.1121/1.387843

Murphy, W. F., Winkler, K. W., & Kleinberg, R. L. (1986). Acoustic relaxation in sedimentary rocks; dependence on grain contacts and fluid saturation. *Geophysics*, *51*(3), 757–766. https://doi.org/10.1190/1.1442128

Nair, V., & Hinton, G. E. (2010). *Rectified Linear Units Improve Restricted Boltzmann Machines*. https://www.cs.toronto.edu/~fritz/absps/reluICML.pdf

Nyquist, H. (1928). Certain Topics in Telegraph Transmission Theory. *Transactions of the American Institute of Electrical Engineers*, *47*(2), 617–644. https://doi.org/10.1109/T-AIEE.1928.5055024

Odebeatu, E., Zhang, J., Chapman, M., Liu, E., & Li, X.-Y. (2006). Application of spectral decomposition to detection of dispersion anomalies associated with gas saturation. *The Leading Edge*, *25*(2), 206–210. https://doi.org/10.1190/1.2172314

Onajite, E. (2014). Chapter 2—Understanding Seismic Wave Propagation. In E. Onajite (Ed.), *Seismic Data Analysis Techniques in Hydrocarbon Exploration* (pp. 17–32). Elsevier. https://doi.org/10.1016/B978-0-12-420023-4.00002-2

Pal-Bathija, A., Prasad, M., Liang, H., Batzle, M., Lu, N., & Upmanyu, M. (2008, November 9). *Elastic Properties of Clay Minerals*. 2008 SEG Annual Meeting. https://dx.doi.org/

Papageorgiou, G., Amalokwu, K., & Chapman, M. (2016). Theoretical derivation of a Brie-like fluid mixing law: Brie-like fluid mixing law. *Geophysical Prospecting*, *64*(4), 1048–1053. https://doi.org/10.1111/1365-2478.12380

Papageorgiou, G., & Chapman, M. (2015). Multifluid squirt flow and hysteresis effects on the bulk modulus–water saturation relationship. *Geophysical Journal International*, *203*(2), 814–817. https://doi.org/10.1093/gji/ggv333

Papageorgiou, G., & Chapman, M. (2017). Wave-propagation in rocks saturated by two immiscible fluids. *Geophysical Journal International*, *209*(3), 1761–1767. https://doi.org/10.1093/gji/ggx128

Partyka, G., Gridley, J., & Lopez, J. (1999). Interpretational applications of spectral decomposition in reservoir characterization. *The Leading Edge*, *18*(3), 353–360. https://doi.org/10.1190/1.1438295

Perozzi, L., Gloaguen, E., Giroux, B., & Holliger, K. (2016). A stochastic inversion workflow for monitoring the distribution of CO2 injected into deep saline aquifers. *Computational Geosciences*, *20*(6), 1287–1300. https://doi.org/10.1007/s10596-016-9590-3

Prasad, M., Glubokovskikh, S., Daley, T., Oduwole, S., & Harbert, W. (2021). CO2 messes with rock physics. *The Leading Edge*, *40*(6), 424–432. https://doi.org/10.1190/tle40060424.1

Rahman, M. J., Fawad, M., & Mondol, N. H. (2020). Organic-rich shale caprock properties of potential CO2 storage sites in the northern North Sea, offshore Norway. *Marine and Petroleum Geology*, *122*, 104665. https://doi.org/10.1016/j.marpetgeo.2020.104665

Rashid, A. B., & Kausik, M. A. K. (2024). AI revolutionizing industries worldwide: A comprehensive overview of its diverse applications. *Hybrid Advances*, *7*, 100277. https://doi.org/10.1016/j.hybadv.2024.100277

Ren, H., Goloshubin, G., & Hilterman, F. J. (2009). Poroelastic analysis of amplitude-versus-frequency variations. *Geophysics*, *74*(6), N41–N48. https://doi.org/10.1190/1.3207863

Reuss, A. (1929). Berechnung der Fließgrenze von Mischkristallen auf Grund der Plastizitätsbedingung für Einkristalle . *ZAMM - Journal of Applied Mathematics and Mechanics / Zeitschrift Für Angewandte Mathematik Und Mechanik*, *9*(1), 49–58. https://doi.org/10.1002/zamm.19290090104

Ricker, N. (1953). The form and laws of propagation of seismic wavelets. *Geophysics*, *18*(1), 10–40. https://doi.org/10.1190/1.1437843

Russell, B. H. (1988). *Introduction to Seismic Inversion Methods*. Society of Exploration Geophysicists. https://doi.org/10.1190/1.9781560802303

Shannon, C. E. (1949). Communication in the Presence of Noise. *Proceedings of the IRE*, *37*(1), 10–21. https://doi.org/10.1109/JRPROC.1949.232969

Shuey, R. T. (1985). A simplification of the Zoeppritz equations. *GEOPHYSICS*, *50*(4), 609–614. https://doi.org/10.1190/1.1441936

Shute, V. J., Curt Fulwider, G., Liu, Z., & Rahimi, S. (2023). Machine learning. In *International Encyclopedia of Education(Fourth Edition)* (pp. 83–91). Elsevier. https://doi.org/10.1016/B978-0-12-818630-5.14013-8

Simm, R., & Bacon, M. (2014a). Fundamentals. In *Seismic Amplitude: An Interpreter's Handbook* (pp. 3–22). Cambridge University Press. https://doi.org/10.1017/CBO9780511984501.003

Simm, R., & Bacon, M. (2014b). Well to Seismic Ties. In *Seismic Amplitude: An Interpreter's Handbook* (pp. 38–57). Cambridge University Press. https://www.cambridge.org/core/books/seismic-amplitude/rock-physics-for-seismic-modelling/D4004732891AD6BA6F2CA0B4A657C09F

Simmons, G. (1965). Single Crystal Elastic Constants and Calculated Aggregate Properties. *Journal of the Graduate Research Center*, *34*(1). https://scholar.smu.edu/journal_grc/vol34/iss1/1

Smeaheia Dataset:CO2DataShare. (2021, February 23). https://doi.org/10.11582/2021.00012

Smith, T. M., Sondergeld, C. H., & Rai, C. S. (2003). Gassmann fluid substitutions: A tutorial. *Geophysics*, *68*(2), 430–440. https://doi.org/10.1190/1.1567211

Span, R., & Wagner, W. (1996). A New Equation of State for Carbon Dioxide Covering the Fluid Region from the Triple-Point Temperature to 1100 K at Pressures up to 800 MPa. *Journal of Physical and Chemical Reference Data*, *25*(6), 1509–1596. https://doi.org/10.1063/1.555991

Srivastava, N., Hinton, G., Krizhevsky, A., Sutskever, I., & Salakhutdinov, R. (2014). *Dropout: A Simple Way to Prevent Neural Networks from Overfitting*. https://www.cs.toronto.edu/~rsalakhu/papers/srivastava14a.pdf

Statoil. (2016, June). *Selected extracts from Statoil internal report on Subsurface Evaluation of Smeaheia as part of 2016 Feasibility study on CO2 storage in the Norwegian Continental shelf*. https://doi.org/10.11582/2021.00012

Sun, S. Z., Jiang, S., Sun, X., Yang, H., Han, J., & Li, Y. (2012, November 4). *Fluid Identification Using Frequency-Dependent AVO Inversion in Dissolution Caved Carbonate Reservoir*. 2012 SEG Annual Meeting. https://dx-doi-org.eux.idm.oclc.org/

Talisman, E. (2008). *Trow 32-2-1:End of Well Report* (PDF No. Volumes 1 & 2; p. 118). TALISMAN ENERGY NORGE AS. https://doi.org/10.11582/2021.00012

The wells 32/7-1 and 32/4-4 proved suitable properties for injection and storage of CO2. (2025, May 14). [Norwegian Offshore Directorate]. Norwegian Offshore Directorate. https://www.sodir.no/en/whats-new/news/exploration-drilling-results/2025/the-wells-327-1-and-324-4-proved-suitable-properties-for-injection-and-storage-of-co2/

Tisato, N., & Quintal, B. (2013). Measurements of seismic attenuation and transient fluid pressure in partially saturated Berea sandstone: Evidence of fluid flow on the mesoscopic scale. *Geophysical Journal International*, *195*(1), 342–351. https://doi.org/10.1093/gji/ggt259

Toksoz, M. N., Johnston, D. H., & Timur, A. (1979). Attenuation of seismic waves in dry and saturated rocks; I, Laboratory measurements. *Geophysics*, *44*(4), 681–690. https://doi.org/10.1190/1.1440969

Tosaya, C. A. (1982). *ACOUSTICAL PROPERTIES OF CLAY-BEARING ROCKS - ProQuest*. https://www.proquest.com/docview/303254949?pq-origsite=gscholar&fromopenview=true

Trow:32_2_1 (Version 2.0). (2020). [PETREL; LAS File]. https://doi.org/10.11582/2021.00012

Voigt, W. (1910). *Lehrbuch der Kristallphysik.*

Wang, P., Chen, X., Li, X., Cui, Y., & Li, J. (2021). Moduli variations in two-phase fluid rocks considering squirt flow and patchy saturation. *Journal of Petroleum Science and Engineering*, *206*, 109041. https://doi.org/10.1016/j.petrol.2021.109041

Wang, Y. (2007). Seismic time-frequency spectral decomposition by matching pursuit. *Geophysics*, *72*(1), V13–V20. https://doi.org/10.1190/1.2387109

Wang, Y. (2015). The Ricker wavelet and the Lambert W function. *Geophysical Journal International*, *200*(1), 111–115. https://doi.org/10.1093/gji/ggu384

Wang, Y. (2022a). Nonstationary Signals and Spectral Properties. In *Time–Frequency Analysis of Seismic Signals* (pp. 1–18). https://doi.org/10.1002/9781119892373.ch1

Wang, Y. (2022b). The Gabor Transform. In *Time–Frequency Analysis of Seismic Signals* (pp. 19–46). https://doi.org/10.1002/9781119892373.ch2

Wang, Z. (Zee). (2001). Y2K Tutorial: Fundamentals of seismic rock physics. *Geophysics*, *66*(2), 398–412. https://doi.org/10.1190/1.1444931

White, J. C., Williams, G. A., Grude, S., & Chadwick, R. A. (2015). Utilizing spectral decomposition to determine the distribution of injected CO_2 at the Snøhvit Field. *Geophysical Prospecting*, *63*(5), 1213–1223. https://doi.org/10.1111/1365-2478.12217

White, J. C., Williams, G., Chadwick, A., Furre, A.-K., & Kiær, A. (2018). Sleipner: The ongoing challenge to determine the thickness of a thin CO2 layer. *International Journal of Greenhouse Gas Control*, *69*, 81–95. https://doi.org/10.1016/j.ijggc.2017.10.006

Williams, G., & Chadwick, A. (2012). Quantitative seismic analysis of a thin layer of CO2 in the Sleipner injection plume. *GEOPHYSICS*, *77*(6), R245–R256. https://doi.org/10.1190/geo2011-0449.1

Wu, X., Chapman, M., Li, X.-Y., Angerer, E., & Boston, P. (2013, September 22). *Bayesian Inversion for Porosity and Saturation Using Frequency-Dependent Rock Physics Models*. 2013 SEG Annual Meeting. https://dx-doi-org.eux.idm.oclc.org/

Wu, X., Chapman, M., Li, X.-Y., & Boston, P. (2014a). Quantitative gas saturation estimation by frequency-dependent amplitude-versus-offset analysis. *Geophysical Prospecting*, *62*(6), 1224–1237. https://doi.org/10.1111/1365-2478.12179

Xu, D., Wang, Y., Gan, Q., & Tang, J. (2011). Frequency-dependent seismic reflection coefficient for discriminating gas reservoirs. *Journal of Geophysics and Engineering*, *8*(4), 508–513. https://doi.org/10.1088/1742-2132/8/4/003

Yan, Y., Borhani, T. N., Subraveti, S. G., Pai, K. N., Prasad, V., Rajendran, A., Nkulikiyinka, P., Asibor, J. O., Zhang, Z., Shao, D., Wang, L., Zhang, W., Yan, Y., Ampomah, W., You, J., Wang, M., Anthony, E. J., Manovic, V., & Clough, P. T. (2021). Harnessing the power of machine learning for carbon capture, utilisation, and storage (CCUS) – a state-of-the-art review. *Energy & Environmental Science*, *14*(12), 6122–6157. https://doi.org/10.1039/D1EE02395K

Yin, H., Zhao, J., Tang, G., Zhao, L., Ma, X., & Wang, S. (2017). Pressure and Fluid Effect on Frequency-Dependent Elastic Moduli in Fully Saturated Tight Sandstone. *Journal of Geophysical Research: Solid Earth*, *122*(11), 8925–8942. https://doi.org/10.1002/2017JB014244

Yun, A., & Song, I. (2022). Pore fluid substitution effects on elastic wave propagation in Berea sandstone: Implication to seismic monitoring of CO2 geologic storage. *International Journal of Greenhouse Gas Control*, *115*, 103609. https://doi.org/10.1016/j.ijggc.2022.103609

Zhang, M.-L., & Zhou, Z.-H. (2014). A Review on Multi-Label Learning Algorithms. *IEEE Transactions on Knowledge and Data Engineering*, *26*(8), 1819–1837. https://doi.org/10.1109/TKDE.2013.39

Zhao, T., Wang, S., Ouyang, C., Chen, M., Liu, C., Zhang, J., Yu, L., Wang, F., Xie, Y., Li, J., Wang, F., Grunwald, S., Wong, B. M., Zhang, F., Qian, Z., Xu, Y., Yu, C., Han, W., Sun, T., … Wang, L. (2024). Artificial intelligence for geoscience: Progress, challenges, and perspectives. *The Innovation*, *5*(5), 100691. https://doi.org/10.1016/j.xinn.2024.100691

Zhu, X., & McMechan, G. A. (1990, September 23). *Direct Estimation of the Bulk Modulus of the Frame In a Fluid-saturated Elastic Medium By Biot Theory*. 1990 SEG Annual Meeting. https://onepetro-org.ezproxy.is.ed.ac.uk/SEGAM/proceedings/SEG90/All-SEG90/SEG-1990-0787/82026

Zucchet, N., & Orvieto, A. (2024). *Recurrent neural networks: Vanishing and exploding gradients are not the end of the story* (No. arXiv:2405.21064). arXiv. https://doi.org/10.48550/arXiv.2405.21064